ULTRASONIC SUBWAVELENGTH ACOUSTIC FOCUSING AND IMAGING USING A 2D MEMBRANE METAMATERIAL

A Thesis
Presented to
The Academic Faculty

by

Shane Lani

In Partial Fulfillment
of the Requirements for the Degree
Doctor of Philosophy in the
School of Mechanical Engineering

Georgia Institute of Technology
May 2015

ULTRASONIC SUBWAVELENGTH ACOUSTIC FOCUSING AND IMAGING USING A 2D MEMBRANE METAMATERIAL

Approved by:

Dr. Karim G. Sabra, Advisor
School of Mechanical Engineering
Georgia Institute of Technology

Dr. F. Levent Degertekin, Advisor
School of Mechanical Engineeing
Georgia Institute of Technology

Dr. Michael Leamy
School of Mechanical Engineering
Georgia Institute of Technology

Dr. Massimo Ruzzene
School of Aerospace Engineering
Georgia Institute of Technology

Dr. William D. Hunt
School of Electrical and Computer Engineering
Georgia Institute of Technology

Date Approved: March 4, 2015

To my ever loving and supportive wife, Jenette

ACKNOWLEDGEMENTS

Looking back over the previous five years, it is clear that I would not have been able to compile this document without the help of numerous people. These people include my family, my coworkers, and my advisors. Thank you all.

The biggest help has been from my family. My wife, Jenette, has supported me completely during the grueling years of research. She was especially helpful during hard times of studying for the qualifier exams and writing the theses. I do not know how she did it, but I thank her very much. Also I want to thank my daughter Callie for being the perfect distraction. You were always able to make all the stress from work just melt away. My Mom and Dad also deserve a huge thanks for all the support and nurturing they have given me over the years, and I need to thank my Dad explicitly for taking time to edit this entire document.

The next group of people I would like to thank are my coworkers who are too numerous to name, but you know who you are. They have helped me out from when I first started here all the way through until graduation. They have helped by teaching me new instruments, by advising me on other fields of study, by lending me time on a laser, or just being there for a needed distraction. It has really been a pleasure working alongside very intelligent and interesting people, thank you.

Finally, I would like to thank my advisors Dr. Karim Sabra and Dr. F. Levent Degertekin. I can still recall the day that Dr. Sabra came up to me during a visit to Tech and talked to me about using sound to image. From that moment I knew what I wanted to study. I have been very fortunate that I have been able to work on very fruitful and

productive projects under both advisors. I have learned a lot from each of them from acoustics, to leadership, to management. Thank you both very much, it has been a real pleasure.

TABLE OF CONTENTS

Page

LIST OF TABLES

LIST OF FIGURES

Page

SUMMARY

A metasurface or 2D metamaterial composed of a membrane array can support an interesting acoustic wave field. These waves are evanescent in the direction normal to the array and can propagate in the immersion fluid immediately above the metasurface. These waves are a result of the resonant membranes coupling to the fluid medium and propagate with a group and phase speed lower than that of the bulk waves in the surrounding fluid. This work examines and utilizes these evanescent surface waves using Capacitively Micromachined Ultrasonic Transducers (CMUT) as a specific example. CMUT arrays can generate and detect membrane displacement capacitively, and are shown to support the surface waves capable of subwavelength focusing.

A model is developed that can solve for the modes of the membrane array in addition to transiently modeling the behavior of the array. It is found that the dispersive nature of the waves is dependent on the behavior of the trapped modes of the membrane array. Two-dimensional dispersion analysis of the metasurface shows evidence of four distinct frequency bands of surface wave propagation: isotropic, anisotropic, directional band gap, and complete band gap around the first resonance of the membrane. Some of the frequencies in the partial band gap show concave equifrequency contours capable of negative refraction. The dispersion and modal properties were also examined as to how they are affected by basic array parameters.

Potential applications of this wave field are examined in the context of subwavelength focusing and imaging. Several methods of acoustic focusing are used on an array consisting of dense grid of membranes and several membranes spatially removed

from the structure. Subwavelength acoustic focusing to a resolution of $\lambda/5$, limited by the size of one membrane, is shown in simulations and verified with experiments. This focus can be achieved to any membrane in the control array of 7x7. An imaging test is also performed in which a subwavelength defect is localized. The imaging method uses the fact that any object placed on or near the array distorts the evanescent wave field. Hence, the information contained in the distorted signals is extracted to locate the defect. This fundamental work in characterizing the waves above the membrane metasurfaces is expected to have impact and implications for transducer design, resonant sensors, 2D acoustic lenses, and subwavelength focusing and imaging.

CHAPTER 1

INTRODUCTION

1.1. Prologue

One of the first interesting problems encountered by acoustic students is what happens when an incident pressure wave encounters an interface. If the first medium happens to have a slower sound speed than the second medium, there exists a critical angle. For incident waves greater than the critical angle (with the angle being measured from normal), all of the energy is reflected back into the first medium. If the acoustics instructor is thorough, then they will also mention to the students that the transmitted wave still has a solution which is an evanescent wave travelling along the interface with energy decaying away from the interface. These evanescent waves are often neglected. However, evanescent waves are the key to subwavelength imaging, or imaging with resolution finer than the wavelength of the signal. This dissertation studies evanescent waves propagating above a surface of membrane arrays. These waves are modeled to determine the waves' properties and if these properties could be utilized for the potential development of subwavelength focusing and imaging systems.

In my initial phase of researching these waves, I referenced them as acoustic crosstalk. Acoustic crosstalk is a term used in transducer design that refers to the acoustic disturbances that one transducer has on its neighbors. In other terms, when one transducer is vibrating (transmitting or receiving) the vibrations travel through the surrounding fluid and subsequently vibrate neighboring transducers. I learned when I started working with capacitive micromachined ultrasonic transducers (CMUTs) that acoustic crosstalk can be a problem. The

CMUTs are ultrasonic transducers, but differ from the more commonly known piezoelectric varieties that are used for medical ultrasounds and non destructive evaluation. CMUTs detect and transmit electrostatically as opposed piezoelectric transducers which operate by the piezoelectric effect. A current application of CMUT is medical imaging which uses a pulse echo method. For these applications, the transducer array emits a strong pulse and then captures the reflections from the various interfaces it encounters to construct an image. This type of imaging requires a dense transducer array with the individual elements being spaced very close together which leads to strong acoustic crosstalk. The acoustic crosstalk is detrimental to the far field imaging capabilities of transducer arrays and hence a topic that needs additional investigation. However, my original objective was not to study these waves to enhance the far field application of the transducer arrays, although such work does give good insight on this topic as well. It was to understand the physics and propagation of these waves and the potential for applications to near field acoustic focusing and imaging.

1.2. Overview

The primary objective of this research is to study and characterize the propagation of evanescent surface waves traveling across a membrane array. The same evanescent waves that comprise the main component of acoustic crosstalk with CMUT arrays has also been called "Spoof Surface Acoustic Waves (SSAW)," "Rayleigh-Bloch waves," and "Dispersive Guided Modes" [3, 7, 36, 44, 65]. In considering these waves in a larger context, it is shown that the array structure and membrane resonances support the evanescent waves and the wave propagation [45]. These waves are modeled with a semi-analytic model with the results being verified by experiments. The model allows for testing of many different array structures and gives insight to how different parameters affect the evanescent waves. The fundamental study of

these waves leads to potential applications of subwavelength focusing and imaging in the ultrasonic regime. Several other important implications of this research pertain to the research areas of metamaterials, transducer array design, and resonant sensors and will be highlighted throughout the document.

1.3. Motivation

The fundamental motivation to this work is to obtain a near field imaging system that can image at subwavelength scales. The imaging system sought is different from the majority of the imaging techniques which sends waves into a medium and then compile an image from the reflections of those waves. The majority those imaging systems are limited by diffraction, Rayleigh criterion, and hence the best resolution is limited to $\lambda/2$, where λ corresponds to the wavelength of the wave [59]. An example of the Rayleigh criterion in which two sources are distinguished with different separations is shown in Fig. 1.1. The only way to obtain resolutions better than $\lambda/2$ is to use an evanescent wave field [59].

The imaging system proposed would consist of a membrane array metasurface. Above the membranes an evanescent field exist which carries information at the subwavelength scales [45]. The imaging system would control the evanescent wave field and each membrane in the array would be one pixel in the near field image. The goal of this imaging system would be to extract the changes from subwavelength targets such as cells or other matter that would rest on the surface of the array as shown in Fig. 1.2.

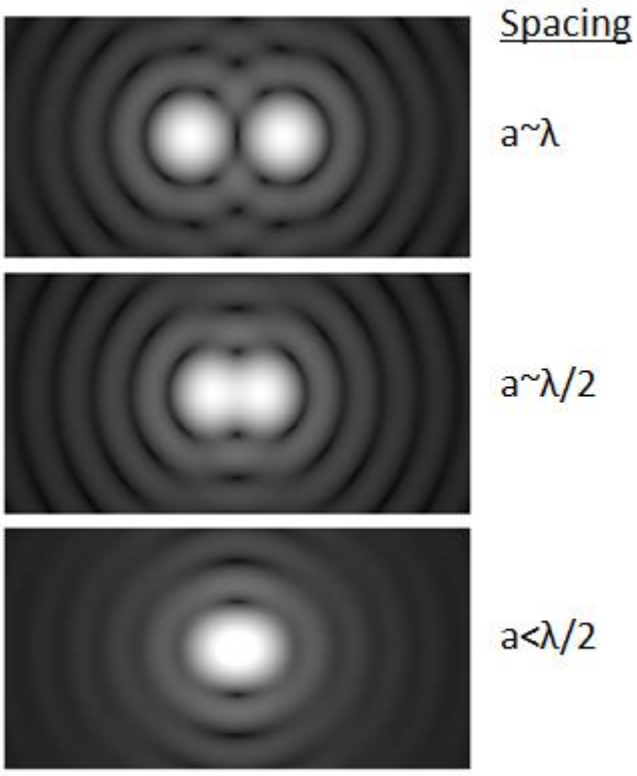

Figure 1.1 Example of the Rayleigh criterion with regard to resolving two sources with different separations. For spacing less than λ/2 the sources cannot be distinguished when only using information from propagating waves, but can be if information from evanescent waves is available.

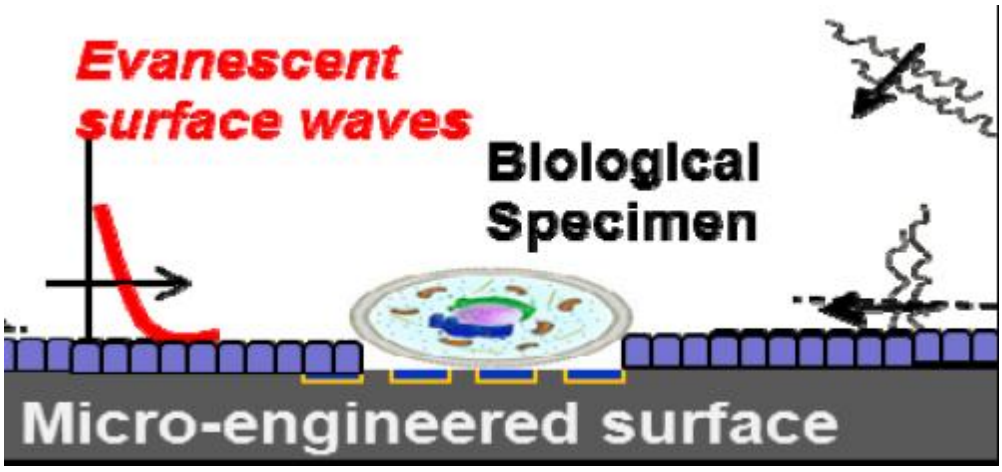

Figure 1.2 Example of imaging system using evanescent waves to obtain a subwavelength image of a specimen.

1.4. Objectives

The first step in this research is to complete a broad literature review of metamaterials which are composite structures with resonant inclusions, similar to the membrane arrays in this work. The literature review will aid in understanding how these materials are characterized so that similar methods can be applied to the membrane array (Chapter 2). Some interesting wave phenomena exhibited by metamaterials include negative effective mass density, band gaps, and negative refraction. Hence, the first objective is to understand how metamaterials are characterized and evaluated so that the evanescent waves above the membrane arrays can be evaluated similarly.

The second objective is to develop or adapt a model capable of simulating the evanescent waves above the membrane arrays (Chapter 3). This model needs to efficiently simulate the membrane dynamics, the acoustic propagation, and the electromechanical actuation when the membranes are modeled as CMUTs. There are already many different models available to model CMUTs, including finite element analysis (FEA) and analytical methods that can be used or adapted for the purposes of this work [3, 23, 29, 54, 66].

For this work, a semi-analytic model is used to characterize the evanescent waves on the membrane arrays (Chapter 4). The model solves the modes of the structure and compares the properties of the modes to the transiently propagating evanescent waves. The properties of the evanescent waves that are examined include the dispersion relationship, transmission through the array, and occurrence of band gaps in both 1D and 2D. These properties are then verified with experiments on a membrane array in addition to showing that an array of CMUTs acts as a tunable metasurface (Chapter 5).

Once the evanescent waves are characterized, then their use in potential applications is determined. Two interesting potential applications include subwavelength focusing of acoustic energy and subwavelength imaging (Chapter 6). Several methods of subwavelength focusing and imaging will be presented along with simulation results and experimental verification.

The key contributions of this research are as follows:

- Using modal analysis, the modes of the membrane array are calculated, along with their resonant frequency, wavenumber, and quality factor and compared to the propagating evanescent waves to illustrate how the supporting structure effects the wave propagation. (Chapter 4)
- The mode's properties and dispersion is examined to how they are altered by varying parameters such as pitch and membrane variation
- The dispersion relation and transmission of the evanescent waves across the arrays are simulated and experimentally verified (Chapter 5)
- Evidence of concave equifrequency contours in the 2D dispersion analysis indicates that this material exhibits the potential for negative refraction (Chapter 4).
- Subwavelength focusing to focal widths of $\lambda/5$ as limited to the dimensions of a single membrane is demonstrated both in simulation and with experimental verification by using a method of time reversal (Chapter 6)
- Subwavelength imaging by localizing a subwavelength defect is simulated and experimentally verified using time reversal methods

CHAPTER 2

ACOUSTIC METAMATERIALS

Metamaterials and phononic crystals are composite structures that exhibit interesting properties such as band gaps, negative group velocity, and negative refraction. These properties result from different mechanisms. In phononic crystals, the properties are due to Bragg scattering. While in metamaterials, the properties are due to interactions between the locally resonant inclusions. This chapter reviews the relevant literature in regard to metamaterials, metasurfaces, focusing with metamaterials and phononic crystals, and imaging. One section also describes the past work concerning acoustic crosstalk on CMUT arrays and their operation and fabrication as these arrays are used for experimental verification as a specific example of membrane arrays. Concurrent with this review, basic principles of wave propagation are explained that are used in later chapters.

2.1. Properties of Phononic Crystals and Metamaterials

2.1.1. Band Gaps

Both phononic crystals and acoustic metamaterials tailor elastic wave dispersion, but in different manners. Phononic crystals derive their band structures from Bragg scattering which requires the spacing between scatters to be close to the wavelength of the wave. The phononic crystal has forbidden bands or band gaps in frequency ranges in which the scattered waves exhibit destructive interferences resulting in incident waves not propagating through the composite structure. Metamaterials can also have band gaps, but these are due to the inclusions

of local resonances. These inclusions can be spaced much smaller than a wavelength and do not need to be periodically arranged to exhibit band gaps [19]. Band gaps have been shown to exist in phononic crystals and metamaterials for bulk waves traveling through 3D materials, lamb waves in 2D plates, as well as surface acoustic waves above 2D structures [19, 33, 36, 80].

2.1.2. Negative Refraction

Subwavelength focusing and imaging with acoustic waves has been performed with both phononic crystals and metamaterials, primarily by using negative refractive materials [1, 35, 73, 74, 86, 90]. These types of materials refract waves differently than normal materials. The refraction angle, θ', is governed by Snell's Law in terms of the incident angle, θ, and the associated refractive indices, n_1 and n_2, which is given in Eq. (2.1) and illustrated in Fig. 2.1.

$$\frac{\sin(\theta)}{\sin(\theta')} = \frac{n_1}{n_2} \tag{2.1}$$

For a material with a negative refractive index, the refracted angle is negatively refracted as shown by the dashed line in Fig. 2.1. In 2000, Pendry showed how negative refraction with a 2D material can be used to make a superlens which allows the focusing of both the propagating and evanescent waves [61]. The focusing is accomplished by using a flat lens that exhibits negative refraction and allows the propagation of the evanescent field as shown in Fig. 2.2. The rays are emitted from a source on the left side of the lens, negatively refracted at the first edge of the lens, cross each other inside the negative refractive material, and then are negatively refracted again when entering back into the surrounding medium and focusing with subwavelength resolution.

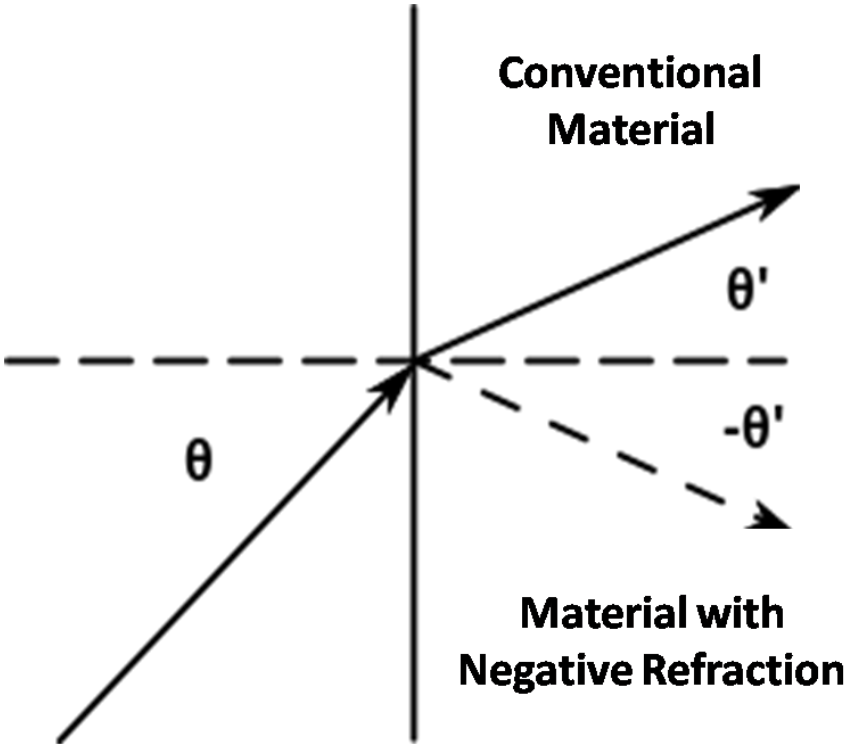

Figure 2.1 Example of refraction for a conventional material and material that exhibits negative refraction

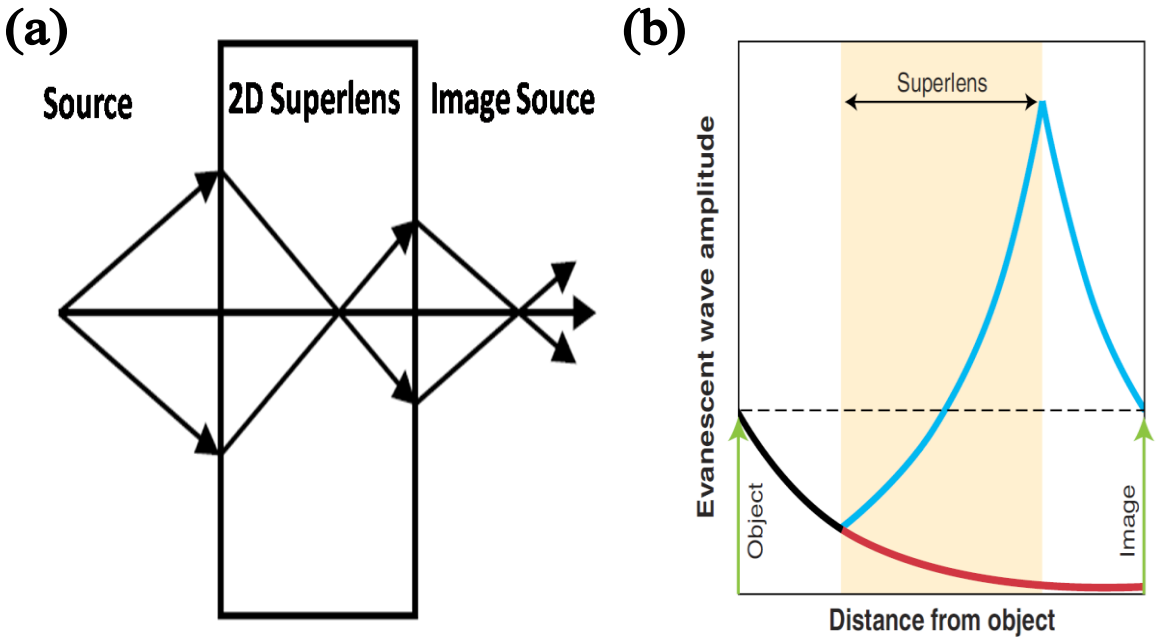

Figure 2.2 Focusing from negative refraction with a 2D superlens (a) showing the rays undergoing negative refraction and (b) Showing the how the amplitude of the evanescent waves are increased through a 2D superlens [adapted from 61 and 71]

Since the refractive index, n, depends on both the bulk modulus, β, and the mass density, ρ, both of these values need to be negative to exhibit a negative refractive material [19, 39].

$$n = \sqrt{\frac{\rho}{\beta}} \tag{2.2}$$

A few acoustic metamaterials have been fabricated that exhibited negative effective mass density and then negative effective bulk modulus and capable of negative refraction [21, 86], but the majority of examples using negative refraction use a different method.

The other way to have negative refraction is to have concave equifrequency contours, also known slowness curves or wavenumber-wavenumber plots. A typical non-dispersive medium has circular frequency contours. If these contours are concave, the materials exhibit negative refraction. The frequency contour for a 3D phononic crystal of tungsten beads is shown from the work of Yang et al. in Fig. 2.3. Notice that while the 1.66 MHz contour is roughly circular, the frequency contour at 1.57 MHz has concave edges. In this narrow frequency range, the phononic crystal exhibits negative refraction while behaving more conventionally at other frequencies. While Yang et al. did not achieve a subwavelength focal spot, others succeeded using the same principles with the majority of this research using bulk waves for focusing [35, 72, 87, 89].

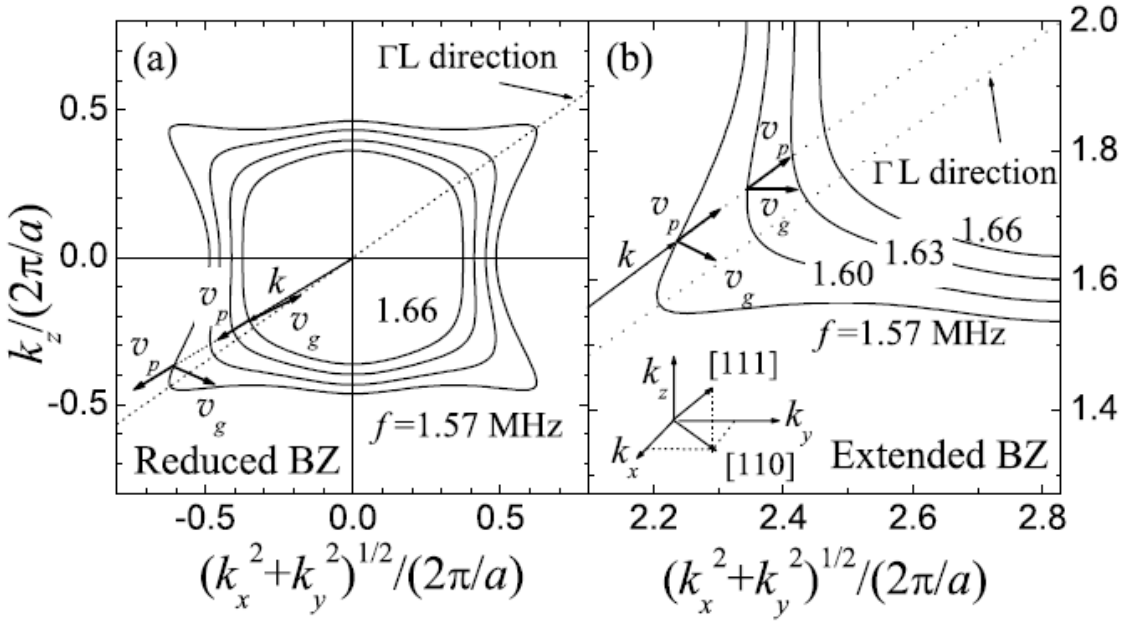

Figure 2.3 Equifrequency surfaces at frequencies near 1.60MHz in the reduced (a) and extended Brillouin zones (b) [87]

2.2. Dispersion Relation and Derivations of 1D Structures

This section summarizes the derivation of the dispersion relation for a 1D phononic crystal and the effective mass density for acoustic metamaterials [19]. Throughout the derivations, important terminology and figures will be explained and examined.

2.2.1. 1D Phononic Crystal

A 1D phononic crystal can be modeled as an infinite chain of springs and masses as shown in Fig. 2.4. Each mass and spring in the monotonic configuration is the same and is denoted by m or β respectively and is separated by a distance of a. The equation of motion for the n^{th} mass is given by the following equation.

$$m\frac{d^2u_n}{dt^2} = \boldsymbol{\beta}(\mathbf{u_{n+1}} - \mathbf{2u_n} + \mathbf{u_{n-1}})$$

(2.3)

The equation of motion (Eq. 2.3) can be solved by assuming a solution of a propagating wave (Eq. 2.4).

$$u_n = Ae^{i(kna+\omega t)}$$

(2.4)

The wavenumber and angular frequency are denoted by k and ω respectively. The dispersion relation for propagating waves can be solved and is given by:

$$\omega(k) = \omega_0 \left|\sin\left(\frac{ka}{2}\right)\right|$$

(2.5)

where ω_0 is the upper limit of the angular frequency given by $\omega_0 = 2\sqrt{\beta/m}$. Figure 2.5 is the dispersion relation plotted on a frequency-wavenumber plot as solid black curves. The y-axis corresponds to the angular frequency while the x-axis corresponds to the wavenumber. The wavenumbers are displayed from $-\pi/a$ to π/a. Traveling waves with a wavelength greater than 2a ($\lambda=2\pi/k>2a$) can be represented within the fundamental period. This fundamental period $k \in \left[-\frac{\pi}{a}, \frac{\pi}{a}\right]$ corresponds to first Brillouin zone. From the dispersion relation there are two important wave parameters that can be determined, the phase speed and the group velocity. The phase speed is the speed at which a wavefront is traveling and is given by the following:

$$c_{ph} = \frac{\omega}{k}.$$

(2.6)

The group velocity is defined as:

$$c_{gp} = \frac{\partial\omega}{\partial k},$$

(2.7)

and is the speed at which energy propagates. From Fig. 2.5 it is clear that the phase speed and the group velocity change with various wavenumbers. However, in a nondispersive medium (such as bulk waves through fluids), the dispersion relation is linear (as shown with the black dashed line) and has the same phase speed and group velocities for all wavenumbers.

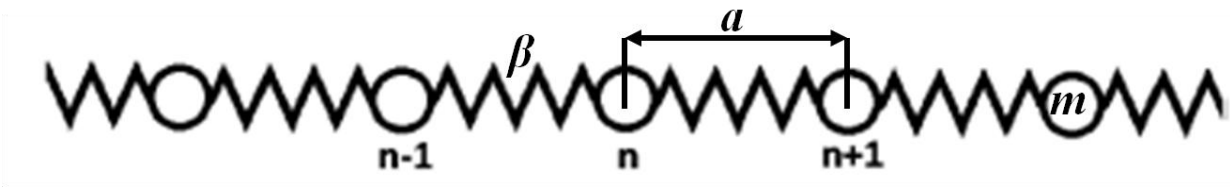

Figure 2.4 Schematic of a 1D monotomic phononic crystal. [Adapted from 19]

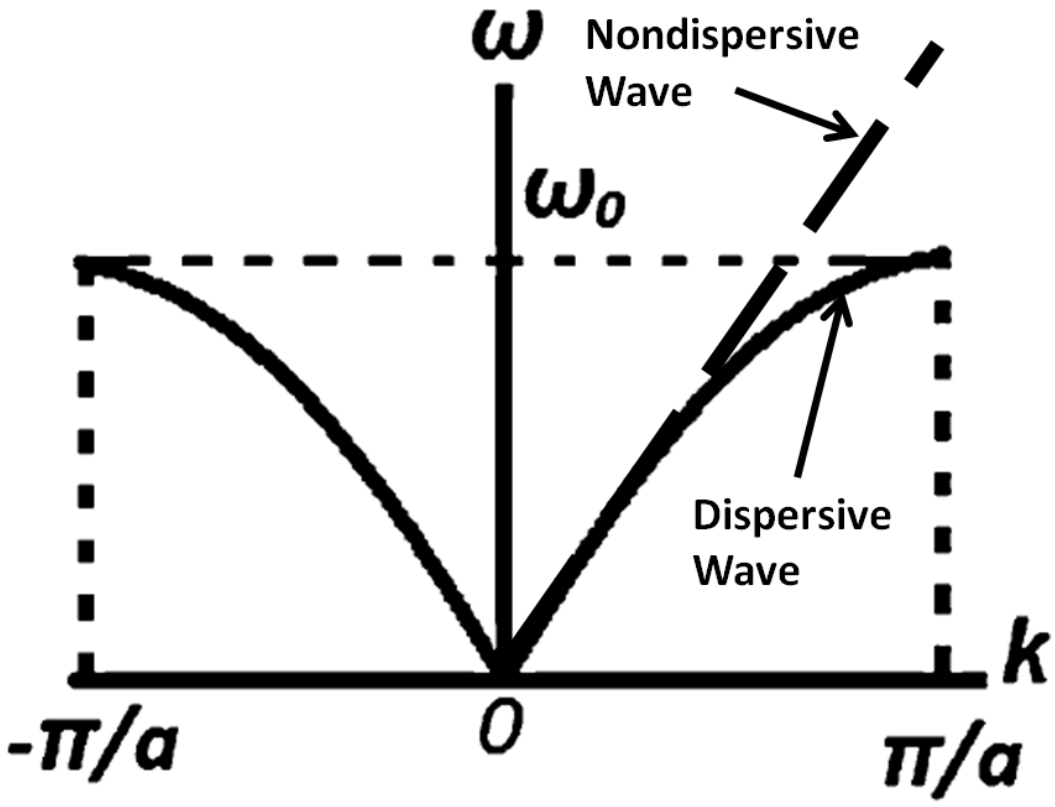

Figure 2.5 Wavenumber-frequency plot of the dispersion curve (black line) of the 1D chain of springs and masses compared to the dispersion relation of a nondispersive medium (black dashed line). [Adapted from 19]

To determine what occurs above the cut off frequency of $\omega_{0,}$ a new solution of nonpropagating or evanescent waves can be assumed and substituted into Eq. (2.3).

$$u_n = Ae^{Im(k)na}e^{i(Re(k)na+\omega t)} \tag{2.8}$$

In this case, the wavenumber is a complex value and *Im(k)* is the imaginary component of the wavenumber and *Re(k)* is the real part. A solution exists when the *Re(k)*=π/a and $\omega>\omega_0$ and is given by

$$\omega = \omega_0 cosh(Im(k)a/2)\ for\ \omega > \omega_0. \tag{2.9}$$

The combined solution of the propagating waves and evanescent waves show that only evanescent waves propagate above an angular frequency of ω_0. Consequently, ω_0 is the start of a band gap.

2.2.2. 1D Metamaterial

An acoustic metamaterial obtains its dispersion from the inclusions of local resonances in the composite structure. When a wave passes through a medium, it is usually assumed that all constituents of the medium are moving in unison or in phase. However, this is not the case with a composite medium with embedded resonators which can actually have acceleration in the opposite direction of the forcing for certain frequencies. An example of a 1D acoustic metamaterial, a rigid bar of mass M_0 and with *n* resonators contained within the bar, is shown in Fig. 2.6. There are two displacements that are tracked, the displacement of the rigid bar, U, and the displacement of the inclusion mass, u, with the inclusion having a mass of m. The solution to the force balance to an external forcing input is given by Eq. (2.10). Additional details of the solution can be found in the reference [19].

$$F = (-i\omega)^2[M_0U + nmu] = (-i\omega)^2\left(D_{eff}V\right)U. \tag{2.10}$$

where D_{eff} is the dynamic mass density and V is the total volume of the system. The dynamic mass can be rewritten.

$$D_{eff}V = \frac{F}{(-\omega^2 U)} = M_0 + \frac{nmu}{U} = M_0 + \frac{nm}{1 - (\omega^2/\omega_0^2)} \tag{2.11}$$

with ω_0 = 2K/m. It is clear from the above equation that for some frequencies the dynamic mass density can be negative, namely for angular frequencies above ω_0 in this example.

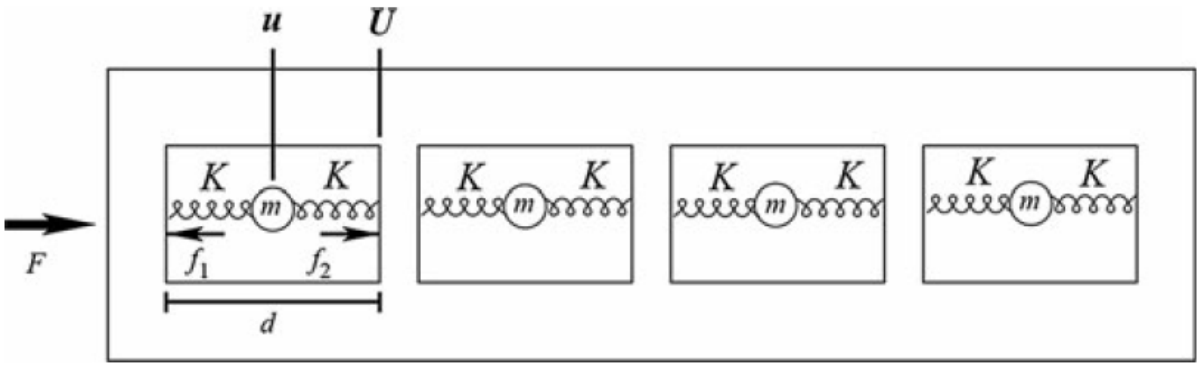

Figure 2.6 Representation of a 1D metamaterial which is a solid structure with local resonances present within the structure [19].

2.3. Membrane Metamaterials, CMUTs, and Metasurfaces

This section examines the most pertinent recent literature as it pertains to the related topics of membrane metamaterials, acoustic crosstalk on CMUT arrays, and the propagation of surface waves above metasurfaces. Two applications of these structures are also reviewed. The first being focusing of acoustic energy using a time reversal method. The second application is subwavelength focusing and imaging using metamaterials and metasurfaces.

2.3.1. Membrane Metamaterials

As membranes are an attractive method for low frequency sound absorption, the use of membranes as metamaterials has been previously examined. However, these studies were not focused on the interaction of surface acoustic waves on the structures [53, 58, 86, 91]. Some of these studies utilized a stacked structure of membranes [58] or membranes with hybrid resonances [53] to optimize the absorption properties of the structures from waves incident on the metamaterial. In addition to the absorption properties, a dual membrane structure was shown to have simultaneous negative mass density and negative bulk modulus [86]. Furthermore, a cell

of three membranes was used as a metasurface, but only for the study of absorption from incident waves, not for waves traveling across the surface of the membranes as is discussed in this work [53].

2.3.2. CMUTs and Acoustic Crosstalk

The particular membrane arrays that are used for this work are Capacitive Micromachined Ultrasonic Transducer (CMUT) arrays. These transducers are comprised of many micromachined thin membranes that can be actuated and detected electrostatically. When operated in immersion, the mechanical coupling between the CMUT membranes results in acoustic crosstalk within the array [3, 22, 37]. The main component of acoustic crosstalk is an evanescent wave above the CMUT array.

CMUT Operation

The CMUTs utilized in this research are fabricated at the Georgia Institute of Technology using a low temperature plasma-enhanced chemical-vapor deposition (PECVD) nitride process [40]. A schematic of the cross-section of a CMUT membrane is shown in Fig. 2.7 (not to scale). Each membrane contains a parallel plate capacitor with the bottom electrode being fixed and the top electrode being imbedded in a flexible top membrane. Separating the electrodes is a vacuum gap and dielectric material. When DC voltage is applied across the electrodes, the top membrane deflects towards the bottom electrode. If an AC voltage is applied to the electrodes, the membrane will oscillate concurrently with the voltage. Consequently, the membrane movement will transmit pressure waves into the surrounding fluid. The CMUT also acts as a receiver by generating an AC current when stimulated by incoming pressure waves [30].

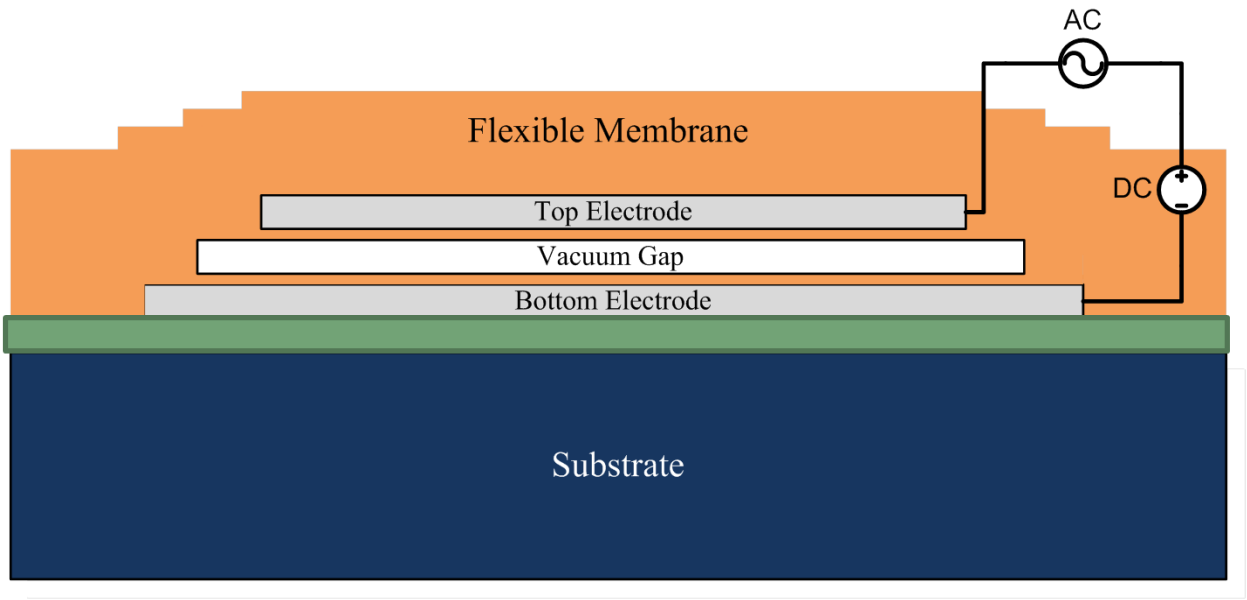

Figure 2.7 Cutaway schematic of a CMUT (dimensions are not to scale for better visualization)

Acoustic Crosstalk in CMUT Arrays

For a typical CMUT array operating in immersion, the acoustic crosstalk is the result from a combination of Lamb waves, Scholte waves, and the dispersive surface waves. The acoustic crosstalk waves that are the most interesting to this research are the dispersive surface waves that propagate above the CMUT array in the semi-infinite fluid. Figure 2.8 is a frequency-wavenumber plot from Bayram et al. which illustrates the different types of waves present in acoustic crosstalk above CMUT arrays. Notice that the wave denoted as the dispersive guided mode is stronger by 25 dB than both the Scholte and Lamb waves [3].

These surface acoustic waves have been analyzed and found to be the source of undesired crosstalk and resonances. These undesired effects degrade the performance of the array in the frequency regime of the crosstalk by a poor angular response and range resolution [3, 10, 20, 22, 29, 66, 82]. Considerable research has been done to reduce the effects of these waves [3, 20, 22, 34, 82]. Boulme et al. performed a modal decomposition for a small 1-D CMUT array and

analyzed radiated pressure from each mode, but the method was not thoroughly detailed [7]. Most recently, similar results are obtained using an electrical impedance based approach [2].

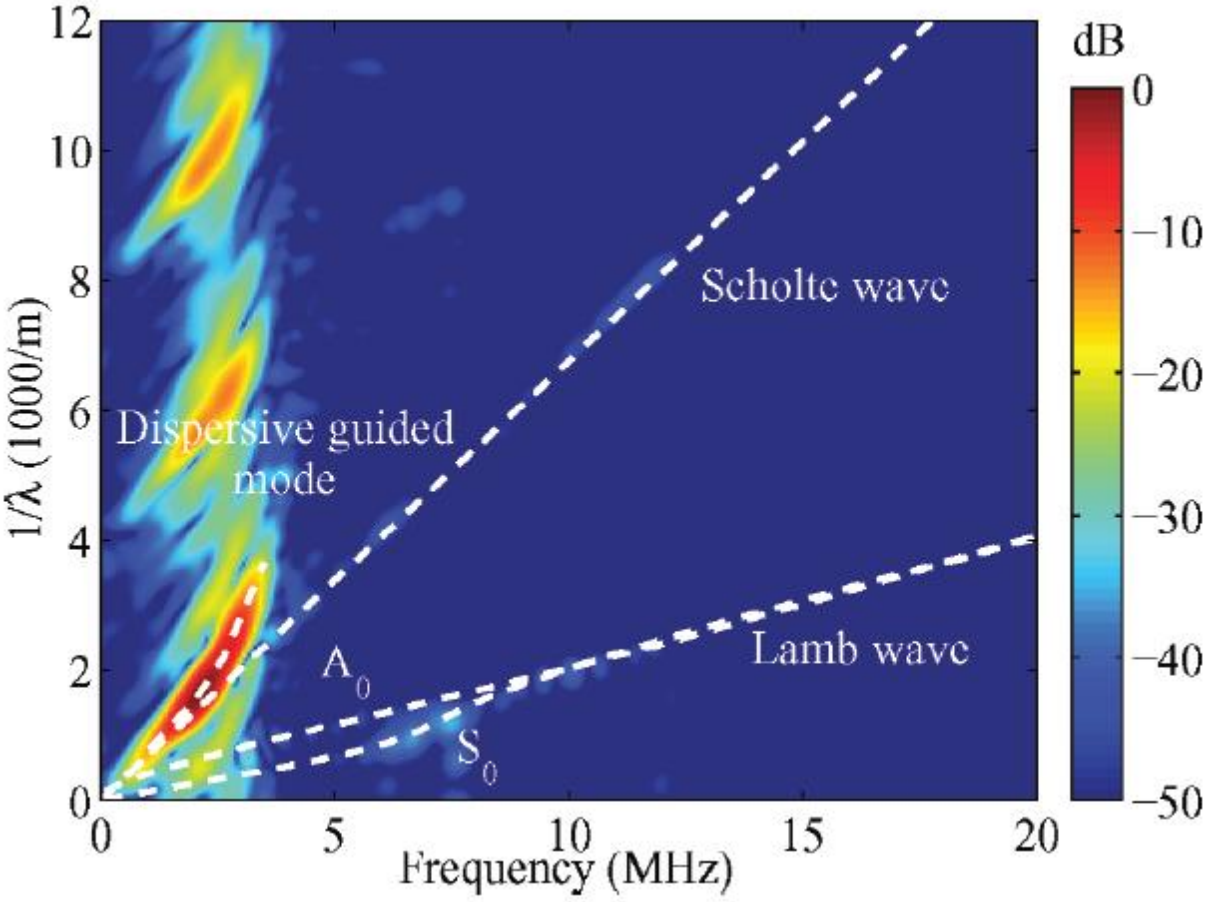

Figure 2.8 Experimental frequency-wavenumber plot depicting the different waves present in acoustic crosstalk of CMUT arrays in immersion [3]

2.3.3. Metasurfaces

Previous studies of the propagation of the surface acoustic waves above a 1D or 2D metasurfaces typically used structures fabricated out of a rigid substrate with corrugations for a 1D case or holes drilled into the substrate for a 2D case. The 1D case of a corrugated surface or grating has been studied by researchers who understood that the grating affected the speed of the wave directly above the surface in addition to the presence of band gaps [12, 33, 38, 52, 65, 93].

These results and structures have also found use in extraordinary transmission [52] and collimation of acoustic energy [12, 93]. The 2D equivalents have been shown to have interesting features such as tunable stop bands, negative refraction, subwavelength focusing, and gradient index lenses [6, 36, 43, 45, 80, 89]. An elegant demonstration of subwavelength focusing was conducted with a metasurface of soda cans and a time reversal method. Additionally this effort analyzed the modal response of the metasurface, a technique which will be explored further in this paper [47].

2.3.4. Focusing Above a Metasurface Using Time Reversal

In 2011, Lemoult et al. used time reversal techniques to achieve subwavelength focusing above a metamaterial of soda cans [47]. The evanescent wave field above the soda cans resulted from the acoustic coupling of the 49 Helmholtz resonators through the air. The experimental setup, illustrated in Fig. 2.9, shows the excitation speakers (1) positioned in the far field from the metamaterial grid of Helmholtz resonators (2). The field was measured by recording the pressure field with a microphone (3) controlled by a moveable stage (5).

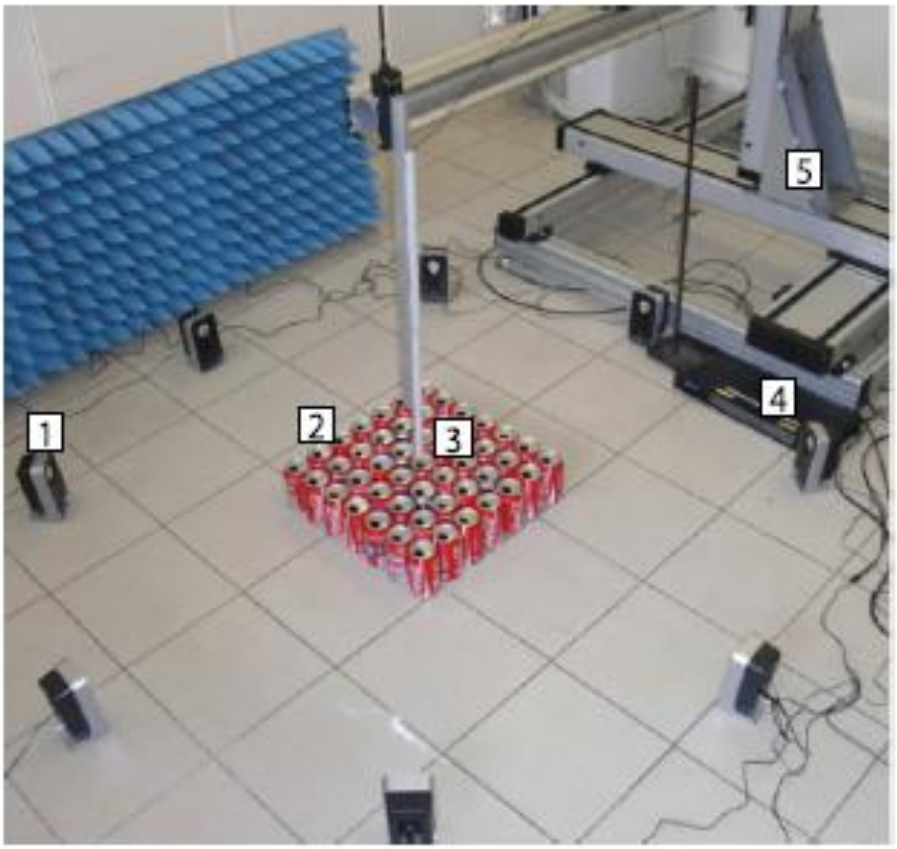

Figure 2.9 Setup of subwavelength focusing above a metamaterial of soda cans [47]

A time reversal technique was used focus acoustic intensity above the cans. This technique relies on acoustic reciprocity to achieve focusing and can be broken into the following three steps which are explained in more detail in Chapter 6.

- Pulse from the desired eventual focal point and record the temporal response on an array of exterior transducers.
- Time reverse the signal received on each of the exterior transducers (phase conjugation).
- Play back the time reversed signal through the exterior transducers to obtain a focus at the location of the original pulser

A diagram explaining the process is shown in Fig. 2.10.

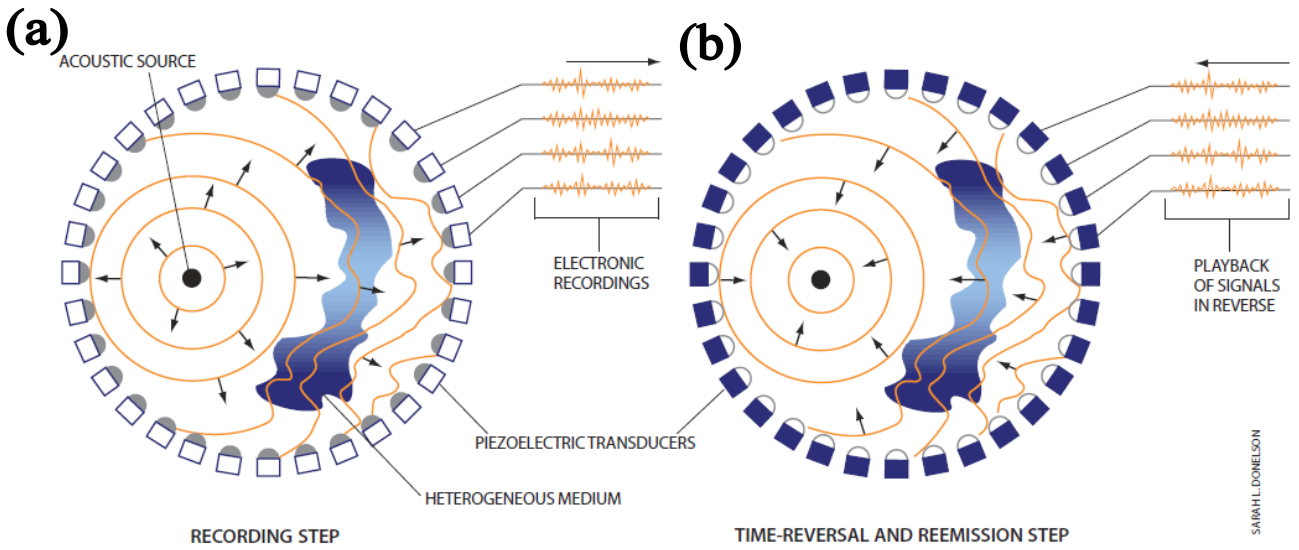

Figure 2.10 Time reversal works by (a) first pulsing from an acoustic source which is then recorded on an array of transducers. (b) The captured signals can then be time reversed and retransmitted which results in a focus of acoustic energy in the location of the original acoustic source [25]

The time reversal focusing results from Lemoult et al. are shown in Fig. 2.11(c,d) and compared to focusing in which no metamaterial is present Fig 2.11(a,b). One drawback of time reversal is that it only accounts for the phase information. Hence, any frequencies that are highly attenuated or not easily excited from the far field sources are not compensated with time reversal. To remedy this shortcoming and undo the information lost by attenuation, Lemoult et al. used an iterative method of time reversal to enhance the focusing from $\lambda/8$ to $\lambda/25$ as shown in Fig. 2.11(e,f) [25, 56]. These methods are used in this work to achieve subwavelength focusing and imaging above a membrane array in the ultrasonic regime.

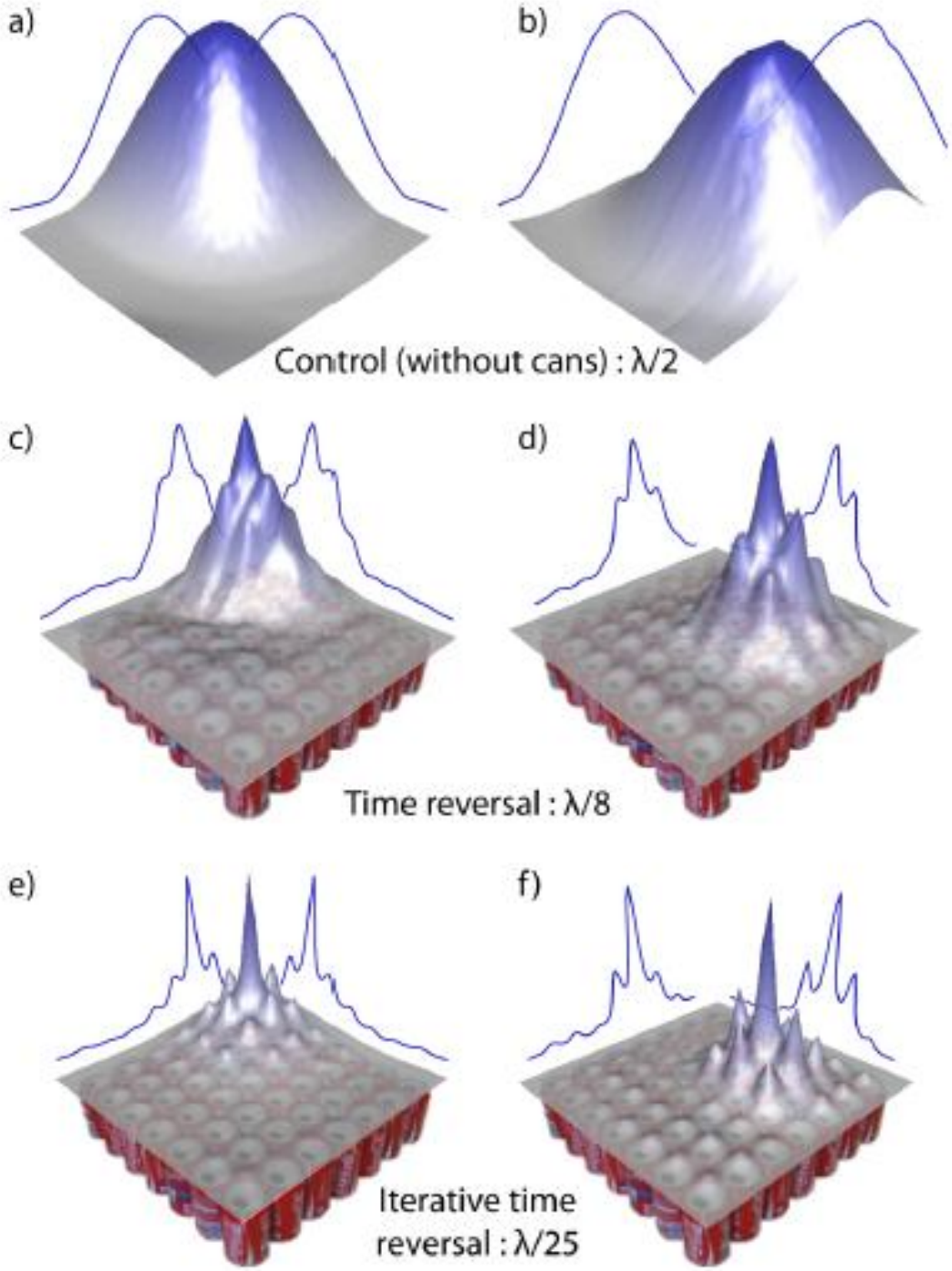

Figure 2.11 Acoustic intensity maps illustrating focusing with and without the metamaterial [25]

2.4. Imaging with Metamaterials and Phononic Crystals

One of the potential goals of metamaterials and phononic crystals is to design imaging systems that have subwavelength resolution. Subwavelength resolution refers to the well-known diffraction limit on imaging, the Rayleigh criterion. This criterion states that the imaging resolution is limited to the λ/2, where λ corresponds to the wavelength of the sound wave in the propagation medium. The only true way to capture a subwavelength image is to capture the evanescent field which contains the subwavelength information [59]. A traveling wave in spatial dimensions X and Z is given as follows.

$$u(x,z,t) = A_0 e^{i(k_x x + k_z z - \omega t)} \tag{2.12}$$

The dispersion relation in terms of k_z is

$$k_z = \sqrt{\frac{\omega^2}{c^2} - k_x^2} \tag{2.13}$$

If k_x is less than ω/c, then k_z is real and results with propagating waves in both the X and Z directions. However, if k_x is greater than ω/c, then k_z is imaginary which leads to exponential decay for propagation in the Z direction. This dictates that the wave can travel along one direction, k_x, without loss of amplitude, but when the wave is propagating in the Z direction there is an exponential decay of amplitude. Another direct result of k_x being greater than ω/c is that the wave traveling in the X direction has slower phase speeds (ω/k_x). From an imaging standpoint the slower phase speeds also results in smaller wavelengths (λ_x=2*pi/k_x). The easiest way to capture the subwavelength image is to capture the evanescent field. These evanescent

fields can occur at the interface of two materials and is shown to exist on the interface of a semi-infinite fluid and a metasurface of membranes.

There have been a few notable works concerning acoustic subwavelength imaging. Most have utilized a negative refractive lens to transport the evanescent portion of the waves from one location to the image source on the other side of the lens [1, 61, 73, 87]. An example of using a 2D lens obtains results by using a substrate with holes drilled in a substrate as depicted in the work of Veres et al in Fig. 2.12 [80]. From these 2D lenses, focal points have been achievable as small as .14λ [36].

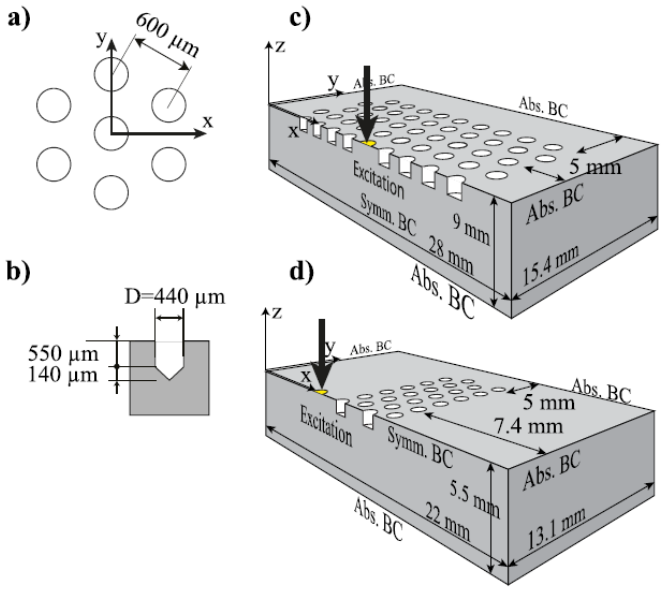

Figure 2.12 Example of a metasurface design capable of subwavelength imaging as a 2D lens [80]

Another method of subwavelength imaging have used tunneling methods based on the Fabry-Perot resonances of certain structures to capture the evanescent wave field and transport it to where it can be imaged [50, 51, 72, 94]. The most spectacular of these results is the imaging of a deep subwavelength letter "E" using a perforated structure metamaterial by Zhu et al and

shown in Fig. 2.13 [94]. For all of these methods of imaging, only a single frequency or a very narrow frequency band was used. The method of imaging for this work will instead be based on the time reversal focusing literature and use a broadband approach.

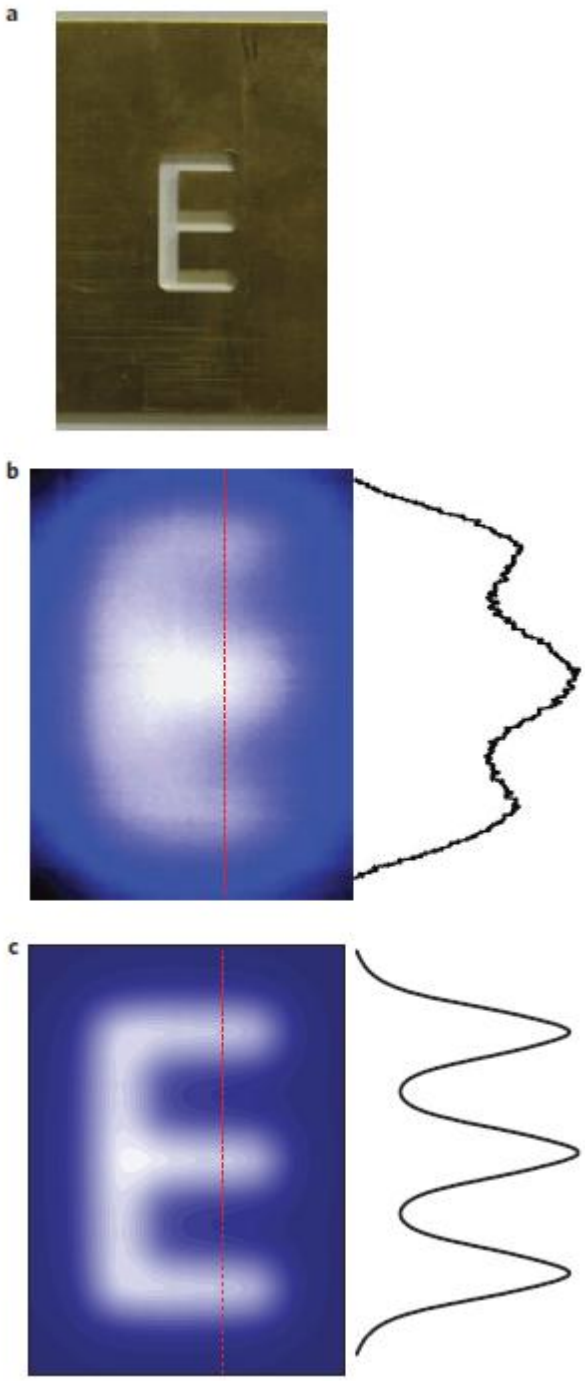

2.13 Simulation and experimental imaging of the letter "E" with a line width of λ/50. (b) experimental results (c) simulated results [94]

CHAPTER 3

MODELING OF MEMBRANE METASURFACE

3.1. Introduction

The first step in this work is to develop a model that can simulate wave behavior over the membrane metasurface. There are several tools which can be utilized to model and study the characteristics of metamaterials and phononic crystals. Two commonly used methods are the Bloch theorem, which relies on periodicity, and finite element modeling (FEM), which requires the meshing of the entire acoustic space [3, 19]. As an alternative approach, the model used for this work is a semi-analytic boundary element model based upon calculating the mutual radiation impedance. This model has several advantages. The semi-analytic boundary element model requires only discretization of the vibrating surfaces (membranes) as opposed to FEM simulations which require the entire meshing of the surrounding fluid which is very computationally costly. Another advantage of the mutual radiation impedance model is its flexibility to vary parameters such as random placement of resonators or variation of individual resonators, which is not possible with models that use the Bloch theorem. The model is summarized below with more detailed information, including previous validation through experiments and FEM found in the literature [29, 43, 44, 54, 68].

3.2. Semi Analytic Model

The membrane array is modeled as a two-dimensional nodal mesh. A force balance equation is solved for the displacement, $\{u\}$, in the frequency domain given as

$$\left[[K] + i\omega[Z_R(\omega)] - \omega^2[M]\right]\{x(\omega)\} = \{P(\omega)\} \tag{3.1}$$

where

$$u(t) = Re\left[x(\omega)e^{i\omega t}\right] \tag{3.2}$$

The force balance encompasses the stiffness per surface area, *K*, derived from a finite difference method; the mutual radiation impedance, Z_R (ω); the mass density, M; and forcing per surface area given by *P(ω)*. In the case where the membranes have embedded electrodes as in CMUT operation, *P(ω)* can be calculated from a linearized electrostatic actuation [54].

While the matrix M is diagonal and K is sparse, the mutual radiation impedance is a fully populated matrix relating each node (denoted as nodes p and q) by the Green's function of a baffled point source in a semi-infinite fluid [39].

$$Z_R(\omega)_{pq} = \frac{i\omega\rho_{fl}S}{2\pi r_{pq}} e^{-ikr_{pq}} \qquad for\ p \neq q \tag{3.3}$$

where ρ_{fl} is the density of the fluid, S is the surface area of the node, r_{pq} is the distance between nodes p and q, and k is the angular wavenumber, ω/c_{fl}. The self radiation term for each node (p=q) is given by a small piston radiator in Eq. (4) [39].

$$Z_R(\omega)_{pp} = \rho_{fl}c_{fl}\left(\frac{1}{2}(ka_{eff})^2 + i\frac{8}{3\pi}(ka_{eff})\right) \qquad for\ p = q \tag{3.4}$$

with c_{fl} being the sound speed of the fluid and a_{eff} being the effective radius of a small piston $\sqrt{S/\pi}$. The model can be used to solve a transient solution with forcing by using Fourier synthesis as demonstrated in cited work [29, 34, 43, 44, 54, 68]. Alternatively, modal analysis

can be performed on the system by solving the homogenous problem with an eigenvalue decomposition.

3.2.1. Modal Analysis

To find the homogeneous solution to this system of equations, the forcing is set to zero. Subsequently, a quadratic eigenvalue problem is solved by using a Taylor expansion for narrow frequency ranges since the problem is nonlinear as the radiation impedance, $Z_R(\omega)$, is dependent on ω [27, 67].

$$[K + i\omega Z_R(\omega) - \omega^2 M]\{x\} = 0 \tag{3.5}$$

The eigenvalues are ω_n with n denoting the n^{th} eigenvalue. Each eigenvalue has an associated eigenvector $\{X_n\}$. This gives a linear uncoupled set of solutions to the system in the form of the sum of mode shapes multiplied by their eigenvalue as given by Eq. 3.6, with c_n being a constant set to satisfy the initial conditions.

$$\{u(t)\} = Re\left[\sum_{n=1}^{N}\{c_n X_n\}e^{i\omega_n t}\right] \tag{3.6}$$

where N is the total number of modes in the system. If the eigenvalues are complex, which will occur for systems with loss, then the homogeneous solution can be rewritten as

$$if\ \omega_n = a_n + ib_n \tag{3.7}$$

$$\{u(t)\} = \mathrm{Re}\left[\sum_{n=1}^{N}\{c_n X_n\}e^{-b_n t}e^{ia_n t}\right] \tag{3.8}$$

with the quality factor of each mode given by the following equation [27].

$$QF_n = \frac{1}{2\zeta_n} = \frac{a_n}{2b_n} \; as \; \zeta_n = b_n/Re(\omega_n) \; and \; a_n = Re(\omega_n) \tag{3.9}$$

The eigenvalue solution gives important information on the modes, their associated resonant frequency, mode shape from the eigenvector, and quality factor. In addition, the wavenumber of each mode can be calculated from the Fourier transform of the mode shape across the array. This modal analysis is compared to the transient analysis in the following chapter.

3.2.2. Adding Variation

Since the model is solving the displacement of all membranes, it is not difficult to add variation to the stiffness or mass for each membrane to model more realistic arrays. In practice, manufacturing process variations will cause the membranes to differ in terms of physical dimensions and resonant frequency. Therefore it is important to understand and control the variability of each resonating membrane. This issue is investigated using a normally distributed variable for the stiffness of the membranes, which in turn will make the membrane resonance a random variable as well. The variation applied uses a mean value corresponding to the original stiffness and a standard deviation which controls the variation of the parameter. Typical and realistic variations used are 0.1%-5% standard deviation of the mean [85]. A 2D array used later in this work is measured the resonance of each membrane and showed that the resonances have a standard deviation of 0.4% of the mean resonance when operating in air (Appendix B).

3.3. Data Analysis with Model

The model solves the force balance equation for each individual frequency in the frequency domain. Using the Fourier transform and the inverse Fourier transform allows to visualize the vibration of the metasurface in several different domains.

3.3.1. Time-Space Domain

The time-space domain is one of the most fundamental domains to understand and is a valuable domain to evaluate the data from the model. However, since the model is solving in the frequency domain with a designated frequency step and bandwidth, an inverse Fourier transform must be performed to view the data in the time-space domain. For this transform, there are several steps that need to be followed so that the results in the time-space domain are physical and do not contain artifacts from the processing. The model only needs to solve the force balance in a finite frequency band of interest. Subsequently a new frequency axis needs to be formulated. For this case, sampling frequencies of 50 and 100MHz are used. The frequency step size, *df*, is the same step size that is used in the solver. This frequency step corresponds to the total recording time in the time domain ($1/df=T_R$). This is important as the recording time (T_R) needs to be long enough so that the transient signals are completely attenuated by T_R. If the recording time is too short, then the signal will exhibit a signal processing artifact of wraparound as shown in Fig. 3.1(a) when the inverse Fourier transform is performed. In this figure the model is solving the displacement with frequency steps of 80kHz for one membrane being pulsed at 4μs. The recoding time of 12.5μs is too short for the transient signal to die out. Hence it appears that there is signal existing before the pulse around t=0μs. In this model, the typical frequency

step size used ranged from 1kHz to 10kHz or 1,000μs to 100μs of recording time. The vibration of the membranes typically damp out within 20-50μs when modeled in immersion as shown in Fig. 3.1(b) which uses a frequency step size of 4kHz.

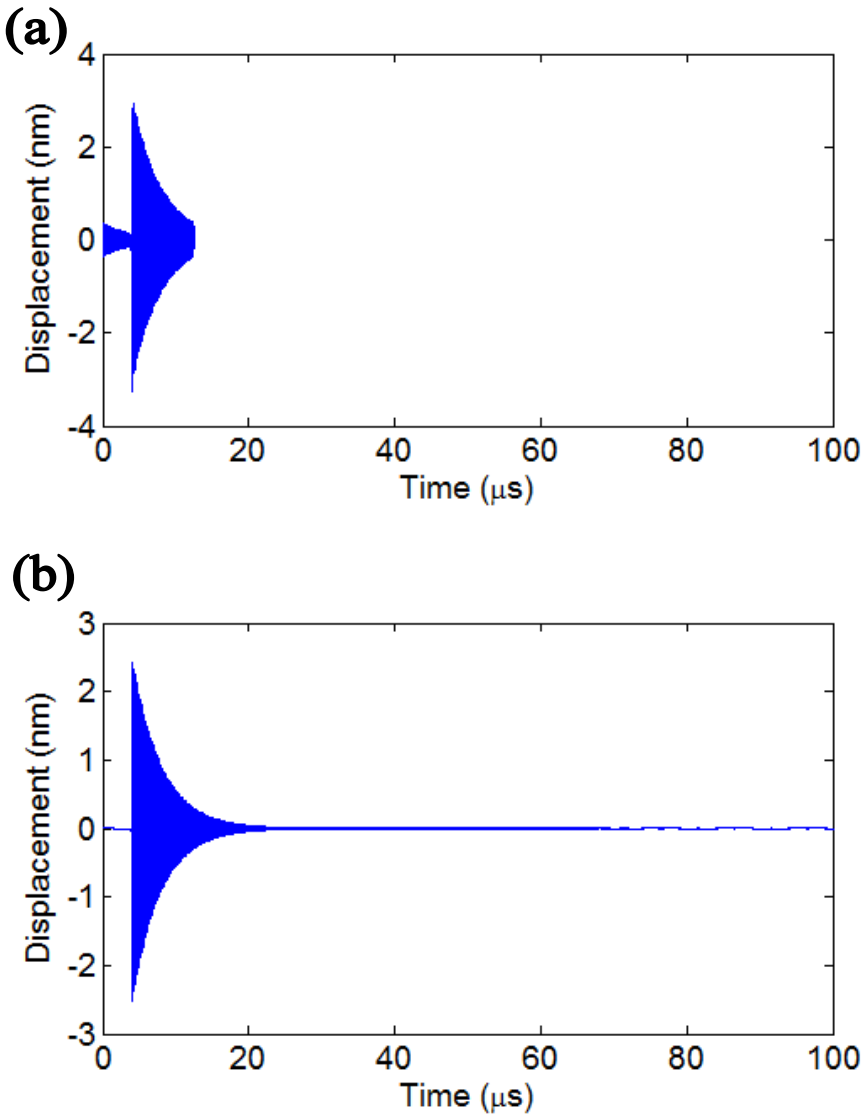

Figure 3.1 Transient analysis of pulsing one membrane using a (a) frequency step of 80kHz which leaves a recording time that is shorter that the time it takes for the transient signal to die out and hence it appears that there is signal existing before the pulse (b) frequency step of 4kHz which leads to little or no wraparound error from the inverse Fourier transform .

3.3.2. Wavenumber-Frequency Domain

The displacement of each membrane node in time, $u(x_i,t)$, does not always give a clear picture of the wave properties. To better understand how the waves propagate, another method of viewing the waves can be used such as a frequency-wavenumber plot. These plots show the different waves and their corresponding dispersion curves and are obtained by utilizing a two-dimensional Fourier transform from the time-space domain. The first Fourier transform is over the time domain and the second is over the space domain, transforming the time into frequency and the space into wavenumber. The two-dimensional image in frequency and wavenumber identifies where energy of the propagating waves is located. A dispersion curve can be obtained by tracing the peak of the energy. An example of this methodology is shown in Fig. 3.2 with the frequency-wavenumber energy plot (Fig. 3.2(a)) and the associated dispersion curve (Fig. 3.2(b)). The dispersion curves are useful to find the phase and group speed of the waves as stated previously.

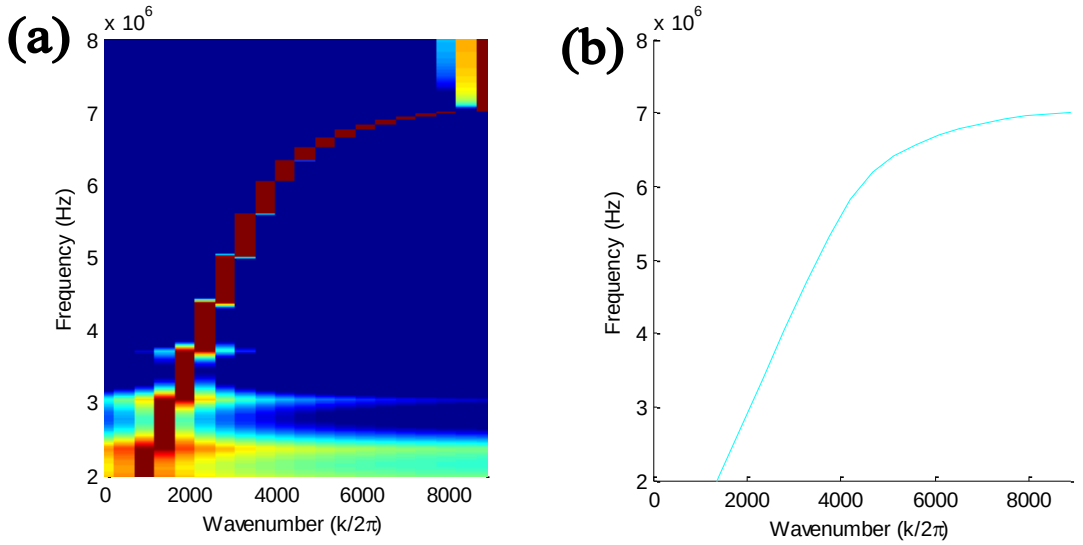

Figure 3.2 Frequency-wavenumber plot of the energy of the waves (a) and the associated dispersion curve (b) of a dispersive surface wave

3.3.3. Wavenumber-Wavenumber Domain

The last domain that is discussed is the wavenumber-wavenumber domain. This is achieved by taking two spatial Fourier transforms across two different spatial dimensions. The result of the 2D spatial Fourier transform obtains equifrequency contours in the k_x and k_y plane as shown as Fig. 3.3. The equifrequency contour, also termed a slowness curve, illustrates how the wave is traveling in each particular direction at the given frequency. The phase speed can be calculated from these plots by dividing the frequency by the wavenumber.

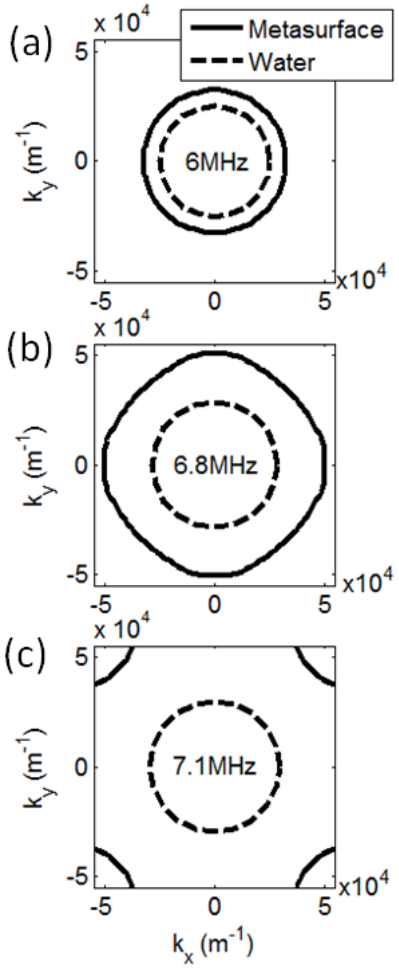

Figure 3.3 Wavenumber-wavenumber plots showing the equifrequency contour or slowness curves for a metasurface (solid line) and water (dashed line) at 3 different frequencies. [45]

3.4. Summary

This chapter introduces an enhanced model, which simplifies the analysis of how the surface acoustic waves propagate above a membrane metasurface. The model was adapted from prior work to focus on how the waves are propagating across the surface in three different domains. This allows identification of modal properties, dispersion relations, and band gaps. The model also has important advantages such as being computationally efficient and flexible to include variation to the system.

CHAPTER 4

PROPERTIES OF SURFACE ACOUSTIC WAVES ON MEMBRANE METASURFACES: SIMULATIONS

To gain a deeper understanding of the waves propagating across of the membrane metasurfaces the model is used to examine various parameters such as mode shapes, dispersion relations, and transmission through the structure. A linear array is examined with modal analysis to obtain modes shapes, resonant frequencies, and quality factors of the modes. These results are then compared with the transient analysis for waves propagating across the array. The transient results on a linear array are verified with experimental results in Chapter 5. The linear arrays also are used to show that the dispersion and transmission of the evanescent waves are dependent on the resonance of the membrane as the membranes' stiffness is altered by adjusting the applied bias voltage to the CMUT membranes (Chapter 5). The array is also modeled in two dimensions to illustrate the dispersion relation in different spatial dimensions. Finally, array parameters are varied to illustrate how the dispersion, mode qualities, and transmission are affected.

4.1. Analysis of Linear Arrays

4.1.1. Modal Analysis

To understand the dispersive properties of a membrane metasurface, a 1x7 linear array is studied. First, this small 1D array of membranes with each membrane vibrating in the fundamental mode (membrane displacement is in phase across the entire membrane) is modeled and analyzed. The mode shapes and the eigenvalues are calculated for the array immersed in

water (Fig. . 4.1) with parameters as defined in Table 4.1. A single membrane has a width of λ/5 (45μm) with a center frequency of 6.55MHz. Since there are seven resonators the eigenvalue solution contains seven modes, when considering membrane motion only in the fundamental mode,. Each modal solution is comprised of the eigenvector $\{X_n\}$, which is the displacement vector of the seven membranes (overall mode shape of the array) and the eigenvalue, ω_n (Eq. (3.6)). Note that the eigenvalue in the polynomial eigenvalue problem is equivalent to the radial frequency, ω, in contrast to the generalized linear eigenvalue problem in which the eigenvalues correspond to ω^2. Table 4.2 lists the eigenvalues of the seven modes sorted by quality factor.

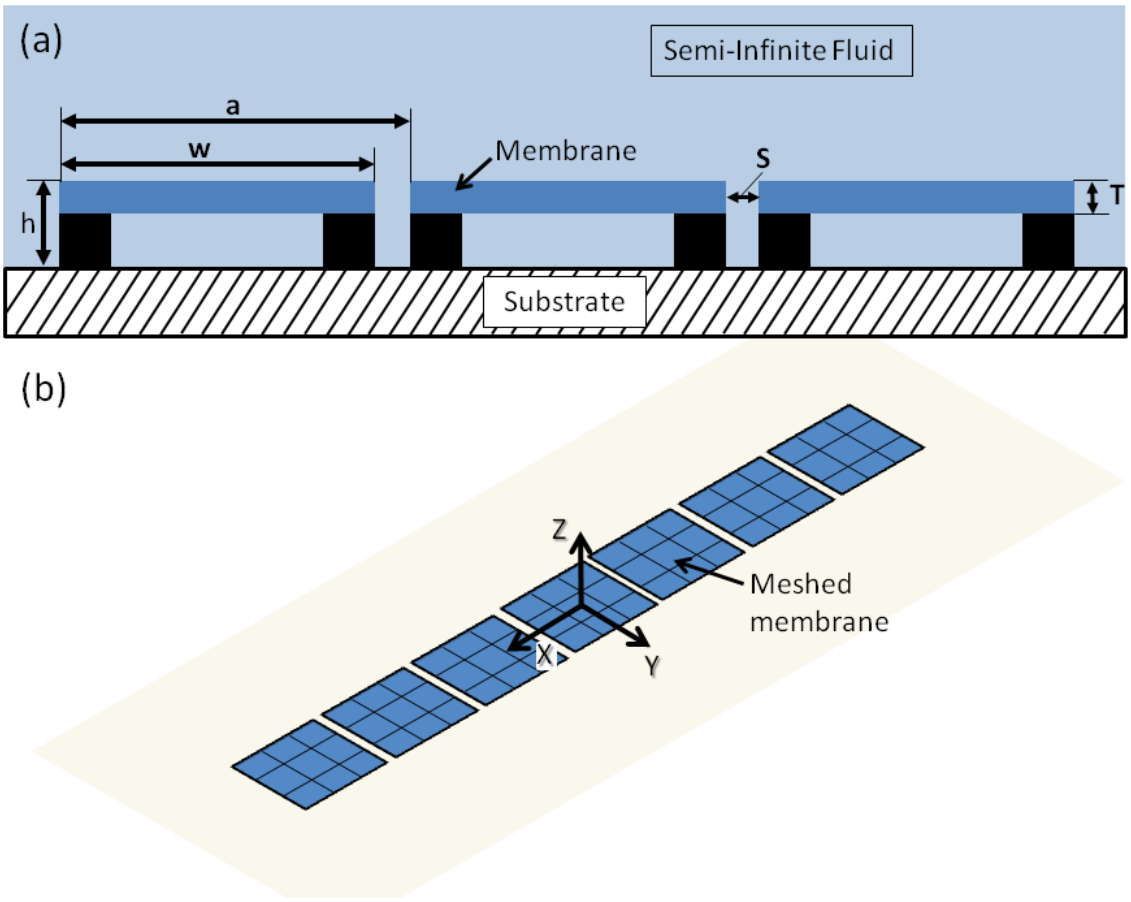

Figure 4.1 Schematic of a membrane metasurface (a) side profile of the metasurface of flexible membranes on a rigid substrate. (b) top view of a 1x7 array of membranes showing the meshed surface used for calculations

Table 4.1 Properties of membrane metasurface

Parameter	Value
w	45μm
s	10μm
a	55μm
H	2.5μm
T	2μm
fc	6.55MHz (in water)

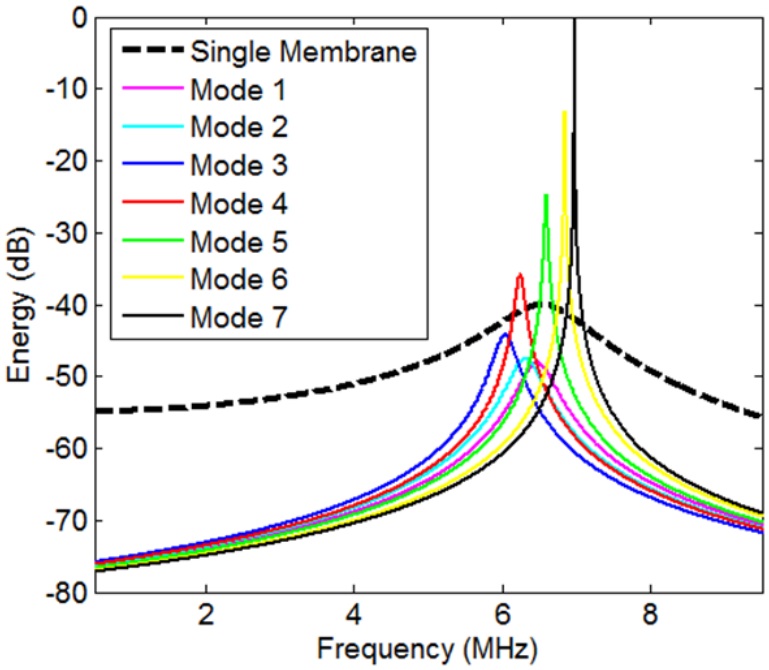

Figure 4.2 Frequency spectra of a single vibrating membrane (black dashed line) with a resonance of 6.55MHz in addition to the Fourier transform of the 7 modes from the temporal eigenvalue solution Eq. (4.1) showing the resonance frequency as well as the mode's quality factor.

Table 4.2 Eigenvalues and associated quality factor of the 7 modes (sorted by quality factor)

Mode Number	a_n (MHz)	b_n*1e6	Q Factor
1	6.47	1.4234	14.3
2	6.31	1.3404	14.9
3	6.04	0.9088	20.1
4	6.24	0.3455	57.3
5	6.60	0.0969	220
6	6.85	0.0259	856
7	6.98	0.0053	6980

Each eigenvalue is a complex number (see Eq. (3.7)). The real component of the eigenvalue corresponds to the resonant frequency of that mode. All modes are within 0.5MHz to the single membrane resonance frequency of 6.55MHz. The imaginary component of the eigenvalue corresponds to the losses associated with a given mode, which varies four orders of magnitude over the seven modes. Since the membranes are simulated without any material damping, the loss for each mode is solely due to radiation loss, which occurs at different rates for the different modes. In practice, other loss mechanisms such as the material losses in the membrane and support losses can limit or dominate the quality factor [60].

$$\{y(t)\} = Re\left[e^{-b_n t} e^{i a_n t}\right] for\ t \geq 0 \tag{4.1}$$

Equation (4.1) is the time dependent portion of Eq. (3.8). The amplitude spectrum of the Fourier transform of Eq. (4.1) for each mode (n) is shown in Fig. 4.2 to highlight the relative variations in resonant frequency and quality factor for each mode as well as the frequency response of a single membrane (black dashed line). The quality factor of each mode is calculated by Eq. (3.9) and listed in Table 4.2 for comparison.

The mode shapes of the array can be obtained from the set of eigenvectors, $\{X_n\}$. For simplicity, the mode shapes can be represented by a reduced vector of 7 values taken from the center node of each membrane since it is vibrating in the first mode and denoted by $\{\tilde{X}_n\}$. Figure 4.3 plots the normalized mode shapes along with a waveform of a bulk wave traveling in water (c_{fl}=1500m/s) at a frequency of 6.55MHz with its wavelength of 230μm identified. Notice that the three modes (Fig. 4.3 (b-d)) with the lowest quality factors have a modal wavelength that is longer than the wavelength of sound waves in water. Hence these modes are highly radiative or leaky modes. To illustrate this fact and also the fact that the imaginary component of the eigenvalue can be related to the relative acoustic radiation for each mode, radiation patterns were simulated. The associated beam patterns for each mode in X-Z plane are shown in Fig. 4.4. These were obtained by using the eigenvector's displacement, $\{X_n\}$, and then exciting the membrane at the mode's resonance frequency as determined by the real part of the eigenvalue. The pressure around the array in the far field was computed using the Rayleigh integral, squared, time averaged, and normalized to the maximum values obtained for all seven modes. It can be seen that the lower modes (Modes 1-3) radiate energy away from the linear array more readily. While for the Modes 5-7, energy is trapped at the surface resulting in narrowband features in the far field (Fig. 4.4) [7]. It is noted that the beam patterns in the X-Y plane, which are important for the excitation of these modes using sources on the plane of the metasurface, are similar to the beam patterns in X-Z plane, as expected.

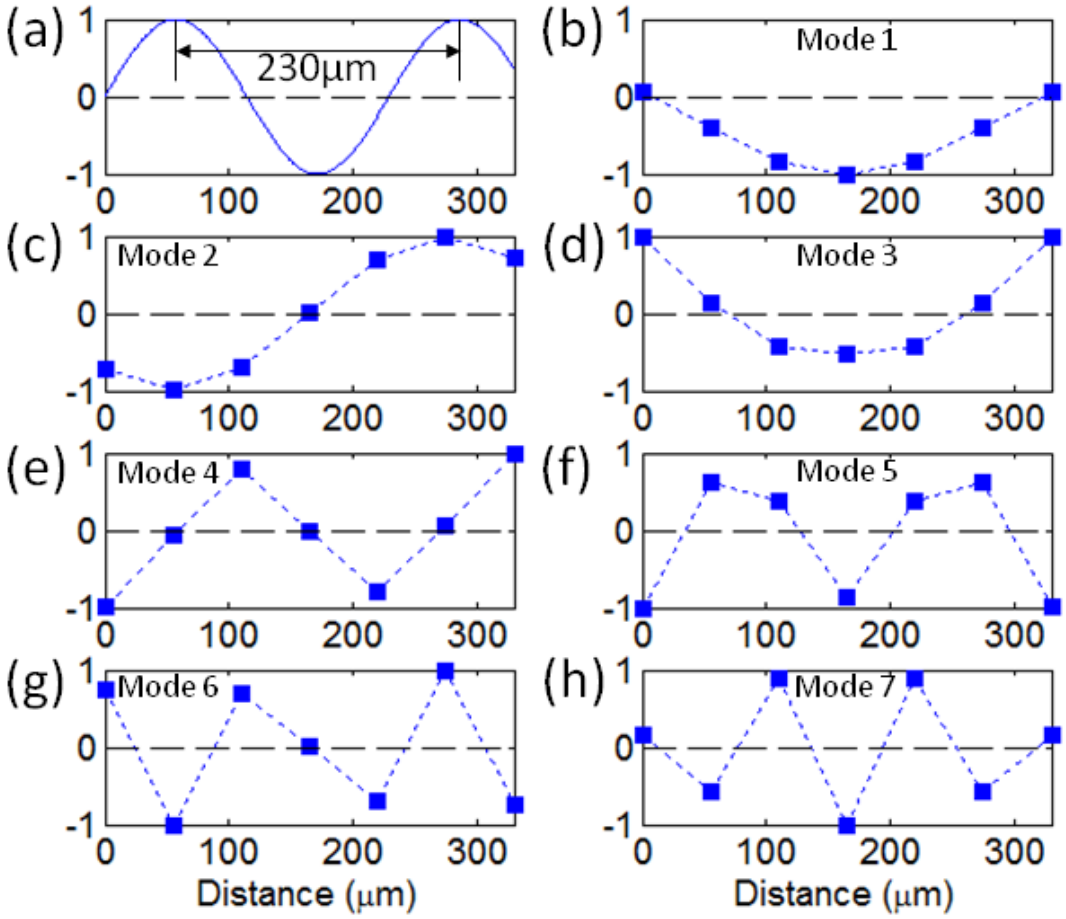

Figure 4.3 (a) Bulk wave traveling in water at 6.55MHz with a wavelength of 230μm (b-h) Mode shapes of the seven modes, $\{\widetilde{\boldsymbol{X}}_n\}$.

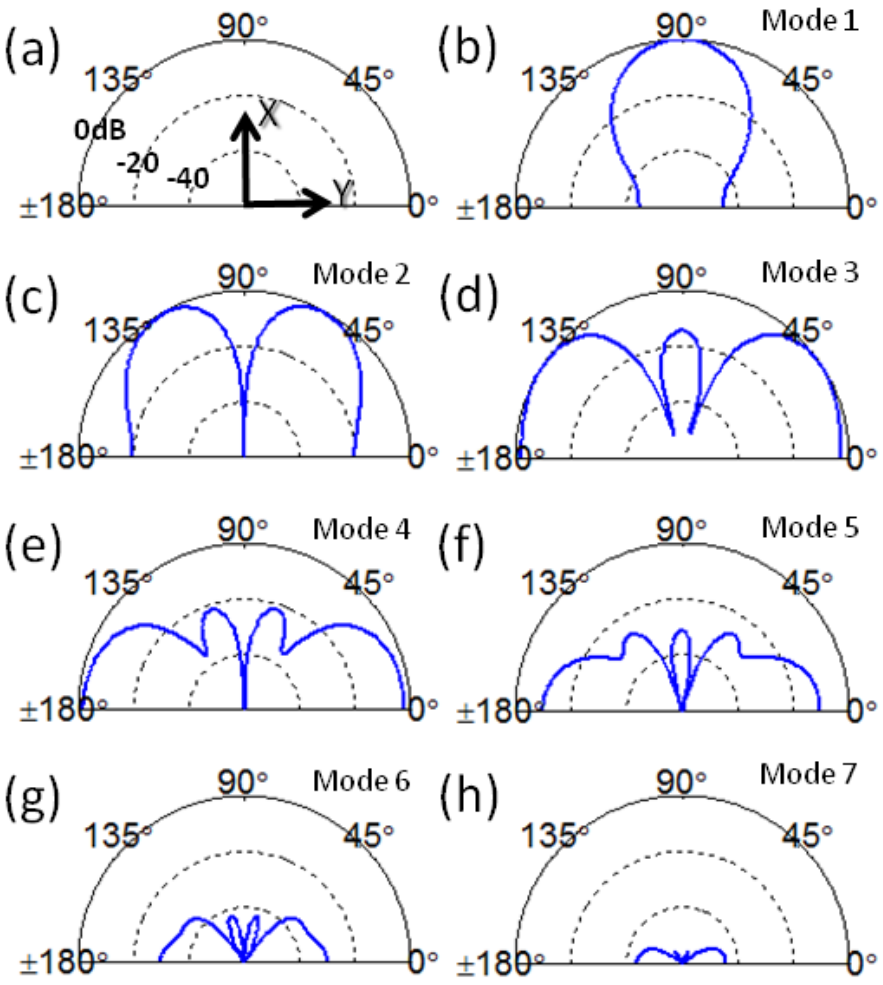

Figure 4.4 Beam patterns in the X-Z plane for the seven modes normalized to the peak of the first mode

4.1.2. Comparing Modal and Transient Analysis

Next, the dispersive behavior of each mode is displayed on Fig. 4.5 using a wavenumber-frequency plot. For each mode, the wavenumber is obtained by taking a spatial Fourier transform of its eigenvector's modal shape as illustrated on Fig. 4.3. Since the Fourier transform resolution is poor with only seven points, zero padding was used to increase the resolution to 77 points. The resonance frequency of each mode is obtained from Table 4.2. The frequency bandwidth of each mode is also displayed as it aids in visualizing the quality factor of each mode and is determined by a -10dB amplitude decay from the peak resonance amplitude. The black

dashed line is the reference dispersion relation for the immersion fluid, water (c=1500m/s). Modes 1-3, which have the lowest quality factors, lay on the left of that reference line, as they have an associated wavelength greater than that of water (Fig 4.3 (a-d)). These modes are leaky because they are supersonic or have an associated phase speed (ω/k) that is greater than that of the surrounding fluid and hence makes those modes effective radiators into the fluid. The four other modes, the trapped modes, appear to the right of the dispersion curve of water. These modes are subsonic to the surrounding fluid with the highest wavenumbers corresponding to the modes with the highest quality factors.

Similar results can be seen on a longer 1x40 array with its 40 modes and -10dB bandwidth depicted by thin black lines. In addition to the modal analysis of the 1x40 array, transient analysis was conducted by pulsing the first membrane with a 40ns long pulse to excite a wave travelling along the length of the array. The traveling wave's dispersion curve was evaluated by taking a spatial and temporal Fourier transform with the result plotted as a solid blue line in Fig. 4.5 [9]. Notice that the transient analysis predominantly captures information from the subsonic modes, as the supersonic modes were not efficiently excited compared to the subsonic modes. The subsonic modes can also be used to extract information about subwavelength scale features. With very slow phase speeds (ω/k) and group velocities ($\delta\omega/\delta k$), the spatial resolution of these modes can be utilized to achieve subwavelength focusing and imaging as previously reported [46, 47].

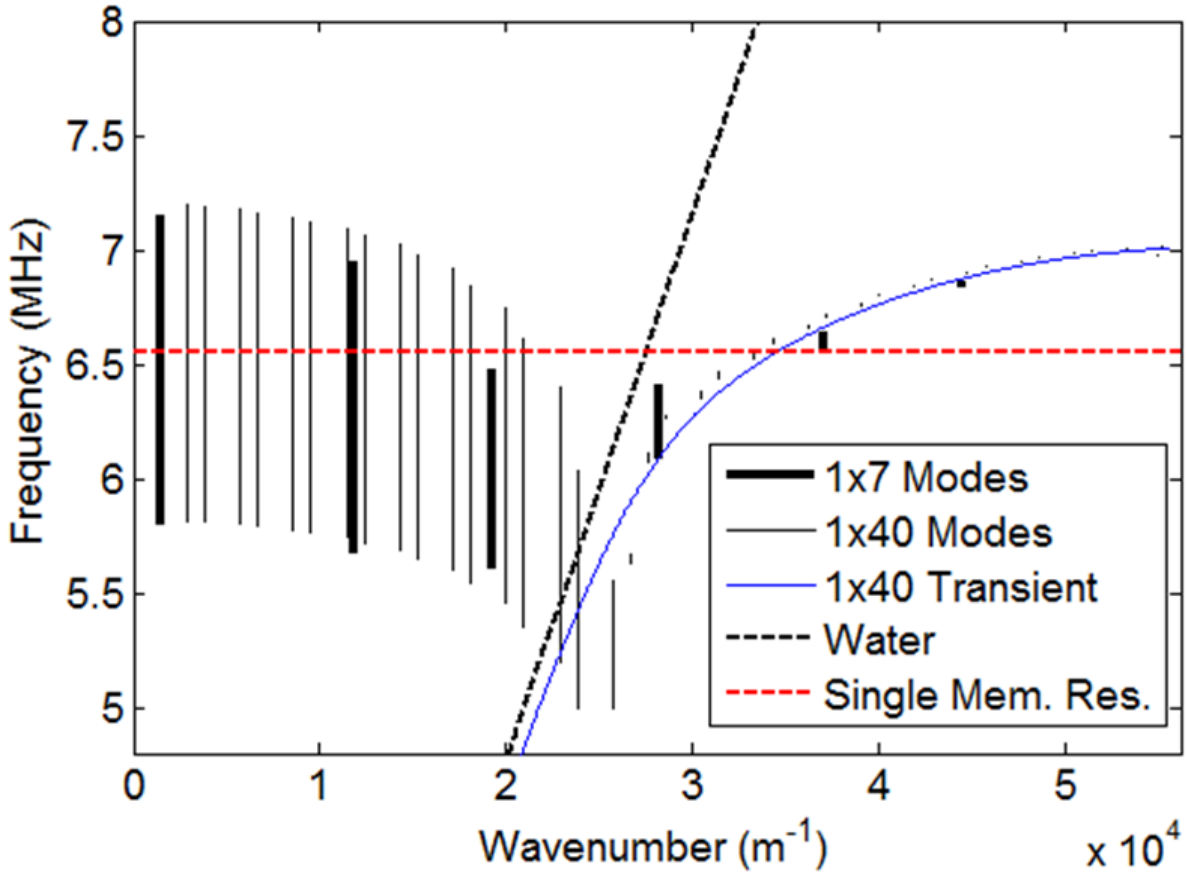

Figure 4.5 Wavenumber-frequency analysis of the 7 modes of the 1x7 array by plotting the wavenumber and resonant frequency of the seven modes with an associated -10dB frequency bandwidth. The black dashed line corresponds to the dispersion curve of water, the immersion fluid. Similar modal results for a 1x40 array yield similar dispersion curves. The solid blue line is the dispersion curve that is obtained by using transient analysis and the red dashed horizontal line denotes the resonance of a single membrane in immersion [45]

4.2. Analysis of Two-Dimensional Array of Membranes

4.2.1. Modal Analysis

Modal analysis is also applied to a grid of 7x7 membranes with 10μm spacing. Two example modes are presented in Fig. 4.6 and Fig. 4.8. The first mode shown, with a resonant frequency of 7.17MHz, has each membrane alternating in an up-down pattern or checkerboard pattern. This alternating pattern is the highest wavenumber supported on the array. The

corresponding 2D spatial Fourier transform is presented in Fig. 4.7 which shows that the energy in this mode is at the edge of Brillouin zones in both the X and Y direction. Since this mode contains the highest wavenumber this mode can determine the resolution limit of the array. The second mode presented with a resonant frequency of 5.66MHz (Fig. 4.8) is also obtained through the eigenvalue solver. However, this mode is more ambiguous concerning where the energy is located as illustrated in Fig. 4.9 from the wavenumber-wavenumber plot. Consequently due to the blurring of energy in the wavenumber-wavenumber domain some of these modes give limited information about the system. The lack of resolution in the wavenumber domain is due to the limited spatial information which only contains 7 data points in both the X and the Y directions. Even with zero padding, the energy is heavily blurred in the wavenumber domain. Hence a better way to understand the properties of the 2D metasurfaces is to use a much larger array. The larger array is cumbersome to run with the eigenvalue analysis, but the transient solver is adept to handle the larger problem.

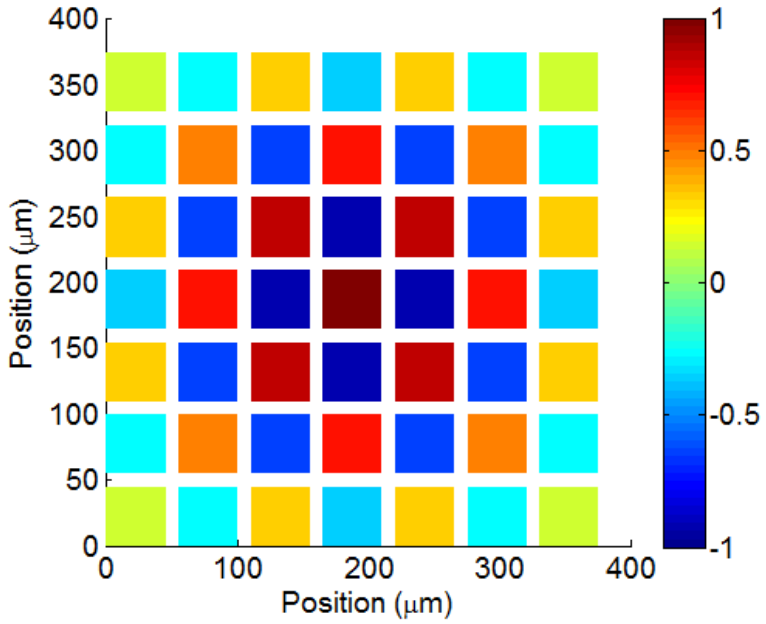

Figure 4.6 Normalized displacement of a mode for the 7x7 system of membranes with a resonant frequency of 7.17MHz.

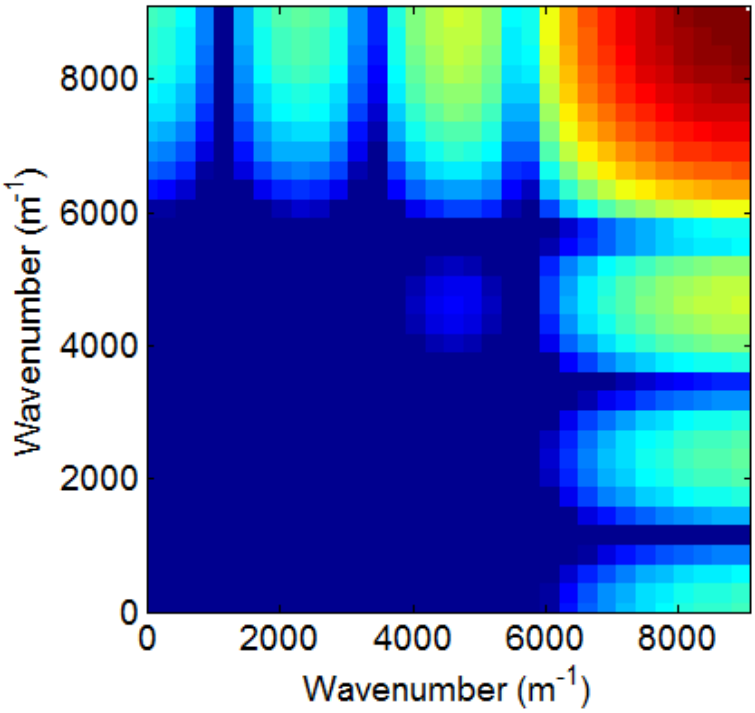

Figure 4.7 Wavenumber-wavenumber plot of Fig. 4.6 from using a 2D spatial Fourier transform which illustrates the energy is at the edge of both wavenumber domains.

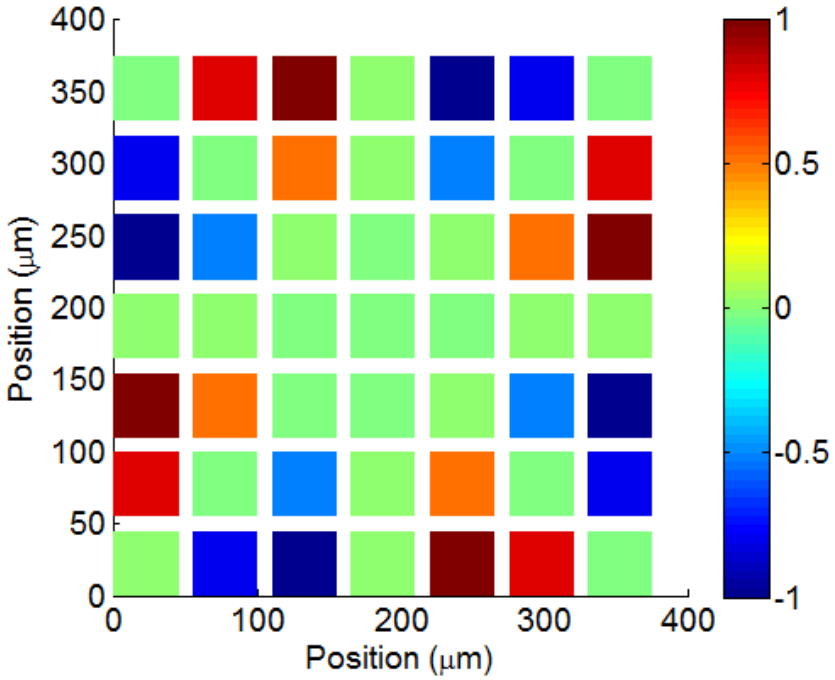

Figure 4.8 Normalized displacement of a mode for the 7x7 system of membranes with a resonant frequency of 5.66MHz.

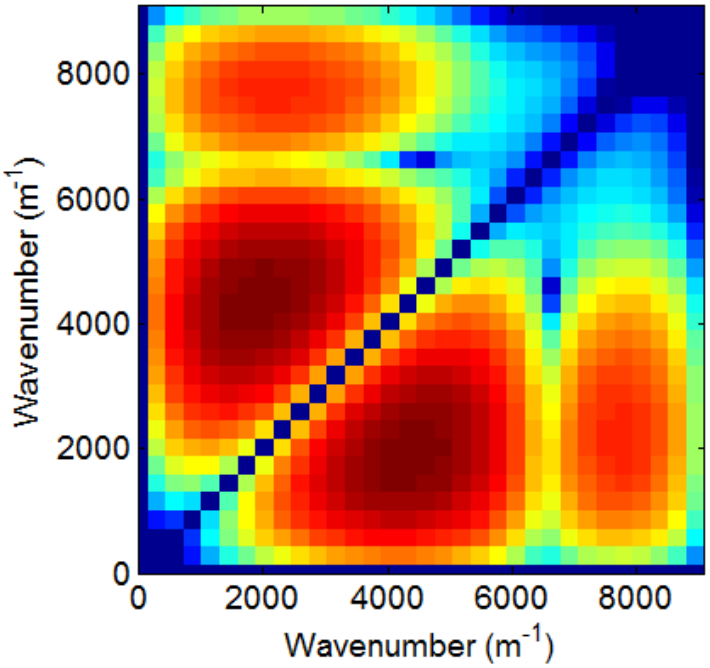

Figure 4.9 Wavenumber-wavenumber plot of Fig. 4.8 from using a 2D spatial Fourier transform which illustrates the energy is not localized due to the limited spatial information.

4.2.2. 2D Dispersion Relationship

A two-dimensional analysis of the metasurface is performed to determine the directional dispersion of the surface acoustic waves. To accomplish this task, a 40x40 membrane array arranged with a rectangular periodicity as shown in Fig. 4.10(a) is transiently modeled to obtain the displacement for all space and time. Subsequently, a 2D spatial Fourier transform was performed to obtain dispersion curves in the ΓX (y=0) and ΓM (y=x) directions in the reciprocal space as shown in Fig. 4.10(b). Note that while both curves exhibit a slow travelling wave, the dispersion curves do not terminate at the same frequency. This indicates that there is a range of frequencies in which a directional band gap exists. A closer examination of the equifrequency contour in the k_x and k_y plane show that there are four frequency bands of interest. At low frequencies (f < 6.65MHz), the metasurface is isotropic as shown in Fig 4.11(a). The

equifrequency contour of water is also included as the dashed black line for comparison. At higher frequencies the equifrequency contour begins to deviate from that in water, meaning that the metasurface is slowing the surface waves. The next frequency band of interest (6.65MHz < *f* < 6.85MHz) occurs when the metasurface begins to exhibit anisotropic behavior in which waves traveling in the direction of ΓX are slower than the waves propagating in the ΓM direction. For frequencies above 6.85MHz and below 7.2MHz, a directional band gap occurs (Fig. 4.11(c)). Notice that the equifrequency contour of the metasurface at 7.1MHz is concave, which is indicative of negative refraction. Normal isotropic materials such as water exhibit a circular equifrequency contour and have no focusing effects. However with a concave equifrequency contour, incident angles incoming at an angle around 45 degrees from normal of the metasurface in the XY plane will actually be focused by the concave equifrequency contour. These contours are a visual representation of the trace matching principle required for wave interactions between two materials. Beyond 7.2MHz, there is a complete band gap. Previous work has shown that a rectangular lattice of square holes drilled in aluminum exhibited negative refraction from concave equifrequency contours seen within the partial band gap around 2kHz and could be utilized for subwavelength focusing [36]. Hence, a future application of this metasurface would use negative refraction in the partial band gap frequency range for subwavelength focusing at frequencies much higher than previously researched.

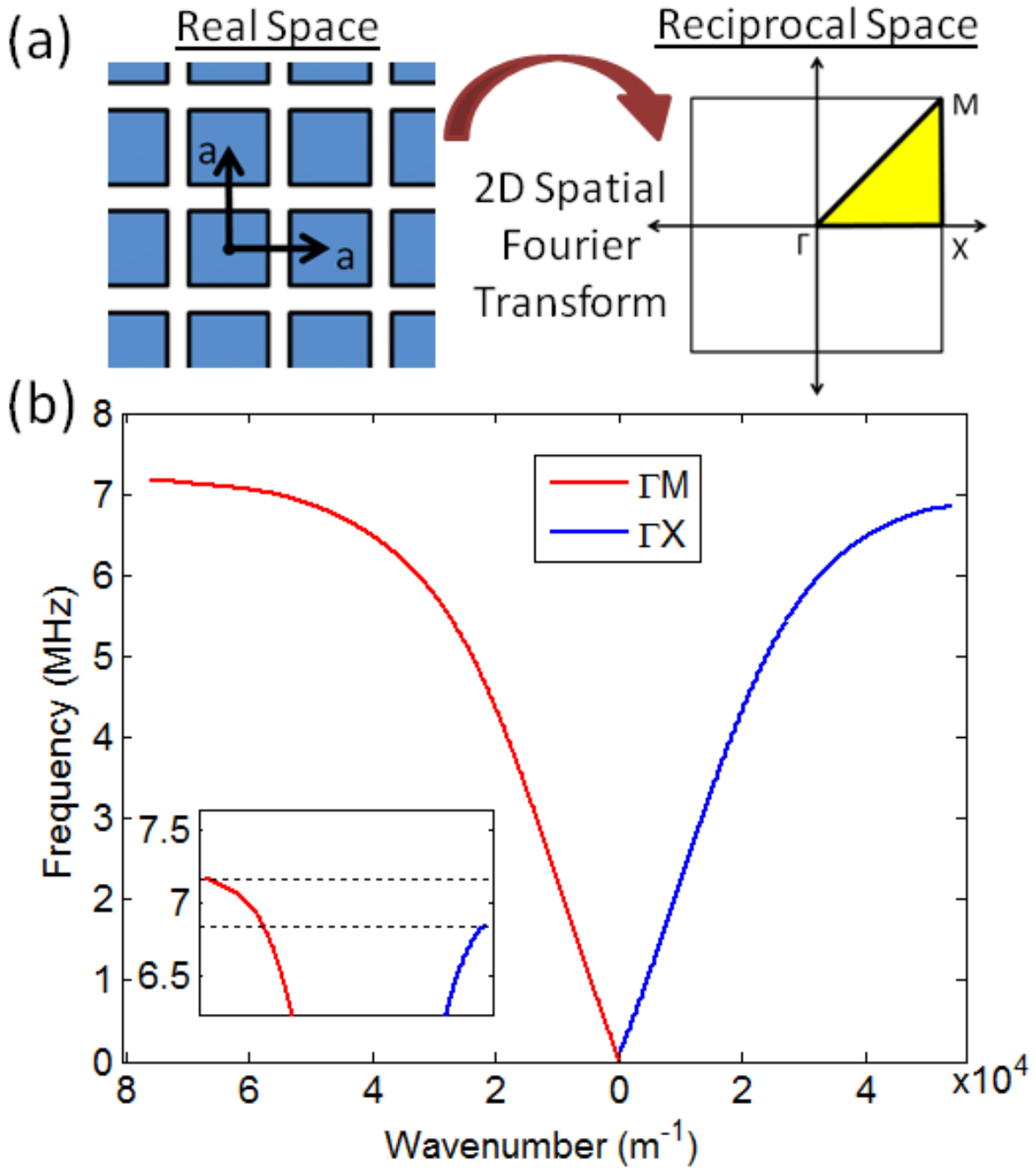

Figure 4.10 (a) Array of membranes arranged in a square lattice as shown along with the transform into the wavenumber domain. (b) Dispersion curves along the directions of ΓX and ΓM with the inset showing the directional band gap [45]

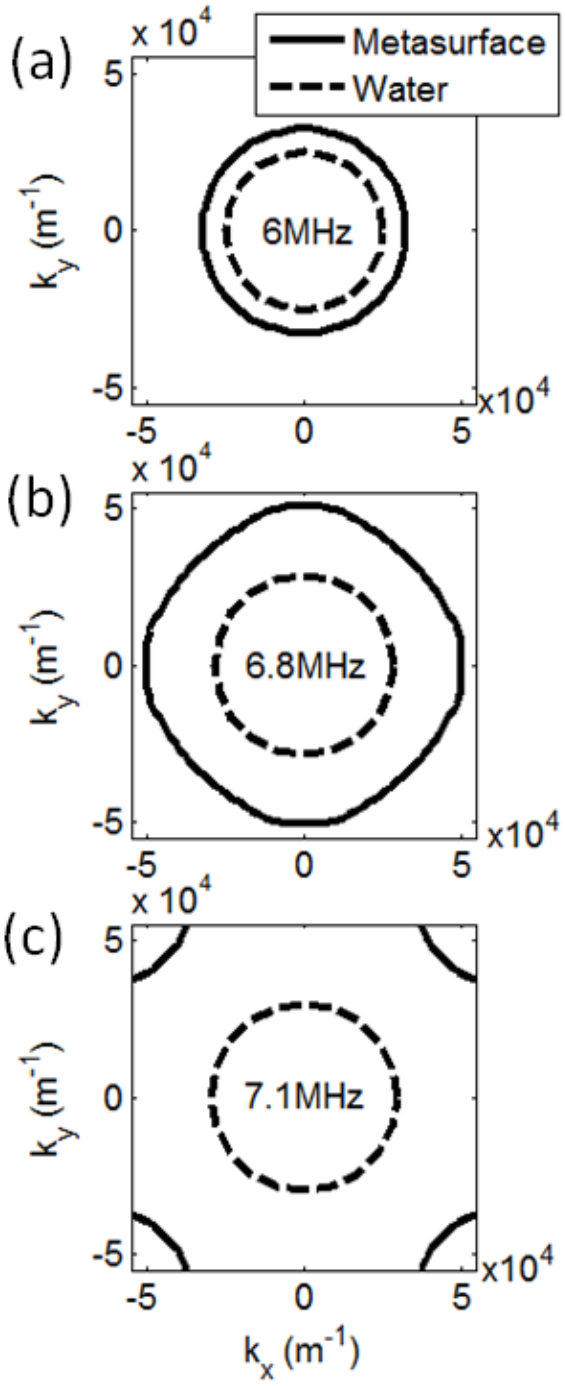

Figure. 4.11 Equifrequency contours of the metasurface (solid line) and water (dashed line) at frequencies of (a) 6MHz, which shows isotropic behavior of the metasurface (b) 6.8MHz anisotropic behavior of the metasurface and (c) 7.1 MHz directional band gap with concave contours. A complete band gap was seen at frequencies above 7.2MHz [45]

4.3. Effect of Array Structure on Dispersion and Modal Properties

The analysis of a metasurface of membranes can have implications in several different areas, such as subwavelength focusing and imaging, resonant devices, and transducer array design. Each of these research areas need to have the metasurface optimized for certain parameters. With subwavelength focusing to locations above the metasurface, similar to the work conducted by Lemout et al. [47], it is important to know the mode shapes of the array. Most important of these is the mode shape of the highest mode, which has the smallest wavelengths and thus determines the achievable focusing resolution on the metasurface. For creating a resonant sensor, the modes will ideally have very high quality factors and hence will be able to detect changes at the surface by shifts in the resonant frequency or a change of the quality factor [5, 32, 77]. For designing transducers for far field operation, it is important that the energy is not trapped at the surface and resonances are avoided in the frequency range of interest, as these affect the array's angular response and range resolution [3, 20]. In addition, the dispersion of the metasurface will be examined and how it is impacted by changes in the structure (e.g. as occurring due to manufacturing imperfections). Consequences of varying the three parameters of membrane spacing, nonuniform resonators, and aperiodic spacing of membranes and how they affect the dispersion, modal properties, and transmission are examined.

The parameter studies focus on the analysis of propagation across linear arrays for simplicity. A 1x40 array is analyzed with transient and modal analysis in order to gather information about the dispersion of the traveling wave and the features of individual modes (in particular the slowest mode). The dispersion curves are obtained with the transient analysis by performing a 2D Fourier transform in time and space to obtain a wavenumber-frequency plot. The dispersion curves are normalized (unless otherwise noted) by π/a where a is the pitch, which

is the summation of the membrane width, *w*, and the membrane spacing, *s*. This normalization corresponds to the edge of the Brillouin zone and the highest wavenumber that the particular array can support. In the case where the spacing is aperiodic, the pressure field is calculated directly above the array with a Rayleigh integral with 10μm steps in order to perform the 2D Fourier transform. The modal results are from the solution of the eigenvalue problem. The mode with the slowest phase velocity is examined because it has the highest wavenumber and is examined with respect to its changes in terms of resonant frequency and quality factor.

The transmission of acoustic energy across the array is also examined. The transmission simulations utilized a 5x40 array with the first column of membranes acting as the transmitter and the last column being the receiver. The transmission loss is calculated using the average displacement of the 5 membranes that were part of the transmitter and the receiver. The average displacement of the transmitter, $u_{avg,1}$, was first calculated in isolation to eliminate any of the array effects in the transmitted signal. Then the same pulse was applied to the transmitter (now part of the 5x40 array) with the last element (40^{th} column of membranes) measuring the average displacement, $u_{avg,40}$. These average displacements are used for the transmission calculations.

$$TL = 20log_{10}\left(\frac{u_{avg,40}}{u_{avg,1}}\right) \tag{4.2}$$

4.3.1. Membrane Spacing

To examine membrane spacing, this parameter was varied while the other membrane parameters from Table 4.1 remained constant. The dispersion curves from the transient analysis are shown in Fig. 4.12(a). Notice that all of the dispersion curves have some slowing of the wave near higher wavenumbers with the exception of the 70μm case, in which the dispersion is

nearly linear. This is because for the spacing of 70μm, the array pitch is 115μm which corresponds to λ/2. Hence for a given frequency, if the highest wavenumber supported (π/a) is equal to the wavenumber of water (ω/c), then no dispersive behavior occurs as the coupling between the membrane arrays vanishes for such large separation distances. In this case, the array of 40 membranes still has 40 modes, but instead of half of the modes being supersonic and half being subsonic to the immersion fluid (such as in Fig. (4.5)), all 40 modes are supersonic and are positioned to the left of the dispersion curve of water. Fig. 4.13 shows the transmission across the array. As expected, each band stop occurs at the highest associated frequency of the corresponding dispersion curve (Fig. 4.12(a)). Fig. 4.12(b-d) examines the slowest mode on the array for each arrangement and shows the resonant frequency, the quality factor, and the wavenumber. While the resonant frequency tends to get lower with increasing separation, it is interesting to see that there are relatively high quality factors for the majority of the array setups with the exception of the 45μm and 70μm spaced arrays. These results show that slow modes and traveling waves will be present as long as the membranes are spaced with a pitch smaller than λ/2. For membranes spaced farther than λ/2 apart, the highest wavenumber supported is below that which is supported in the surrounding immersion fluid which makes any modes present on the array supersonic relative to the immersion fluid (Fig. (4.5)). A resonant sensor can take advantage of the high quality factor for a range of different membrane spacing values (0-22μm) to either make a compact sensor or one that covers a larger area. On the other hand, subwavelength focusing above the array would be best with the membranes as tight as possible to have the smallest focal spot as seen from the associated wavenumbers in Fig. 4.12(d).

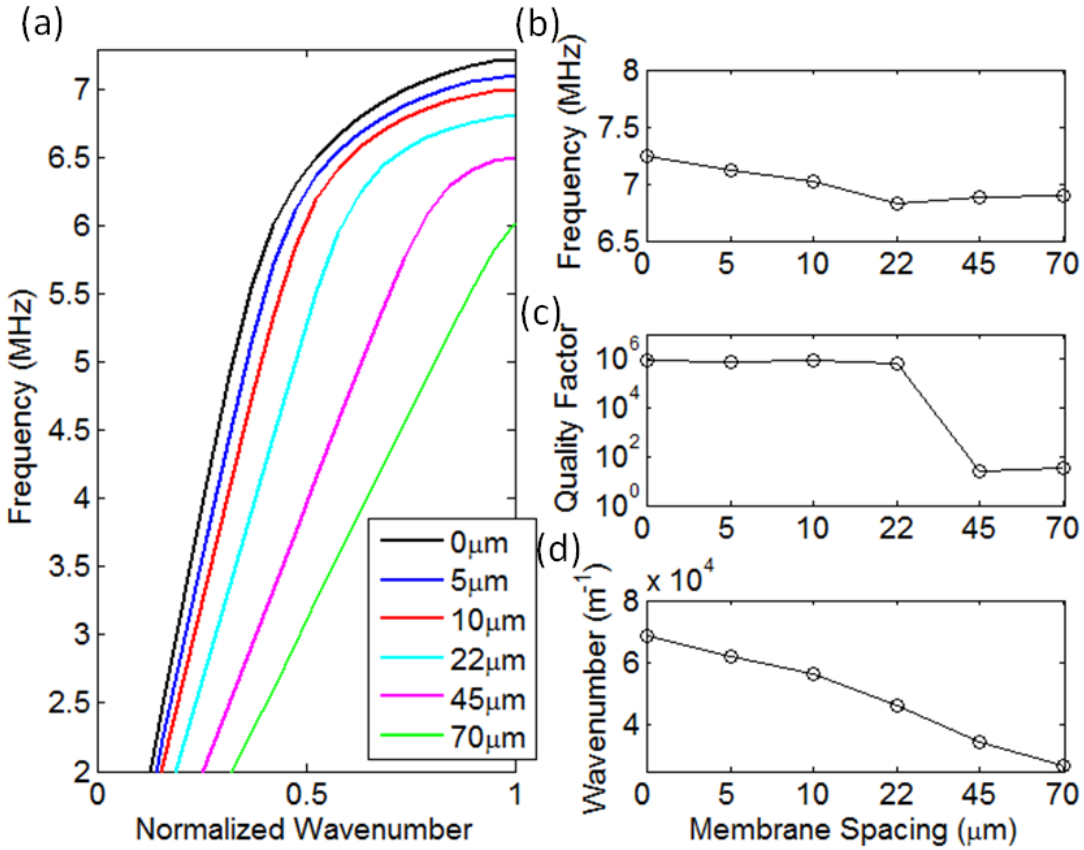

Figure 4.12 Effects of altering the membrane spacing on (a) dispersion curves and the slowest mode's properties of (b) resonant frequency (c) quality factor and (d) wavenumber [45]

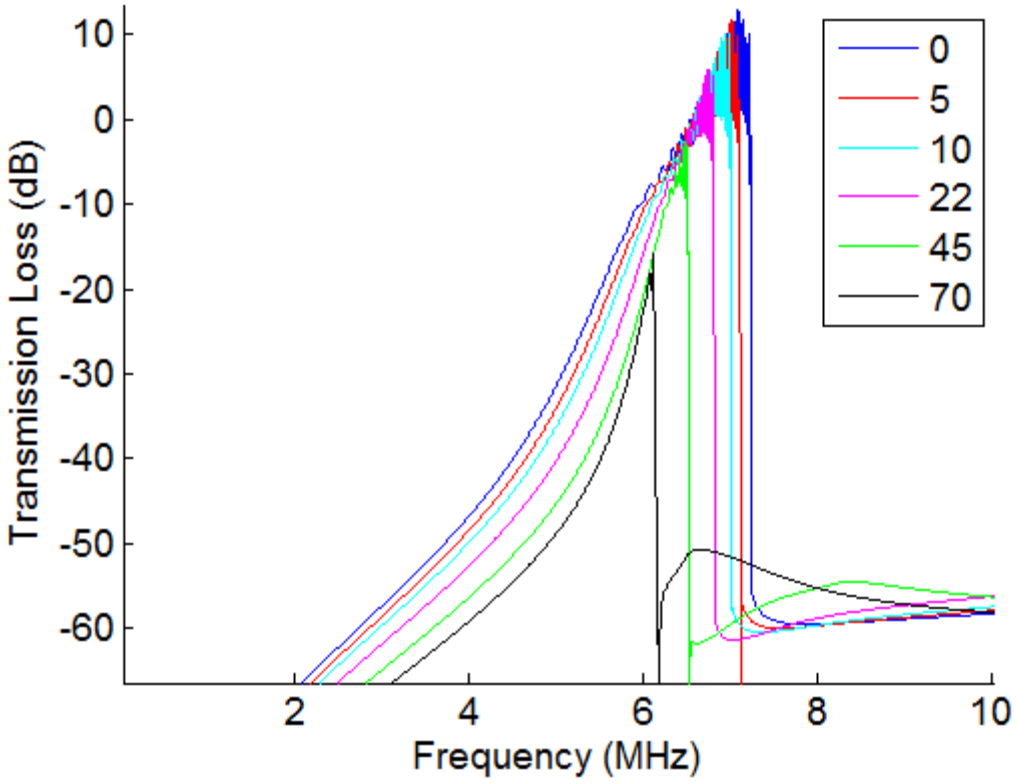

Figure 4.13 Transmission through a 5x40 membrane array with varying membrane spacing in μm which shows a moving band stop from 7.1MHz down to 6MHz

4.3.2. Nonuniform Resonators

In practice, manufacturing process variations cause the membranes to differ in terms of physical dimensions and/or resonant frequency. Therefore it is important to understand the variability of each resonating membrane while still maintaining an effective device. This issue is investigated using a normally distributed variable for the stiffness of the membranes, which in turn will make the membrane resonance a random variable as well. Standard deviations from 0.1% to 5% of the mean stiffness were used to see the effect on the dispersion and the modes. Dispersion curves of the wave propagation with the membranes having variations in the 0-1% range are shown on Fig. 4.14(a) which highlights that there is actually little effect in the dispersion for small variations in the stiffness. However, for higher standard deviations, the non-

uniformity of the resonators results in significant energy to propagate at the bulk speed of water, as opposed to being trapped in modes of the metasurface. This observation is shown in more detail in Fig. 4.15. Increasing random variation of the membrane stiffness, and subsequently its resonance, distorts the dispersion curve and then the dispersive wave becomes very weak compared to the propagating bulk waves in fluid. This shows that with the increasing variation, less energy is trapped in the subsonic modes and instead most of the energy propagates at the speed of the immersion fluid. In each of these cases, the band gap ($f > 7.2$MHz) has some energy due to the wavenumber-frequency plots being an average over the entire array and not from only the last membrane as band gaps and transmission losses would usually be calculated. This phenomena is similar to what is seen with Anderson localization systems although instead of stiffness coupling this system is couple weakly by mass coupling due to the radiation impedance term [62].

As for the modal analysis, it shows that the quality factor of the slowest mode decreases with the increasing variation, which continues the similar trend to 5%. The transmission plot in Fig. 4.16 is significant as it indicates that when the membranes resonances is greater than σ=1%, then the very sharp spectral peaks that are associated with the trapped modes no longer appear. Hence, if these structures were to be used as a resonant sensor, then the variation of the membranes would be an important design criterion as it is directly related to the quality factor. For transducer design, it would be advantageous, to a point, to introduce these variations in order to disrupt the resonances and reduce crosstalk effects.

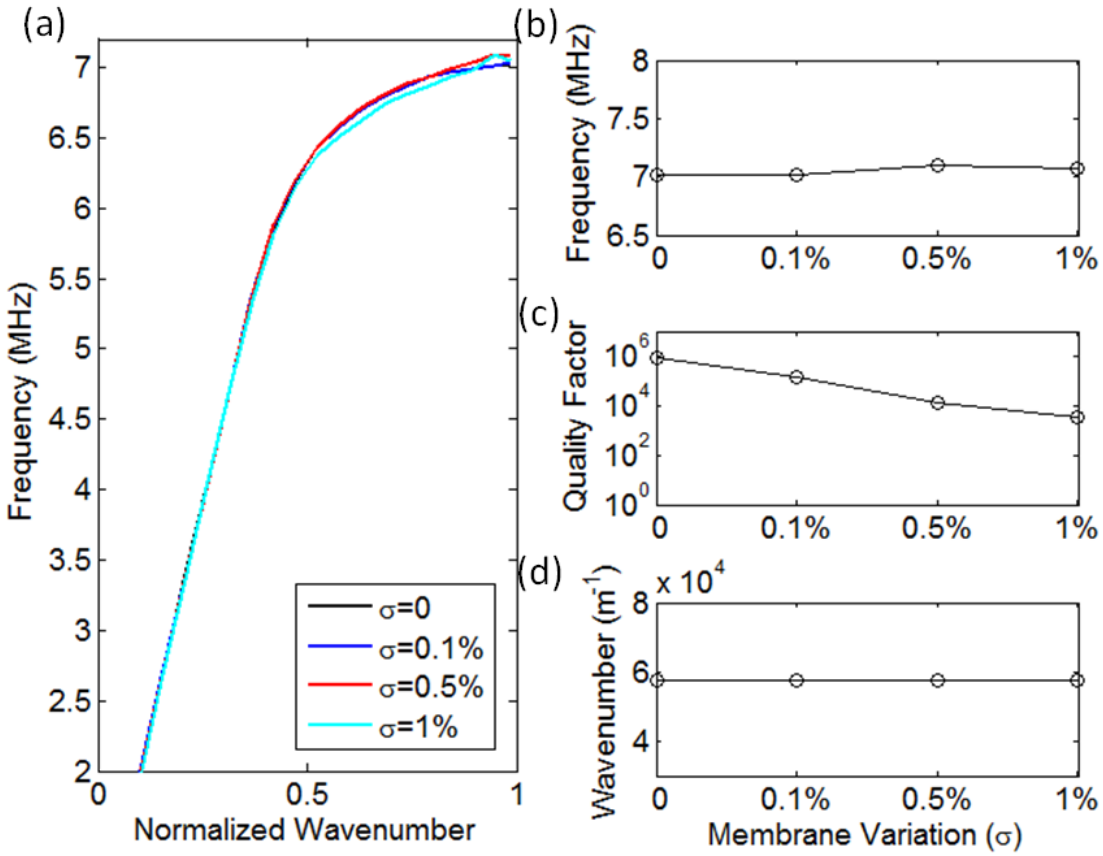

Figure 4.14 Effects of randomizing the membrane stiffness with different standard deviations on (a) dispersion curves and the slowest mode's properties of (b) resonant frequency (c) quality factor and (d) wavenumber. [45]

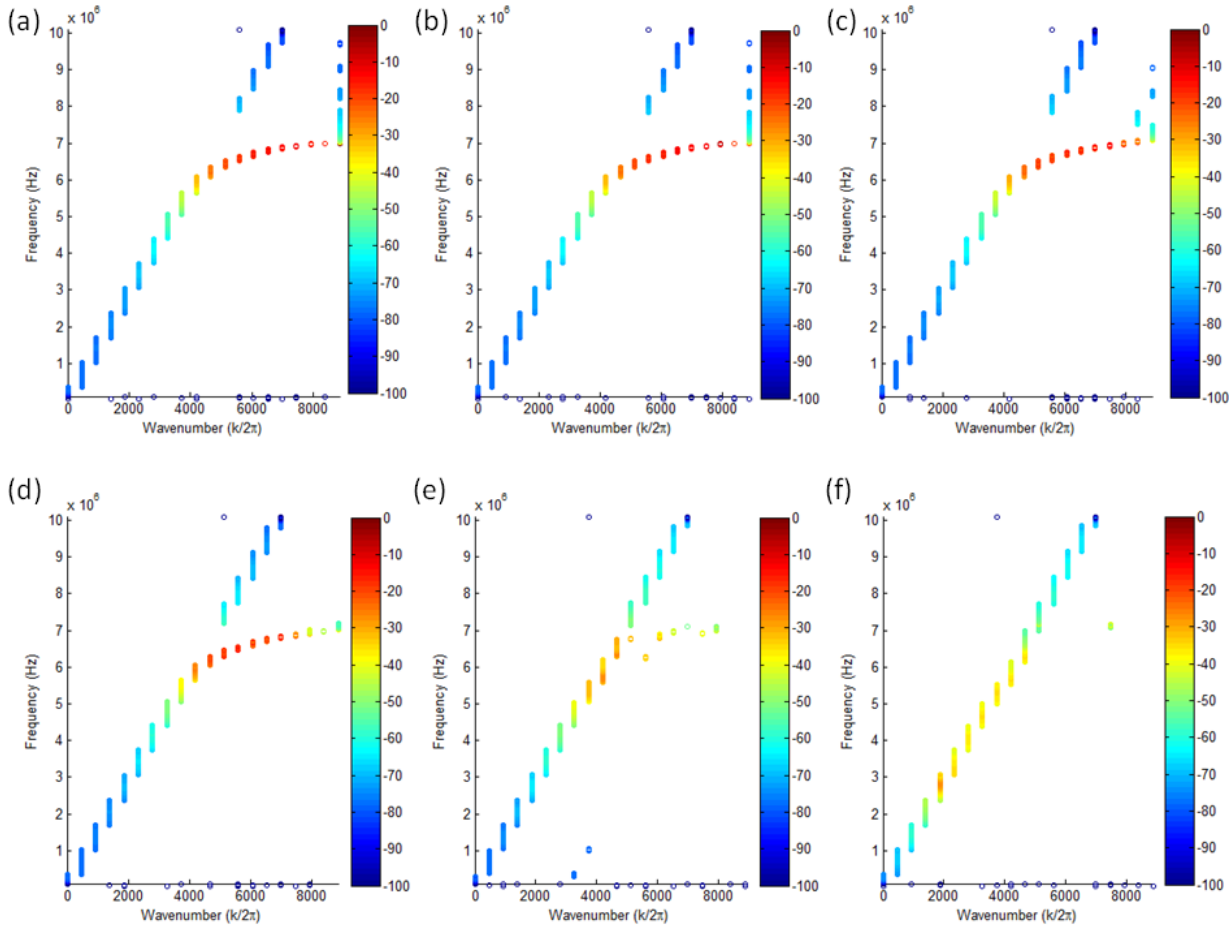

Figure 4.15 Wavenumber-frequency plots obtained by taking the maximum value for each frequency for different standard deviations of variation (a) 0% (b) 0.1% (c) 0.5% (d) 1% (e) 2.5% and (f) 5%. The color bar is normalized to the maximum value across all subfigures. [45]

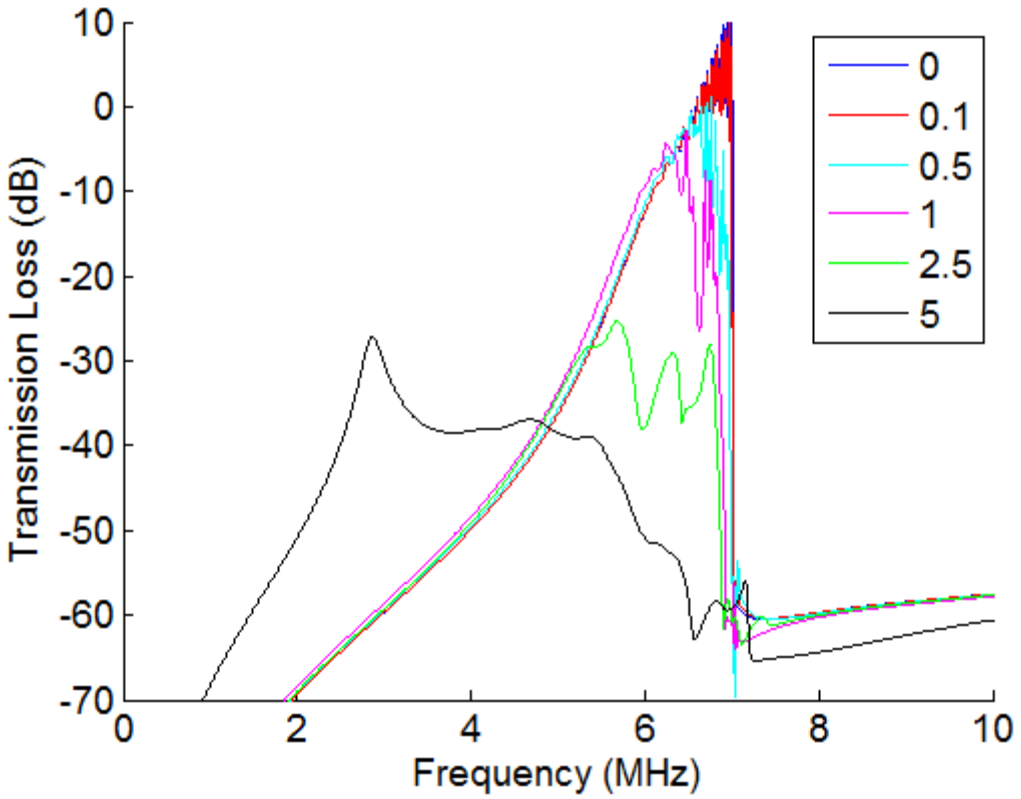

Figure 4.16 Transmission through a 5x40 membrane array with varying membrane stiffness by different standard deviations

4.3.3. Aperiodic Spacing

Since the modeling approach utilized in this research does not depend on periodicity, it allows analysis of arrays where the membrane spacing is not periodic. For this purpose, the membrane spacing was spatially randomized with a uniform distribution, U(0,b), where b is changed from 5, 10, 22, 45, 70, and 100μm. The resulting dispersion curves are shown in Fig. 4.17(a). Due to the aperiodic spacing of the membranes, there is no set edge of the wavenumber space (Brillouin zone) and hence the wavenumber is not normalized as it had been in the prior plots. The results are very similar to Fig. 4.14(a) and show that even in the presence of random membrane spacing, dispersive effects still occur. As the randomness is increased, the maximum wavenumber is reduced. However the slow wave is still present until random variations become

large (i.e. b=100), such that the energy mainly propagates at the speed of sound in water as membranes become significantly decoupled. This illustrates that the metasurface will retain its dispersive characteristics, even with significant randomness as long as the majority of the membranes are spaced closer than $\lambda/2$. This is further supported by analysis of the transmission plots in Fig. 4.18. For random spacing with $b<45\mu m$ there still appears sharp spectral peak in the transmission while for the larger variations the transmission is more smoothed and loses the sharp spectral peaks. When observing the results from the modal analysis, it is clear that the quality factors are lower than that for a periodic structure. Hence, resonant sensors should use the metasurface with periodic arrangement of membranes.

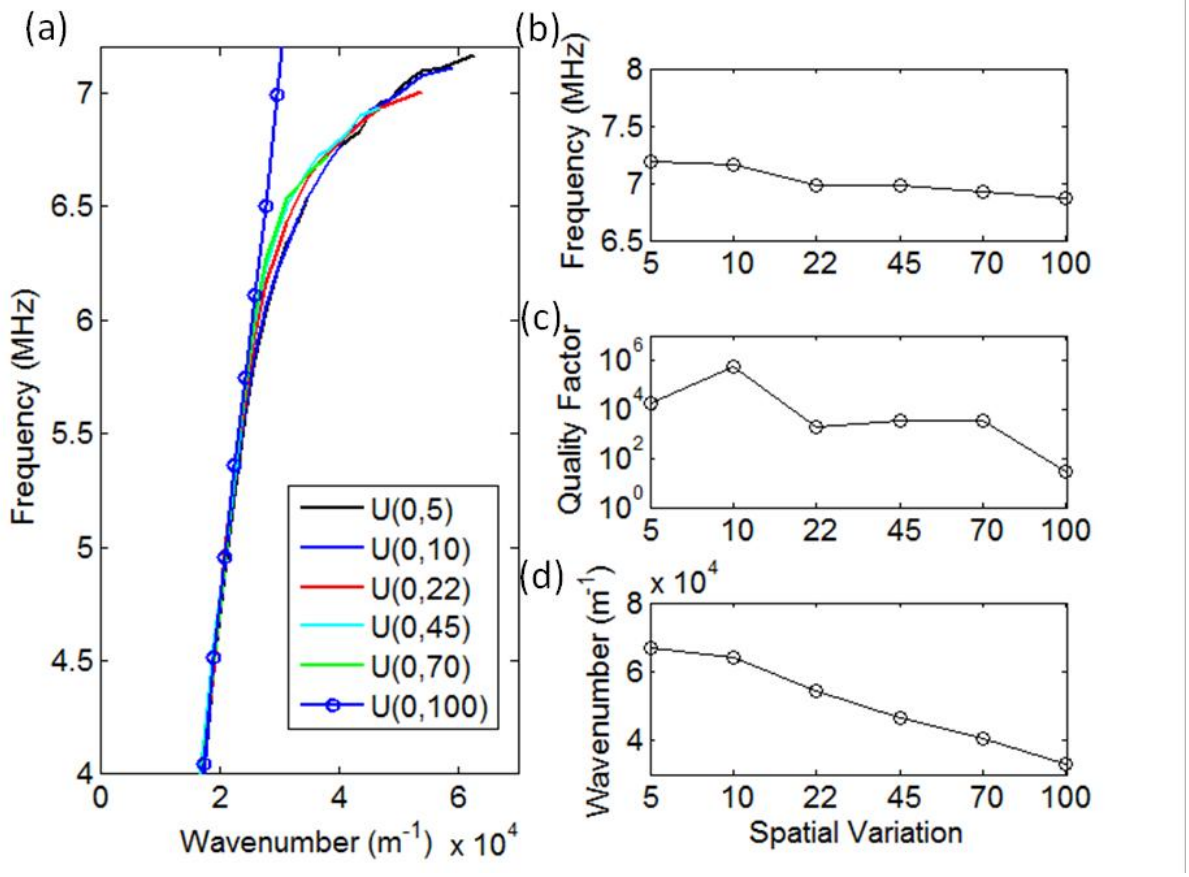

Figure 4.17 Effects of randomizing the membrane spacing by using a uniform distribution, U(0,b) on (a) dispersion curves and the slowest mode's properties of (b) resonant frequency (c) quality factor and (d) wavenumber [45]

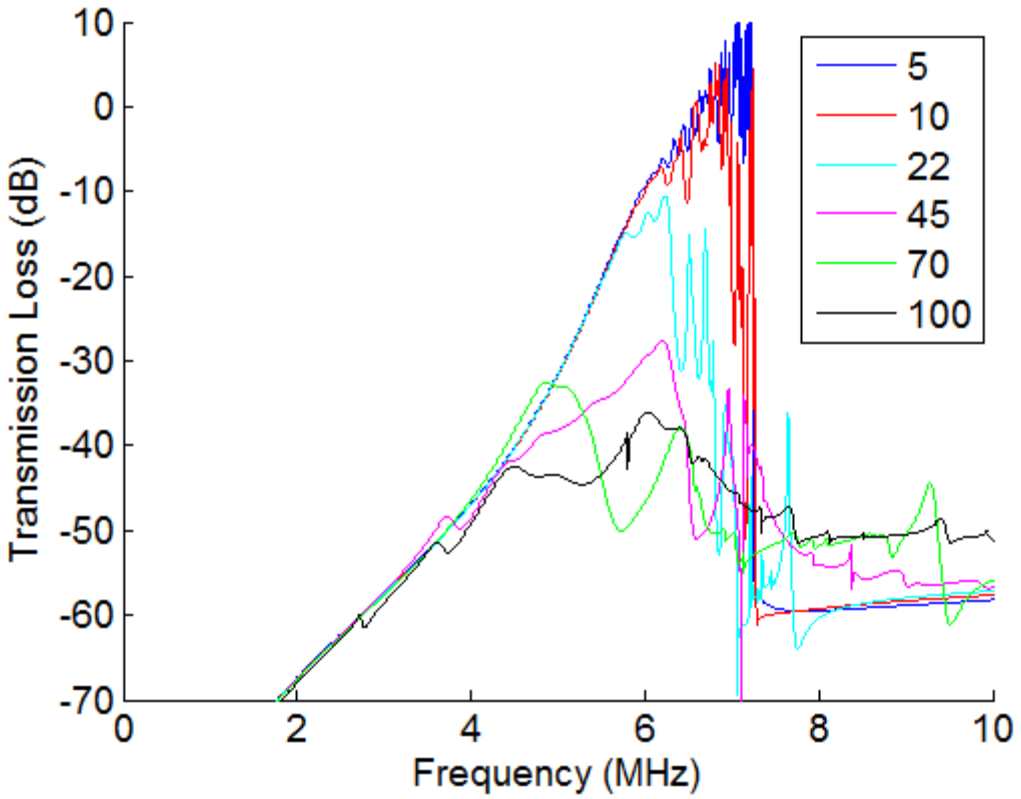

Figure 4.18 Transmission through a 5x40 membrane array with random membrane spacing using a uniform distribution of U(0,b) where b changed from 5 through 100μm

4.4. Summary

This section is very important as the fundamental findings in this section are applied in later sections. The first main point is that the trapped modes of the metasurface determine the dispersion of the evanescent waves. To prove this fact the modes of a two linear arrays were computed and compared to transient results via a wavenumber-frequency plot. Some of the modes are supersonic and radiate energy into the surrounding fluid. While the other modes are trapped modes that radiate very little energy into the fluid, contain information at the subwavelength scale, and determine the propagation of the evanescent waves.

The second main point is that this metasurface is capable of negative refraction. Two-dimensional transient analysis on a large array shows evidence of four distinct frequency bands

of surface wave propagation: isotropic, anisotropic, directional band gap, and complete band gap around the first resonant mode of the membrane. Some of the frequencies in the partial band gap show concave equifrequency contours. Hence this narrow frequency range can be used to design 2D acoustics lenses potentially capable of subwavelength imaging.

The final main takeaway is the effects of altering various array parameters on the dispersion, transmission, and modal properties. The pitch, randomized stiffness, and aperiodic spacing of membranes were varied. The most important finding is that if the membranes are spaced farther than $\lambda/2$ then no dispersion occurs as no trapped modes are present on the structure. All waves will then propagate at the speed of sound of the immersion fluid. However, as long as the membranes were spaced closer than $\lambda/2$ the metasurface exhibits the dispersive qualities even in the presence of nonuniform spacing and slight variations of the membrane resonance. Higher variations (greater than 2% of the mean) of the membrane resonance were shown to disrupt the trapped modes and the dispersion. These results and findings should be very useful for transducer array design, resonant sensors, and acoustic filters.

CHAPTER 5

PROPERTIES OF SURFACE ACOUSTIC WAVES ON MEMBRANE METASURFACES: EXPERIMENTS

This chapter utilizes experimental methods to verify the simulations discussed in the previous chapter. Two different membrane arrays are evaluated to validate the simulations. The first is a linear array which is used to measure the 1D dispersion of the surface acoustic wave. These tests are extended to demonstrate how the dispersion relation as well as the transmission through the array can be altered by shifting the resonant frequency of the membranes. A second array is presented that is designed to observe 2D phenomena of the waves on a metasurface. The array, experimental setup, and comparison between simulation and experiments are shown in this chapter. The design of the 2D array is detailed in Appendix A with the design criteria being based on its use for subwavelength focusing as detailed in the following chapter.

5.1. Analysis of Linear Arrays

The linear CMUT array that was utilized in the experiments is shown in Fig. 5.1-5.2. Each element is comprised of 45x4 membranes with each membrane having the lateral dimensions of 45μm x 45μm, a thickness of 2.2μm, and a gap of 47μm. The center frequency of the membranes is 6MHz with the collapse voltage at 30V. Fig. 5.1 shows the top portion of one CMUT element. The CMUT elements have multiple membranes wired in parallel with a common electrode. There are different periodicities contained within this array. The membranes within an array element are separated by 10μm in each direction while different elements are

separated by 35µm. A full view of the experimental array with the first element on the left and the sixteenth element on the right is shown in Fig. 5.2 along the wire bonding to the electronics

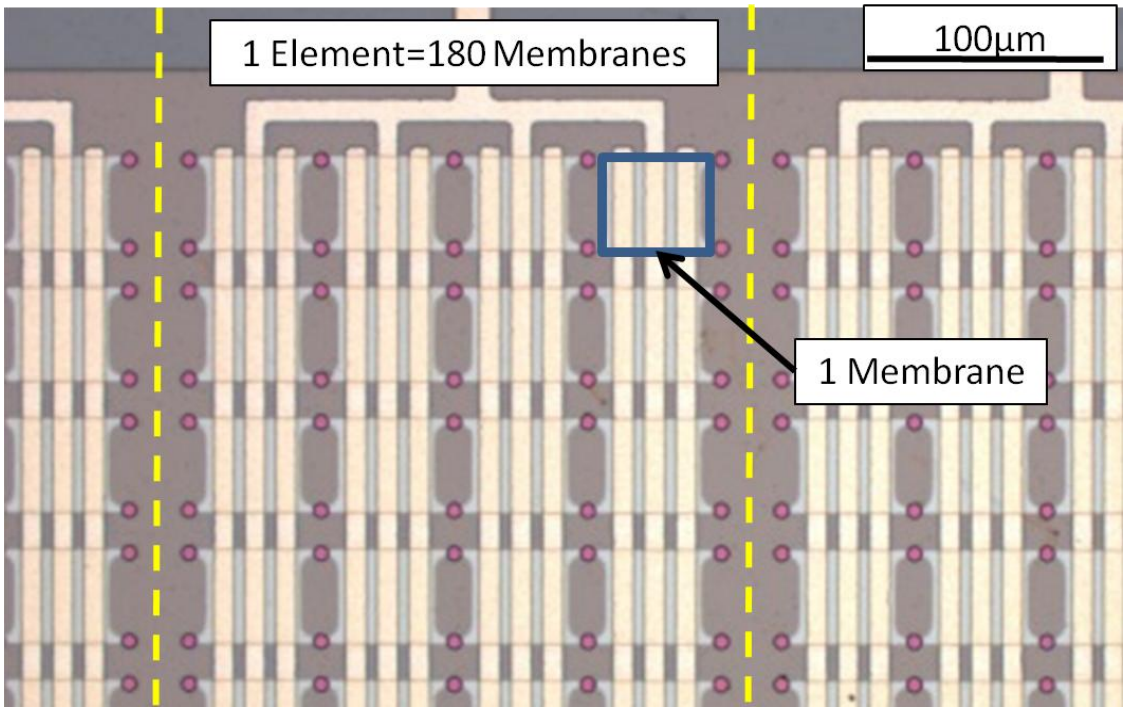

Figure 5.1 Top view of CMUT array zoomed in highlighting the size of one membrane and part of one element delimitated by the yellow dashed lines. The lighter rectangles running along the element and through the membranes are the top electrodes and comprise of a center electrode and two side electrodes.

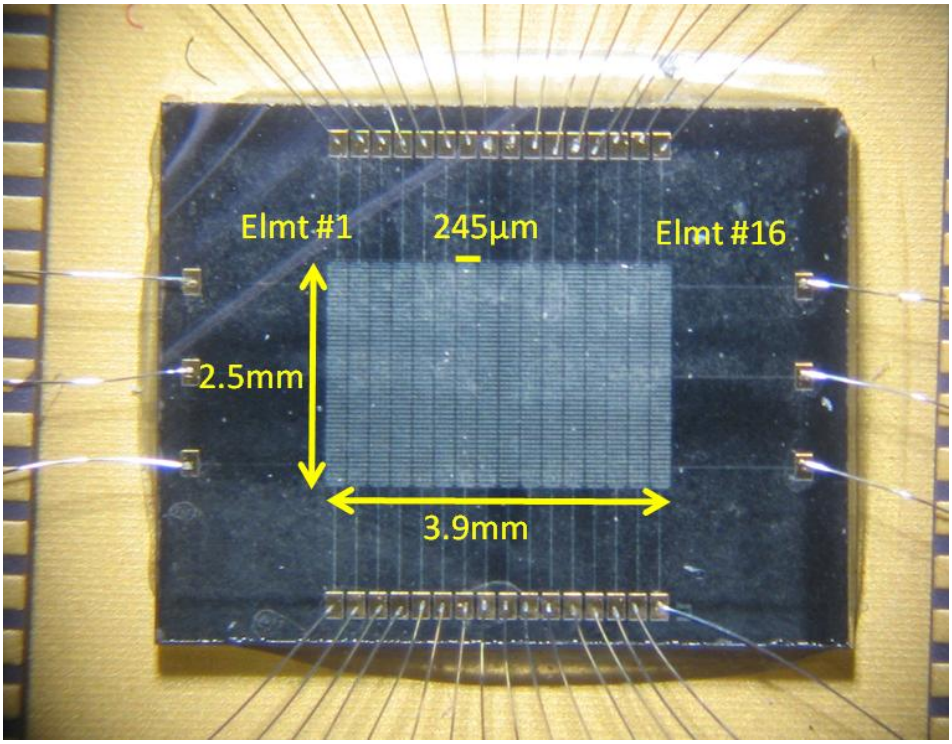

Figure 5.2 Full 1x16 array with wire bond pads and connections used in experiments

5.1.1. Dispersion of Surface Waves

The experiments use the 1x16 array immersed in water. Both the transmitter (first element) and receivers (elements 4, 8, 12, 16) are biased to 20V while the transmitter is excited with an 8V, 40ns, unipolar pulse. Figure 5.3 shows the normalized displacement of the 4th, 8th 12th and 16th element relative to their distance from the first element for three cases. The first two cases are simulations with the Fig. 5.3(a) showing the simulation with uniform membrane stiffness while Fig. 5.3(b) is the simulation with the membrane stiffness randomized with a standard deviation of 5% of the norm. The experimental results are shown in Fig. 5.3(c). These results agree well with the simulation with regard to showing the dispersive nature of the signals, with the lower frequencies arriving before the higher frequencies. The later arrivals (e.g. 6µs arrival on the 4th element) in the simulation with uniform stiffness (Fig. 5.3(a)) are due to the standing or trapped modes on the array. These trapped modes are sensitive to variations in

membrane stiffness and mass as was shown in the previous chapter [44]. Hence, the experimental results and the simulation with stiffness variation results do not show this later resonant arrival as robustly as the simulation with uniform membranes.

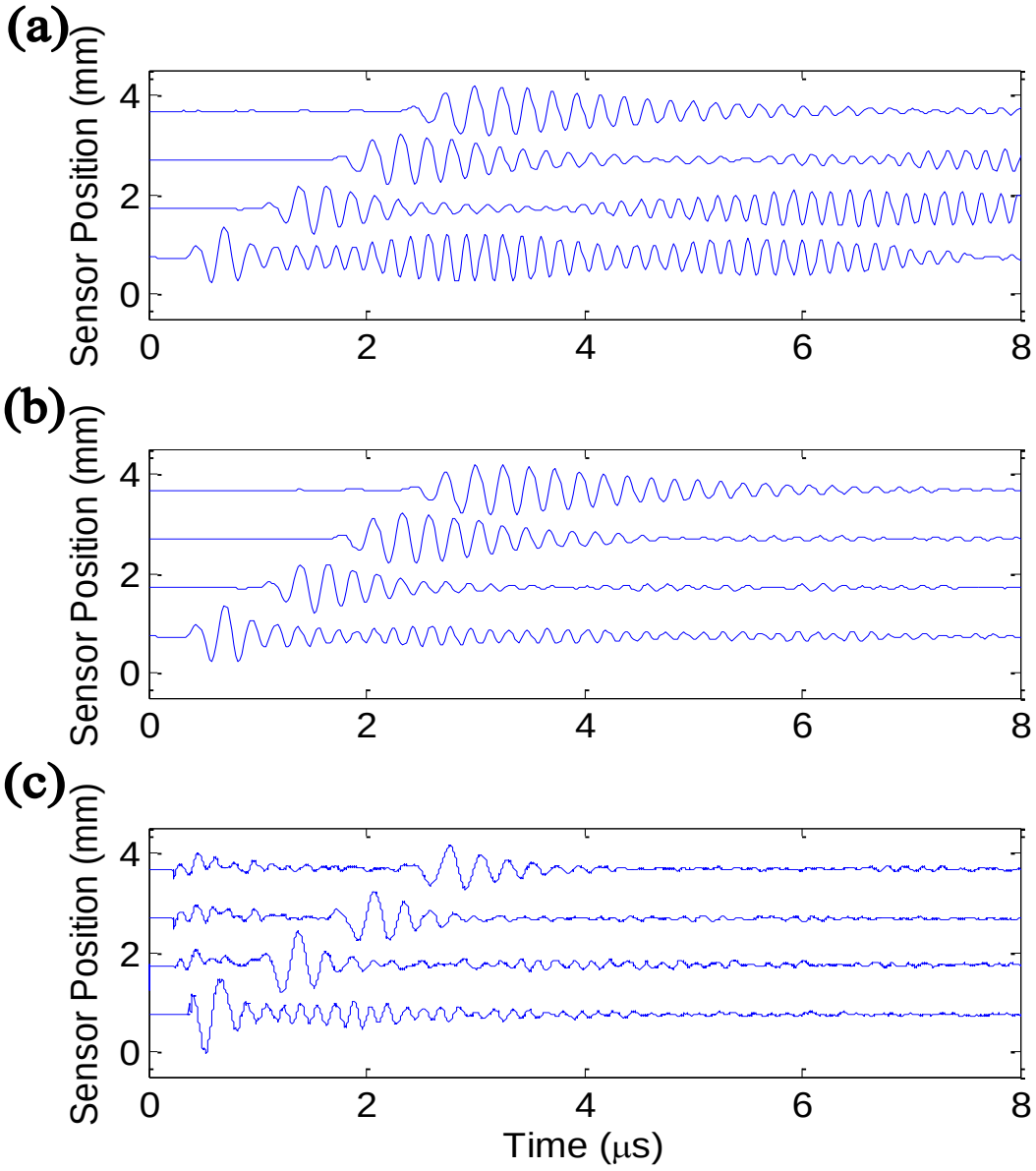

Figure 5.3 The array was submerged in water and pulsed with element 1 while receiving on elements 4, 8, 12, and 16 (a) normalized displacements plotted at the respective lengths between the receive element and the active element for the simulation, (b) simulation with 5% randomized variation on membrane stiffness, and (c) experimental results [44]

In order to estimate the group velocity or dispersion of these surface waves, a time-frequency transform, the Smoothed Pseudo Wigner-Ville (SPWV) transformation, is applied to the simulated and measured waveforms. This transform computes the time-frequency representation of a signal, *s(t)*, and uses time and frequency smoothing windows, functions *h* and *g*, to reduce the interference patterns inherent to the Wigner-Ville transform [15].

$$SPWV(t,\omega) = \int_{-\infty}^{+\infty} h(\tau) \frac{1}{2\pi} \int_{-\infty}^{+\infty} g(u-t) s\left(u+\frac{\tau}{2}\right) s^*\left(u-\frac{\tau}{2}\right) d\boldsymbol{u} e^{-j\tau\omega} d\boldsymbol{\tau} \tag{5.1}$$

The SPWV was used on the 12th element signal for the simulations and the experiment and shown in Fig. 5.4. The main arrival occurs at 2μs for both the simulation and the experiment, with the lower frequencies (~2MHz) arriving slightly before the higher frequencies (5MHz). Following the main arrival, there is the 6MHz arrival, which occurs between 5-6μs for the experiment while the simulations have the arrival between 5-8μs. Since the SPWV gives information about the arrival time for energy at different frequencies, the group speed can be extracted. Several arrivals were selected (illustrated by white circles with black crosses) for each SPWV time-frequency plot (Fig. 5.4). Using the distance between element 1 and element 12 of 2.7mm, the group speeds are plotted in Fig. 5.5 along with the group speed derived from the dispersion curve obtained by the simulation (solid line). Group speed values computed from experimental data and numerical simulations agree closely even when membrane stiffness was randomized (red circle). These results show that the waves are slowed as the frequency is increased which is the expected results from the dispersion relations that were obtained in the previous chapter.

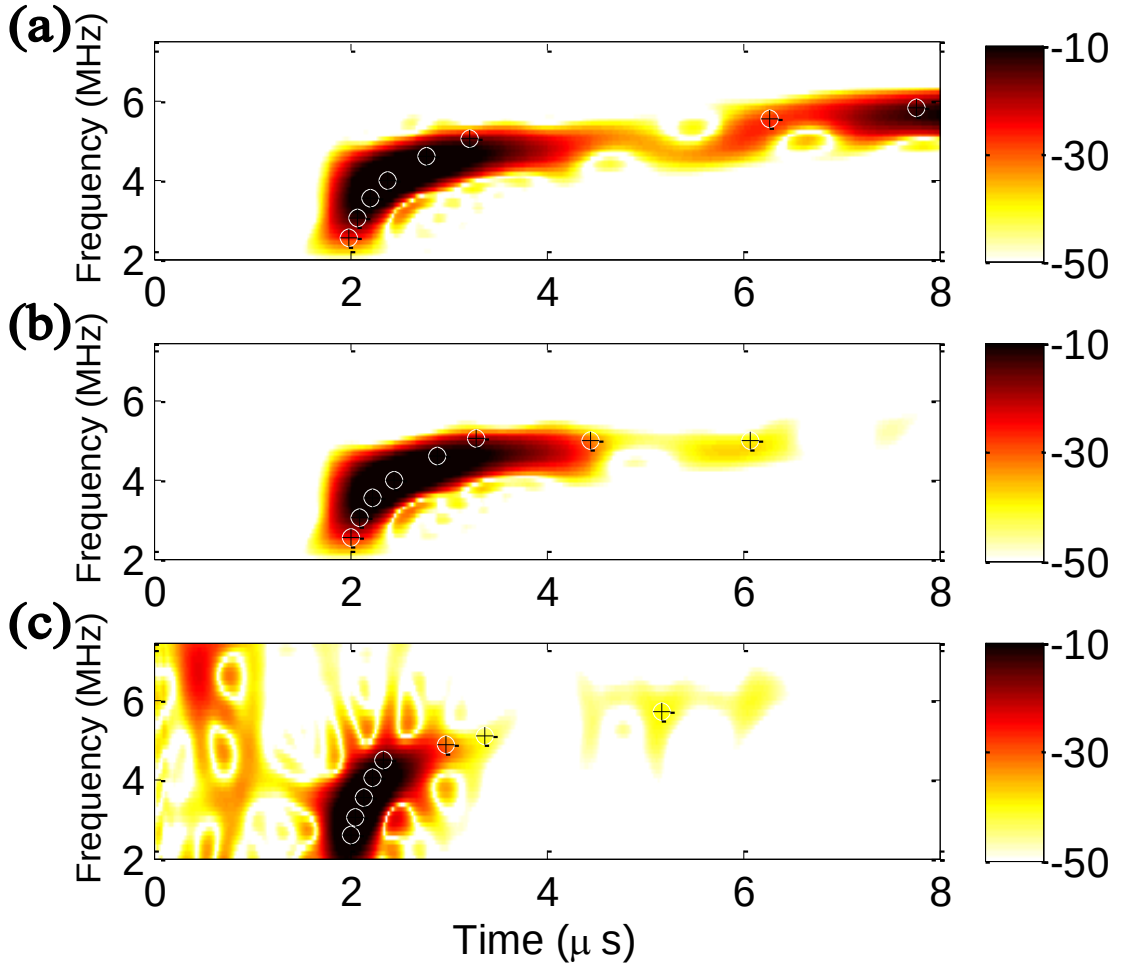

Figure 5.4 Time-Frequency representation obtained from the Smoothed-Pseudo Wigner-Ville of the displacement from the 12th element (d=2.7mm) for (a) the simulation, (b) the simulation with 5% variance of membrane stiffness, and (c) the experimental results. [44]

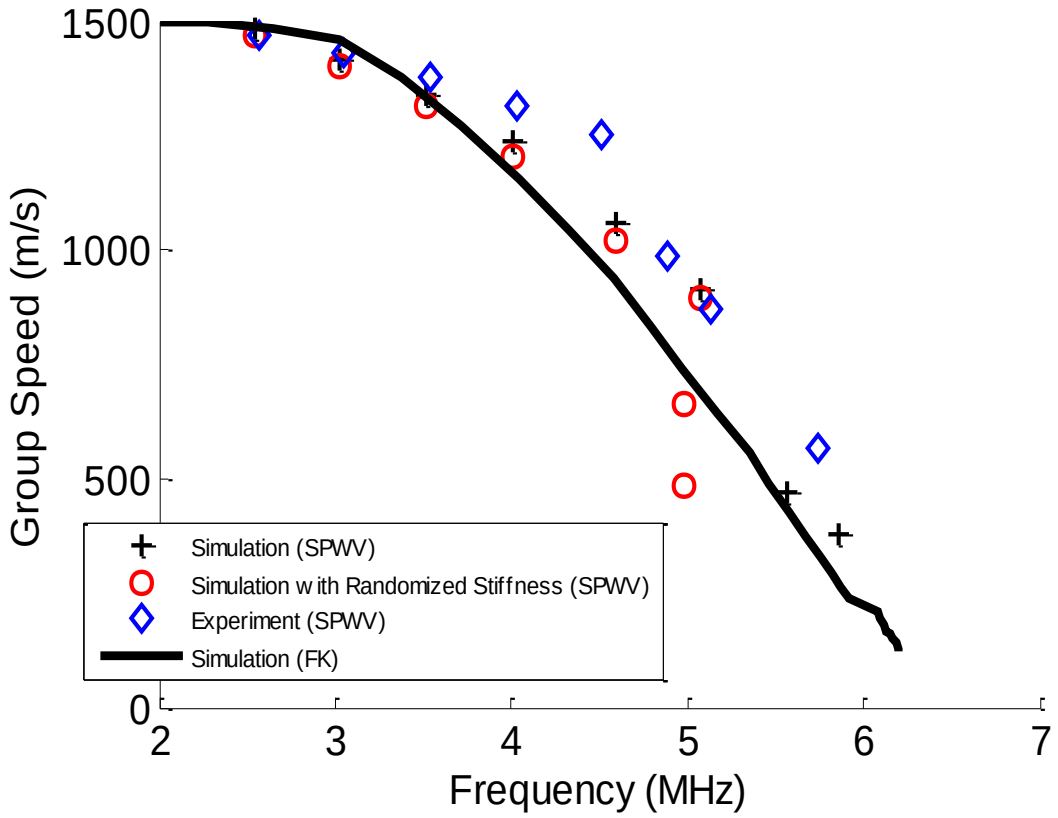

Figure 5.5 The group speeds as obtained by the simulations (black pluses and red circles) and the experimental results (blue diamonds) from the 12th element. The group speeds were calculated using the separation distance between the elements and the energy arrival time obtained by the SPWV with the points used being shown on Fig 5.4(a-c) as white circles and black crosses. The solid black line is the group speed obtained by the frequency-wavenumber (FK) plot calculated from the simulation with uniform stiffness [44]

5.1.2. Tunability of Membrane Metasurface

As stated earlier, a metamaterial derives its properties from the resonant inclusions of the composite structure. Hence, any alteration of the membrane resonance should drastically alter the properties of the propagating surface acoustic waves. While the mass of the membranes remains fixed, the stiffness of the membranes can be controlled by changing the applied bias voltage. As the bias voltage increases (up to collapse voltage when the electrodes are touching each other), the effective stiffness gets softer due to the spring softening effect [79]. Hence, the

dispersive properties and transmission of the surface wave can be controlled by changing the bias voltage applied to the array.

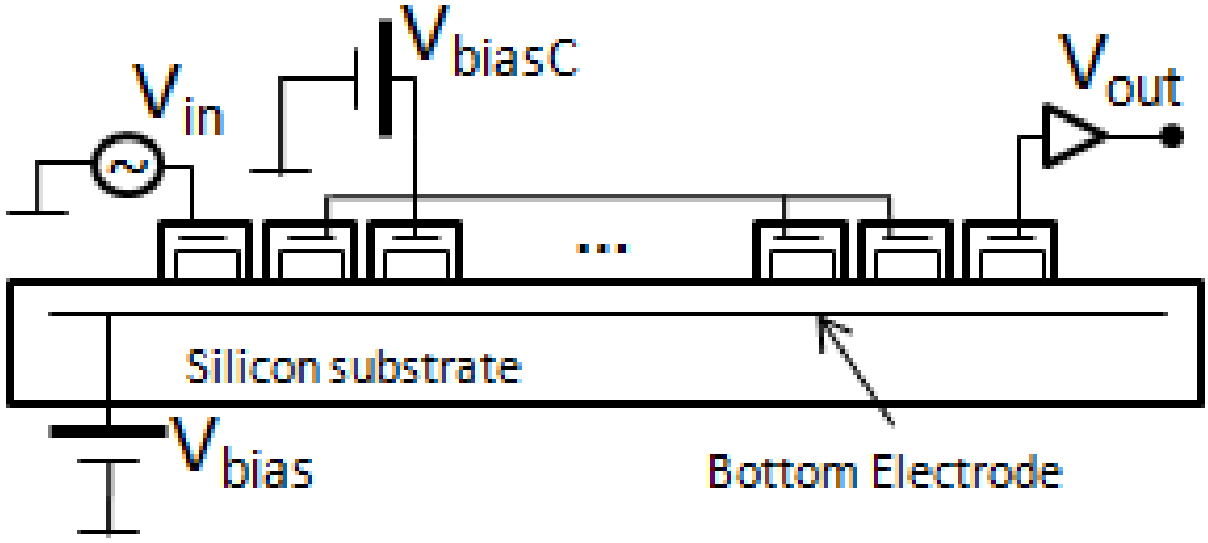

Figure 5.6 (dimensions not to scale) Electrical schematic of the connections to the CMUT array showing that all elements are biased by V_{bias} via the bottom electrode and the center elements (Elmt. 2-15) can have a different bias by them being biased by V_{biasC}.

To further evaluate these concepts, additional experiments are conducted on the 1x16 array with two different DC bias levels applied on the array as depicted in the electrical schematic of Fig. 5.6. All elements in the CMUT array have a common voltage (V_{bias}) applied to the bottom electrode which is fixed on the silicon substrate while the middle elements (Elements 2-15) are biased at different levels (V_{biasC}). This allows the transmitter and receiver to have a high sensitivity while the bias voltage of the middle elements that are part of the propagation medium can be altered to study the effect of different DC bias levels on the evanescent surface wave. The transmitter is excited with a 2V, 40ns pulse, and the receiver's signal is recorded and sampled at 500MHz after being amplified by a transimpedance amplifier (TIA). The simulation modeled each element in the 1x16 array as 5x4 membranes instead of 45x4 membranes of the

actual element for computational considerations. To account for the variation of membrane properties over the array, the simulation also varied the parameters of the membranes by applying a normally distribution to the applied bias voltage with a zero mean and standard deviation of 0.14V. Figure 5.7 shows the calculated normalized velocity signal over the receiver, Element 16, (Fig. 5.7(a)) and the measured TIA output (Fig. 5.7(c)), which is proportional to the average velocity [30]. The received signals are decomposed via the SPWV to better illustrate the dispersive nature of the arrival and are shown under the corresponding time signal. In this particular case, the difference between V_{bias} and V_{biasC} is 0V and this difference will be hereby be referred to as the bias on the middle elements.

The experiments agree well with the simulation with each having an initial arrival time of 2.5μs with higher frequencies arriving later. The amplitude dip in the signals around 4.5μs in time (Fig. 5.7(a,c)) is due to destructive interference resulting from the wavelength of the evanescent wave matching the total width of the CMUT array element of 245μm. This arrival corresponds to the arrival time for 5MHz traveling with phase speed of 1300m/s (computed by simulation). The later arrivals (after 4.5μs) are due to slow waves around 6-6.5MHz, where the group speed of the evanescent wave approaches zero. Above this frequency, there is no significant energy flow, indicating a stop band which is shown with the next tests.

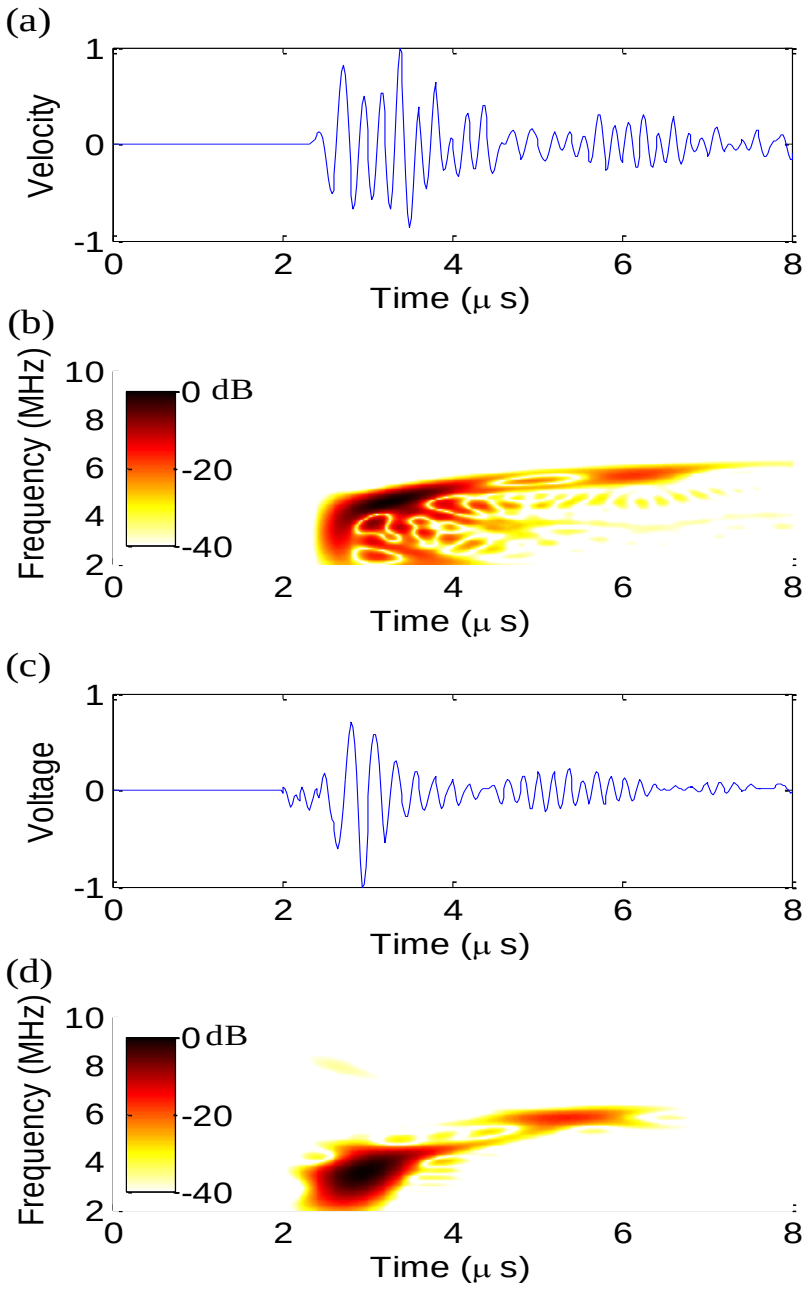

Figure 5.7 The transmitter (Elmt. 1) was excited with a 40ns pulse (a) normalized velocity of the receiver (Elmt. 16) from simulation (b) Time-frequency plot using the SPWV of the velocity from receiver from simulation (c) normalized measured voltage of the receiver from experiment (d) Time-frequency plot using the SPWV of the velocity from receiver from experiment [43]

To demonstrate that the stop band exists and can be tuned electrically by altering the membrane resonance, the center elements are biased with two other voltage levels of 30V and 35V. The Fourier transform of the first 8μs of each signal received is evaluated to determine at which frequencies the evanescent wave is carrying energy effectively along the array from the transmitter to the receiver. These transmission spectra are plotted in Fig. 5.8 for both the simulations and the experiments for 0V (Fig. 5.8(a)), 30V (Fig. 5.8(b)), and 35V bias case (Fig. 5.8(c)). The frequency spectrum of the 0V bias case for both the simulation (blue solid line) and experiment (red dashed line) agree well with each other as both show energy in a frequency band from 2-5MHz and a narrowband around 6MHz along with a stop band edge at 6.5MHz. The dip in the frequency response around 5MHz is due to destructive interference as explained earlier and the small dips in the 2-4MHz band are due to edge effects of the array. Above the stop band, the experimental transmission spectra contains some energy, albeit 20dB below the pass band. Some of the energy above the stop band can be resultant from elastic waves excited in the silicon substrate that reradiate energy to the CMUT elements, which is not accounted by the simulation. As the bias level for the center elements is increased to 30V and 35V, the stop band shifts first to 5MHz (Fig. 5.8(b)) and then to 3.5 MHz (Fig. 5.8(c)). This validates that the properties of the surface waves are dependent on the membrane resonance [22, 47]. As the bias voltage is increased, the stiffness of the membranes is reduced due to the spring softening effect while the mass remains fixed and in turn lowers the membrane resonance causing the shifting band stop [79]. The simulations of transmitted signal spectra at different bias voltages are in agreement with measurements and predict the shift in the stop band edge especially well. Overall, these results indicate that the membrane array has the characteristics of a metamaterial based acoustic

filter with an electrically tunable range from 6.5MHz to 3.5MHz and a drop off of about 20-25dB.

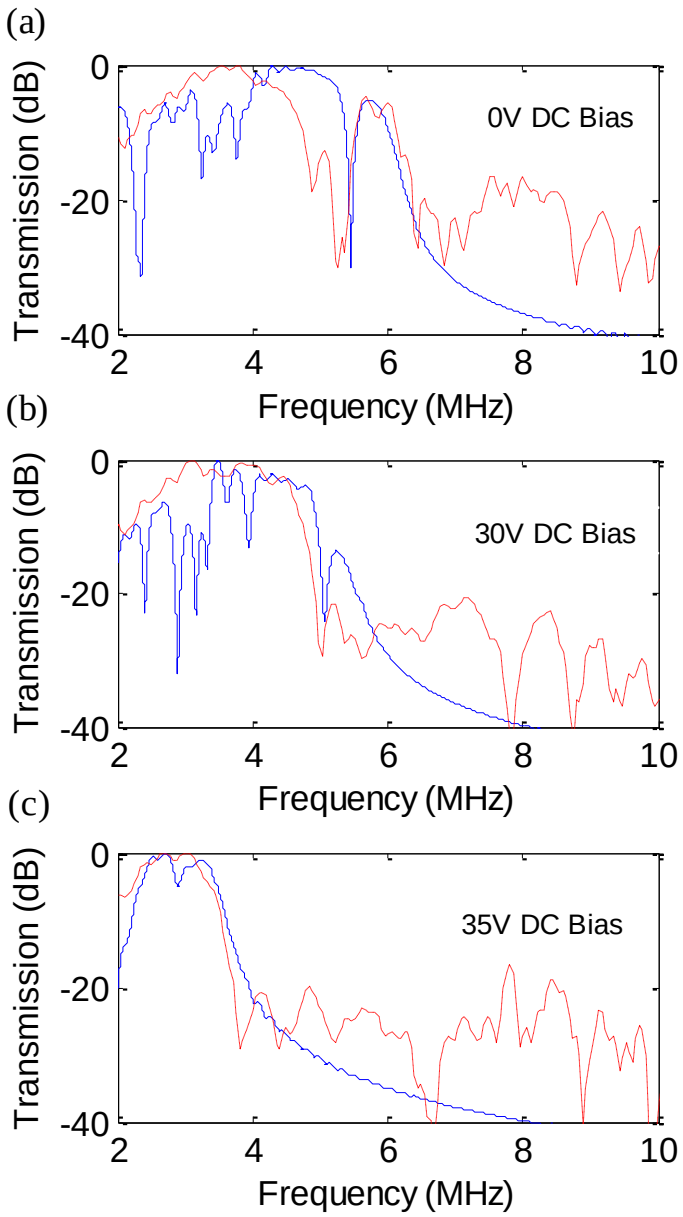

Figure 5.8 Transmission spectra of the first 8μs for both the simulation (blue solid line) and experiment (red dashed line) for (a) center bias at 0% of collapse (b)center bias at 75% of collapse and (c) center bias at 95% of collapse which show a stop band that shifts to lower frequency as the bias level is increased from 0% of collapse (band stop of 6.5MHz) to 75% and 95% of collapse which have a band stop of 5MHz and 3.5MHz respectively. [43]

In addition to altering the band gap, the subsonic group speed of the surface waves over the array can be controlled by the applied bias. The group speeds were obtained from the SPWV analysis of the simulations and experimental signals with a least squares fit to an exponential function as shown in Fig. 5.9 for different bias voltages. Both the simulation (solid lines) and the experiments (dashed lines) are in agreement while showing that the group speed approaches zero near the stop band.

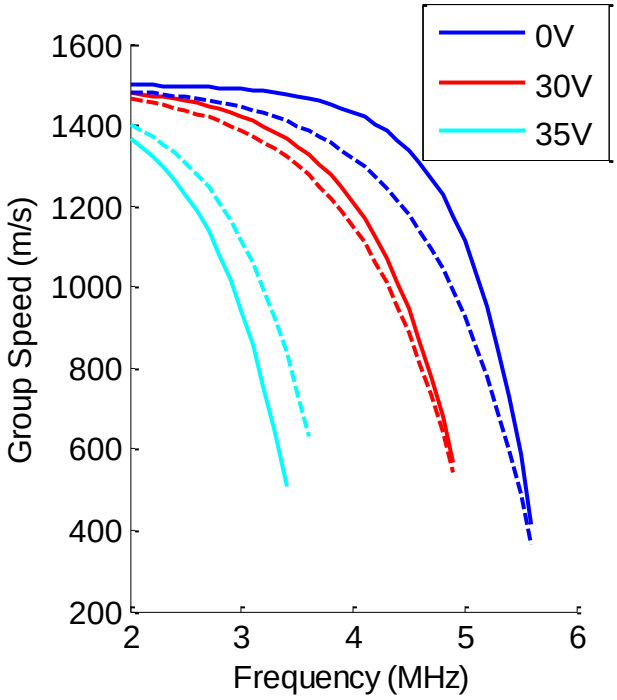

Figure 5.9 The group speeds as obtained by the simulations (solid lines) and the experimental results (dashed lines) for different DC bias voltages applied to the center elements. The group speeds were calculated using the separation distance between the elements and the energy arrival time obtained by the SPWV. [43]

5.2. Analysis of Two-Dimensional Array of Membranes

A second experimental array was designed and tested to observe and verify the 2D properties of the surface acoustic waves on the membrane metasurface. In addition to verifying the 2D properties, this array is also used for the application of subwavelength focusing and

imaging. A parameter study was performed to help determine the array properties and this dictated the setup of the array that was fabricated (Appendix A).

5.2.1. Laser Doppler Vibrometer

One large obstacle to performing tests in two dimensions is the spatial resolution of received signals. The model is able to compute the displacement for a mesh of nodes on any membrane with a spatial resolution as fine as desired. However, to have a strong signal in experiments, it is important to have many CMUT membranes wired in parallel to increase the signal strength at the cost of spatial resolution. This technique worked well in the 1D case in which each element was composed of 180 membranes as this method was looking at how the waves were dispersive over the length of the array. However, to obtain the best spatial resolution, each membrane would need to be wired separately. Consequently signals are not strong enough to be recorded capacitively, so a new method of utilizing a laser Doppler vibrometer to measure the displacement of the membranes.

A laser Doppler vibrometer is a measurement tool that uses the Doppler Effect to measure the velocity or displacement of a vibrating target [26]. This is a noncontact measurement that requires line of sight to the measurement location which works great for measuring the displacement of membranes in the metasurface. The laser Doppler vibrometer employed is a Polytech OFV-534 Compact sensor head with a 10x microscope objective and controlled by the OFV-5000 with a displacement decoder (DD-300). With this configuration, the laser can focus to spot sizes of 3μm diameter and measure displacements in the frequency range from 30kHZ to 24MHz with 0.1pm/$\sqrt{Hz}$ resolution at 100% reflectivity [63, 64].

5.2.2. Experimental Setup

The CMUT array that is used in the experiments is shown in Fig. 5.10. It consists of a dense grid of 7 membranes in both the X and Y directions. Surrounding the dense grid are 8 membranes that are removed from the structure and will be described as either Source/Receivers or the emitting array throughout the remainder of this work. All 57 membranes are the same size with a lateral dimension of 45μm and the spacing in between the membranes in the grid is 10μm. All but 6 membranes were wired as an individual capacitive transducer allowing manipulation of the individual membrane as opposed to having the membranes wire in parallel. The schematic of the top electrode layer is shown in Fig. 5.11 and shows the membranes that can be controlled. The membranes that were physically used for experiments are highlighted red. The top electrode traces can also be seen in Fig. 5.12 with the leads connecting the top electrodes of the membranes to bond pads for the electronics. A full view of the experimental array mounted on a printed control board (PCB) with the laser and electrical connections is shown in Fig. 5.14 with a close up of the setup shown in Fig. 5.13. The full experimental setup consisted of

- Stereo microscope for visual feedback with focusing of laser and positioning the focal spot onto the appropriate membrane for measurement.
- The Polytech OFV-534 Compact sensor head with a 10x microscope objective capable of producing a focal spot of 3μm in diameter. The focal spot can be seen in Fig. 5.12 on the center membrane of the grid as viewed through the stereo microscope.
- The CMUT array was mounted and wire bonded to a PCB. Electrical connections were used for leads that included the 8 exterior Source/Receivers, the center membrane (4,4) and the (2,6) membrane in addition the bottom electrode (Fig. 5.11). A plastic dish was added to the PCB in order that it could hold water above the array as more clearly seen in

Fig. 5.13. The PCB is mounted to a 3 axis stage with the XY plane being controlled by two motorized actuators. For all experiments the laser head remains in a fixed position while the array and setup is translated in the XY plane via the motorized actuators.

- Rigid mounting poles for support of (2) the laser head and (3) the CMUT array.
- Controller for motorized actuators which is connected to and controlled by a computer (not shown) via GPIB connection.
- Switch box to control which membranes are being actuated.
- Laser controller OFV-5000 with a displacement decoder (DD-300).
- Function generator
- DC bias box.

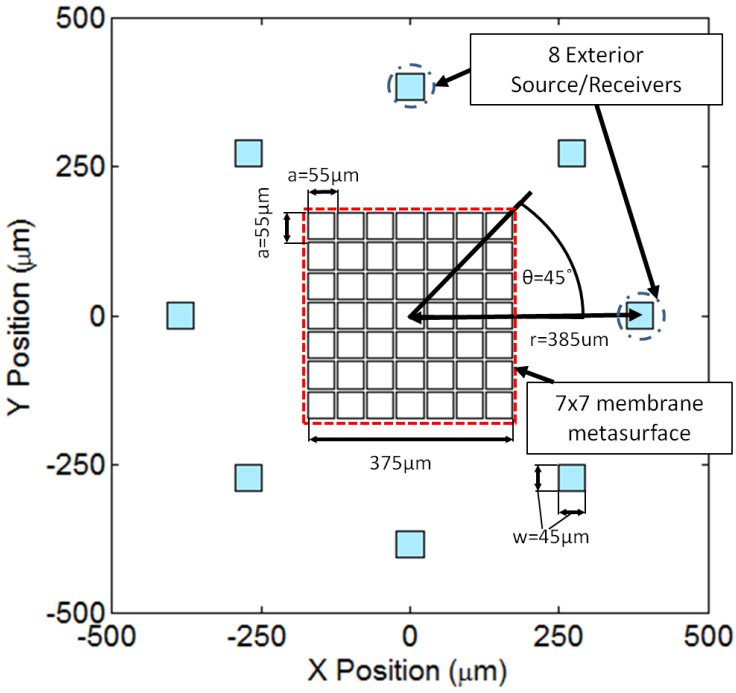

Figure 5.10 Schematic of the membrane array consisting of a dense grid of membrane to support the surface acoustic waves and 8 membranes spatially removed from the grid for excitation purposes.

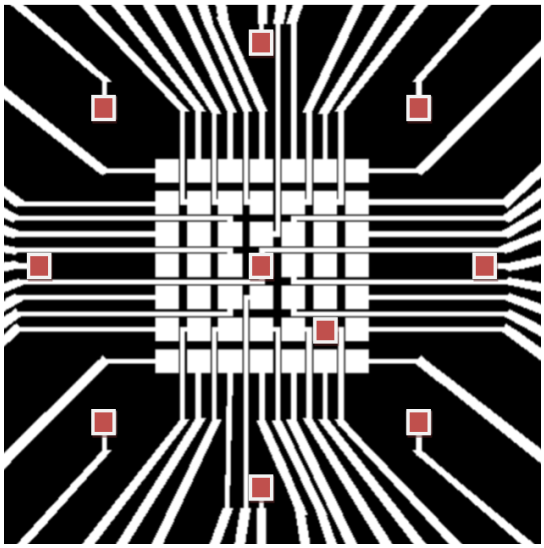

Figure 5.11 Schematic that illustrated the electrical connections of the top electrodes for each membrane. The red highlighted membranes were able to be controlled for the experiments performed in later chapters.

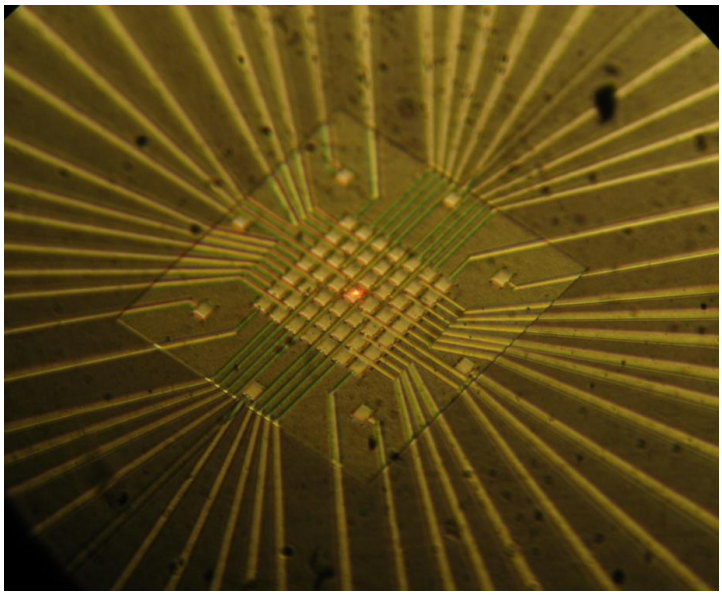

Figure 5.12 Membrane array viewed through a microscope. The laser can be seen as it is focused to the center membrane of the grid.

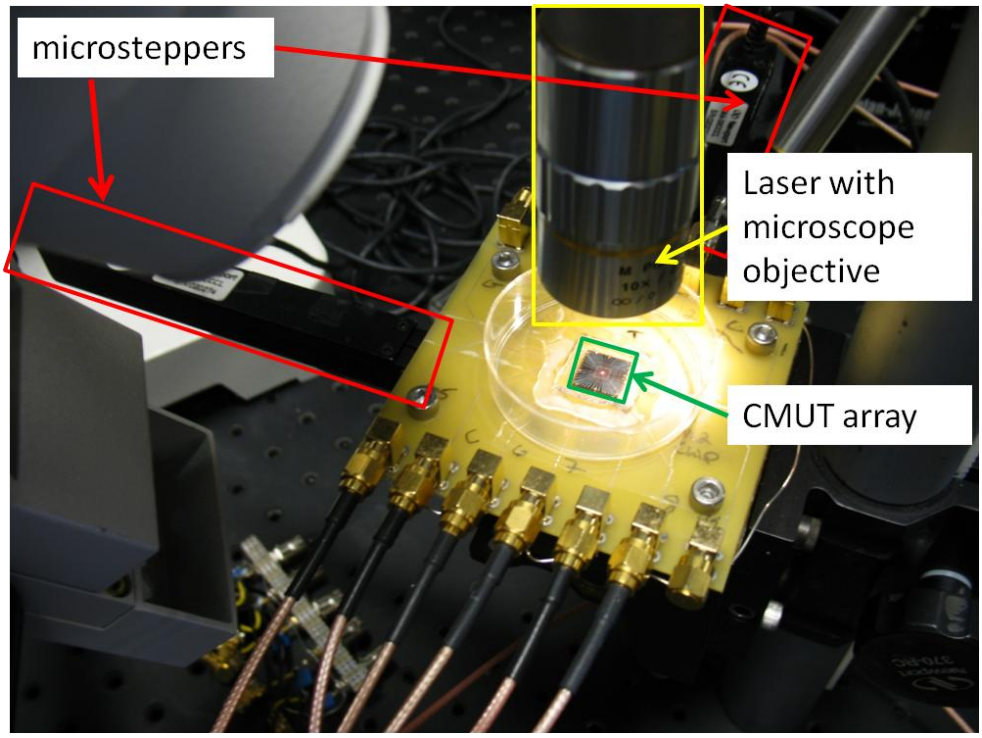

Figure 5.13 Close up of the CMUT membrane array mounted to a PCB, which is anchored to a 3 axis stage with the XY directions controlled by 2 motorized actuators or microsteppers (highlighted red). The laser and the focusing objective of the laser are highlighted in yellow.

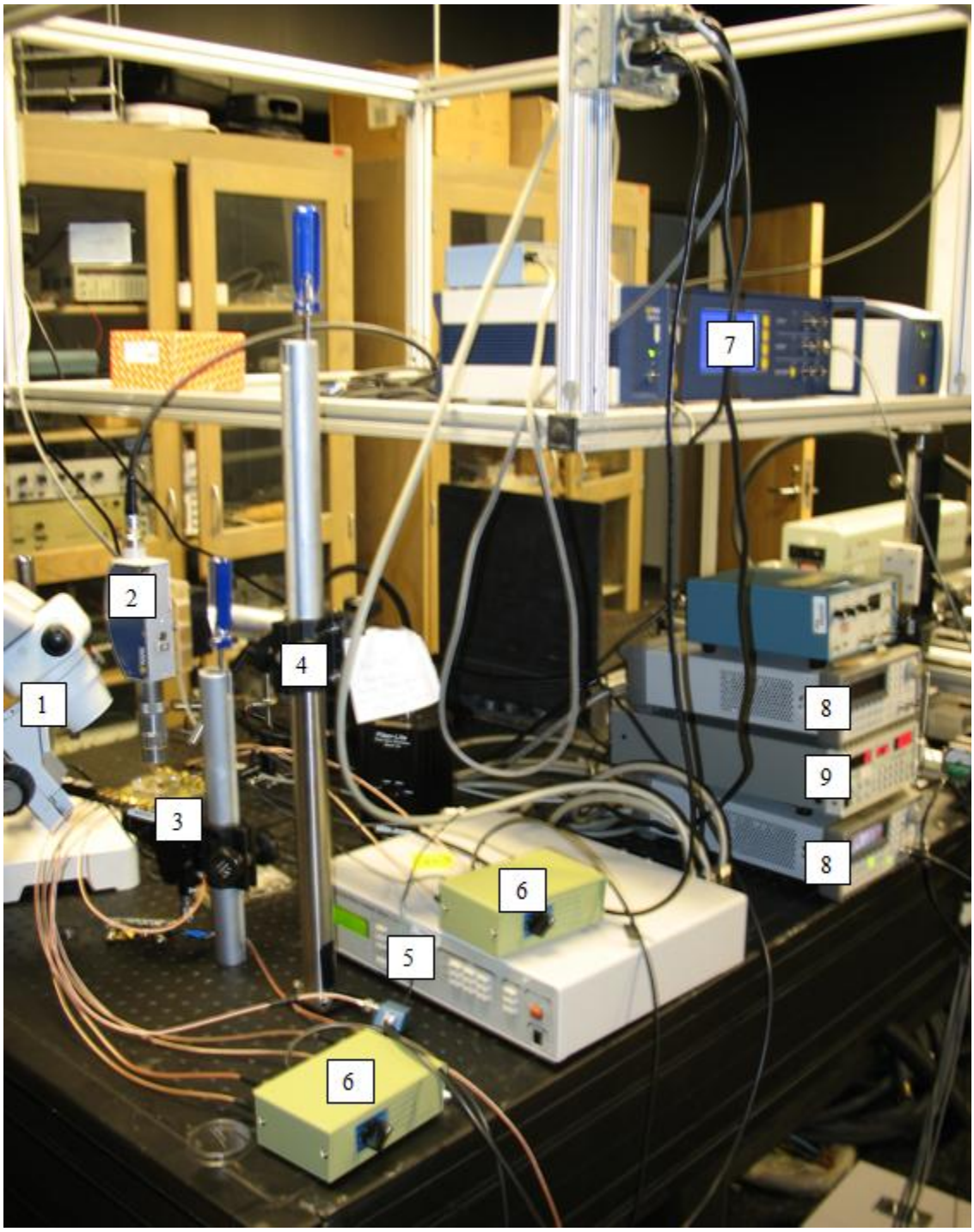

Figure 5.14 Experimental setup which contains (1) stereo microscope (2) laser (3) membrane array mounted on PCB and a 3 axis stage (4) mounting supports for laser and membrane array (5) controller for XY directions for the 3 axis stage supporting the membrane array (6) electrical switch boxes to control the active transducers (7) laser controller (8) function generators (9) DC bias box

5.2.3. Simulation and Experimental Comparison of the 2D Array

To validate the laser measurement system to the model, the 2D array is setup with water above the array and aligned as detailed in Appendix E. The model has several features that need to be matched with the experiments to ensure a correct simulation. While the model accurately solves the stiffness and the mass of the membranes the material damping of the membranes is not easily calculated. Instead to obtain the correct damping the simulation is compared to the experiments and the damping factor is obtained by matching the decay time of the transient signal which also corresponds to the quality factor of the resonance. For the 2D array a damping factor of 2500Pa/(m/s)/m^2 is used (more detail in Appendix B).

The simulation and the experiment compared the displacement of the center membrane in the grid as it was pulsed. A 5V, 50ns, unipolar pulse is transmitted from the center membrane in the grid. Fig. 5.15 shows both the time and frequency response of the center membrane which is pulsed for the simulation (Fig. 5.15(a)) and for the experiment Fig. (5.15(b)). The comparison shows great agreement between the results of the model and those of the experiment in both the time and frequency domains. In the time domain similar amplitudes of displacement can be seen. The beating effects in the time domain are resultant from the coupling of the membranes and is very sensitive to the modes of the metasurface, hence why there is some deviations between the experiments and simulations. The frequency domains are also very similar with 4 distinct peaks present. These spectral peaks are resultant of the presence of the trapped modes on the 7x7 grid of membranes. A more detailed explanation of evaluating the laser measurement system with the model is presented in Appendix B.

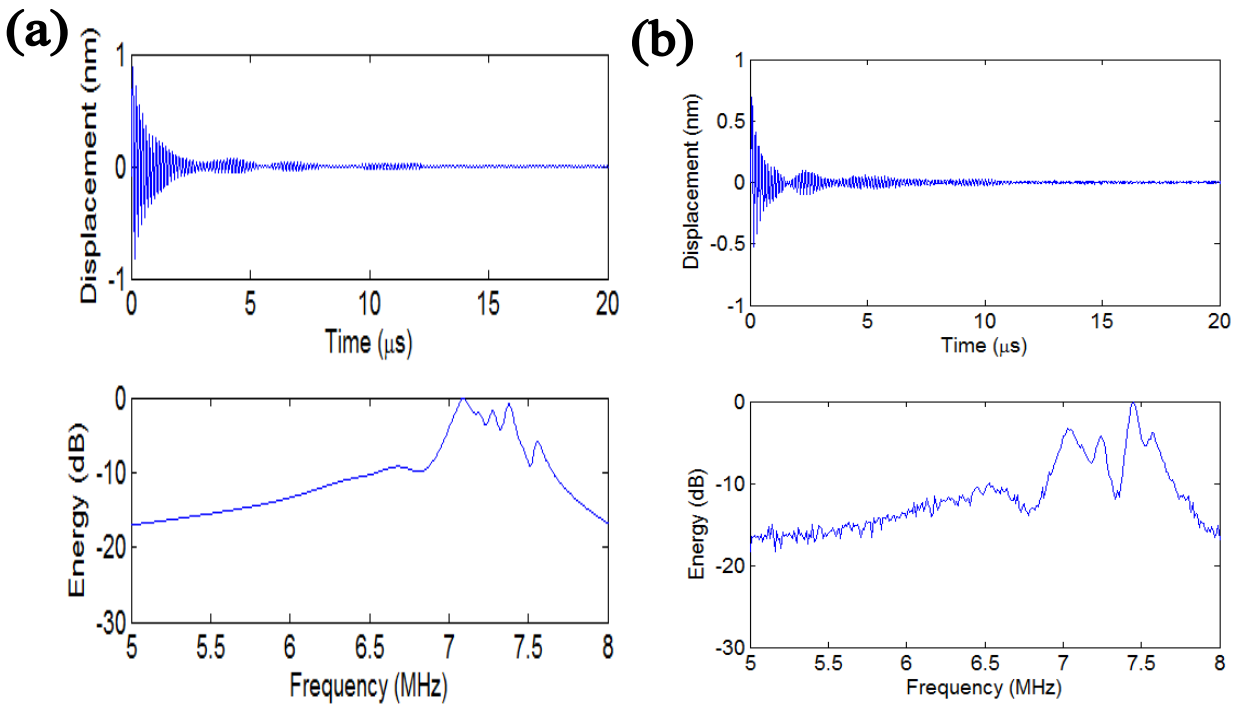

Figure 5.15 Time domain and frequency domain response of the center membrane in the 7x7 grid after being excited with a 50ns 5V pulse for (a) simulation and (b) laser Doppler measurement of the experiment. The spectral peaks are due to the presence of the modes on the 2D metasurface.

5.3. Summary

This section presented the results and verification of the 1D dispersion and transmission of the evanescent waves using a linear array and also presented the experimental setup of the 2D array. The first test verified the dispersive nature of the waves in both the time domain and by means of a time-frequency transform. These results showed that as expected the lower frequencies (f<4MHz) arrive at the same time since there is little to weak dispersion at those frequencies, but around the membrane resonance (6MHz) there is significant slowing of the waves which is a result from the trapped modes on the structure.

Another important conclusion is that a CMUT array is a tunable metasurface. The tunability is controlled by changing the applied DC bias to the membranes which controls the membrane resonance. Both the dispersion and transmission characteristics of the waves were

shown to be dependent on the membrane resonance. Finally, the 2D array was compared to simulations and is discussed in the following chapter with regard to demonstrating the potential for subwavelength focusing and imaging.

CHAPTER 6

SUBWAVELENGTH FOCUSING AND IMAGING

This chapter examines several techniques to focus the surface acoustic waves above the membrane metasurface and extends one of these focusing techniques to image by localizing a subwavelength defect. The metasurface studied is a 7x7 grid of membranes that was detailed in the previous chapter with 8 membranes separated from the structure. The aim is to focus the sound to a subwavelength spot above the grid of 7x7 membranes. The most direct way to focus sound in free space is using spherical beamforming. In this method, the distances between the focal point and all of the transducers are known. A distance can be converted to a time delay by knowing the speed of sound in the fluid. If each transducer sends the appropriate time delayed signal, then the sound will add coherently at the focal region. The key in this method is to have an accurate speed of sound throughout the entire medium which difficult to obtain in dispersive media such as a membrane metasurface. Due to the complex media of the membrane metasurface this focusing method is difficult to implement and hence other methods of focusing are explored (Appendix C).

Another method of focusing is to directly capture the Green's functions from the one array to another array on which the focusing will be accomplished. Once the Green's function between the arrays is known, then an inverse filter can be used to obtain a focus [56, 75, 76]. A similar method is time reversal [24, 25, 47, 56]. This method finds the Green's function experimentally and uses the acoustic reciprocity to refocus the sound. This method does deteriorate if the medium has significant attenuation or poor sampling in space. An iterative method of time reversal can also be performed in an attempt to alleviate the effects of the

attenuation [47, 56]. These methods are executed in both simulations and experiments to show that the subwavelength focusing can be achieved with a focus of $\lambda/5$.

The imaging method that is implemented is based off of the time reversal focusing methods. The proposed technique is used regularly in structural health monitoring literature and is based off of a difference or perturbation method [18, 31, 81]. To perform this imaging a control or baseline measurement is taken of the system. Then the medium in altered in some way and another measurement set is taken. The difference between measurements of the control system and the defect system is taken and is used to localize the defect. This method is used to detect and localize subwavelength defects present within the array.

6.1. Inverse Filter Focusing

One method to achieve sound focusing is through the use of an inverse filter. This method measures the Green's function from the M elements of an emitting array to the control or imaging array of N elements. This collection of signals contains all information with regards to how sound propagates from each of the elements in the control array to each of the elements in the emitting array. This propagation includes the dispersion effects and can be viewed as a spatiotemporal filter. To reverse the effects of the wave propagation, an inverse filter can be utilized. The combination of the forward and reverse propagation allows for the focusing of sound.

The theory of this method follows closely to the paper by Tanter et al. [75]. The first step is to obtain the Green's functions. Experimentally this is accomplished by pulsing individually from the emitting array to the exterior transducers (e_m) with a strong short pulse. The displacement, h(t), is then recorded on the control array of each of the N elements (c_n). In the

frequency domain and matrix notation, the relation between the emitting array, E(ω), and the control array, C(ω), is the propagation operator, H(ω).

$$C(\omega) = H(\omega)E(\omega) \tag{6.1}$$

To invert this propagation, an inverse filter can be devised that will reverse the propagation in addition to negating the attenuation. However, H(ω) is not required to be square since it relates the propagation of M elements of the emitting array to N elements of the control array and hence the inverse of this matrix cannot be directly solved. Instead of obtaining the inverse of H(ω), a pseudoinverse can be performed by using a singular value decomposition as shown in Eq. (6.2-6.3).

$$H = USV^H \tag{6.2}$$

The matrices U and V are the singular vectors with ^{H} denoting the complex transpose operation. The matrix S has the same dimensions as H with the singular values along the diagonal in decreasing magnitude. The pseudoinverse of H can now be written as

$$H^+ = VS^+U^H \tag{6.3}$$

where H^+ denoted the pseudoinverse of H, and S^+ is the pseudoinverse of S which is the transpose of S with each singular value replaced by its reciprocal. Using the pseudoinverse, the focusing can be done by applying the ideal spatiotemporal pattern on the control array by $C_0(\omega)$. The signal then is multiplied by the pseudoinverse and then the propagation operator to obtain the projected field for each frequency and space $C_{pr}(\omega)$.

$$C_{pr}(\omega) = H(\omega)E(\omega) = H(\omega)H^+(\omega)C_0(\omega) \tag{6.4}$$

This projected field is a least squares solution to the focusing problem.

For the experiment and simulations that use the 2D array as described in the previous chapter there are M=8 elements of the emitting array which are spatially removed from the N=49 membranes in the control array. To obtain the propagation operator in simulation the proper Green's functions can be extracted from the model. To obtain this operator experimentally each element is pulsed from the emitting array and the displacements are recorded on the control array by using the laser Doppler vibrometer to measure the displacement. A plot of the singular values of the propagation operator from simulation is given in Fig. 6.1. There are eight singular values which correspond to the minimum rank (column or row) of the propagation operator which in this case happens to correspond to the M=8 elements of the emitting array. These values are used to obtain the pseudoinverse used for focusing. Fig. 6.2 shows the singular values from the propagation matrix that was obtained experimentally. In this case, it is apparent that the last singular value is much less than the others. This singular value is removed as it is likely due to the noise in the signal and not a representation of the physical information between the emitting array and the control array [75, 88]. The results of the focusing by using the inverse filter are shown later in this chapter for comparison to the other methods.

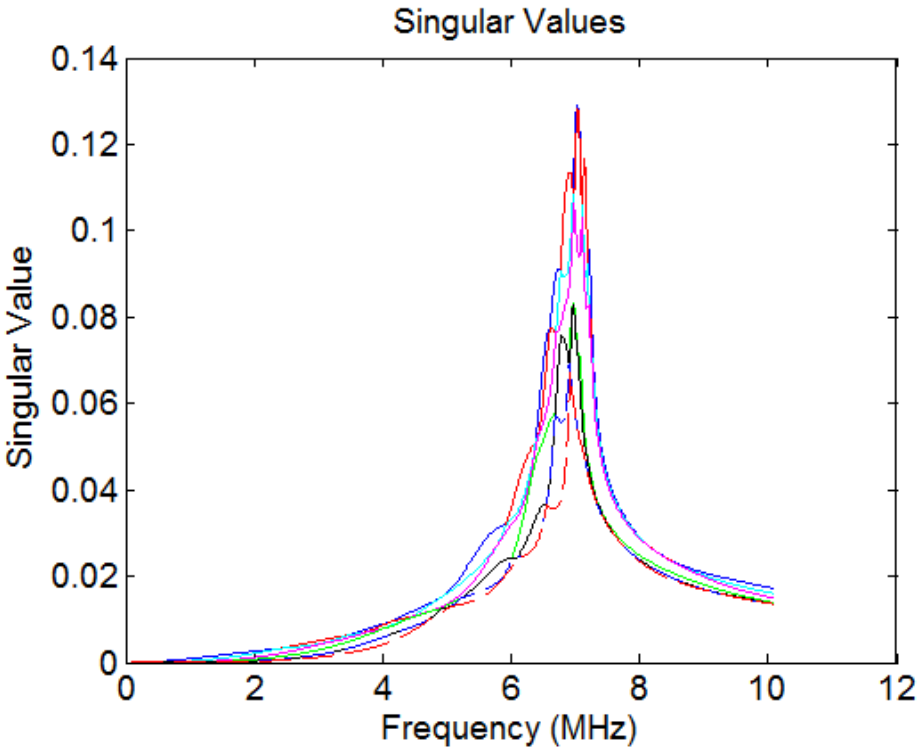

Figure 6.1 Singular values of the propagation operator for each frequency obtained through simulation

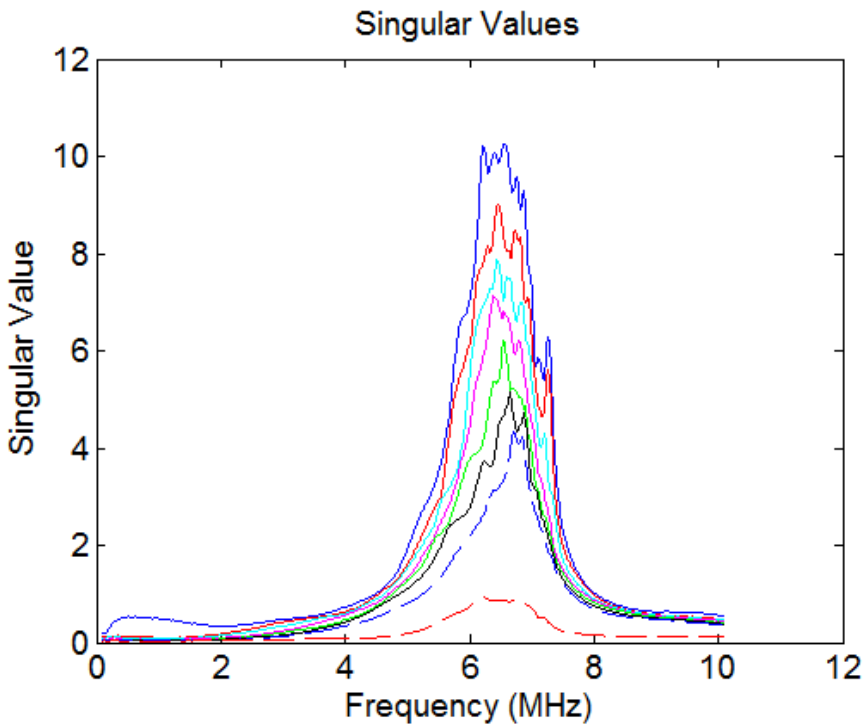

Figure 6.2 Singular values of the propagation operator obtained through experiments. Notice that the 8th singular value (red dashed line) is significantly lower than the others indicative of nonphysical information or noise

6.2. Time Reversal Focusing

6.2.1. Description of the method

Time reversal is a method to refocus sound through a complex medium. It is based on acoustic reciprocity which states for a given source and receiver location the same signal would be received on the receiver as if the source and receiver locations were switched. This method has been used extensively to focus sound in complex media such as seismic, shallow water, and ultrasonic environments [18, 24, 25, 42]. It is shown that the time reversal process is an effective alternative to the inverse filter method of focusing.

The steps of time reversal are relatively straightforward and require two arrays; one that is a control array and the other an emitting array. The first step is to pulse from the location that is the desired focus (the control array). The pulse propagates and is recorded on a set of set of

transducers (emitting array). The recorded signals contains all of the propagation information from the control array or pulser to the emitting array. The signal received is then time reversed on each element of the emitting array and then retransmitted. These signals then propagate back through the medium and refocus at the location where the original pulse was emitted. In essence, it is the practical implementation of an inverse filter in which there is a forward step followed by the utilization of the inverse step to arrive back at the original input signal.

This method can be used for focusing, but it has several requirements for effective focusing. The first requirement is that the emitting array must create a time reversal closed cavity [24] in which the emitting array is placed in locations that can obtain the entire spatial field of the pulse. Often this is not possible and the emitting array may be placed on a limited aperture, termed a time reversal mirror [76]. The second requirement is that the medium is not highly dissipative, as dissipation breaks the acoustic reciprocity of the wave equation. In time reversal focusing, signals that are captured on the emitting array and resent (time reversed) will experience twice the dissipation effects upon refocusing. One method to counteract dissipation effects in time reversal focusing is to use an iterative time reversal method that will correct for the dissipative medium.

For iterative time reversal, in addition to having the pulser and emitting array, there needs to be a control array around the eventual focus as seen in Fig. 6.3 which is an example setup from Montaldo et al. [56]. An illustrative example of the iterative time reversal is presented in Fig. 6.4 with the control array on the left and the emitting array on the right. This control array captures additional information around the pulser which is used in the iterative process to enhance the focus. In the iterative process, the time reversal procedure is first performed as shown in Fig. 6.4(a-b). The focus from the time reversal is shown in Fig. 6.4(b). It is clear that

there is a focus at the proper location but also unwanted signals are present and are received on the control array. These signals are then subtracted from the ideal focal pattern, time reversed, and pulsed from the control array to the emitting array (Fig. 6.4(c)). At this point, both sets of signals received on the emitting array ($e_1(t)$ and $e_2(t)$ from Fig. 6.4) are added and pulsed back through the emitter being time reversed to obtain an improved focus as shown in Fig. 6.4(d).

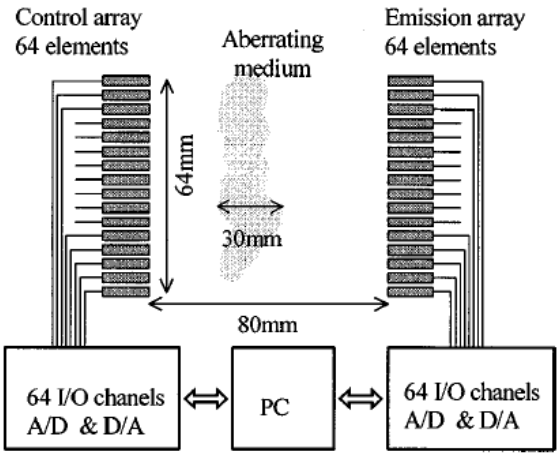

Figure 6.3 Schematic of two arrays used for time reversal with sound propagating through a complex medium [56]

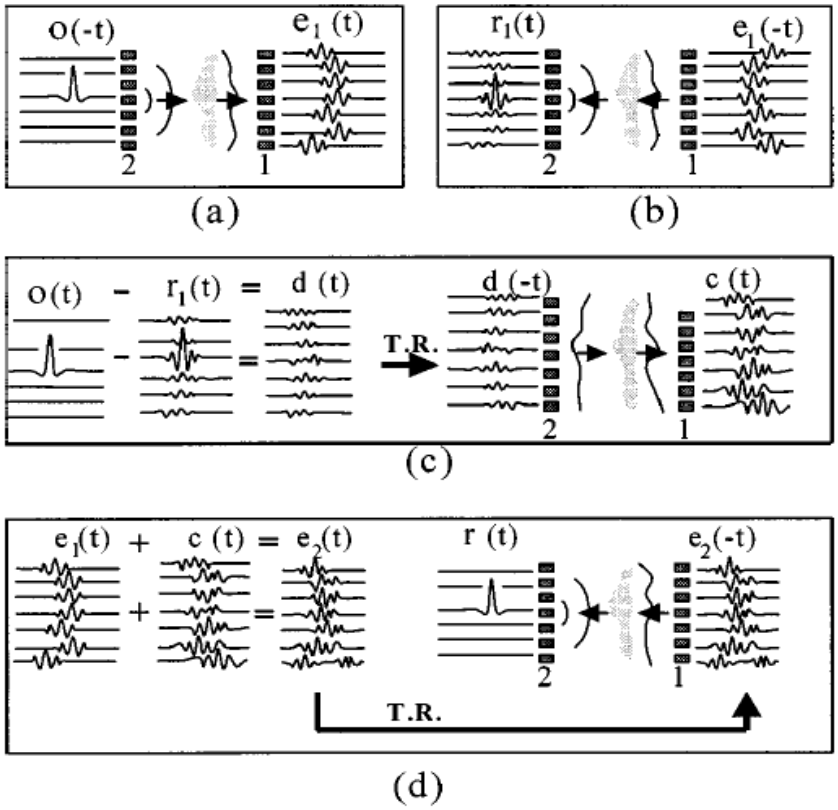

Figure 6.4 Steps of time reversal and the iterative time reversal method (a) pulse the desired spatial-temporal pattern from the control array and record on the emitting array (b) time reverse the recorded signals and transmit back from the respective sensors. (c) Take the difference of the ideal focal pattern and the actual pattern and use these time reversed signals to pulse from the control array. (d) add the two sets of signals that were received on the emitting array, $e_1(t)$ and c(t), to obtain new signals to transmit. The result will be an improved focus [56].

6.2.2. Theory of Time Reversal

This section reviews the mathematical process of the time reversal focusing method and outline the steps of the iterative method of time reversal which follows closely from the reference of Montaldo et al. [56]. For generality and eventual necessity of a control array in the iterative time reversal method, the time reversal theory also uses a control array of N transducers capable of receiving and transmitting. If only one iteration of time reversal is desired, then the additional sensors (other than the pulsing sensor) of the control array are not needed. The emitting array consists of M transducers and is placed in a location that can be termed an

acoustic closed cavity or an acoustic time reversal mirror. The emitter sensors need to be positioned such that they can capture enough information about the field to be able to refocus [24].

The relation between the n^{th} element in the control array and the m^{th} element in the emitting array is related by the Green's function $H_{nm}(\omega)$ or propagation operator. In matrix form, the full relation between the control array and the emitting array can be given as

$$C(\omega) = H(\omega)E(\omega) \tag{6.5}$$

To obtain the response of the control array, the relation is just the transpose of the propagation operator, $H(\omega)$, or

$$E(\omega) = H(\omega)^T C(\omega) \tag{6.6}$$

Notice that the relation does not include the inverse of H(ω), as that matrix would undo any dissipation that had occurred and would instead be the inverse filter rather than time reversal.

The first step in time reversal is to pulse from the control array. The ideal signal, if a spatial and temporal impulse is desired, is given by

$$f(t) = [0 \ \cdots \ 0 \ \delta(t) \ 0 \cdots \ 0] \tag{6.7}$$

in the time domain or

$$F_0(\omega) = [0 \ \cdots \ 0 \ 1 \ 0 \ \cdots \ 0] \tag{6.8}$$

in the frequency domain where $\delta(t)$ is applied to the transducer in the control array that will be the eventual focus. This ideal focus is first time reversed, or phase conjugated in the frequency domain, and sent through the control array and received on the emitting array as $E_1(\omega)$.

$$E_1(\omega) = H(\omega)^T F_0^*(\omega) \tag{6.9}$$

The received signals on the emitting array are then time reversed and sent back to the control array.

$$F_1(\omega) = H(\omega)E_1^*(\omega) = H(\omega)\left(H(\omega)^T F_0^*(\omega)\right)^* \tag{6.10}$$

This equation can be rewritten as

$$F_1(\omega) = H(\omega)H(\omega)^H F_0\ (\omega) \tag{6.11}$$

where ^{H} denotes the conjugate transpose or the Hermatian of the matrix. This equation explains that to obtain the exact focusing field, $F_0\ (\omega)$ then $H(\omega)H(\omega)^H$ should be the identity matrix, $I(\omega)$. This term of $H(\omega)H(\omega)^H$ is called the time reversal operator and given the symbol Δ. If the system entails a nondissipative medium and the emitting array consists of an acoustic closed cavity, then the time reversal operator is approximately the identity matrix.

The above theory outlines the time reversal process. However, when this method is performed in a dissipative medium, then the iterative method can be used to improve the focusing. The iterative time reversal method uses the same first steps as time reversal. The next step is to take the difference of the ideal focusing $F_0(\omega)$ and the obtained focal pattern from the time reversal process $F_1(\omega)$.

$$F_{D1}(\omega) = F_0(\omega) - F_1(\omega) \tag{6.12}$$

This difference of focal patterns, $F_{D1}(\omega)$, is then time reversed and transmitted by the control array and recorded on the emitting array.

$$E_{D1}(\omega) = H(\omega)^T F_{D1}^*(\omega) \tag{6.13}$$

These received signals on the emitting array, $E_{D1}(\omega)$, are added to the original signal, time reversed, and transmitted through the emitting array, which is essentially repeating the time reversal process but using the undesired signals.

$$E_2(\omega) = E_1(\omega) + E_{D1}(\omega) = E_1(\omega) + H(\omega)^T F_{D1}^*(\omega) \tag{6.14}$$

$$F_2(\omega) = H(\omega) E_2^*(\omega) \tag{6.15}$$

This same process can be repeated until convergence to a solution which happens to be the inverse filter [56]. Note that the solution only converges to the inverse filter if the eigenvalues of the time reversal operator, Δ, are between 0 and 2 [56]. Therefore it is important to inspect the time reversal operator before implementing the iterative procedure. To ensure convergence, the amplitude of the signals can be amplified or reduced to ensure that the conditions of the time reversal operator are met. Montaldo et al. also performed a comparison of the inverse filter, time reversal, and iterative time reversal with regards to the eigenvalues and the associated error when noise is present with the summary listed in Table 6.1.

Table 6.1 Comparison of the different focusing methods

	Operator	Eigenvalue	Error
Inverse filter	$\mathbf{H}\hat{\mathbf{H}}^{-1}$	1 for highest, 0 for lowest	$\sigma_{if}^2=\sigma^2\sum_{i=1}^{M}\frac{\lvert b_i\rvert^2}{\lambda_i}+N_c\sigma^2$
Time reversal	$\mathbf{\Delta}=\mathbf{H}\mathbf{H}^{\dagger}$	λ_i	$\sigma_{tr}^2=2N_c\sigma^2$
Iterative inv. filt.	$\mathbf{I}-(\mathbf{I}-\mathbf{\Delta})^n$	$1-(1-\lambda_i)^n$	$\sigma_{it}^2=3N_c\sigma^2$

6.3. Focusing Results

6.3.1. Simulations

The above mentioned methods of focusing are implemented on membrane arrays to illustrate the potential application of subwavelength focusing. The first step in focusing with simulations is to obtain the relation from the 8 membranes that are part of the emitting array to the 49 membranes in the grid and vice versa. Once these Green's functions are extracted from the model, the theory can be applied for the time reversal focusing, iterative time reversal focusing, and focusing with the inverse filter.

Focusing to Center Membrane

The results of focusing to the center membrane are shown in Fig. 6.5 with a linear scale and Fig. 6.6 with a logarithmic scale for the different focusing techniques. Figure 6.5(a) is the focusing result using time reversal which shows that the focus is limited to a single membrane or a size of λ/5. The focusing resolution of the metasurface is limited by the membrane size which is the smallest possible focal spot [47]. More information about altering the membrane size and its effects on the focusing are shown in Appendix A. Figure 6.5(b-e) are the focusing results by

using the iterative time reversal method for 3, 10, 30, and 100 iterations, while Fig. 6.5(f) is the focusing result from the inverse filter. It is interesting to observe the focusing improvement as iterations are increased. Notice in Fig. 6.5(a), that the nearest neighbors to the focal spot have nearly zero displacement. However, in general, the side lobe levels are higher than the focusing results from using the iterative time reversal. With more iteration, the side lobe levels are reduced, but the nearest neighbors start to have higher displacements as the iterative time reversal method approaches to the convergence of the inverse filter [56].

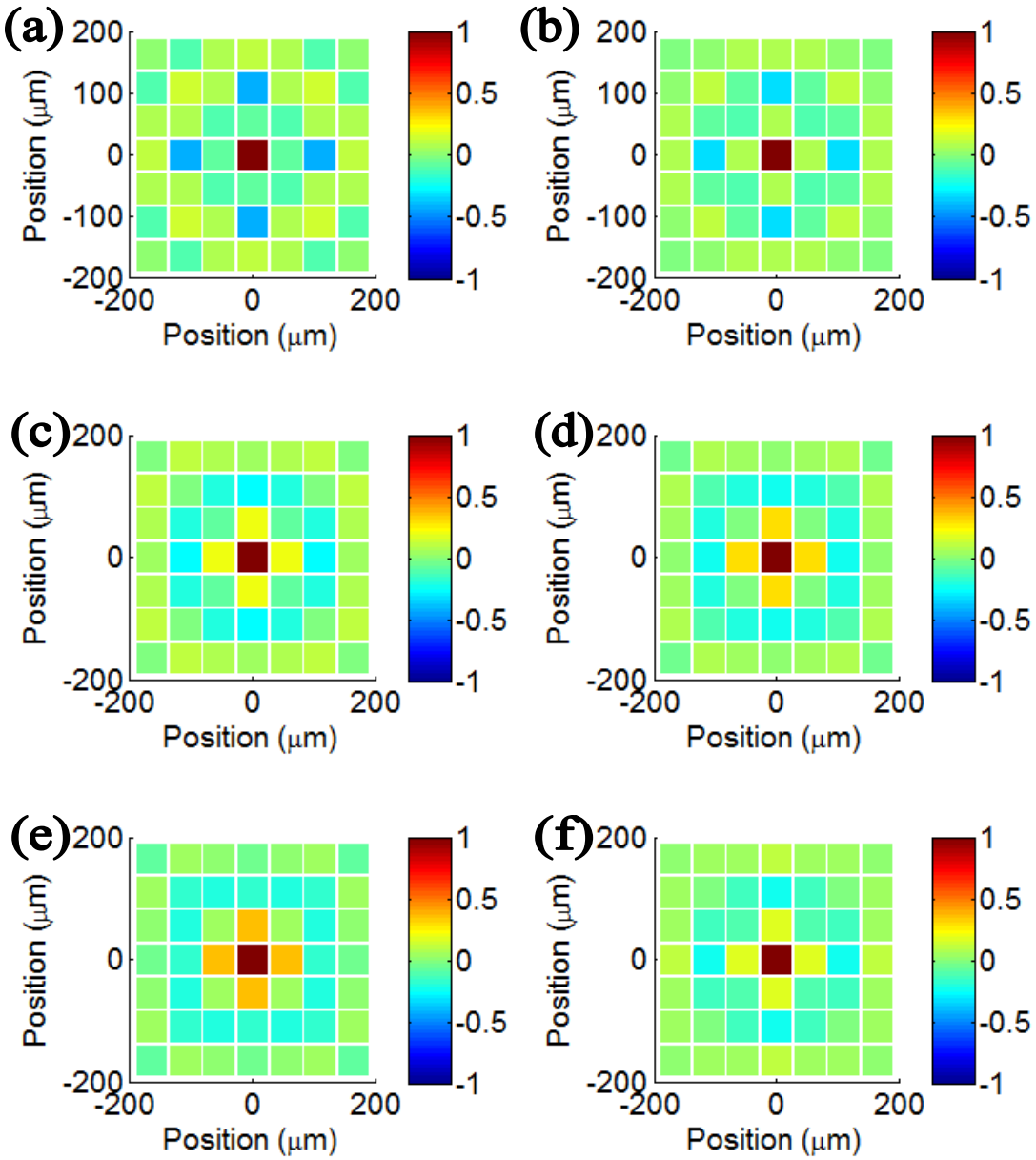

Figure 6.5 Linear scale simulation results of focusing to the center membrane using (a) time reversal and iterative time reversal using (b) 3 iterations (c) 10 iterations (d) 30 iterations and (e) 100 iterations. (f) the focusing from using the inverse filter.

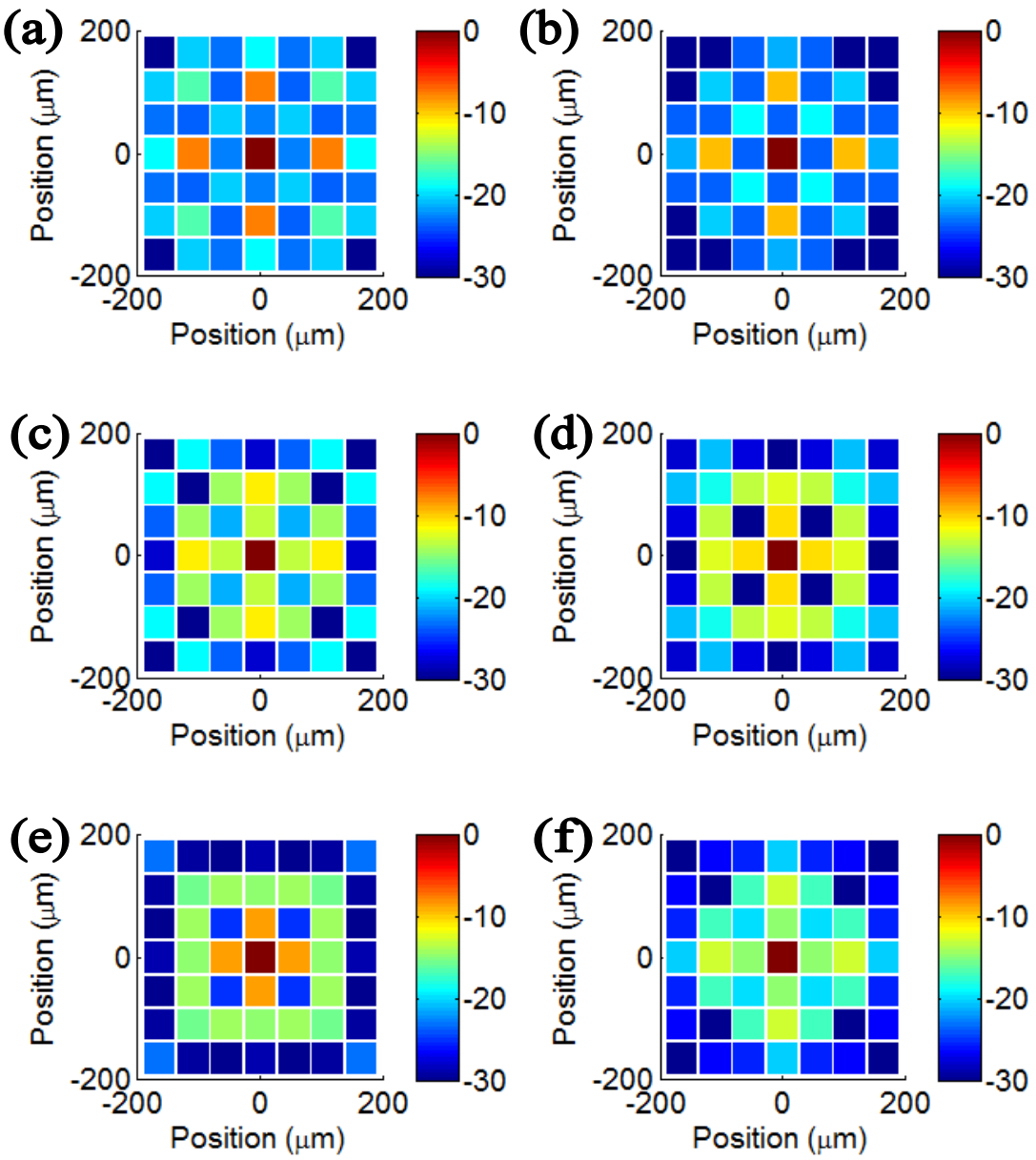

Figure 6.6 Logarithmic scale simulation results of focusing to the center membrane using (a) time reversal and iterative time reversal using (b) 3 iterations (c) 10 iterations (d) 30 iterations and (e) 100 iterations. (f) the focusing from using the inverse filter.

To better understand how the iterative time reversal method is improving with more iterations, the signals that are being transmitted from the emitting array can be examined. The

first element of the emitting array is examined with regards to the signals for different iterations. The signals presented in Fig. 6.7 are obtained by transmitting the ideal focus along with the corrections for the side lobes (if relevant) from the control array. Both the time domain and frequency domain of these signals are examined (Fig. 6.7-6.8). The signal received from the first iteration of time reversal (Fig. 6.5(a)) has temporal ringing in the signal. The frequency response (Fig. 6.8) confirms that the first iteration of time reversal is the most narrow band signal with the majority of the energy in a frequency band around 7MHz. As the number of iterations is increased, the received signals become more and more broadband with less temporal ringing. On first glance, the iterative method appears to be performing frequency whitening on the signals to enhance the focus, but a closer inspection at 7MHz confirms that this frequency is actually being reduced as opposed to being uniform with the other frequencies.

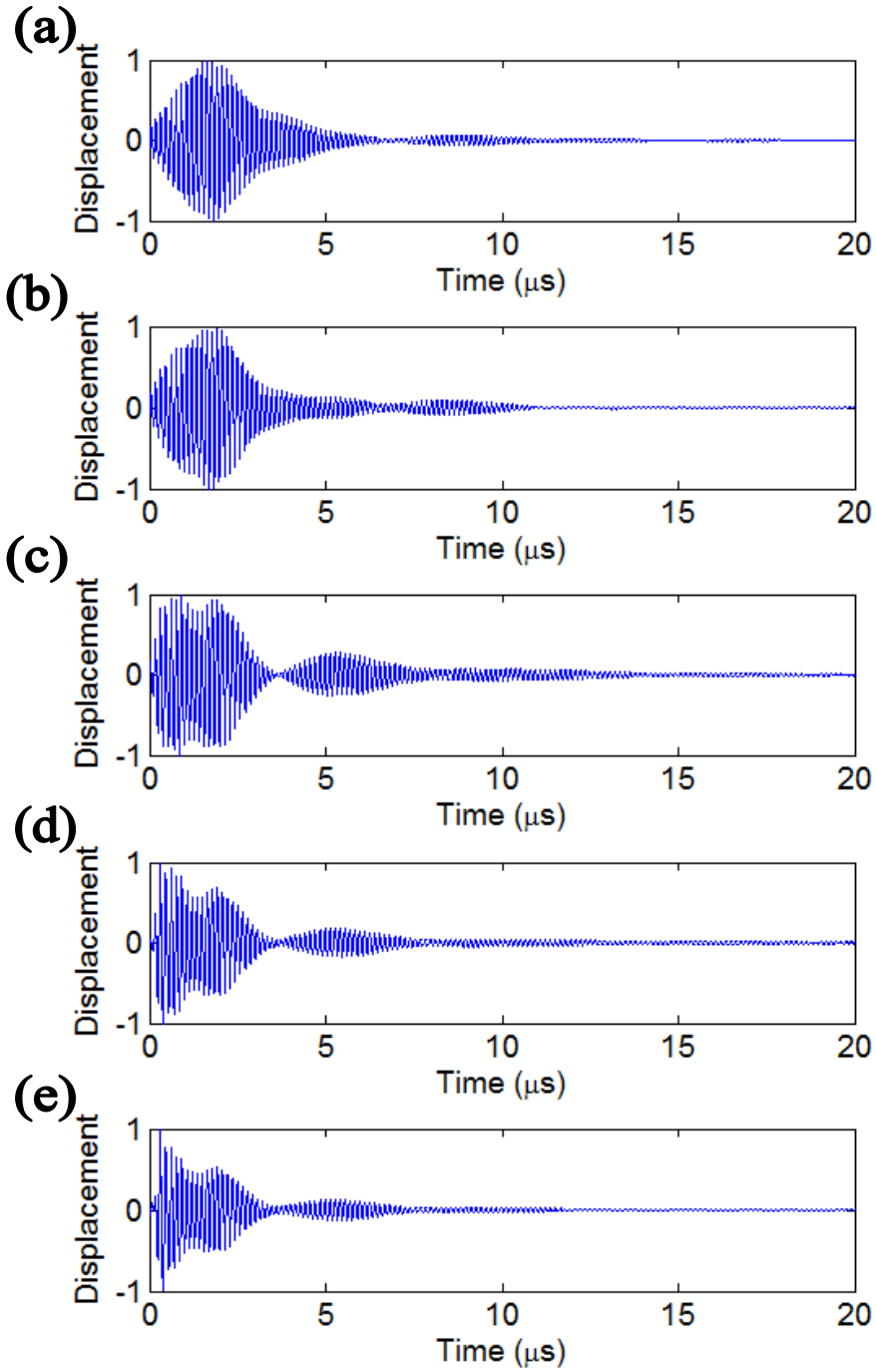

Figure 6.7 Received signal on the first element of the emitting array from the emission of the control array after (a) 1 iteration, basic time reversal (b) 3 iterations (c) 10 iterations (d) 30 iterations (e) and 100 iterations.

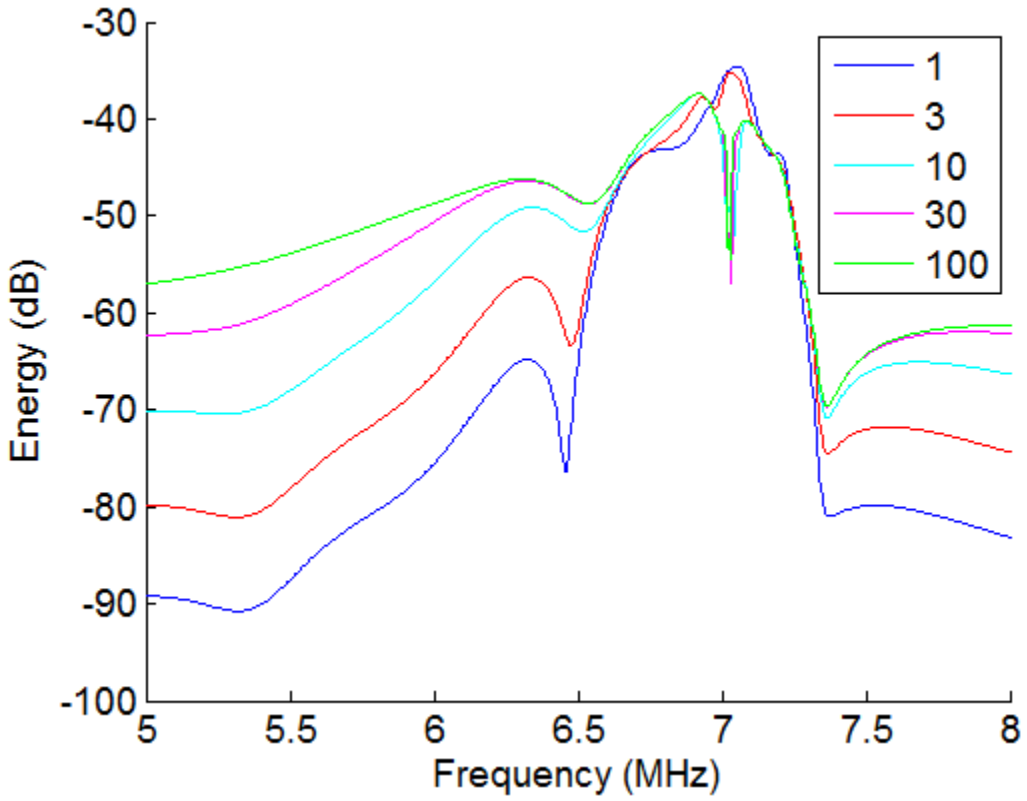

Figure 6.8 Frequency content of the time received signals from Fig. 6.7 for the different number of iterations.

Focusing to Off Center Membrane

Focusing can be performed to any membrane in the grid. The 13th membrane (2nd row, 6th column) is used as another membrane for focusing to illustrate that the center membrane focusing is not unique. The linear and logarithmic focusing for the iterative time reversal and the inverse filter are shown in Fig. 6.9-6.10. Notice that with the focus closer to the edge of the grid there is more significant side lobe structure although the focal spot is still one membrane or $\lambda/5$. Again, with more iterations of time reversal, the focal field converges to the inverse filter focus pattern.

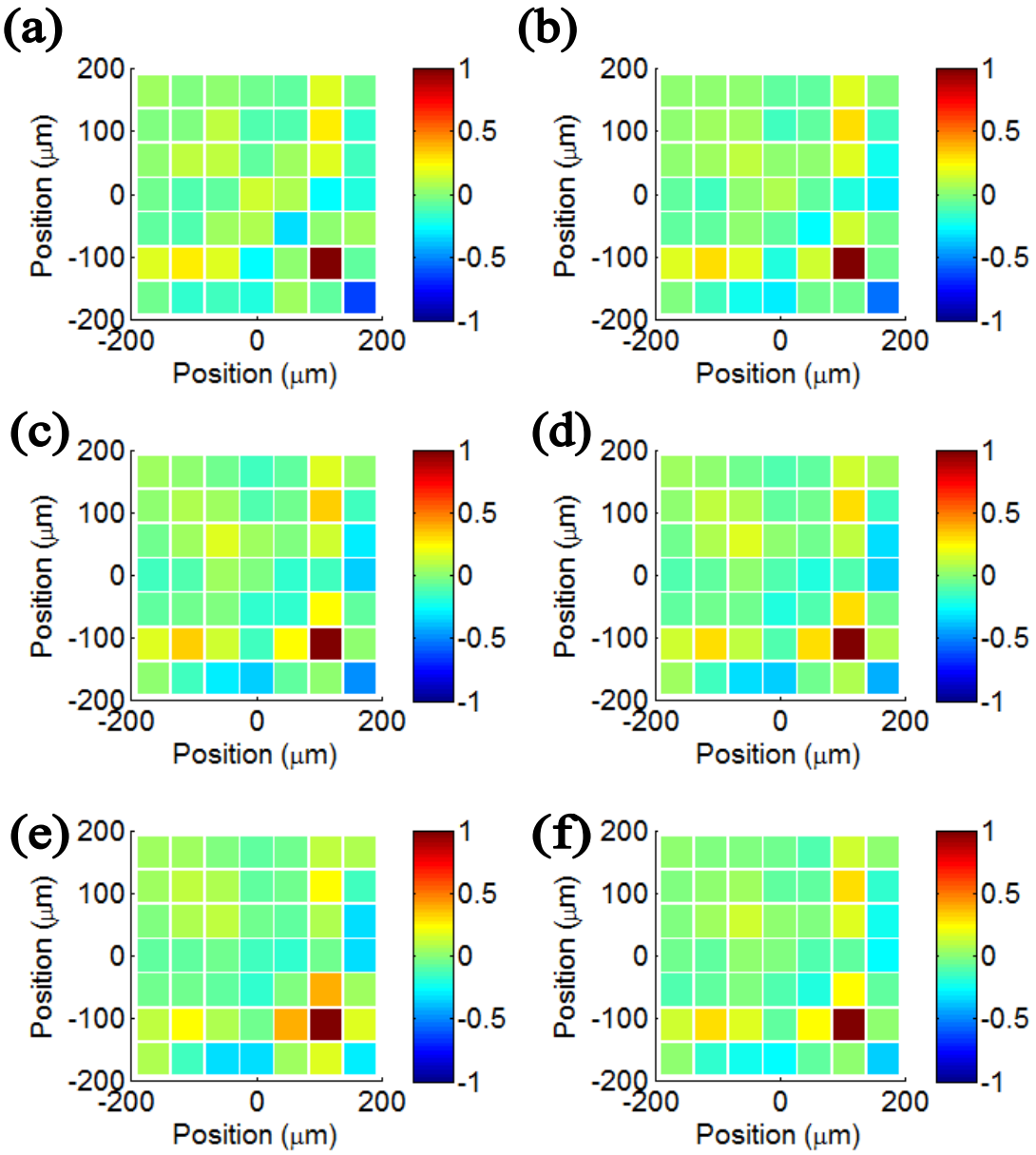

Figure 6.9 Linear scale simulation results of focusing to the 13th membrane using (a) time reversal and iterative time reversal using (b) 3 iterations (c) 10 iterations (d) 30 iterations and (e) 100 iterations. (f) the focusing from using the inverse filter.

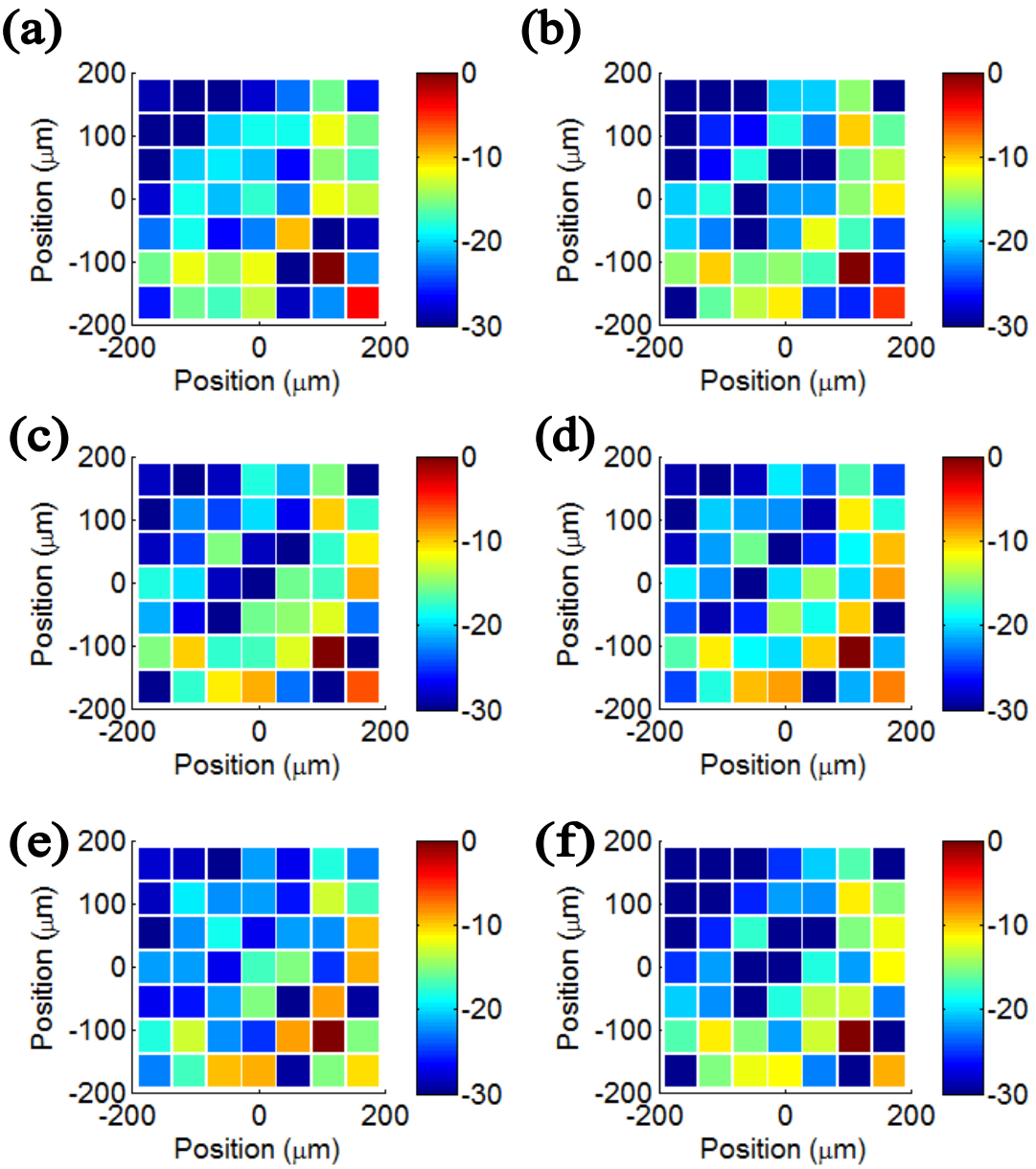

Figure 6.10 Logarithmic scale simulation results of focusing to the 13th membrane using (a) time reversal and iterative time reversal using (b) 3 iterations (c) 10 iterations (d) 30 iterations and (e) 100 iterations. (f) the focusing from using the inverse filter.

6.3.2. Experimental Results

Experiments are performed on the array and setup as described in Chapter 5. The three focusing methods mentioned were experimentally verified. A single iteration of time reversal

was run via the experiments. The iterative time reversal process was not able to be implemented as intended due to a restriction in the experimental setup. This restriction was that the control array was not electrically connected to transmit waves with the exception of the 13^{th} and 25^{th} membranes in the grid (Fig. 5.11). Hence since the control array could not pulse the side lobes then the iterative method could not be done. However, the iterative method was done by experimentally capturing five independent sets of the propagation operator. The captured propagation operator also was used for the inverse filter focusing method. The experimental focus as obtained by time reversal, iterative time reversal using five iterations, and the inverse filter are presented and compared to simulations.

For time reversal focusing to the center membrane, a 10V, 50ns, unipolar pulse was transmitted from the 25^{th} (center) membrane of the control array with a time delay of 1.5μs. The laser Doppler vibrometer recorded the displacement on each of the membranes of the emitting array. Since the laser can only record the displacement of one membrane at a time, the array moved so that the laser could record the displacement of each membrane. Each displacement measurement was averaged 4096 times to improve the signal to noise ratio (SNR). These signals were then time reversed over 20μs, amplified, and retransmitted. Fig. 6.11 shows the time reversed signals used for the focusing to the center membrane. The Y-axis corresponds to the m^{th} sensor in the emitting array (m=1-8) and the displacement plotted about that mean value. Notice that the majority of the signal is only in a 5-10μs window which suggests that even a shorter time reversal time could be used for the focusing. The displacement of the 49 membranes in the control array was measured from the signals used in Fig. 6.11, and the displacement for each membrane over time is shown in Fig. 6.12. Again, the mean value of each trace corresponds to the n^{th} membrane in the control array, with the deviation from the mean

equating to the displacement. Across all traces, there is very little displacement until around 17μs. The strongest signal occurs on the focal membrane (membrane 25) and the focus time is at 18.5μs which corresponds to the time used for time reversal, 20μs, minus the original delay of the pulse, 1.5μs. Fig. 6.13 shows the displacement of all of the membranes at the focal time. It illustrates that the acoustic energy is focused to the center membrane or a focal spot of λ/5.

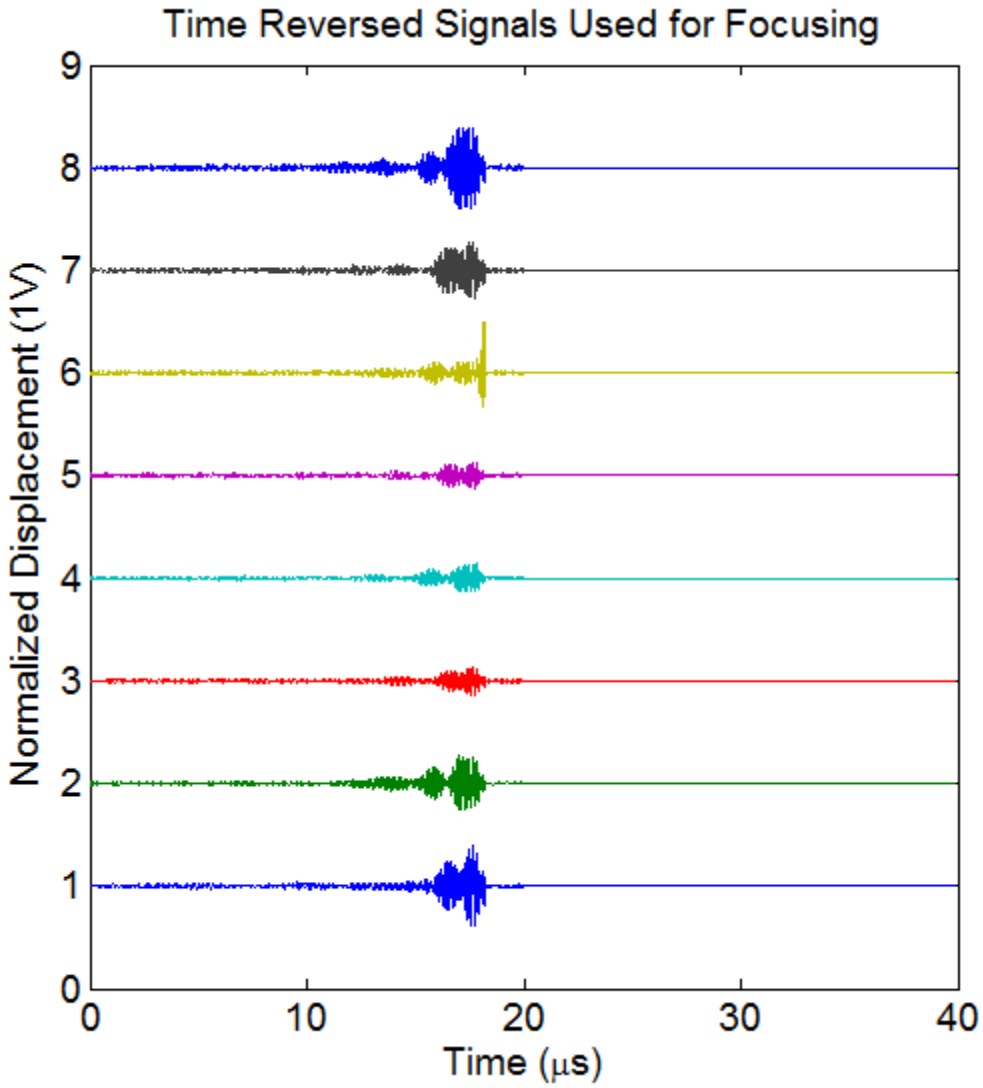

Figure 6.11 Time reversed signals of the 8 different sensors of the emitting array used for focusing back to the center membrane

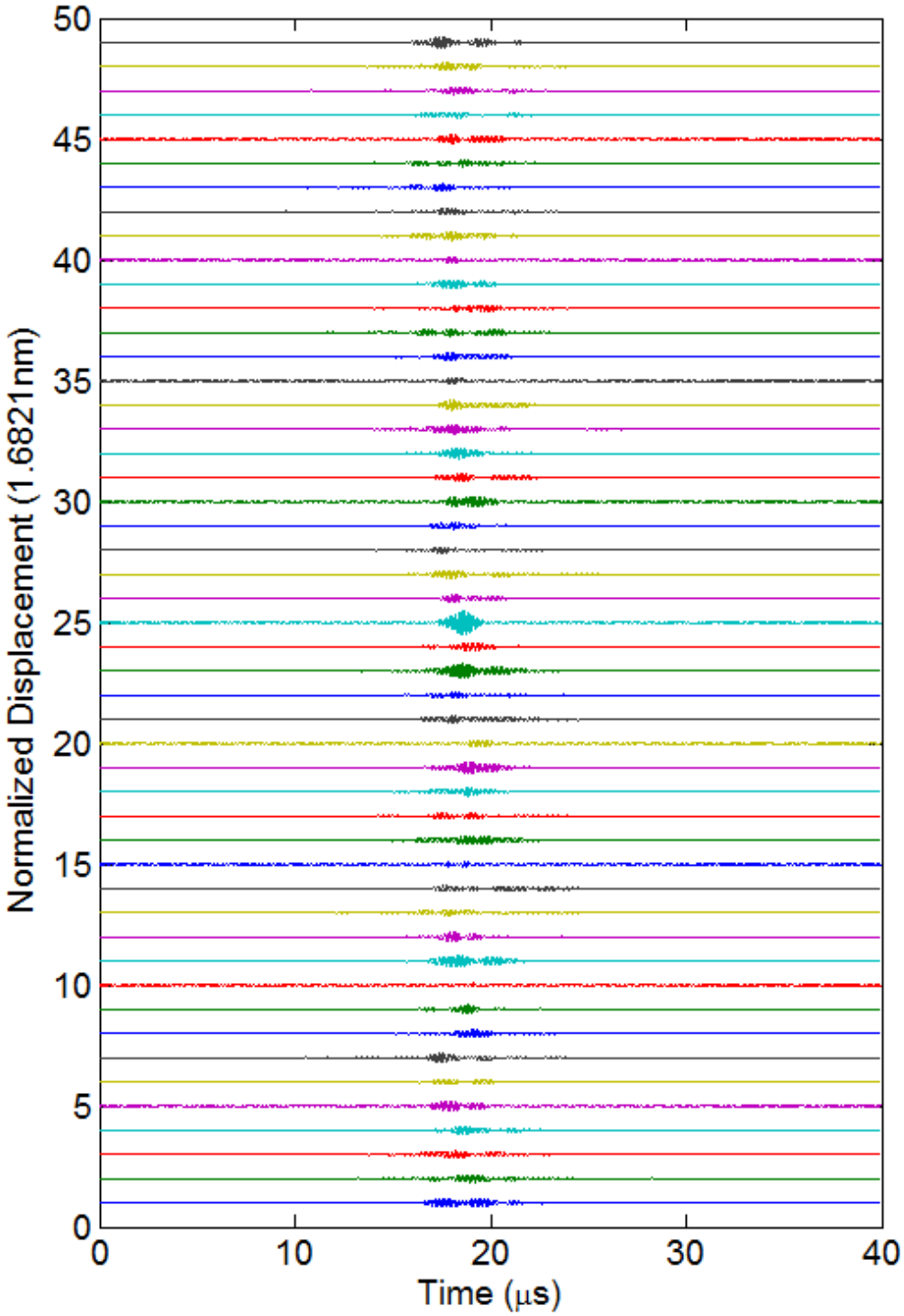

Figure 6.12 Displacement of each membrane normalized to the maximum signal. The focal time occurs at 18.5μs with the energy being focused to the 25th membrane

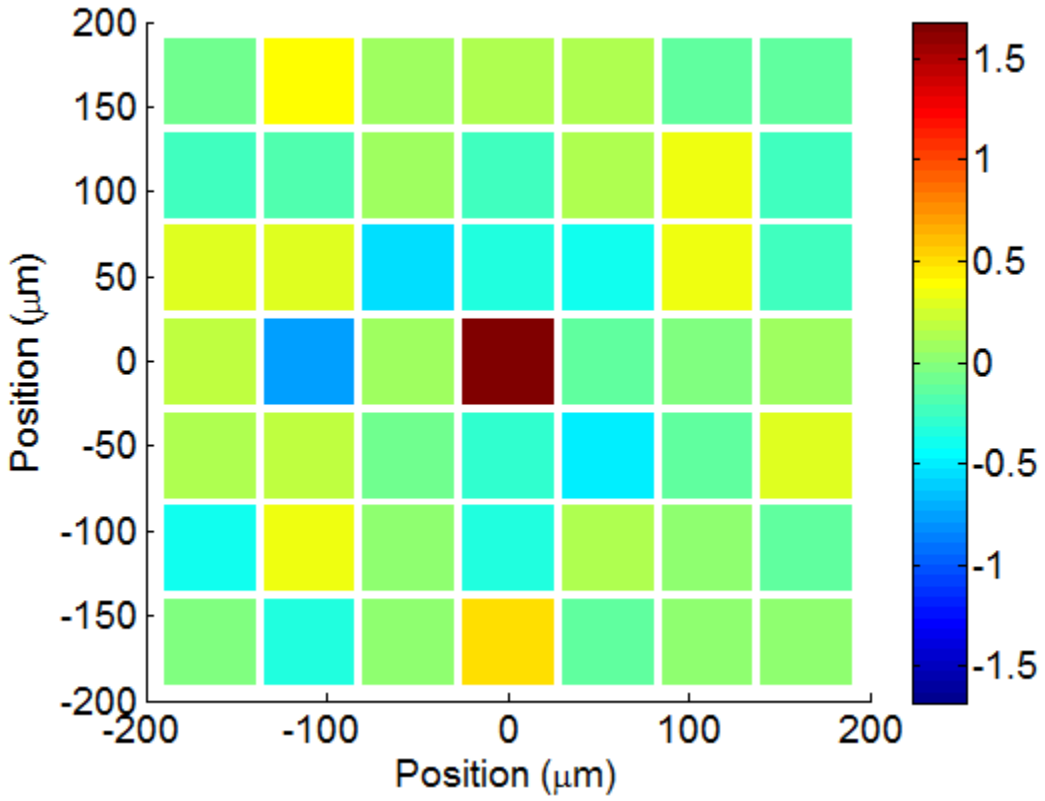

Figure 6.13 Displacement of all membranes at the focusing time illustrating the focus on the center membrane.

The other method used to obtain the experimental focusing was to capture the Green's functions experimentally five times and then use this propagation matrix to do the focusing. To capture the Green's function between each m^{th} sensor in the emitting array to each n^{th} sensor in the control array, each element of the emitting array was pulsed with a strong 60V, 50ns, unipolar pulse. The displacement was recorded on each membrane in the 7x7 grid using 10,000 averages for the best possible SNR. Five independent sets of Green's functions were captured to allow for time reversal with 5 iterations. Multiple iterations of time reversal could be done with a single capture of the propagation matrix, but the noise would act coherently with each successive iteration rather than incoherently as it should. Hence, a more realistic situation can be implemented with the five independent sets of Green's functions.

The inverse filter method of focusing is implemented by using the experimentally obtained propagation operator. The pseudoinverse of the propagation operator is obtained from the singular value decomposition with the singular values across frequency being shown in Fig. 6.2.

The simulation and experimental focus to the center membrane is compared in Figs. 6.14-6.15 and focusing to the an off center membrane 13^{th} in Figs. 6.16-6.17. The left column of images are the experimental focusing while the right column of images are obtained through simulation. The first row is that of time reversal. Notice that the experimental results and the simulations both obtain a well defined focus to the center membrane. The side lobes are more prominent and staggered in the experiment compared to the simulation. The second row of images is the focus obtained after 5 iterations of time reversal. The experiments and the simulation agree very well in terms of focus, side lobe structure, and levels. The last row corresponds to the inverse filter results. It is very clear that the experimental inverse filter is not very clean. This is likely due to problems with the pseudoinverse and the presence of noise in the signals. These experiments verify that by using a method of time reversal acoustic focusing can be achieved to a focal spot of $\lambda/5$. This focal spot while only shown at two locations can actually occur at any membrane in the control array.

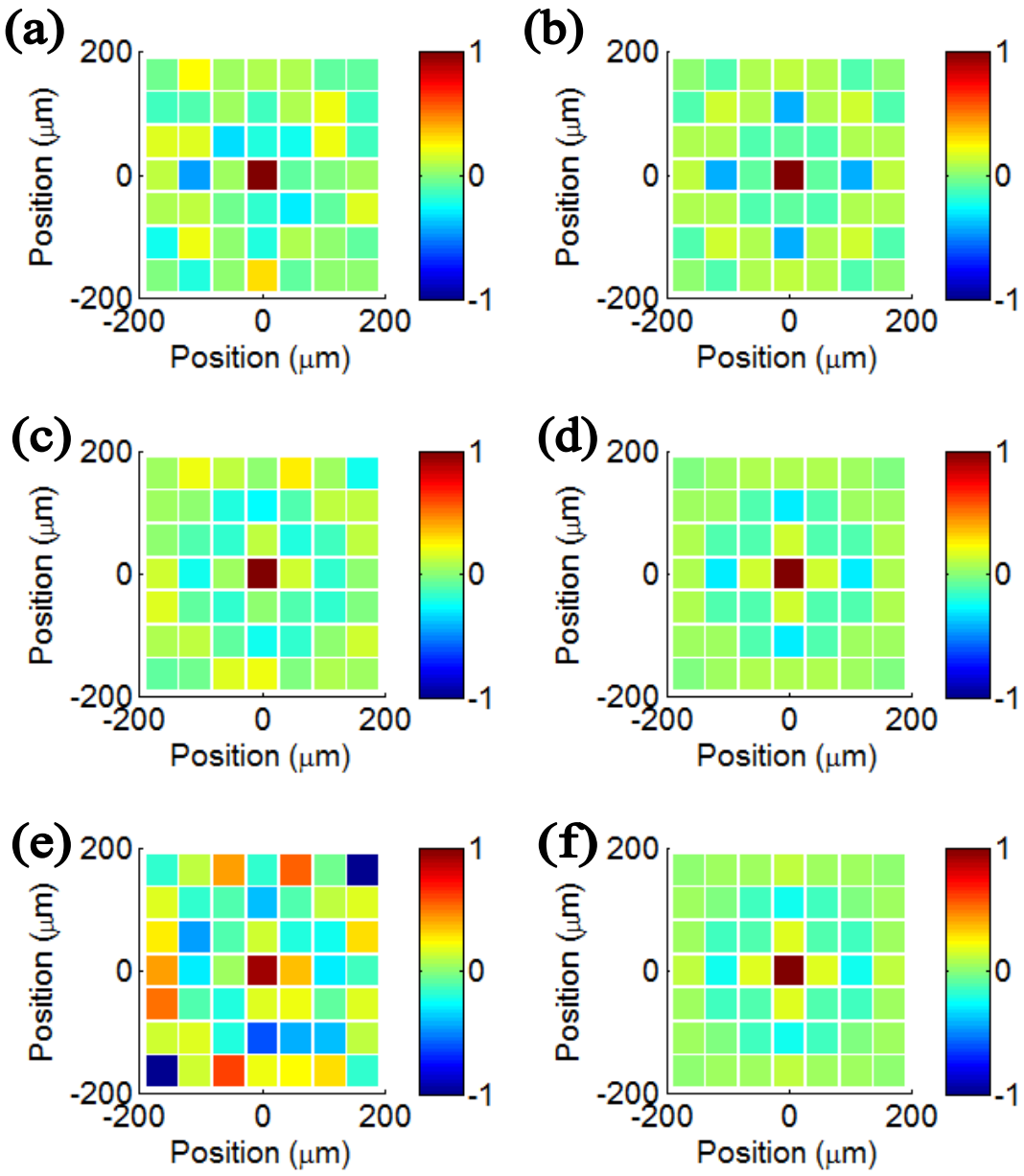

Figure 6.14 Focusing comparison of the experiments (a,c,e) to that of the simulation (b,d,f) for one iteration of time reversal (a,b) 5 iterations of time reversal (c,d) and the inverse filter (e,f)

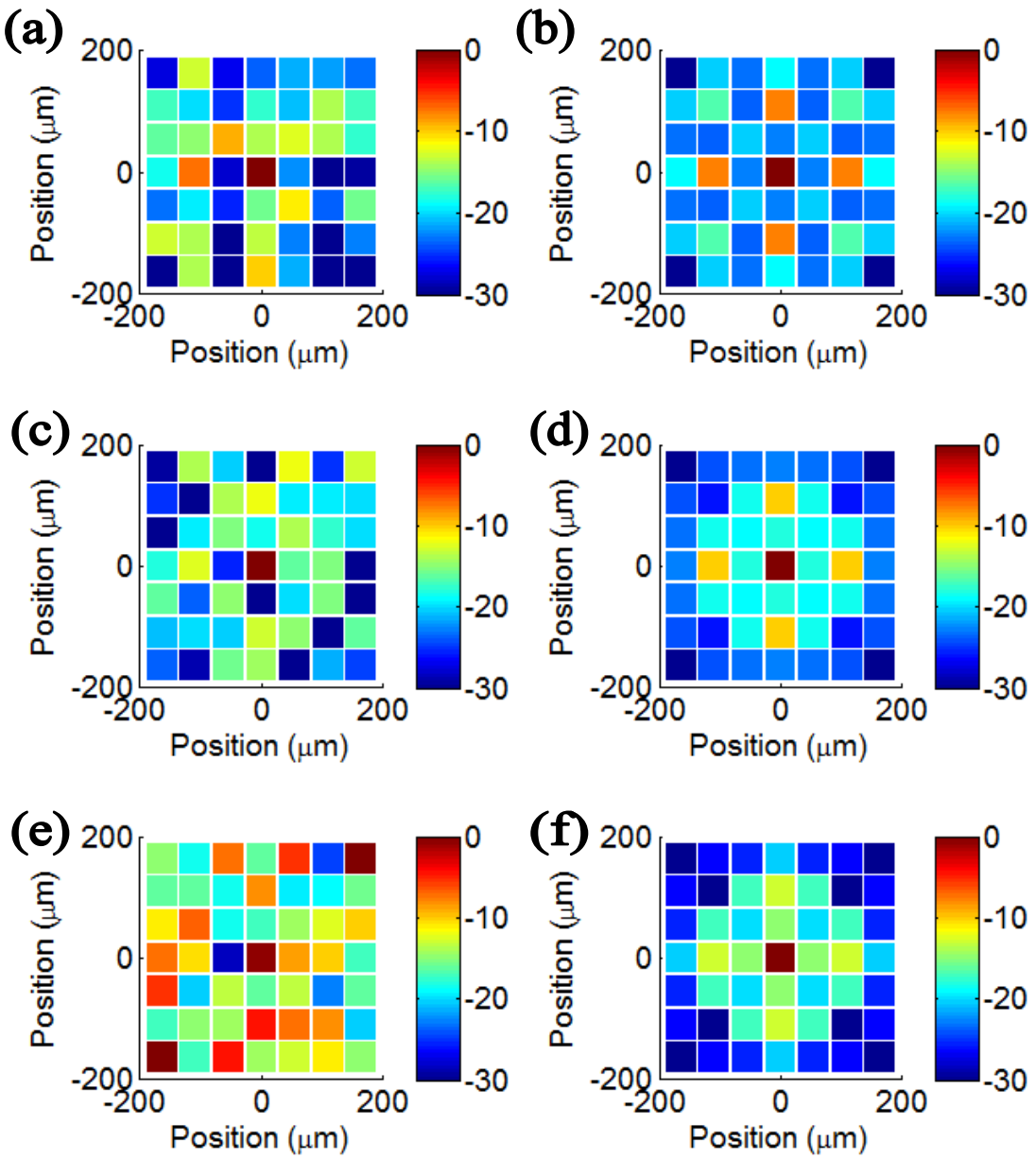

Figure 6.15 Logarithmic focusing comparison of the experiments (a,c,e) to that of the simulation (b,d,f) for one iteration of time reversal (a,b) 5 iterations of time reversal (c,d) and the inverse filter (e,f)

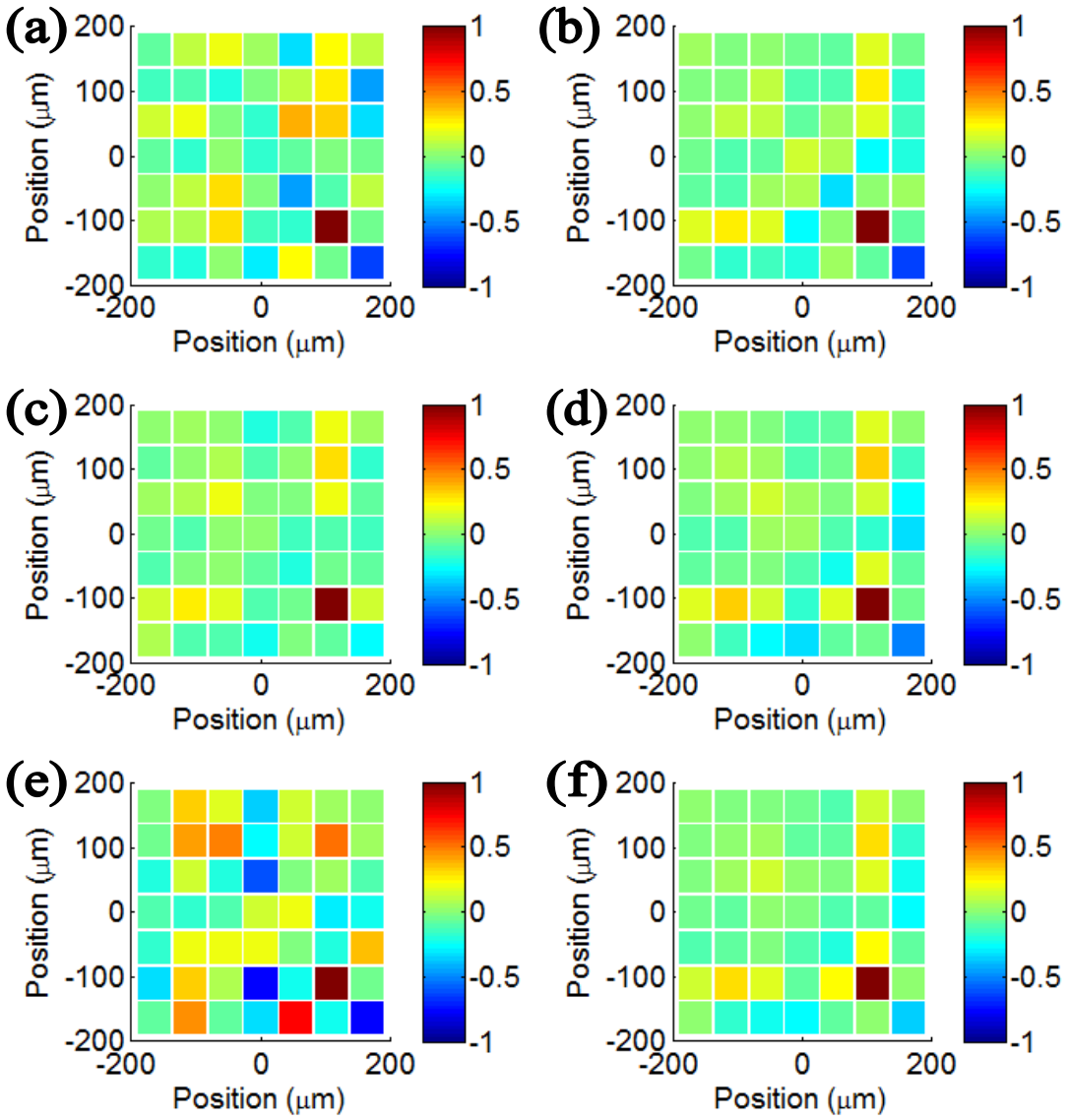

Figure 6.16 Focusing comparison of the experiments (a,c,e) to that of the simulation (b,d,f) to the 13th membrane for one iteration of time reversal (a,b) 5 iterations of time reversal (c,d) and the inverse filter (e,f)

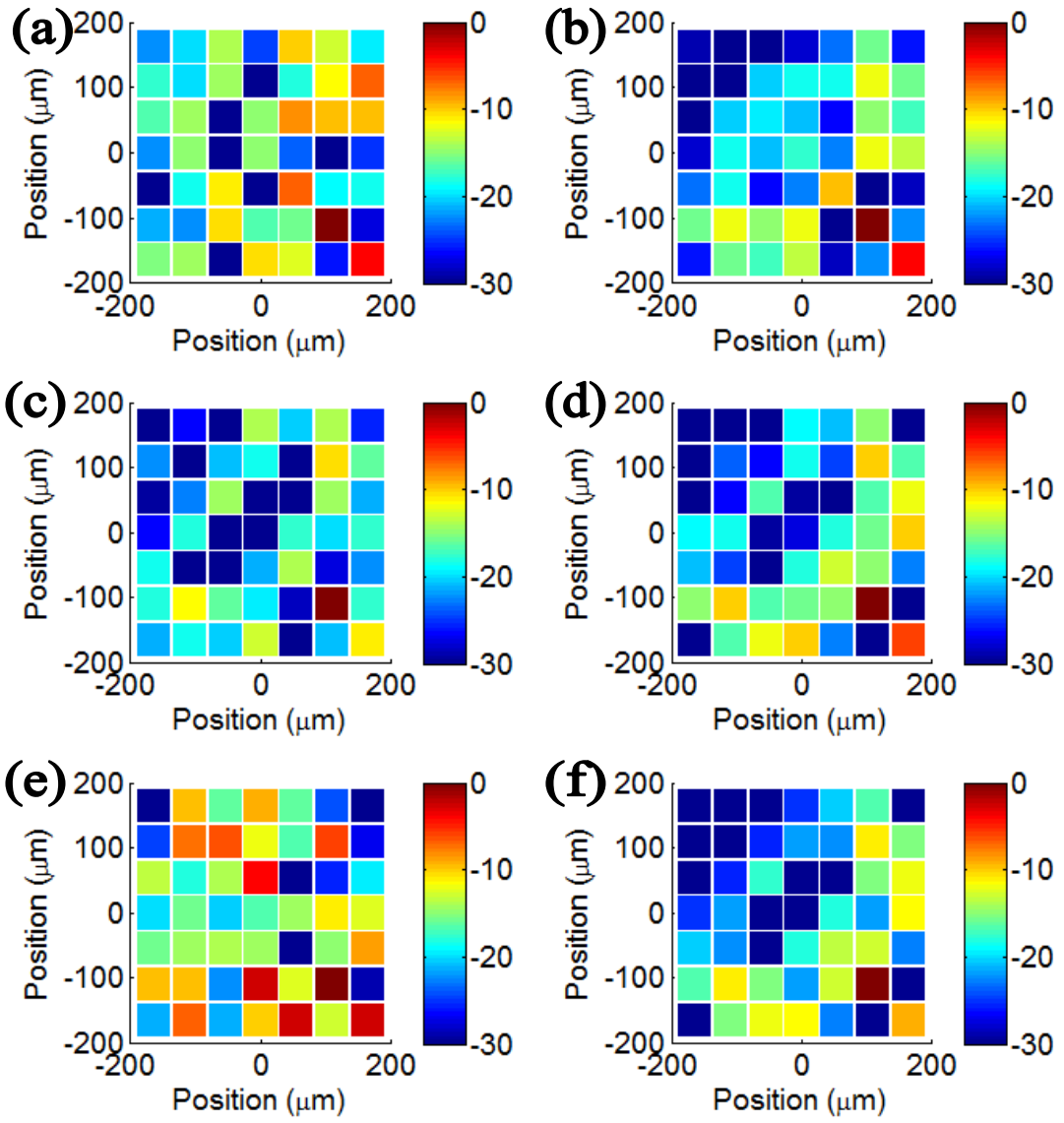

Figure 6.17 Logarithmic scale focusing comparison of the experiments (a,c,e) to that of the simulation (b,d,f) to the 13th membrane for one iteration of time reversal (a,b) 5 iterations of time reversal (c,d) and the inverse filter (e,f)

6.4. Imaging Methods

This section shows the potential to use the surface acoustic waves above the membrane metasurface for near field imaging with subwavelength resolution in the 2D plane directly on and above the array. The majority of work with subwavelength imaging with metamaterials and phononic crystals uses a 2D or flat lens with negative refraction [1, 62, 73, 87]. Other works have instead captured the evanescent waves at the surface and transported them through different structures that contain Fabry-Perot resonances [50, 51, 72]. The imaging method that is described here takes a different approach which is based off of the time reversal focusing methods. The proposed technique is used regularly in structural health monitoring literature and is based off of a difference or perturbation method [18, 31, 81]. To perform this imaging a control or baseline measurement is taken (Fig. 6.18). Then the medium in altered in some way and another measurement set is taken. The difference between measurements of the control system and the defect system is taken and back propagated in to the system to localize the defect. This method is used to localize a subwavelength sized defect of $\lambda/5$. The defect consists of a small impedance change (~1%) of a particular membrane in the control array.

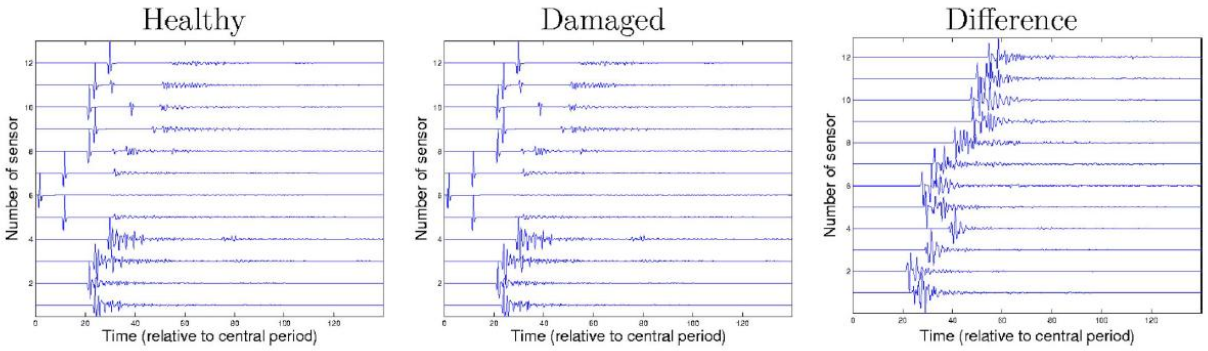

Figure 6.18 Example of the method to obtain signals for imaging a defect by subtracting out the baseline or healthy measurements from the measurements obtained in the same medium but with some damage or defect [18].

The imaging process is detailed as follows. The first step is to take a baseline test. The center membrane of the imaging grid is pulsed with a 5V 50ns unipolar pulse and the received signals are recorded on the 8 transducers of the emitting array. Then one membrane of the imaging grid is altered. Two different subwavelength sized imaging targets or defects are used. Each defect is one membrane with the lateral dimensions of $\lambda/5$. The first defect is a mass change in which the 9^{th} membrane has an increase of mass by 1%. The second defect is induced by an increase in DC bias to the 13^{th} membrane of 10V which corresponds to 1.2% softer stiffness. The second step in the imaging process is to pulse again from the center membrane with the defect introduced into the imaging array. Again 8 signals are recorded on the 8 emitting array elements. These signals are then subtracted from the signals obtained with the perfect array. The difference of these signals is time reversed and transmitted by the emitting array to the ideal 'healthy' control array. The energy is then focused on the array at the location of the defect. An issue with this imaging method is that the focusing time to the defect is unclear. One method to solve this ambiguity is to measure the entropy of the image and choose the appropriate image based on minimum entropy [18]. However, if the energy is being focused to the defect location then the maximum displacement should also occur at the defects location. Hence, this max displacement will determine the time to obtain the image and the defect's location.

6.5. Imaging Results

6.5.1. Imaging a Subwavelength Sized Mass Defect

The array used is the same array that is used in the previous chapter for subwavelength focusing. The first step is to take a baseline measurement which is shown in Fig 6.19 which is the 'healthy' received signals measured by the emitting array. The mass is then altered of the 9^{th} membrane by increasing it just 1%. Then the center membrane is pulsed again and the

displacements were recorded on the emitting array and shown in Fig. 6.20. These are the 'defect' or 'damaged' signals. Notice that it the signals received on the emitting array in the 'healthy' case (Fig. 6.19) appear to be very similar to the 'damaged' case (Fig. 6.20). This is expected with such a small defect. To obtain the signals for the focusing which localizes the defect, the healthy signals were subtracted from the defective signals. The first 20μs of data was used for the time reversal, and is shown in Fig. 6.21. The time reversal focusing was done using the healthy array not the array with the mass defect.

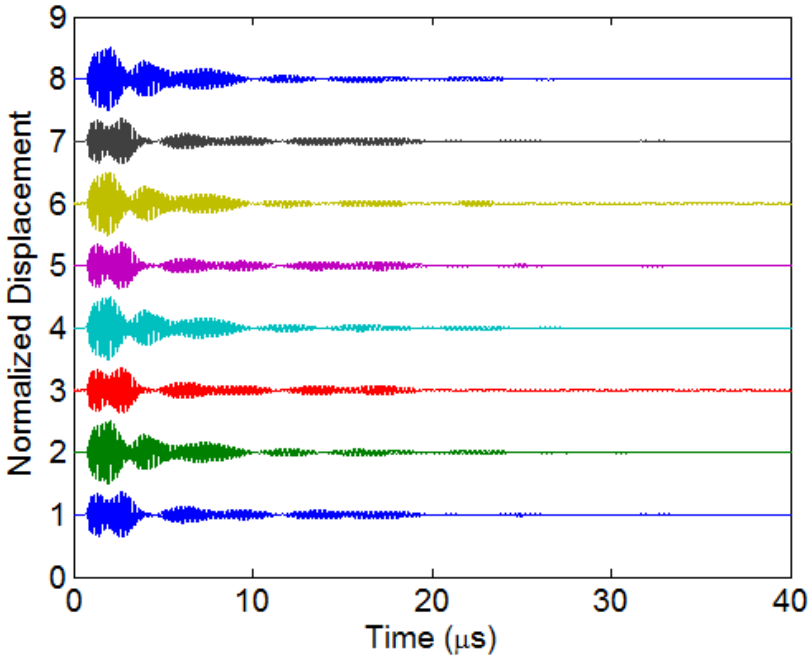

Figure 6.19 Received signals on the emitting array from pulsing the center membrane on a 'healthy' array.

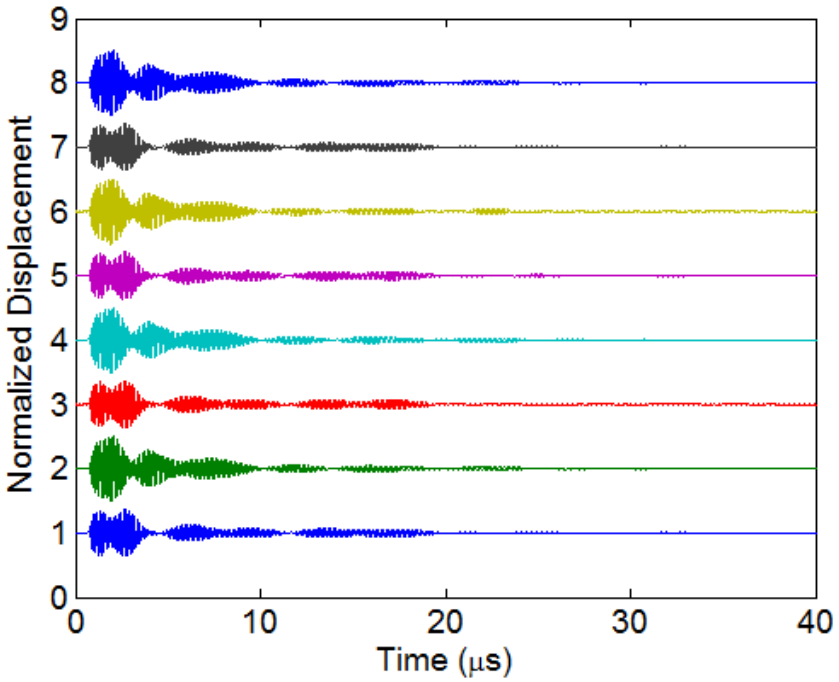

Figure 6.20 Received signals on the emitting array from pulsing the center membrane on a 'damaged" array in which the 9th membrane had an increase of mass by 1%.

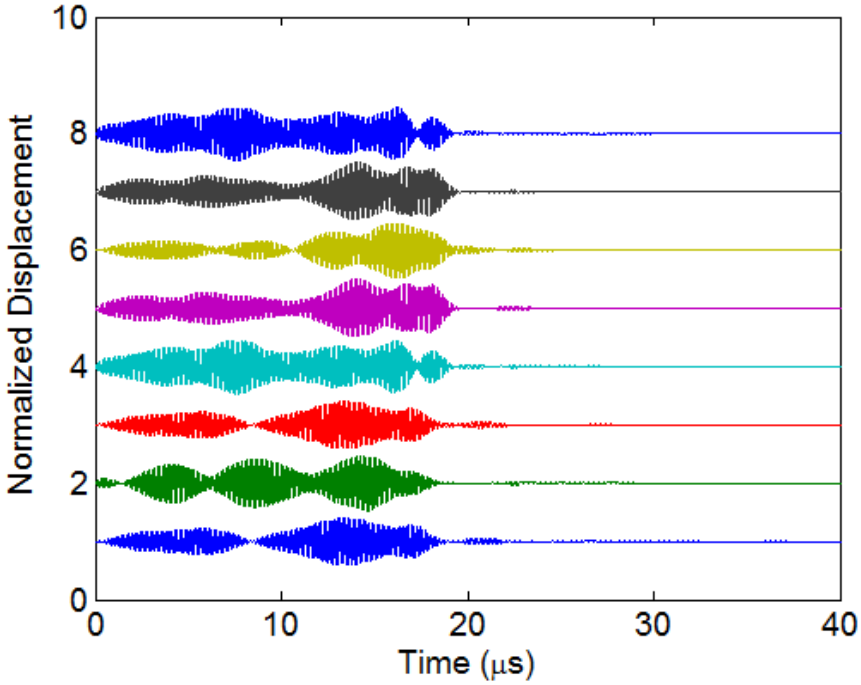

Figure 6.21 Signals used to focus to the defect by subtracting the healthy signals from the defective signals and using 20μs for time reversal.

These difference signals are then transmitted through the emitting array and the displacement of all 49 membranes in the imaging array is calculated. Figure 6.22 shows the displacement of each of these membranes. The mean value of each trace is the membrane number while the variations about the mean are the relative displacements normalized to the strongest displacement over all membranes and time. Two membranes appear to have more energy than the rest. The first is the 25^{th} membrane which has energy, but it is very dispersed in time. The 9^{th} membrane actually has the largest displacement and has the most apparent energy within a tight time window. This means that the time reversal focusing with the difference signals focuses acoustic energy to the membrane with the defect. Without a prior knowledge of the defect location, the focusing to the defect can be found by finding the maximum displacement. This time should occur before the amount of time used for the time reversal (20μs). Hence it is clear that the refocusing to the defect is working properly and a subwavelength defect can be localized.

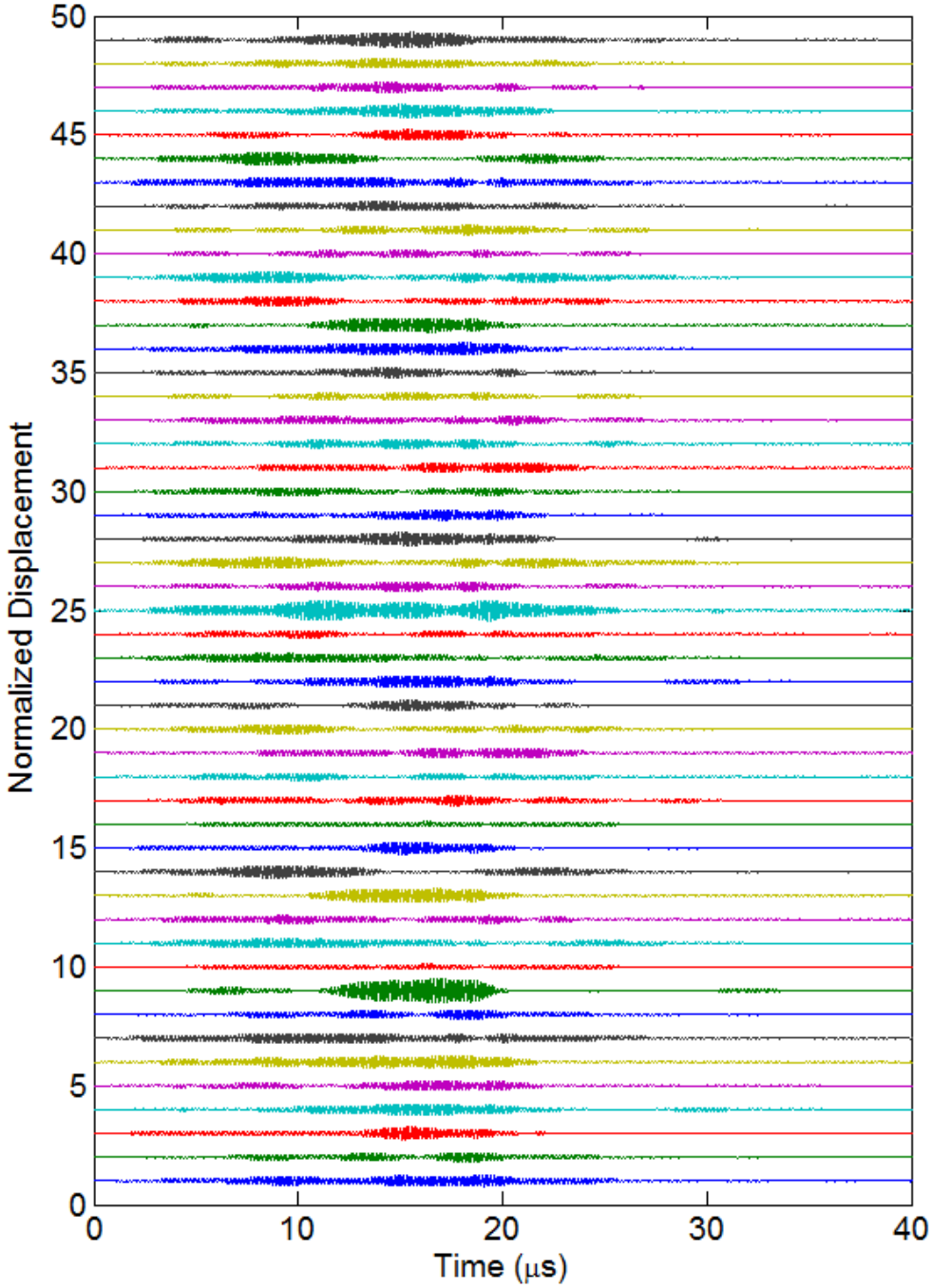

Figure 6.22 Displacement for each membrane in the imaging array over time. Notice two membranes with the most energy are the 25th from which the original focus was to be, but even stronger more concentrated energy is seen on membrane 9. The maximum displacement over all membranes and time occurs at 16.92μs on membrane 9.

The maximum displacement across all membranes occurs on the 9th membrane at 16.92μs, and the displacement of all membranes at that time creates an image for the defect location, shown in Fig. 6.23. Notice that this image clearly shows that the 9th membrane has a higher displacement than the other membranes. This process works with even with just a 1% deviation of the mass. The expected focusing time of the time reversal without using the difference signals is 19.5μs (20μs of time reversal minus the 0.5 μs for the pulse delay). The displacement image for that time is shown in Fig. 6.24 for comparison. This image is not very informative with no clear peak at the defect location or anywhere else, but is shown just for completeness.

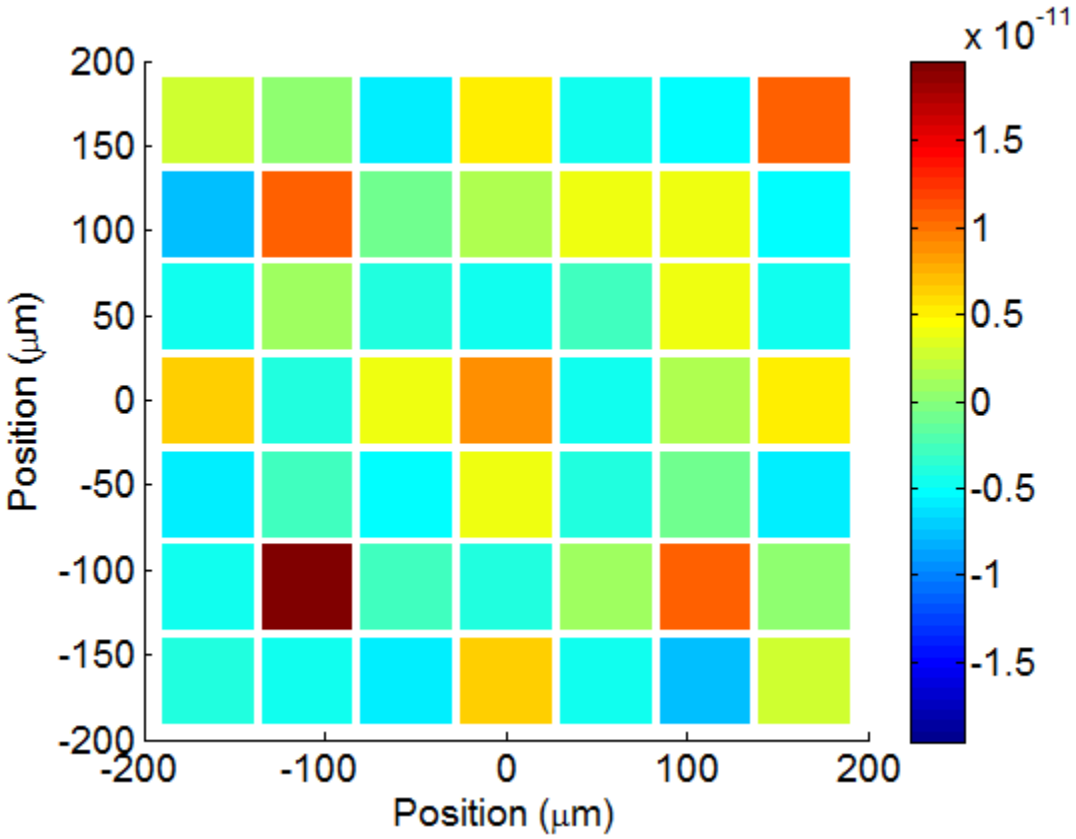

Figure 6.23 Displacement map of the imaging array at 16.92μs corresponding to the maximum displacement of all membranes over all time.

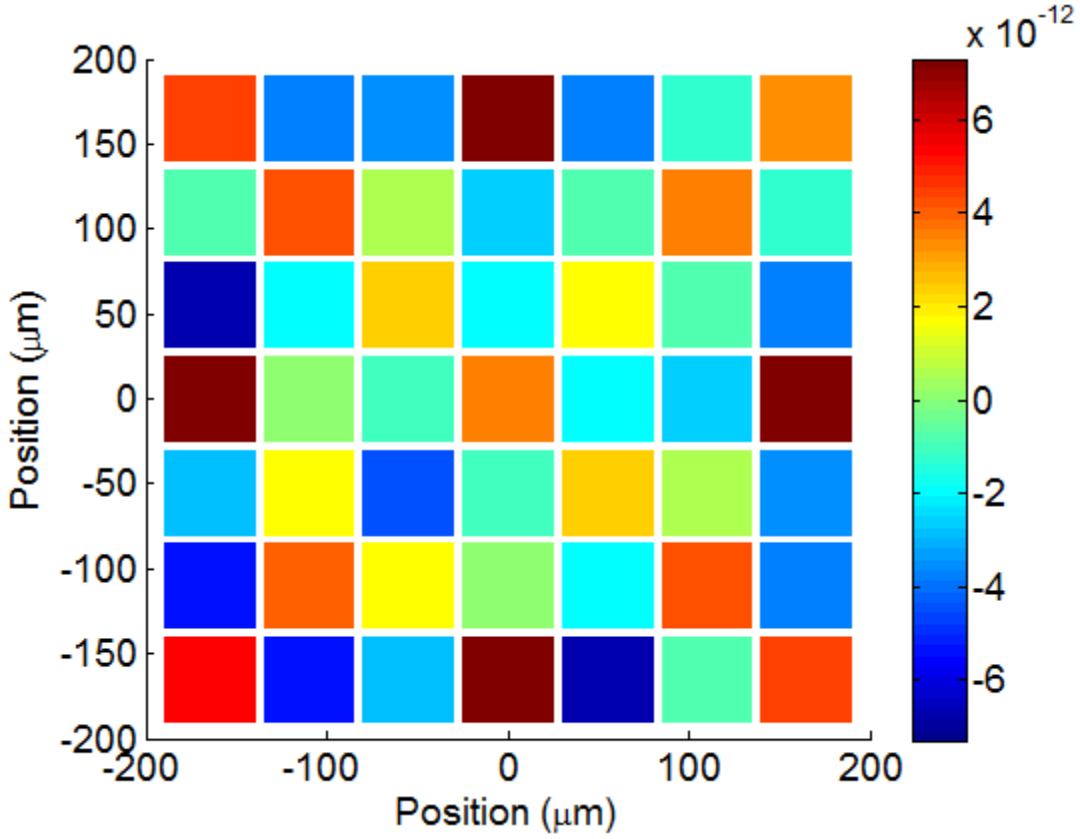

Figure 6.24 Image at a time of 19.5μs, the time corresponding to the time of expected focus in regular time reversal focusing.

6.5.2. Imaging a Subwavelength Sized Stiffness Defect

The same imaging process is repeated for a stiffness defect. The stiffness of the 13th membrane is altered by applying DC bias to the membrane. This makes the membrane less stiff by the spring softening effect [79]. With 10V applied to the membrane (collapse of the membrane is 47V) the stiffness is reduced by 1.2%. Figure 6.25 shows the time reversal focusing of the difference signals with the displacement of each membrane in the imaging array. The maximum displacement occurs on the 13th membrane at 19.02μs. This displacement image at 19.02μs is shown in Figure 6.26 which highlights the 13th membrane as the defect location.

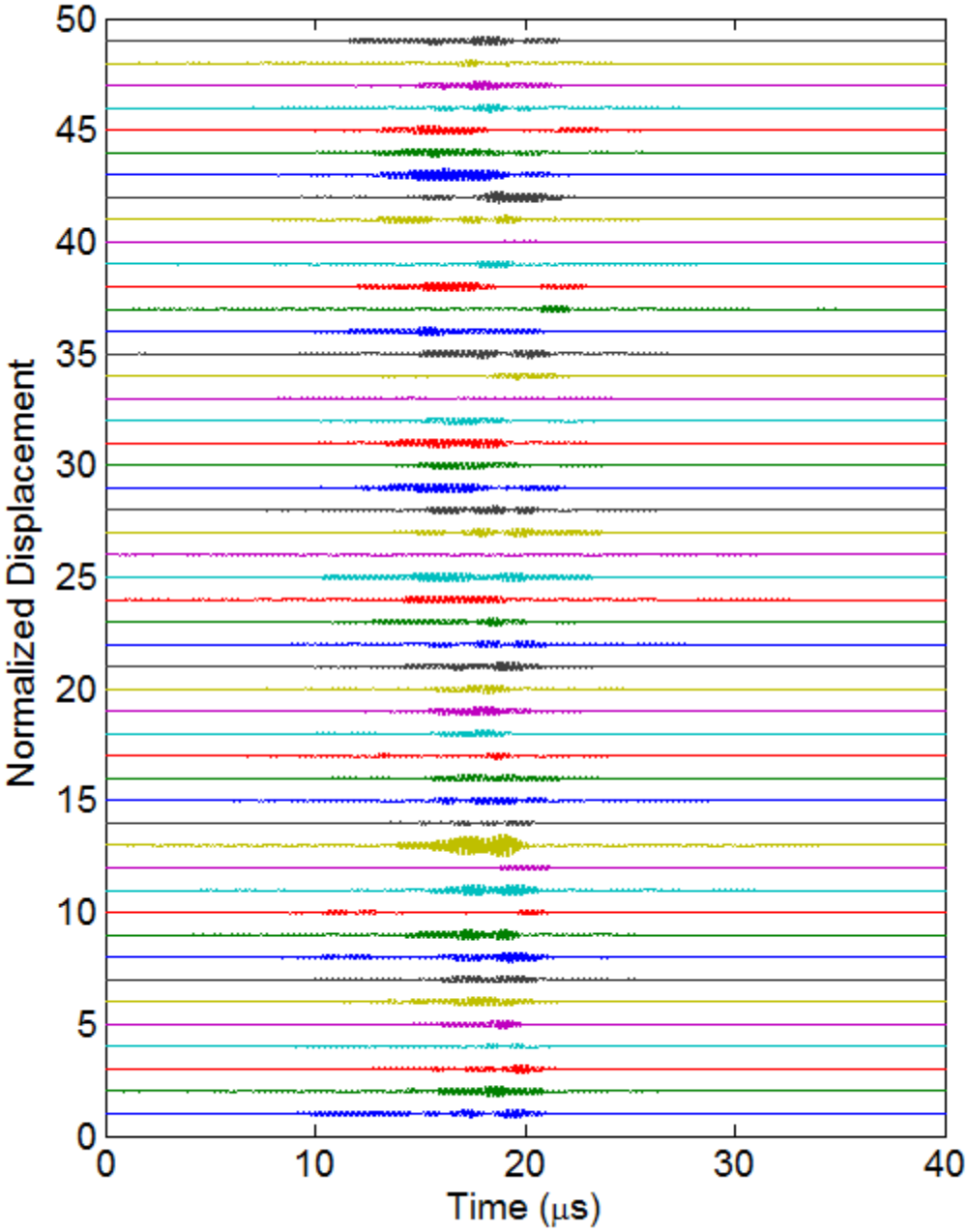

Figure 6.25 Displacement for each membrane in the imaging array over time. The maximum displacement occurs at the defect membrane location on membrane 13 at 19.02μs.

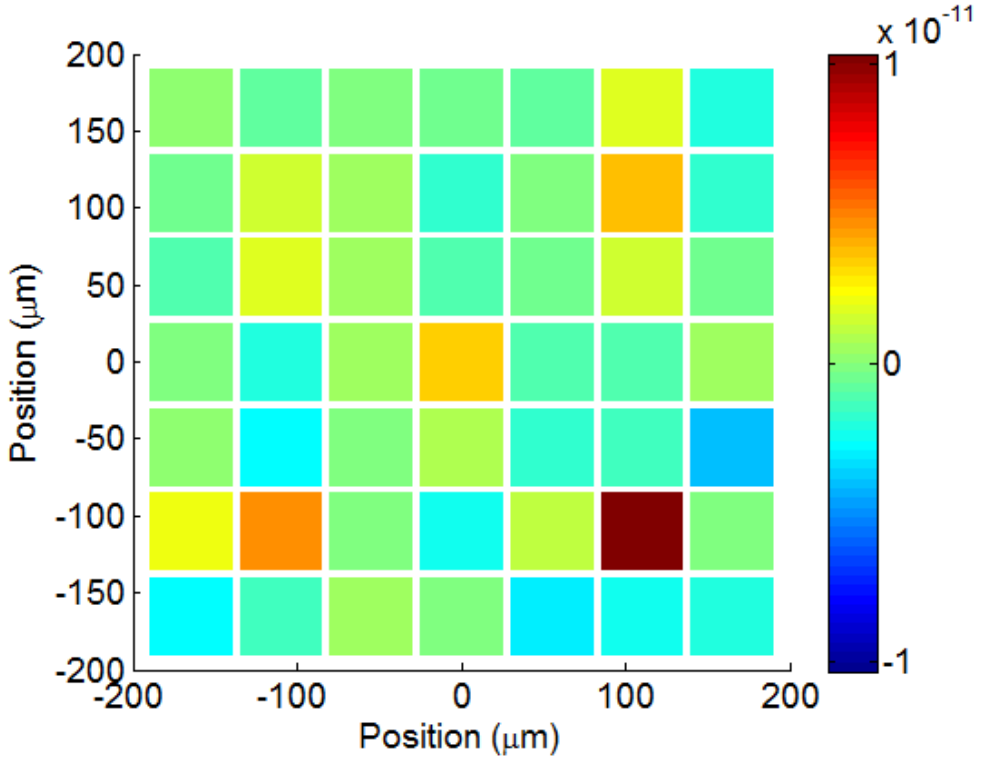

Figure 6.26 Displacement map of the imaging array at 19.02μs corresponding to the maximum displacement of all membranes.

6.5.3. Experimental Verification

Experiments were carried out on the array to localize a subwavelength defect. The center membrane was used as the active pulsing transducer and was pulsed with a 60V 50ns unipolar pulse. The received signal was recorded on the eight elements of the emitting array. To validate the simulation of a stiffness change, the 13th membrane had 10V of DC bias applied to it making it 1.2% softer. The center membrane again pulsed while the eight elements of the emitting array recording the received signals. To check that the array was not permanently changed the center membrane again pulsed with no bias on the 13th membrane. As a check to see that the system was indeed changing by applying the difference bias, the displacement of the center and 13th membrane were recorded with the LDV and are shown in the top row of Fig. 6.27. The first signal (0V) corresponds to the pulse with no bias on the entire array, then the 10V bias is added

and the signal is recorded again (10V). Notice that there is not much change at the center membrane since it is not having its resonance changed and is actively being pulsed. However, there is significant change in the signal of the 13th membrane as expected as the resonance of the membrane is changed by the addition of the 10V bais. The difference of the no bias case and the 10V case is shown in the second row of Fig. 6.27 which confirms that there was not much change with the active sensor but significant change on the membrane with the changing bias. This is expected and is the reason that this imaging method works, is from these differences and changes to the signals. To ensure that the system was stable after removing the 10V bias to the 13th membrane, another pulse was done and is denoted as 0V check in the first row of Fig. 6.27. The difference of the two 0V cases are shown in the third row of Fig. 6.27. The active membrane does appear to have a substantial difference, but more importantly there appears that the difference on the 13th membrane has a very small signal, indicating that there is no significant change in the system.

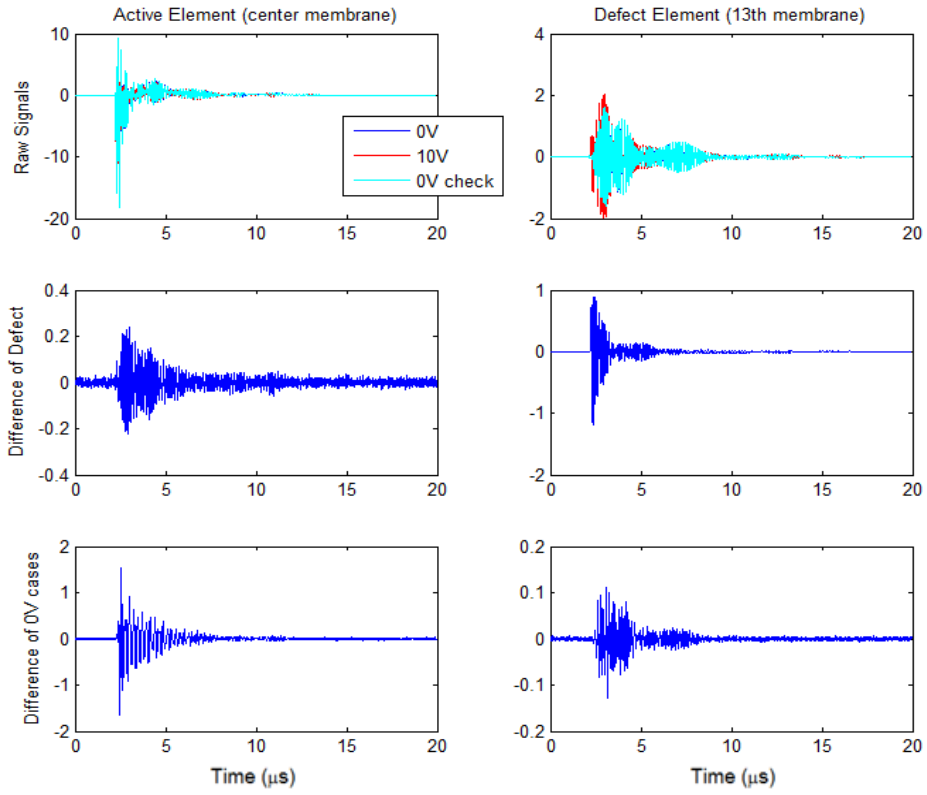

Figure 6.27 Displacements of the center membrane (active element, left column) and the 13th membrane which acted as the defect membrane in this test (right column). Three recordings were done with 0V DC bias then 10V then 0V again on the 13th membrane. The difference of the 0V case and the 10V case is shown in the second row and the difference between the two 0V cases is shown in the last row.

Now that it is apparent that the system is relatively constant, the signals captured on the emitting array can be examined. As stated before, the signals used for the focusing to the defect will use the difference of the signals, in this case the 0V bias case subtracted from the 10V bias case. These difference of signals on the 8 elements of the emitting array are shown in Fig. 6.28 and are already time reversed. These signals are then propagated back to the grid of 49 membranes by using a propagation operator that was captured experimentally. The displacement on each of the grid membranes is shown in Fig. 6.29. The maximum displacement over all time and membranes occurs at 19.95us with displacement of 0.81nm on membrane 13. The center

membrane also has significant energy and has a maximum displacement of 0.79nm (still lower than the displacement on the 13th membrae) which occurs at 20.75μs. The maximum displacements of the 13th and center membranes are very close and could cause a problem when attempting to localize the defect.

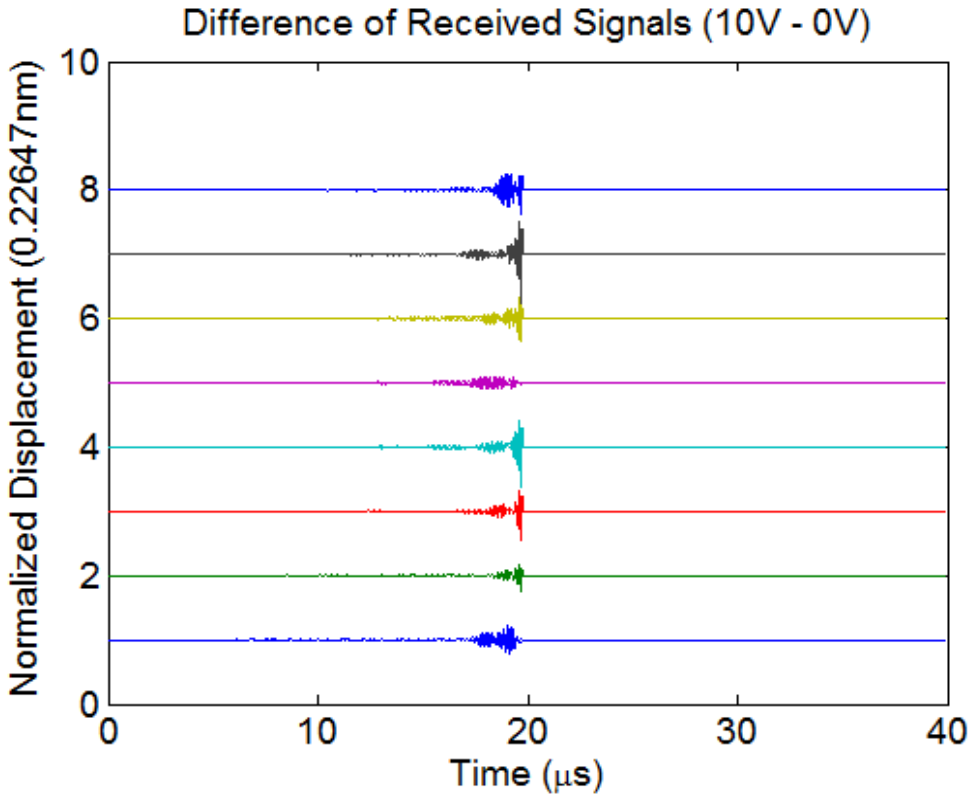

Figure 6.28 Difference signals received on the emitting array elements between the two cases of 0V and 10V.

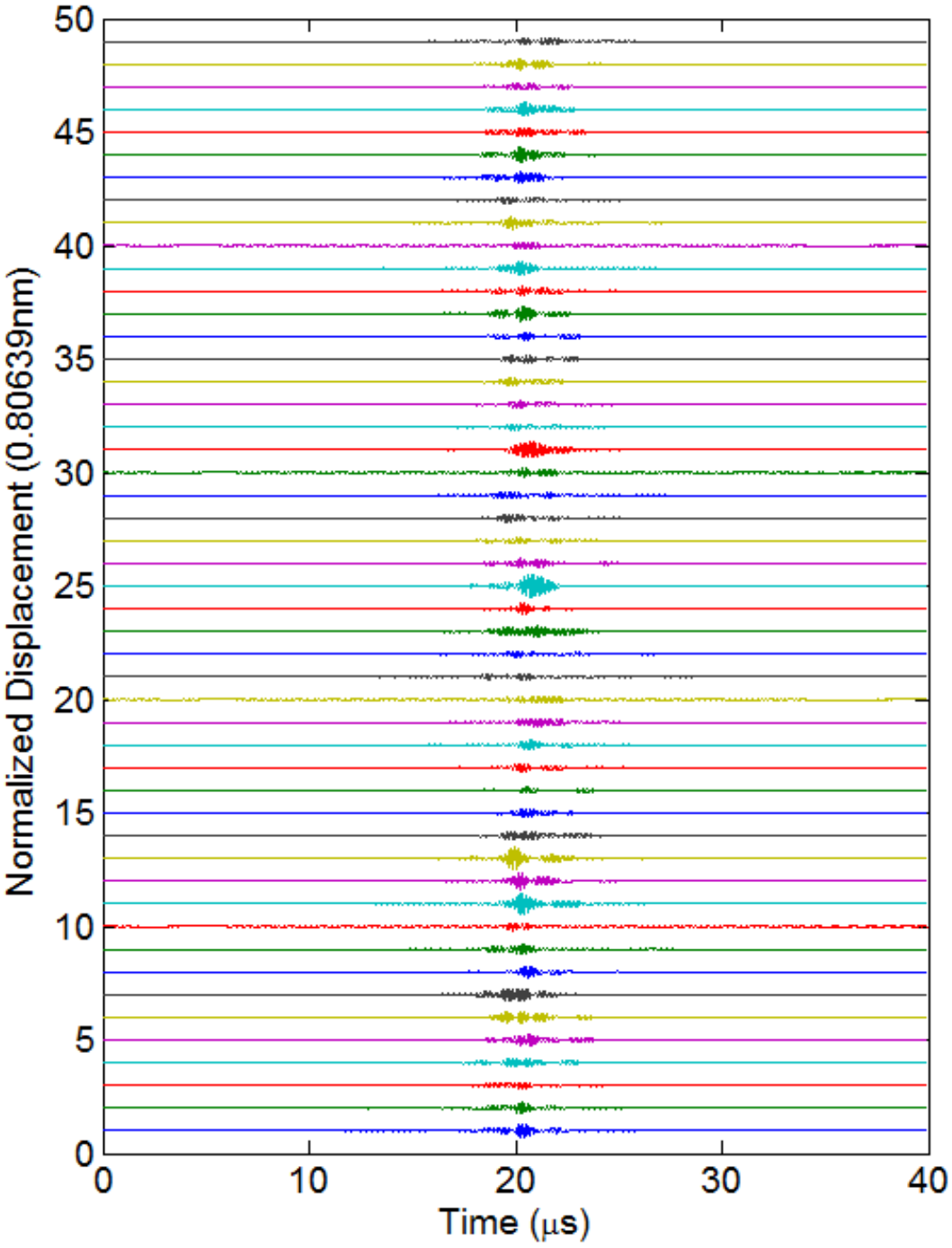

Figure 6.29 Displacement for each membrane in the imaging array over time. The maximum displacement (0.81nm) occurs at the defect membrane location on membrane 13 at 19.95μs. There is significant energy on the 25th or center membrane and its maximum displacement is 0.79nm at a time of 20.75μs.

In an attempt to improve the focusing to the defect, a closer examination of time reversed signals used in the focusing (Fig. 6.28) is given in Fig 6.30. Notice that there are six elements (2, 3, 4, 6, 7, 8) that have a strong peak around 20μs that is identically in phase with each other membranes in the emitting array. This strong peak is due to electrical crosstalk as it occurs at the exact time that the pulse is exciting the center membrane. Hence this section of the signals is not physical and is removed by time windowing 1μs from the signals around the electrical crosstalk peak in an attempt to improve the defect localization. The widowed signals (time reversed) are shown in Fig. 6.31 with the focusing results on all membranes of the grid shown in Fig. 6.32. In these focusing results it is more clear from a visual inspection that the 13^{th} membrane has the largest displacement and is the location of the acoustic focusing. The maximum displacement is 0.46nm on the defect membrane which occurs at 20.89μs. The time shift of the focus is due to removing the 1μs of data in the focusing signals. Also apparent is the reduction of the strong displacement that was present at the center membrane from the prior focusing. The maximum displacement of the center membrane is only 0.31nm occurring at 20.44μs. This concludes that a subwavelength sized defect of just 1.2% variation in stiffness can be localized by using a perturbation method and the time reversal focusing.

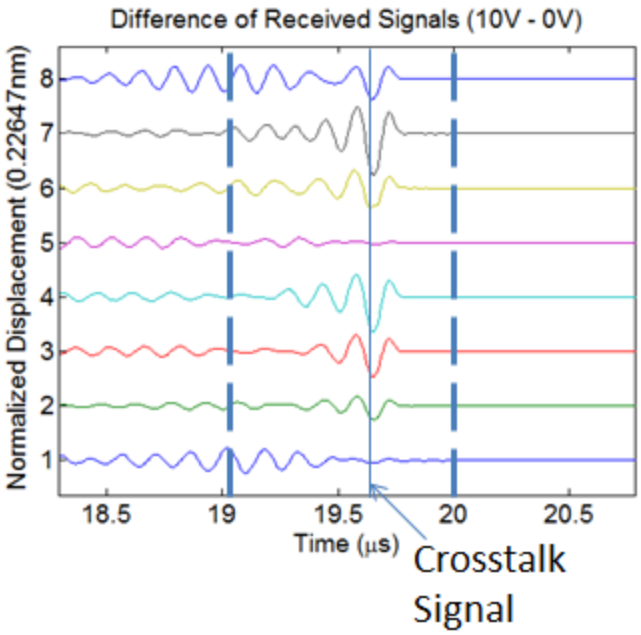

Figure 6.30 Zoomed in view of Fig. 6.28 which shows that there is an electrical crosstalk portion of signal. To obtain cleaner defect localization, 1μs of data around the electrical crosstalk signal was removed.

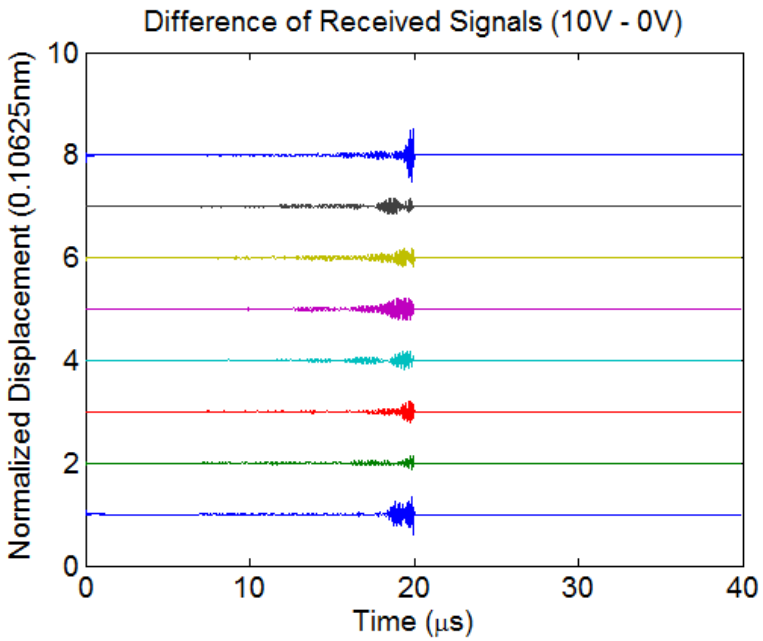

Figure 6.31 Time reversed signals used for the defect localization with the electrical crosstalk portion of the signals removed.

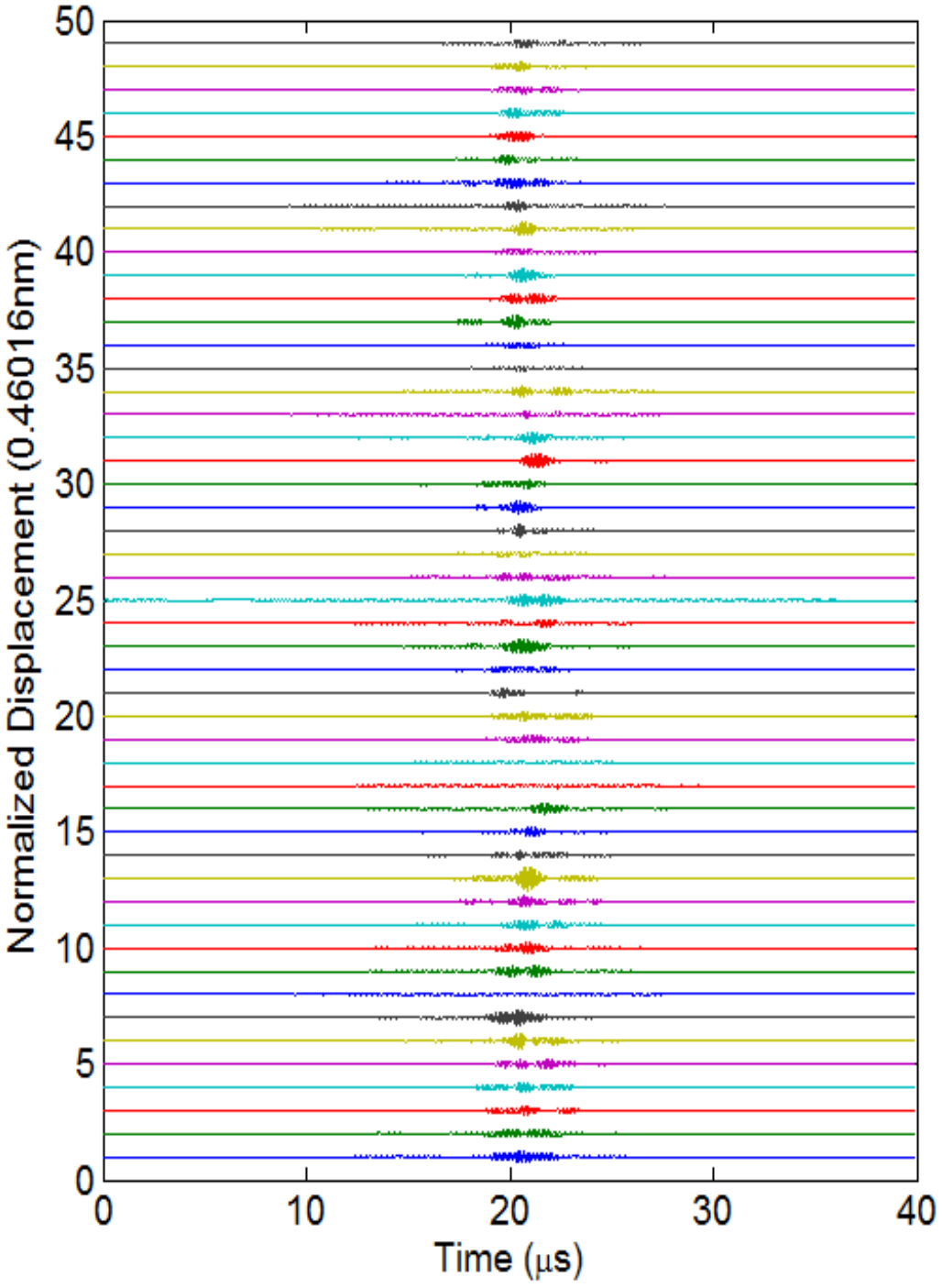

Figure 6.32 Displacement for each membrane in the imaging array over time using the improved time reversed signals. The maximum displacement (0.46nm) occurs at the defect membrane location on membrane 13 at 20.89μs. The energy on the 25th or center membrane has been reduced with the new signals with its maximum displacement of 0.31nm at a time of 20.44μs.

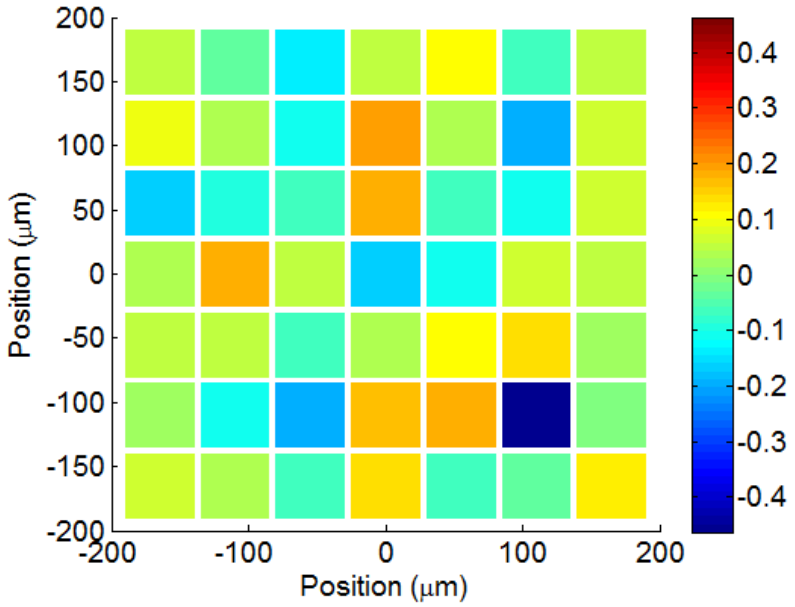

Figure 6.33 Displacement map of the imaging array at 20.89μs corresponding to the maximum displacement of all membranes.

6.6. Summary

This chapter uses the principles of time reversal, iterative time reversal, and the inverse filter to obtain acoustic focusing to a resolution of λ/5, limited to the dimensions of the membrane. It is stressed that while not shown, that this focus can be achieved to any membrane in the control array of 7x7 [47]. The critical component throughout this focusing is understanding the propagation operator, or the Green's function between the emitting array and the control array. Since this is a complex medium with trapped modes and dispersive propagation, the proper use of the propagation operator allows for the sound to be focused. Future work should optimize the propagation operator to design focusing and imaging arrays that can have superior resolution. The subwavelength focusing can be extended to smaller focal spots only if the membrane lateral size is reduced while keeping the same resonant frequency (Appendix A) [47].

An extension of time reversal focusing is shown to be able to detect subwavelength singular defects of mass and stiffness. Two different defects were identified, a mass defect and stiffness defect. These defects consisted of a very small change either a 1% or 1.2% change from the original structure's properties. By taking the difference of the signals on the healthy array and the defected array the defect location can be determined. The time of the refocusing is not directly known since the defect can be of different strengths or locations, but this focus time has to occur before the amount of time used for the time reversal. In this work the focal time is determined by locating the maximum displacement of the all the membranes when the difference signals are refocused.

CHAPTER 7

CONCLUSIONS

This research provides new insights for studies with evanescent surface waves on membrane metasurfaces. There are many opportunities for potential applications to designing transducer arrays, negative refraction, and subwavelength near field imaging systems. A near term application is the fundamental understanding of these waves to reduce crosstalk in transducer arrays. From the results shown in Chapter 4, slight variations in the membrane resonance (around 5% standard deviation of the mean) can nearly completely disrupt any trapped modes on the structure which can alleviate the issues for far field imaging. Due to the ease in designing and fabricating these micromachined structures, masks could be designed with small variations in lateral dimensions of the membrane. These small changes in the lateral dimension can conceivably have a significant positive impact on the transducer's far field operation. Conversely, rather than disrupt the modes on the structure, this research provides new directions to enhance the standing modes for potential use in resonant sensors. The model is a robust tool that can quickly calculate the mode shapes and its corresponding wavenumber, resonant frequency, and quality factor.

Additional work can potentially use the membrane metasurface as a 2D lens for subwavelength imaging as has been done in prior works. This would require further examination of the equifrequency contours of the metasurface at frequencies just before the band gap. It was shown in Chapter 4 that the membrane metasurface has a concave equifrequency contour at 7.1MHz, making this material capable of negative refraction around this frequency. A 2D lens could be designed from this information, which could show the focusing of evanescent waves.

Two other pertinent applications, near field subwavelength focusing and imaging, were shown as proof of concepts in this research. One great benefit of working with the evanescent wave field is that it already contains information at the subwavelength scales. Chapter 6 showed in both simulation and experiments that these waves can be controlled and focused to a $\lambda/5$ spot or the size of one membrane. Chapter 6 extended this control of the evanescent waves to image subwavelength sized defects on the imaging grid. Future work with these topics can look to design arrays that can focus and image to even smaller fractions of a wavelength. This would require a thorough analysis of the propagation operator for each array design considered. Furthermore for a effective imaging system, the model would need to be enhanced to include methods to add imaging targets or impedance changes in the semi-infinite fluid. Eventually, these applications can conceptually be used to measure the mass or density of cells present on top of the array.

In conclusion, the significant contributions of this research are:

- A model was developed that calculates the modes of the membrane array, their resonant frequency, wavenumber, and quality factor
- The dispersive nature of the evanescent waves was directly related to the modes of the structure
- A transient model was developed and experimentally verified to examine the dispersion and modal properties as to how they are effected by basic array parameters.
- A 2D dispersion analysis was conducted which identified interesting frequency bands of the metasurface, including one frequency band with the potential for 2D lenses based on negative refraction

- Subwavelength focusing to focal widths of λ/5 was demonstrated in both simulation and with experimental verification by using time reversal
- Subwavelength imaging of a small impedance change was performed on the membrane array by localizing the subwavelength defect using a difference of signals with time reversal

APPENDIX A

2D FOCUSING ARRAY PARAMETER STUDY

This chapter details the design study for an array capable of subwavelength focusing. The time reversal method is used with the simulations for this focusing as detailed in Chapter 6. This method works best with a dense array of membranes that can support the evanescent waves, and several CMUT membranes removed from the structure that comprised the emitting array. One main parameter, the resonant frequency of the membrane, was kept fixed. If the membrane frequency changed then all of the parameters would have needed to be normalized by λ or the wavelength of sound in water for the give resonant frequency of the membrane. For ease of the parameter study, the center frequency remained at 6.55MHz.

Other design criteria included were the experimental limitations of the CMUTs and the array design. This meant that the membranes needed to be easily fabricated using known methods [40, 85]. Another limitation was the number of membranes that could be electrically connected. The largest number of electrical connections is 64 as determined by the largest chip carrier that was accessible. This set an upper limit of the number of membranes if all of the membranes were to be connected with individual circuits. Within these constraints certain parameters such as membrane spacing, membrane size, number of membranes in grid, number of membranes in emitting array, and location of emitting array were altered. These parameters would be compared by several metrics from the time reversal process including focal width, focal depth, level of side lobes, and membrane displacement.

For each parameter change, the time reversal simulation was run. In each simulation, the focal membrane was pulsed and the signals were recorded on the exterior transducers of the

emitting array (typically 8 in a symmetric pattern around grid). These signals were then time reversed (using a time length of 20μs for most cases) and retransmitted by the emitting array which resulted in the focus at the target membrane. The displacements of the membrane were an important parameter to measure because in experiments these displacements correspond to the signal levels. The first important displacement measurement was the displacement of the exterior transducers which will be called Source/Receivers (S/R) as they were receiving the pulse from the center membrane. It is important that these membranes had a displacement >10pm for up to 20μs after the pulse so that these signals could be recorded in experimental settings. Two measurements of the received signals were taken, one at the max displacement and a second in the vicinity of 20μs. The displacement of the focal membrane during refocusing was also measured. The displacement of all membranes was calculated and was used to calculate the pressure distribution around the array at each particular time by use of the Rayleigh integral [39]. The pressure field was calculated on the XY plane at Z=1μm above the array in addition to the YZ plane with X=0μm. Two examples are shown in Fig. A.1 and Fig. A.2 which show the pressure distribution in decibels at the focal time. The small black circles are representative of the nodes or the membrane mesh which was used in the modeling. These pressure distributions along with a -17dB contour levels were used to determine the focal width, focal depth, and level of the side lobes. The focal depth corresponded to the Z position of the -17dB level of the focused energy and described how far into the fluid the focal point was effecting. In this case, Fig. A.1 shows that the focal depth is 25μm. The focal width is measured on the main focal beam at the Z position that is half of the focal depth. In this case the focal width is measured at Z=12.5μm and is 45μm wide. This focal width corresponds to $\lambda/5$ where λ is the wavelength of 6.55MHz sound wave in water. The last parameter taken from the pressure distributions is the

level of the highest side lobe and is taken from the pressure distribution in the XY plane or Fig. A.2. The results of the metrics are summarize in Table A.1.

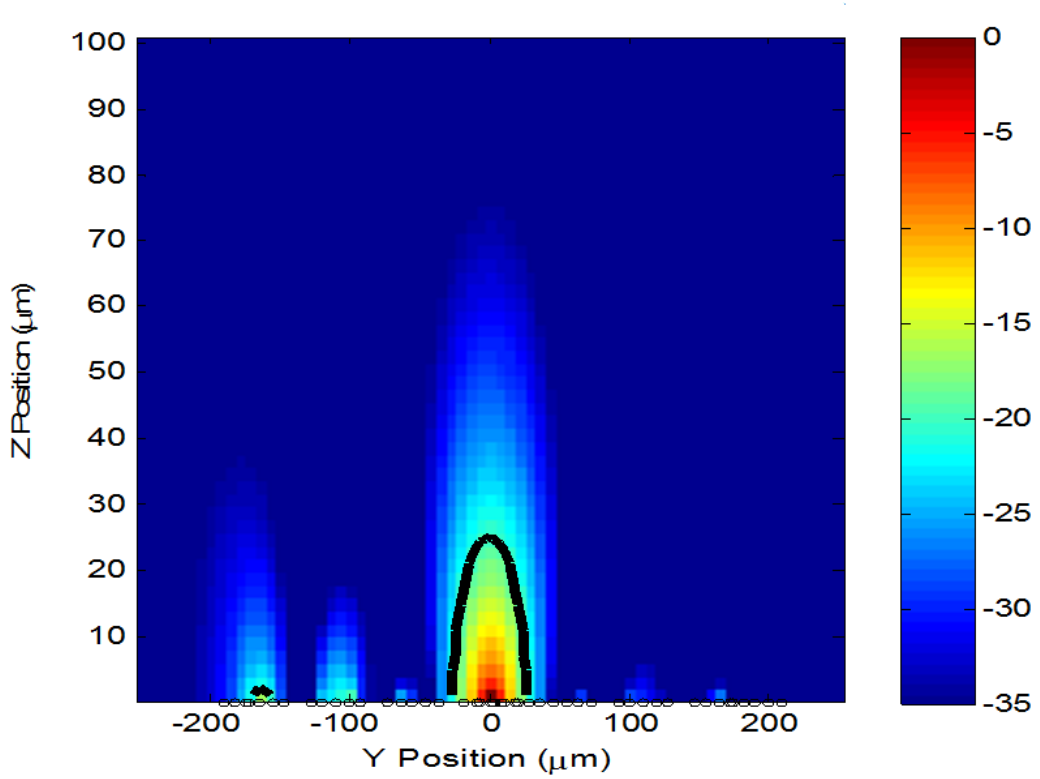

Figure A.1 Logarithmic image of the pressure field around the focusing grid in the YZ plane (X=0μm) at the focal time. The dark black lines are the -17dB contour line and used to measure the how far the focus extends into the fluid (peak in the z-direction) as well as the focal width measured at half of the peak.

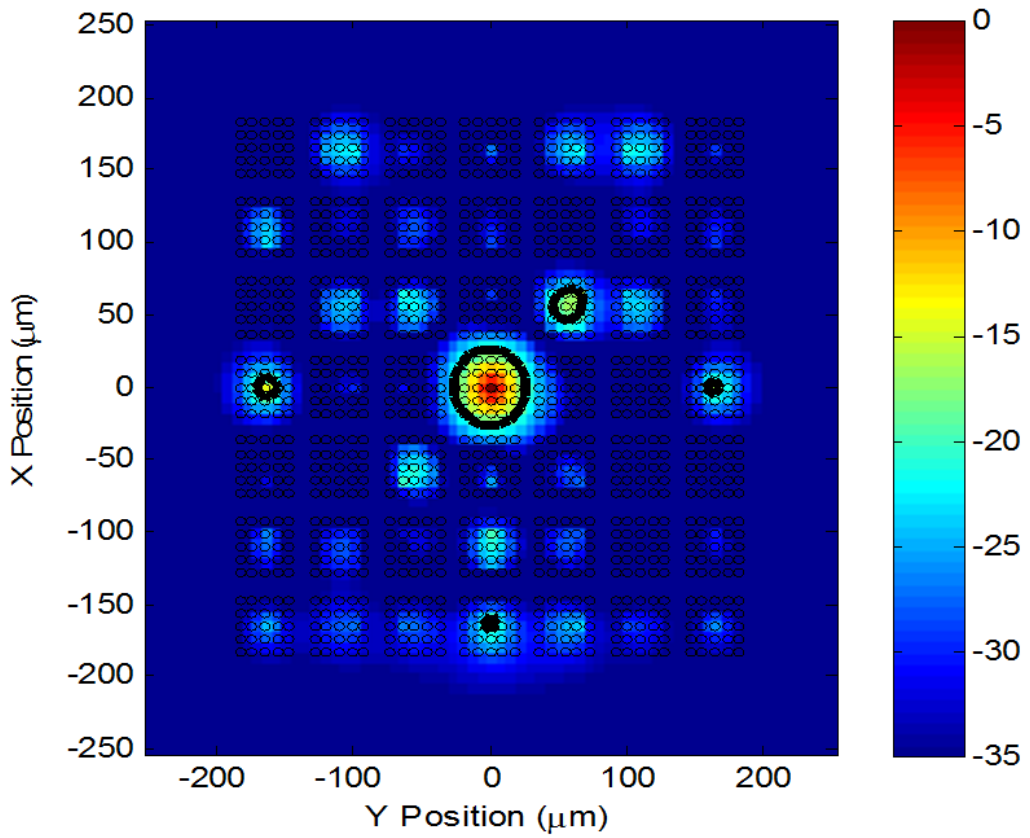

Figure A.2 Logarithmic image of the pressure field around the focusing grid in the XY plane (Z=1µm) at the focal time. The dark black lines are the -17dB contour line. This plane of the pressure allow to see the strength of the side lobes.

Table A.1 Example of the metrics taken with each iteration of the time reversal process.

Focusing	**Peak in z-dir (um)**	**½ peak width (um)**	**½ peak width (lambda)**
-20 dB Focus	25	45	0.20
Membrane Properties	**Max Displacement (pm)**	**Max Current**	**Time of Maximum (us)**
1st S/R ~0 deg (at Maximum)	16	1.5e-15	2.06
(around 20us)	1.3	1.3e-16	~19.9
Focal Membrane	1900	1.7e-13	19.5

Membrane Lateral Dimension

The first parameter altered was the membrane lateral dimensions. By altering the lateral dimensions of the membranes the thickness of the membranes needed to be adjusted accordingly to keep the same center frequency of 6.55MHz. Four different lateral dimensions were used of 20, 30, 45, and 80µm. In each test the membranes were still organized in a 7x7 grid. Figures A.3 and A.4 show how the membrane displacement and the focal beam were altered. The smaller membranes appeared to be advantageous to yield both better displacements and smaller focusing. One caveat is that while the focal width does decrease with membrane's lateral dimension, the focal width actually become larger than a membrane for the smaller membranes. However, it was determined that it would be very difficult to manufacture the smaller membrane sizes of 20 and 30µm. Hence the 45µm membranes were used to build the array.

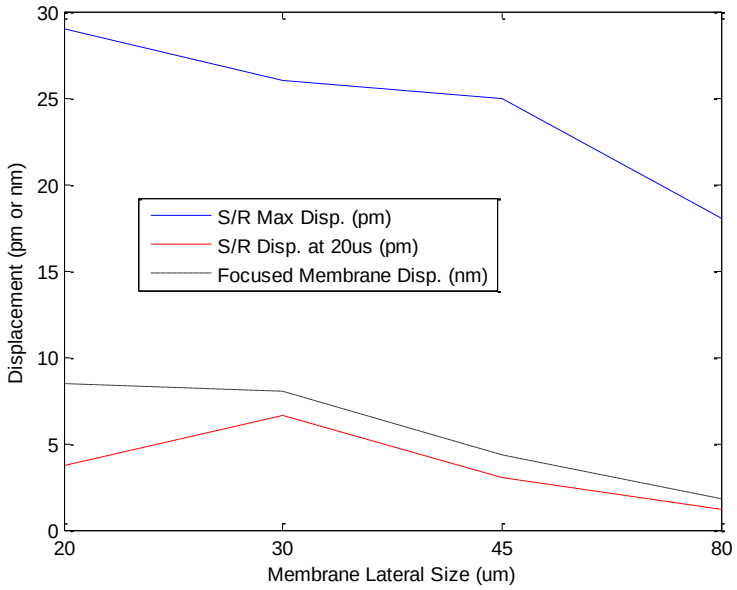

Figure A.3 Displacement effects from altering the lateral dimensions of the membranes

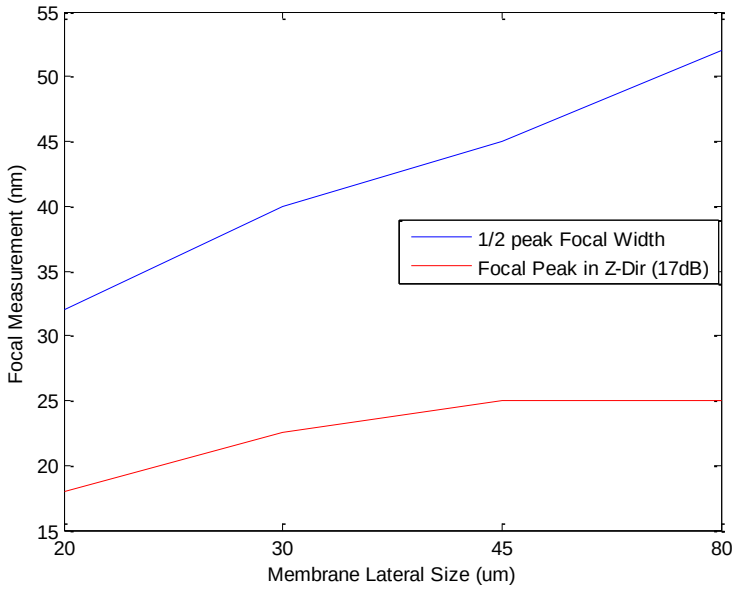

Figure A.4 Focus metrics of focal peak and focal width for various lateral dimensions of the membranes

Number of Elements in the Emitting Array

The next parameter altered is the number of elements in the emitting array (Source/Receivers). Nearly all metrics improve with more elements as shown in Fig. A.5-A.6 (albeit not smoothly) which makes sense from the added energy, the added number of paths, and the improved spatial sampling of the field. It seems that as long as there are more than 6 sources the focal width is optimal. The side lobes are greatly reduced with the larger number of sources as another added plus. For the array it would be best to use 6-8 sources to have the best focus with minimal side lobes. More than 8 sources can lead to experimental complications with the number of electrical connections and function generators required.

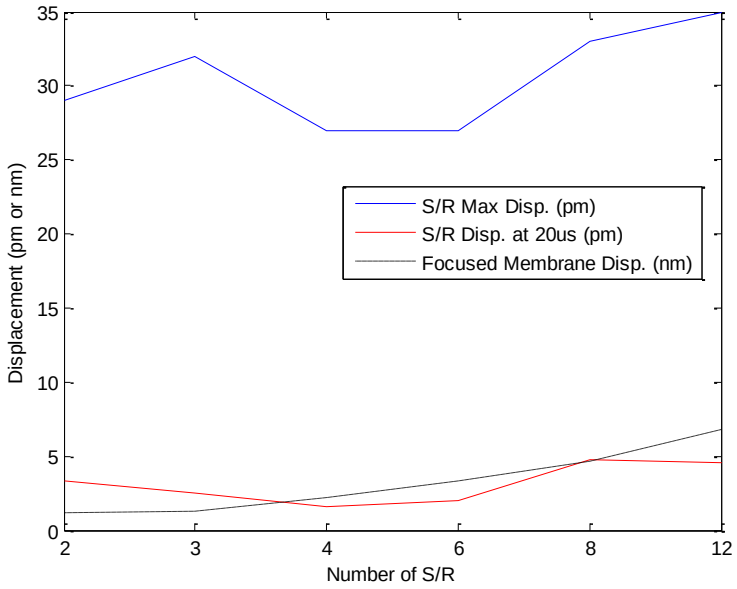

Figure A.5 Displacement effects from altering the number of Source/Receivers (elements in the emitting array)

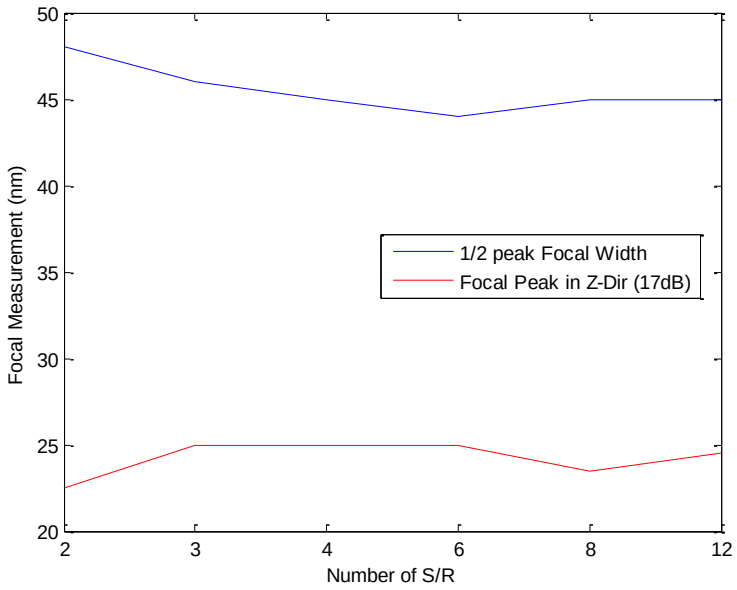

Figure A.6 Focus metrics of focal peak and focal width for various number of Source/Receivers (elements in the emitting array)

Radius of Emitting Array

Another parameter that was changes was the radius of the emitting array. It is seen that the focusing is not overtly changed by the radius of the S/R (small variations are present) in Fig. A.8. The closer the emitting array is to the grid, the better signal strength of all signals due to reducing the attenuation (Fig. A.7). The S/Rs should be placed close to the grid (but not a part of the grid) to obtain the best SNR in the system. If they were a part of the grid it would be hard to excite the membranes individually as they would be heavily coupled to the structure and the modes that are present. For the array design, a radius of 385μm was used.

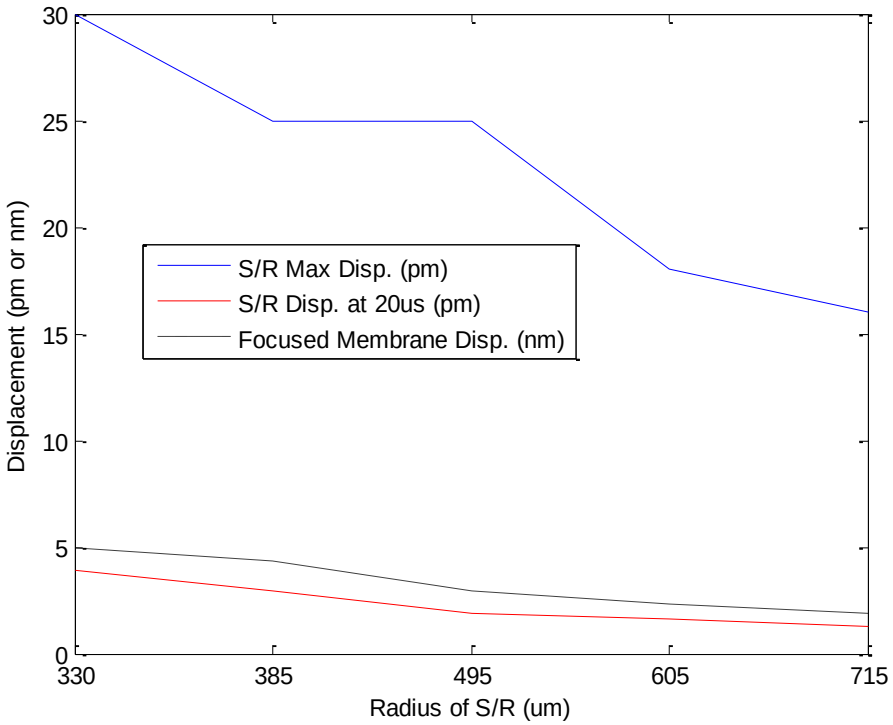

Figure A.7 Displacement effects from altering the radius of the Source/Receivers (emitting array)

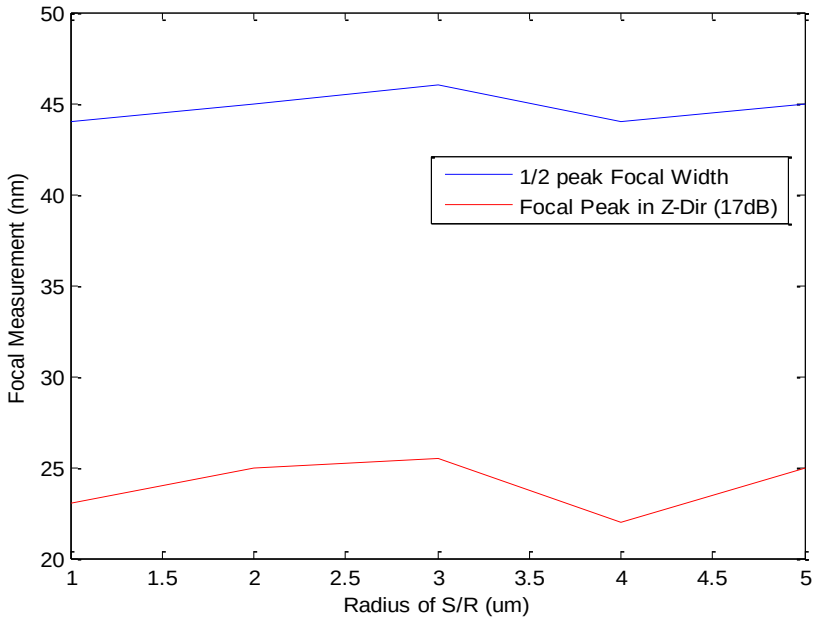

Figure A.8 Focus metrics of focal peak and focal width for various radii of the Source/Receivers (emitting array)

Size of Membrane Metasurface

The size of the grid was changed to see how it affected the experiments. While not effecting the focal width (Fig. A.10), the larger grid size leads to a stronger focal membrane displacement and S/R membrane displacement around 20us while a decrease in the max S/R displacement as seen in Fig. A.9. The growth of the focal membrane displacement and the S/R displacement around 20us might be attributed to the larger grid being closer to the emitting array. The decrease in the max S/R displacement, however is not explained by the grid getting closer to the emitting array. This is likely due to more dispersion occurring in the larger grids which causes the energy to be spread out and not arriving at one time. In the end, this is a flexible design parameter and a smaller grid allows for faster experiments. A 7x7 grid was used based on the limit of the electrical connections and the consideration of experimental time.

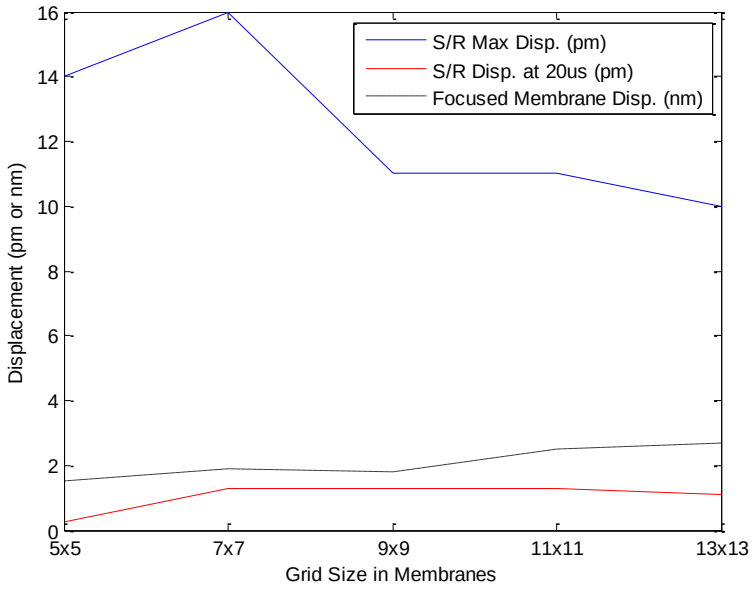

Figure A.9 Displacement effects from altering number of membranes in the grid

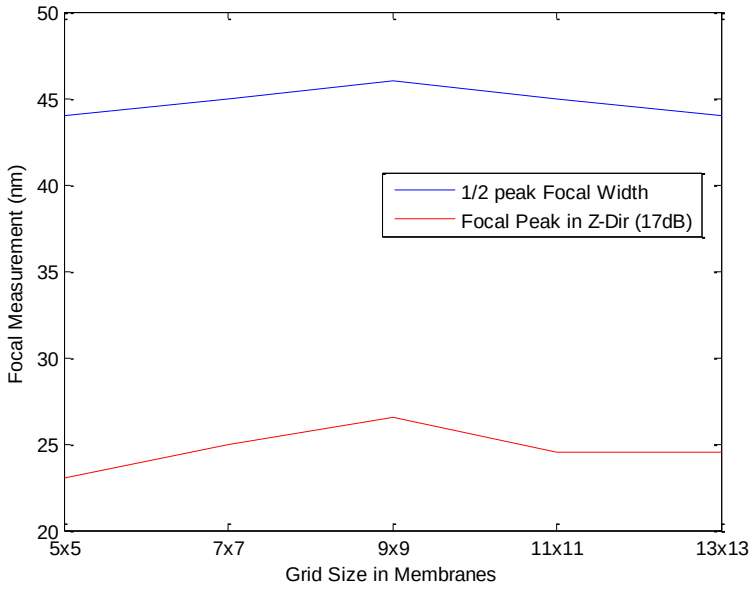

Figure A.10 Focus metrics of focal peak and focal width for various numbers of membranes in the grid

Length of Time Reversal

Both the focused membrane displacement and the focal width improve with a longer time reversal, up to a point as seen in Fig. A.11-A.12. This is clear from the more energy and information you have from the signal then the better the focus will be. Hence it is suggested that the experiments should determine how long of time reversal should be used. The time reversal should use as long of a signal as possible with acceptable SNR. One additional experimental consideration would be reflections from the bulk waves and if they will be present in the signal window. The simulation only models the membrane array and a semi-infinite fluid so there are no reflections from the edge of the water bath. These considerations will also help determine how long of time reversal should be used.

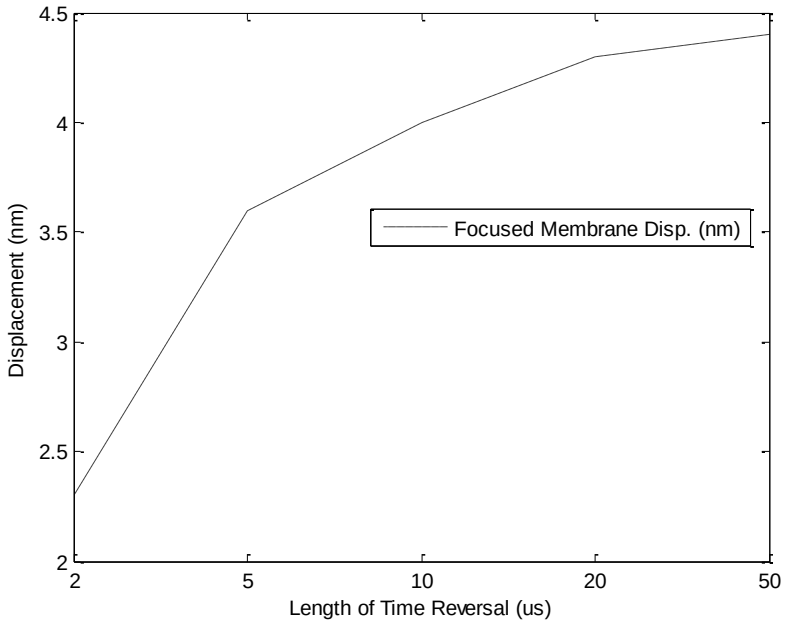

Figure A.11 Displacement effects from altering the length of time used in time reversal

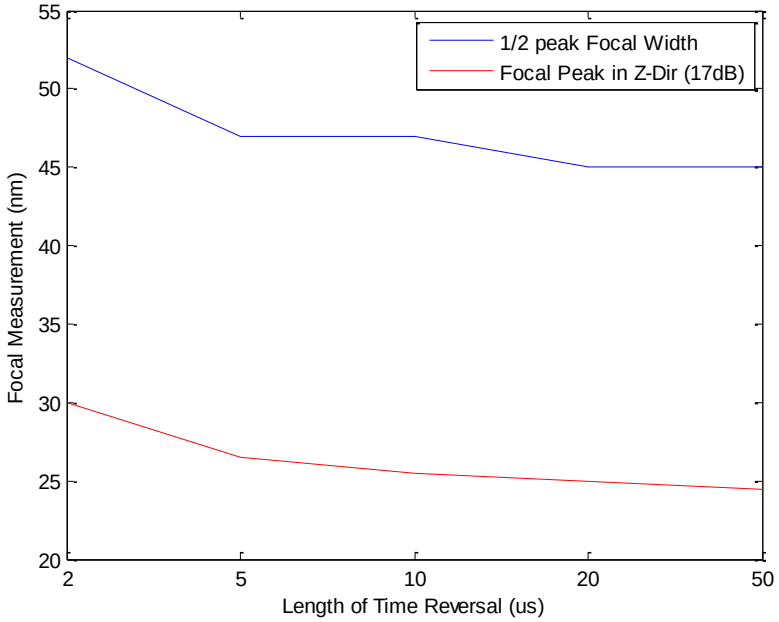

Figure A.12 Focus metrics of focal peak and focal width for various lengths of time used in time reversal

Membrane Spacing

The last parameter examined is the membrane spacing of the metasurface. The focal width does not change greatly with this parameter except for when the pitch is on the order of the membrane (Fig. A.14) as expected from the earlier parameter study (Chapter 4.3.1 Membrane Spacing). The max S/R displacement and the S/R displacement peak around 20μs has no clear trend across this paramater (Fig. A.13). This parameter is not a high impact parameter as long as the spacing is less than half the size of the membrane. The spacing was chosen to be 10μm which was the smallest spacing that could sustain the electrical leads running in between the membranes.

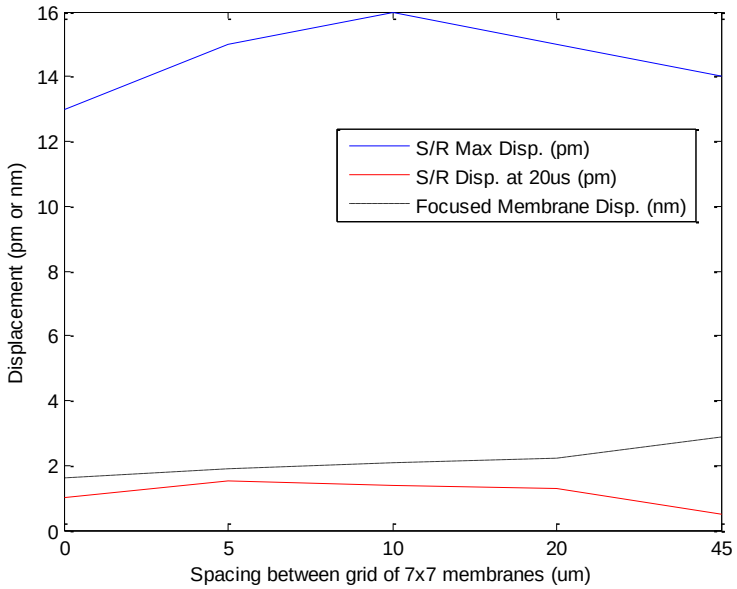

Figure A.13 Displacement effects from altering the spacing between membranes in the grid

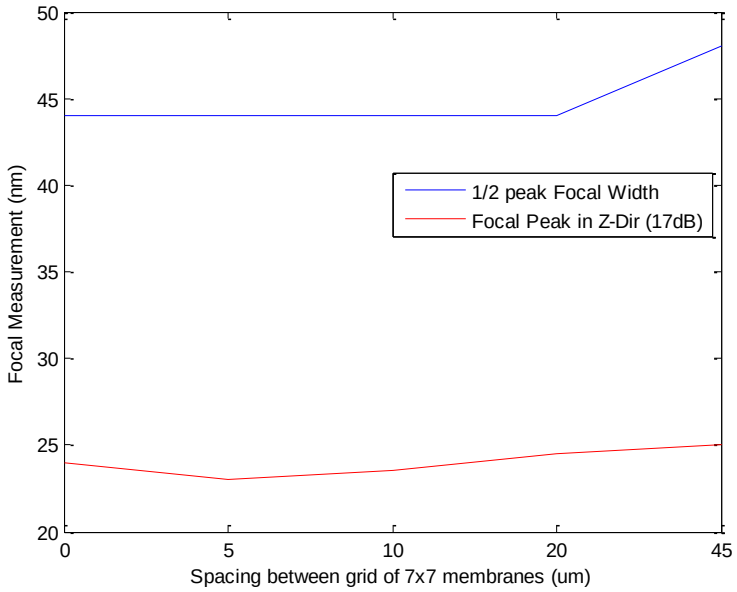

Figure A.14 Focus metrics of focal peak and focal width for various spacing between membranes in the grid

Conclusions

The CMUT array that was fabricated for use in the experiments is shown in Fig. A.15. The metasurface grid consists of 7 membranes in both the X and Y directions 10μm spacing in between each membrane. The number of elements in the emitting array was chosen to be 8 and positioned at a radius of 385μm. All 57 membranes are the same size with a lateral dimension of 45μm and a resonance of 6.55MHz.

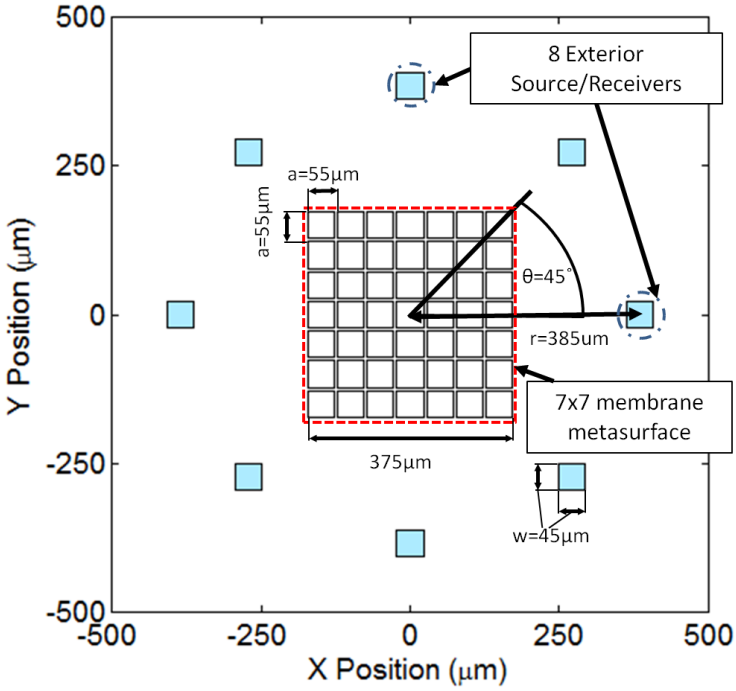

Figure A.15 Schematic of the membrane array consisting of a dense grid of membrane to support the surface acoustic waves and 8 membranes spatially removed from the grid for excitation purposes.

APPENDIX B

CHARACTERIZING THE CMUT ARRAY

The semi-analytic boundary element model is an excellent tool to model the linear vibration of the membrane metasurface. It is computationally efficient and is capable of tailoring the individual parameter of each membrane. However, it does have some limitations one of them being associating the proper material damping term for the membranes. This section walks through the steps it takes to characterize a CMUT array in order to have the best parameter inserted into the model for realistic simulations. The first step is to find the resonance frequency of each membrane. Then the damping factor for each membrane is matched for operation in air. Then again additional damping is used when water is added. In the end the model has all of the necessary parameters to effectively simulate the system realistically.

Find the Resonant Frequency of Each Membrane

The first step in characterizing a CMUT array is to quantify the variation of the membranes in the array. To do this for the 2D array the center membrane is pulsed with a 2V, 50ns, unipolar pulse when operating in air. The resulting displacement of all 57 membranes is recorded with the laser. Each displacement is transformed into the frequency domain. The displacement and spectra of the center (active) membrane operating in air is shown as Fig. B.1. Notice that the signal rings a lot since the membrane is vibrating in air which does not have much damping as compared to water. The resonance of the membrane in air is seen to be at 12.6MHz and this resonance is saved. To obtain the resonant frequency of the other membranes, the spectra of the displacement is used. Figure B.2 is the displacement and associated spectra

from the 2nd membrane in the grid. Notice that there are two peaks in the spectra. One peak corresponds to the resonance of the active membrane and the other is the resonance of the actual membrane. This procedure is repeated for all membranes. A scatter plot of the membrane's resonant frequencies is shown in Fig. B.3. This scatter plot shows some common deviations and can be clearly seen in Fig. B.4 when each membrane is plotted in its XY position with the color of the membrane depicting the its resonant frequency in MHz. The mean resonance is 12.58MHz in air with a standard deviation of 55kHz or just a 0.4% variation of the mean. This step gives information about the variations of the array that can be input into the model.

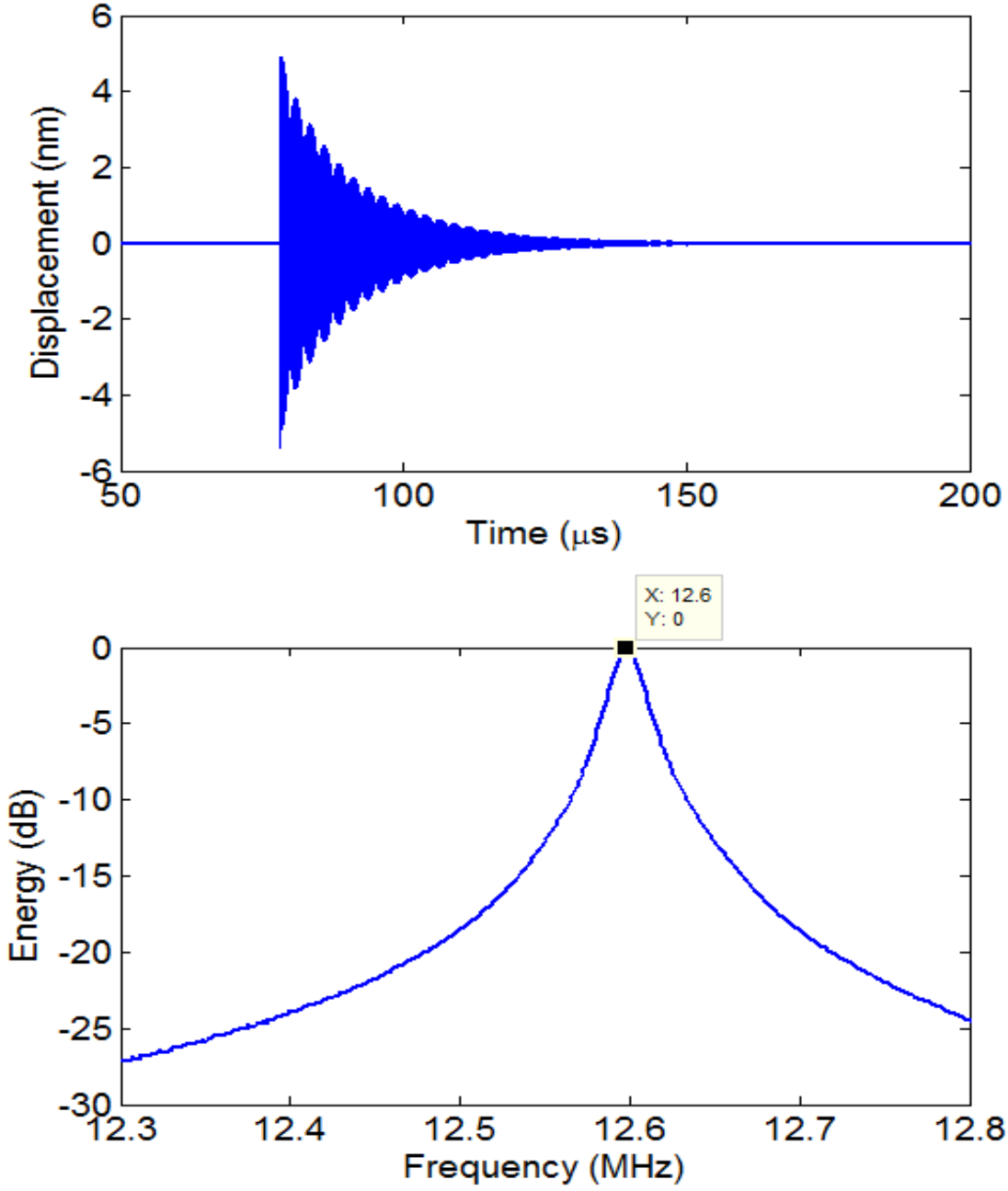

Figure B.1 Displacement (top) and frequency spectra (bottom) of the center membrane in the grid

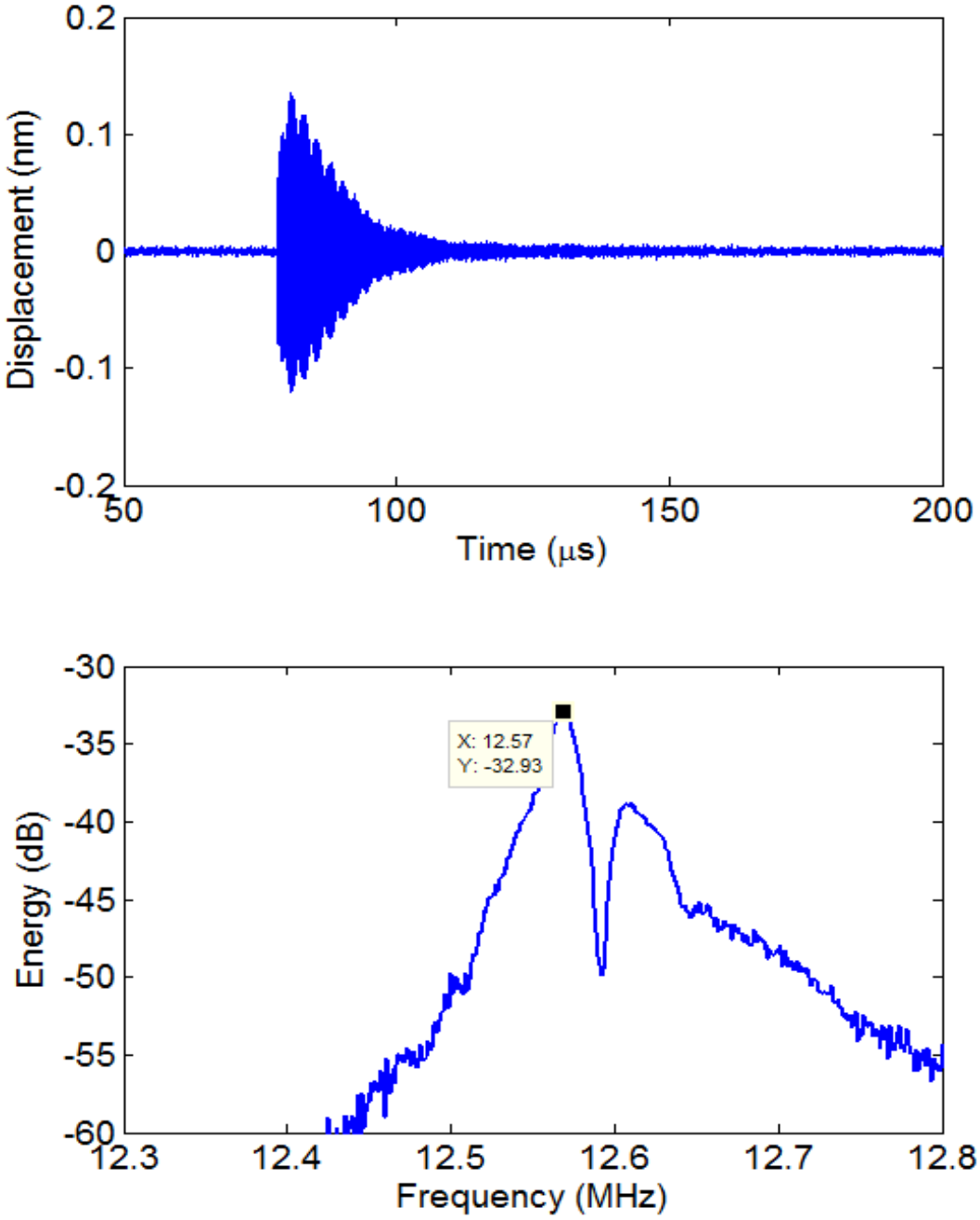

Figure B.2 Displacement (top) and frequency spectra (bottom) of the 2nd membrane in the grid

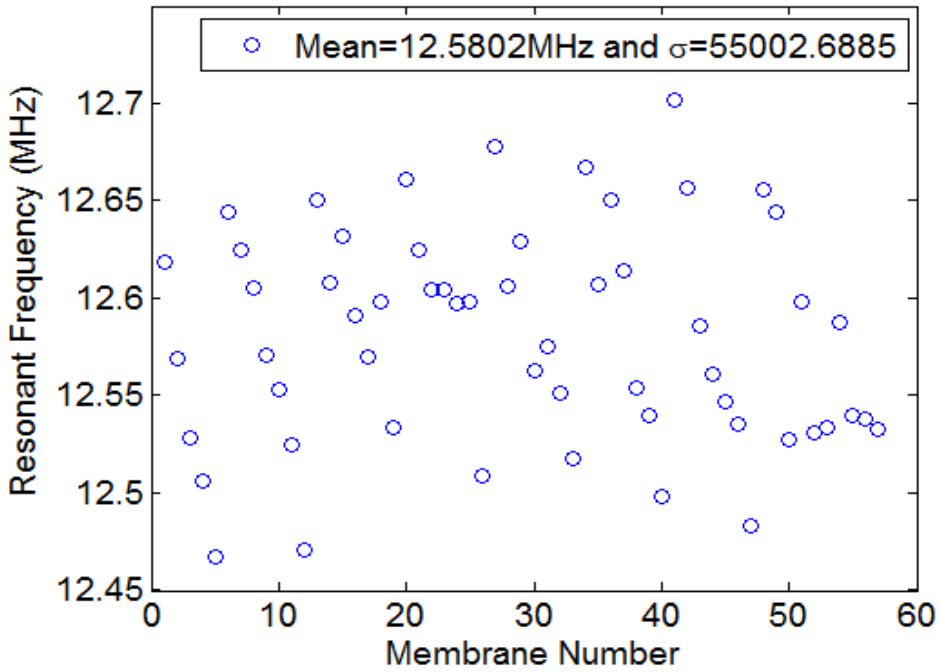

Figure B.3 Scatter plot of the membrane's resonant frequency in air

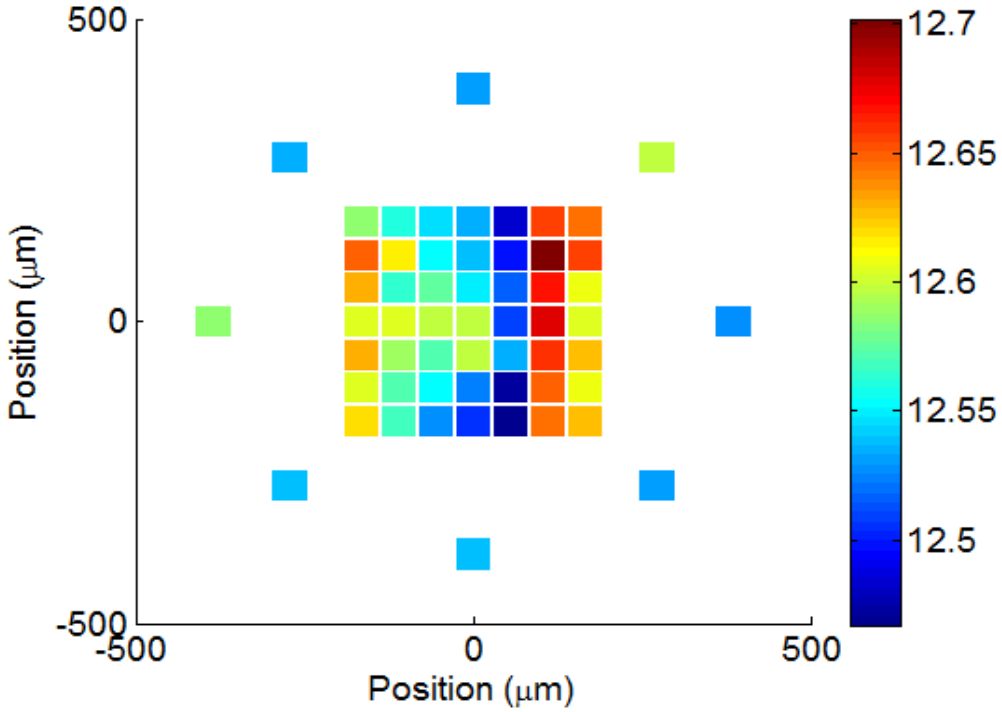

Figure B.4 Array layout in the XY plane with the color of each membrane depicting that membrane's resonant frequency.

Matching the Simulation to Experiments

After the membrane variation is measured, the next step is to match the simulation to the displacement in air by adjusting the membrane damping value. This step is done after parylene is added to the array. Parylene is a coating that is applied to the array to waterproof the electronics for when the array is used in immersion. Figure B.5 is the repeat of Fig. B.1, but not parylene has been added to the array. Notice that the signal in Fig. B.1 took about 70μs to damp out while the coating of parylene reduced the ringing to only 18μs in Fig. B.5. Notice that another effect of the parylene is that the resonant frequency is lowered by around 0.7MHz to just below 12MHz. This transient signal in air and the associated spectra is used to match the model results. To match the experiments the simulation is run for one membrane. The first step is to match the resonant frequency. This is done by keeping the lateral dimensions of the membrane the same and altering the thickness of the membrane until the resonances match. The next step is to match the attenuation of the experimental signal. This is done by using different values of damping for the membrane until the attenuation of the time signals and the quality factor of the spectra matches the experiments. For this array the damping parameter was 2500Pa/(m/s)/m^2. The matched experimental data is shown in Fig. B.6.

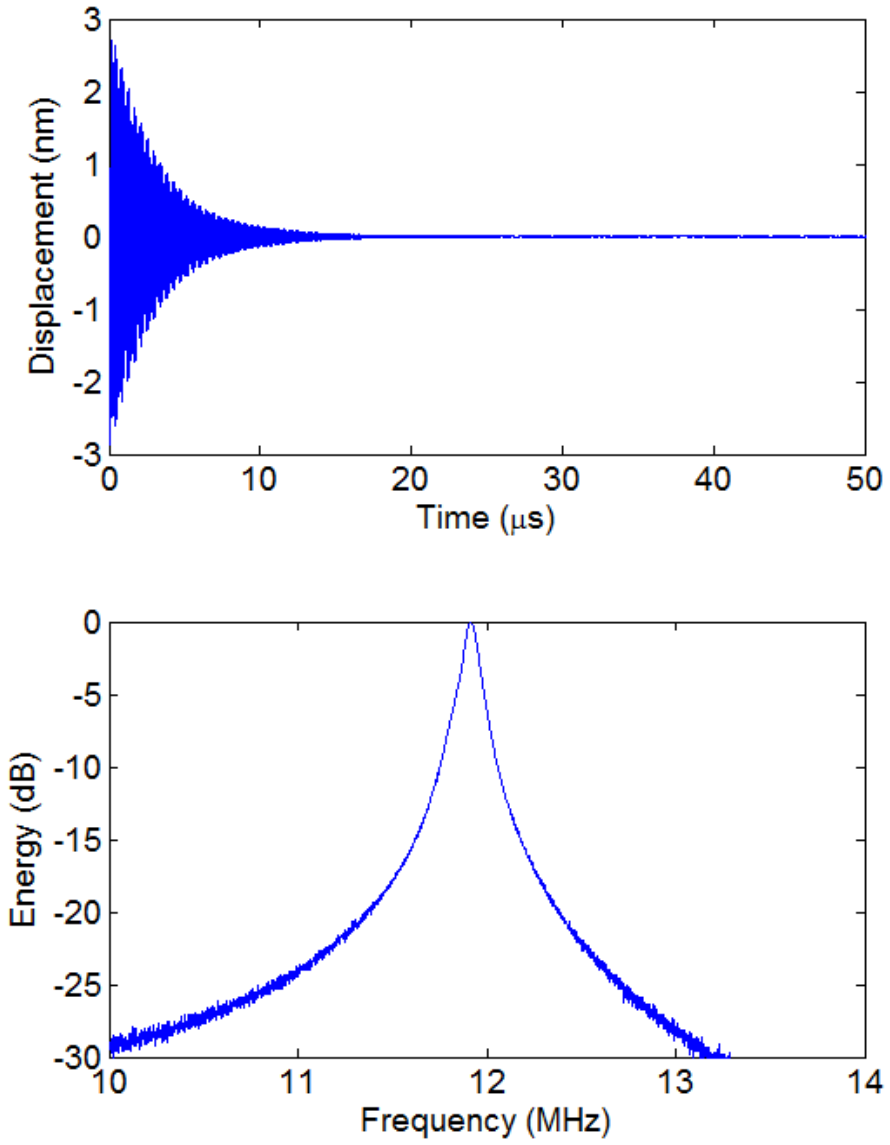

Figure B.5 Experimental displacement (top) and frequency spectra (bottom) of the center membrane in the grid after parylene is added to the array

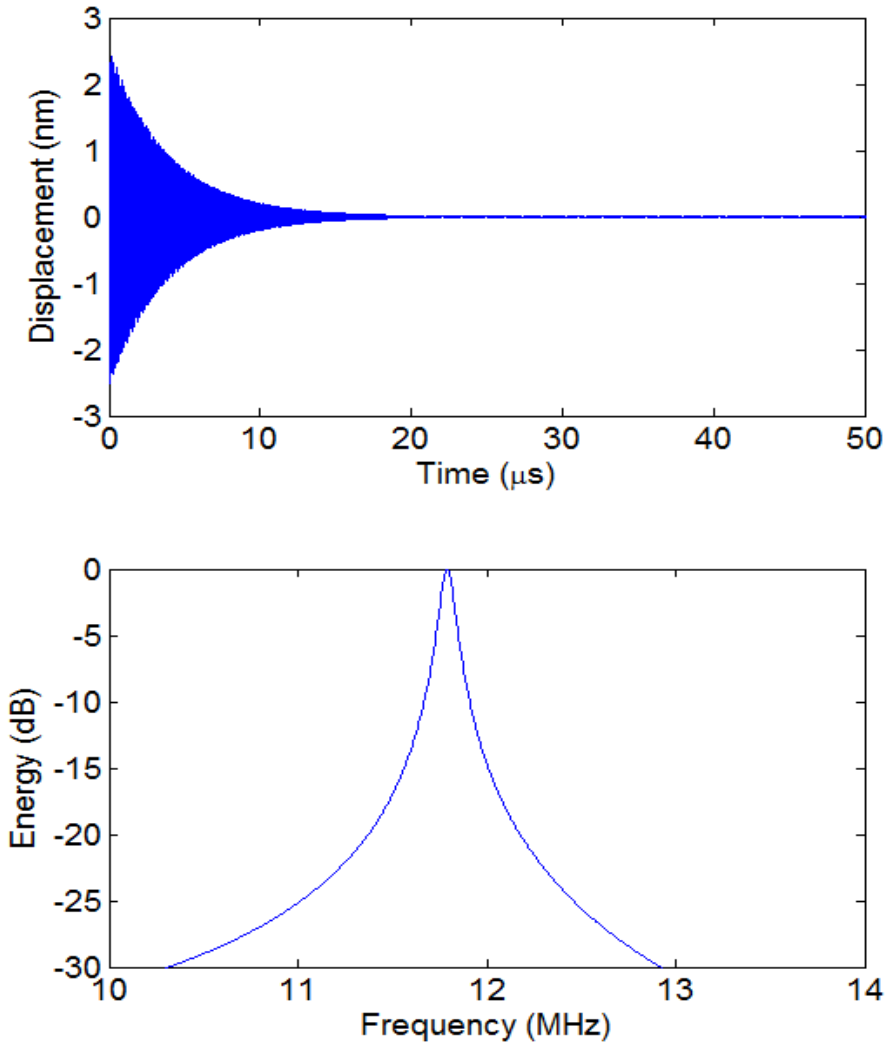

Figure B.6 Simulated displacement (top) and frequency spectra (bottom) of the center membrane in the grid obtained by altering the thickness of the membrane to achieve to proper natural frequency and using a damping factor of 2500 to match the attenuation.

APPENDIX C

FOCUSING BY SOLVING THE FORWARD FORCE BALANCE

Methods

The forcing of the exterior S/R membranes can be determined by a forward problem of the force balance equation used with the modeling. The forcing is given by

$$[K]\{u(t)\} + Z_R\{\dot{u}(t)\} + M\{\ddot{u}(t)\} = \{F(t)\}. \tag{Ap.1}$$

The system is composed of T membranes where N comprise the imaging grid (typically has been 49 a 7x7 grid) and M exterior membranes removed from the imaging grid (typically it has been 8 in a symmetric pattern). The ideal focus is give as

$$u(t) = \begin{bmatrix} 0 \\ \vdots \\ 0 \\ \delta(t) \\ 0 \\ \vdots \\ 0 \\ x_1 \\ \vdots \\ x_M \end{bmatrix} = \begin{bmatrix} \delta_{FM}(t) \\ \overrightarrow{x_m(t)} \end{bmatrix} \tag{Ap.2}$$

This vector states that all of the imaging grid's membranes have a 0 displacement at all time with the exception of the focal membrane which has a displacement of 1 at time equal to zero as denoted by the delta function. As for the exterior membranes their displacement is a variable denoted as x_m.

The forcing of the problem is also constrained as the majority of the imaging grid cannot be electrically controlled. Only the 8 exterior membranes of the emitting array can be forced. The constrained forcing vector is given as follows:

$$\{F(t)\} = \begin{bmatrix} \begin{bmatrix} 0 \\ \vdots \\ 0 \end{bmatrix} \\ f_1(t) \\ \vdots \\ f_M(t) \end{bmatrix} = \begin{bmatrix} \vec{0} \\ \overrightarrow{f_M(t)} \end{bmatrix} \tag{Ap.3}$$

The system matrix is denoted as A and is fully defined from the stiffness, mass, and coupling of all the membranes. Hence the matrix problem with 2*M unknowns is shown in the condensed formulation of the problem.

$$A * \begin{bmatrix} \delta_{FM}(t) \\ \overrightarrow{x_m(t)} \end{bmatrix} = \begin{bmatrix} \vec{0} \\ \overrightarrow{f_M(t)} \end{bmatrix} \tag{Ap.4}$$

Notice that there are M unknowns in the displacement vector and M unknowns in the forcing vector. The steps to solve this problem are as follows:

Step 1: Multiply out the $A * \begin{bmatrix} \delta_{FM}(t) \\ \overrightarrow{x_m(t)} \end{bmatrix}$

$$A * \begin{bmatrix} \delta_{FM}(t) \\ \overrightarrow{x_m(t)} \end{bmatrix} = \delta(t)\, A_{(:,FM)} + A_{(:,N+1:T)} \overrightarrow{x_m(t)} \tag{Ap.5}$$

which results with

$$\delta(t)\, A_{(:,FM)} + A_{(:,N+1:T)} \overrightarrow{x_m(t)} = \begin{bmatrix} \vec{0} \\ \overrightarrow{f_M(t)} \end{bmatrix} \tag{Ap.6}$$

which still has unknown on both sides of the equation. This matrix problem can be solved by two separate problems by taking the top N rows as one problem and then rows (N+1 to T) as the second problem.

The first part is the first N rows:

$$\delta(t)\, A_{(1:N,FM)} + A_{(1:N,N+1:T)}\overrightarrow{x_m(t)} = \left[\vec{0}\right] \tag{Ap.7}$$

Notice that the problem is now reduced to only one unknown $\overrightarrow{x_m(t)}$. This can now be solved by an inverse problem.

$$A_{(1:N,N+1:T)}\overrightarrow{x_m(t)} = -1 * \delta(t)\, A_{(1:N,FM)} \tag{Ap.8}$$

Since N>M this becomes a least squares solutions for $\overrightarrow{x_m(t)}$. Then the least squares solution to $\overrightarrow{x_m(t)}$ can be used in the second half of the problem to solve for the forcing.

$$\delta(t)\, A_{(N+1:T,FM)} + A_{(N+1:T,N+1:T)}\overrightarrow{x_m(t)} = \left[\overrightarrow{f_M(t)}\right] \tag{Ap.9}$$

A simple plug and chug of the values gives the forcing of the M exterior membranes. An example of the this method focusing is shown in Fig. C.1. Notice that indeed the energy is focused to the center membrane, but there is also a lot of energy on the other membranes which is a result of the least squares solution to the inverse problem. Besides the side lobe levels, there are other issues with this method of focusing.

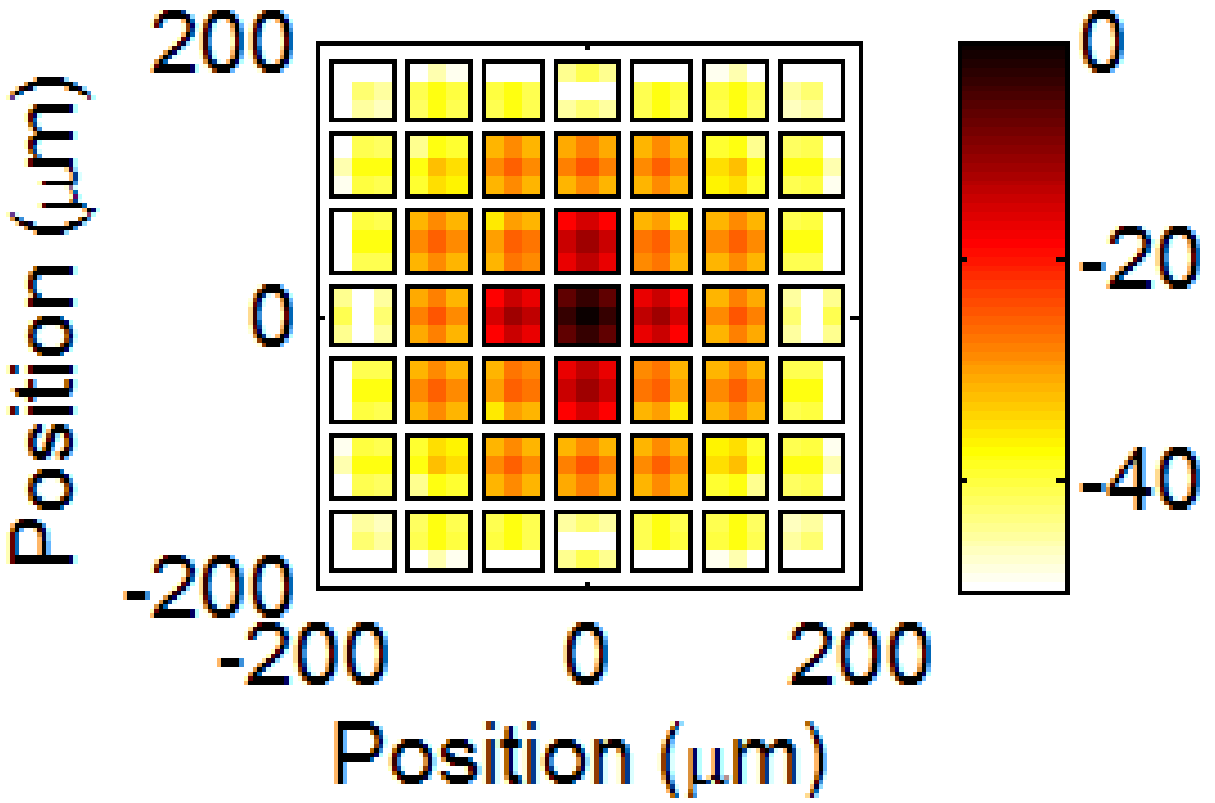

Figure C.5 Focusing to the center membrane by solving the forward force balance equation.

Complications with Implementation of Method

The issues that arise from the least square solution come from unrealistic signals. The first arises since the least square solution is solved in the frequency domain for one frequency at a time. This means that there is no constraint on the continuity from one frequency to another which is unrealistic. This issue can be seen in Fig. C.2-C.3. Figure C.2 is the displacement of the center membrane from the focusing over time. Notice that the focus is very narrow in time. The displacement signal also appears to be very noisy. This should not be a noisy signal since it is obtained through simulations. The noise comes from high spectral peaks as seen in Fig. C.3 which is the frequency content of Fig. C.2. The spectrum is very noisy with many small spectral spikes. These narrow features in the frequency domain result in noise in the time domain when the inverse Fourier transform is performed by causing the signals to wrap around the total

recording time. The best way to solve this problem is to solve all frequencies at the same time and force the result to be smooth, but this problem becomes too large to efficiently compute with the current resources.

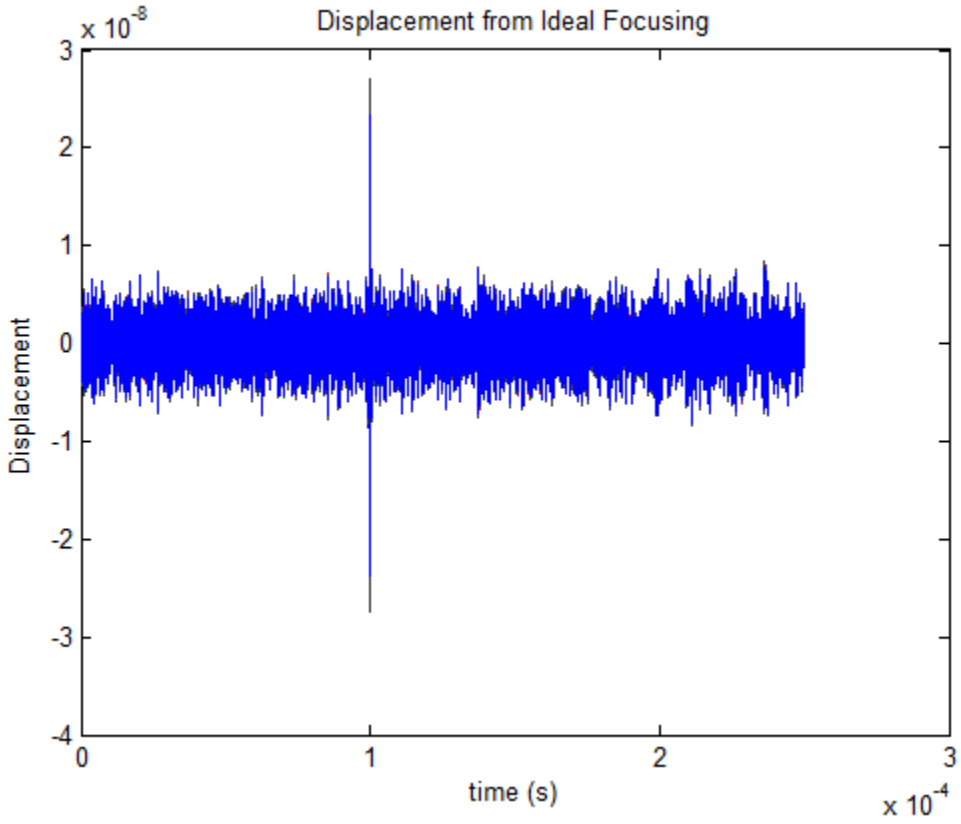

Figure C.6 Displacement of the focal membrane in time obtained by taking an inverse Fourier transform of Fig. C.3 which is the output of the least squares solution to the focusing.

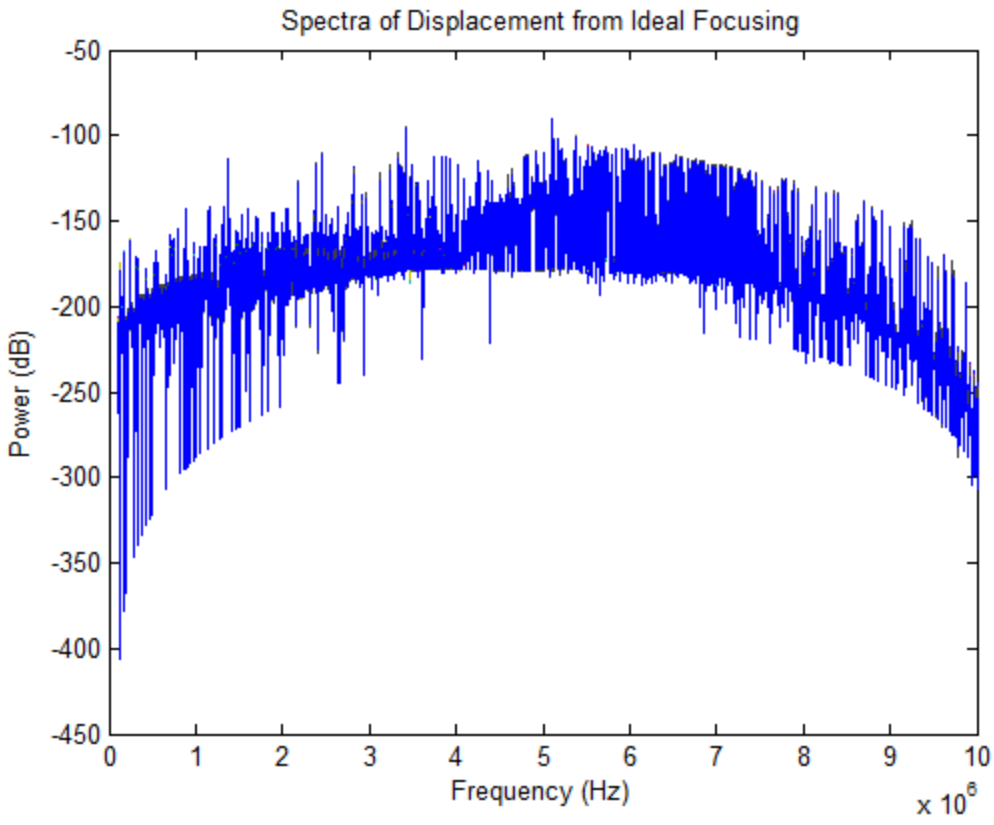

Figure C.7 Solution of the displacement of the focal membrane in the frequency domain. The sharp spectral peak cause unwanted signals in the time domain when an inverse Fourier transform is performed to obtain Fig. C.2.

Another issue with the least square solver for focusing is that there is no constraint on the energy or amplitude of the signals. Hence unrealistic signals can be realized in the frequency domain, but in reality these values cannot be applied as the effective displacement would be much larger than the gap between the membranes. As an example, the required displacements to be transmitted by the elements of the emitting array are shown in Fig. C.4. First of all notice that these signals are again wrapping around as a result of the inverse Fourier transform from the frequency domain. Also the required displacements on the membranes are on the order of hundreds of meters which is not possible. These membranes typically have a gap and maximum swing on the order of tens to hundreds of nanometers.

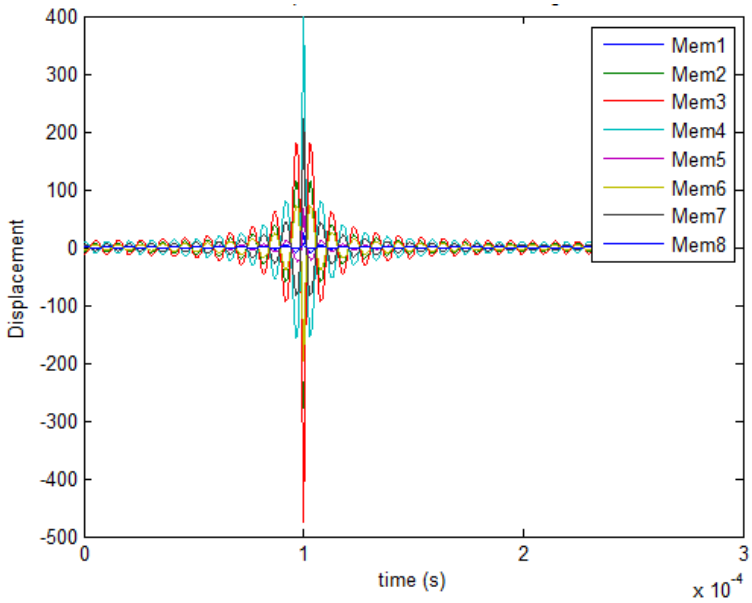

Figure C.8 Focusing signals of the emitting array to obtain the focus seen in Fig. C.1.

While this method of focusing is not a feasible option for this study it is presented so that in the future if the entire problem can be solved with all of its constraints it would be a direct and more suitable focusing method. The constraints include (1) acceptable forcing of emitting array elements with displacements less than the gap of the membranes (2) frequency response should be smooth to avoid processing artifacts when performing the inverse Fourier transform. This would require the least squares problem to solve all frequencies at one time which at this point is not feasible.

APPENDIX D

MODAL DECOMPOSITION OF FOCUSING RESULTS

This section examines the modes of the 7x7 grid of membranes and how they influence the focusing. The mode shapes, as described earlier, were obtained by solving a quadratic eigenvalue problem by using a Taylor expansion for narrow frequency ranges [27, 67].

$$[K + i\omega Z_R(\omega) - \omega^2 M]\{x\} = 0 \tag{Ap.10}$$

Two example modes were presented in section 4.2.1 along with their wavenumber-wavenumber plots. Table D.1 lists all 49 modes with their resonant frequency and quality factor. The mode listed in are sorted by their resonant frequency as opposed to their quality factors as was done before with Table 4.2. Notice that due to the symmetry of the array there are quite a few modes that occur at the same resonant frequency. Similar to the results of the small linear array the modes with the highest quality factor corresponded to the modes with the highest wavenumbers. Often these corresponded to the higher resonant frequencies as well but not necessarily always the case.

These modes create a set of vectors that can be used to decompose any spatial shape on the grid of membranes. To examine the effects of the different focusing methods and see how it correlats with the modes, $\tilde{X}_n$, a modal projection was done for the simulated focusing to the center membrane and the 13th membrane.

$$MW_n = \tilde{X}_n * u(t_f) \tag{Ap.11}$$

where an inner product is taken between $\tilde{X}_n$, the eigenvector of the nth mode, and $u(t_f)$, the displacement of each membrane at the focal time. The result is the modal weights of MW_n.

Table D.2 The 49 modes of the metasurface with their resonant frequency and quality factor

Mode Number	Resonant Frequency (MHz)	Quality Factor	Mode Number	Resonant Frequency (MHz)	Quality Factor
1	7.166	70574	**26**	6.568	53
2	7.125	16922	**27**	6.568	53
3	7.125	24188	**28**	6.483	38
4	7.070	3941	**29**	6.443	51
5	7.062	2887	**30**	6.374	39
6	7.062	6045	**31**	6.279	23
7	6.983	805	**32**	6.279	23
8	6.984	5196	**33**	6.150	16
9	6.984	5196	**34**	6.142	16
10	6.984	708	**35**	6.024	15
11	6.906	520	**36**	6.024	15
12	6.904	768	**37**	5.739	8
13	6.850	432	**38**	5.670	0
14	6.870	206	**39**	5.670	7
15	6.836	350	**40**	5.486	6
16	6.870	976	**41**	5.483	5
17	6.836	366	**42**	5.483	5
18	6.789	262	**43**	4.979	3
19	6.789	272	**44**	4.979	3
20	6.748	124	**45**	4.675	2
21	6.748	123	**46**	4.658	2
22	6.644	71	**47**	4.294	1
23	6.668	123	**48**	3.876	1
24	6.640	75	**49**	3.876	1
25	6.668	123			

Figure D.1 shows the normalized displacement of the 49 membranes at the focal time for different focusing methods as presented in section 6.3.1. The ideal focus is at the center membrane and is also shown. These displacements at the focal time $u(t_f)$, are projected onto

the 49 eigenvectors, $\tilde{X}_n$, or the mode shapes to obtain the modal weights which are presented in Fig. D.2. Notice that there are 14 modes that have significant amplitude and are important for focusing. These modes are not grouped in any particular frequency band. Hence, it is apparent to have an optimal focusing it is important to be able to control the modes at all frequencies. Similar results are shown for the focusing to the 13th membrane in Fig. D.3-D.4. Notice that focusing to the 13th membrane does not require the same modal weights. In fact it appears that more modes need to be controlled for the focusing to the 13th membrane. This may be one of the reasons why the focusing to the 13th membrane has a higher side lobe structure than the focus to the center membrane.

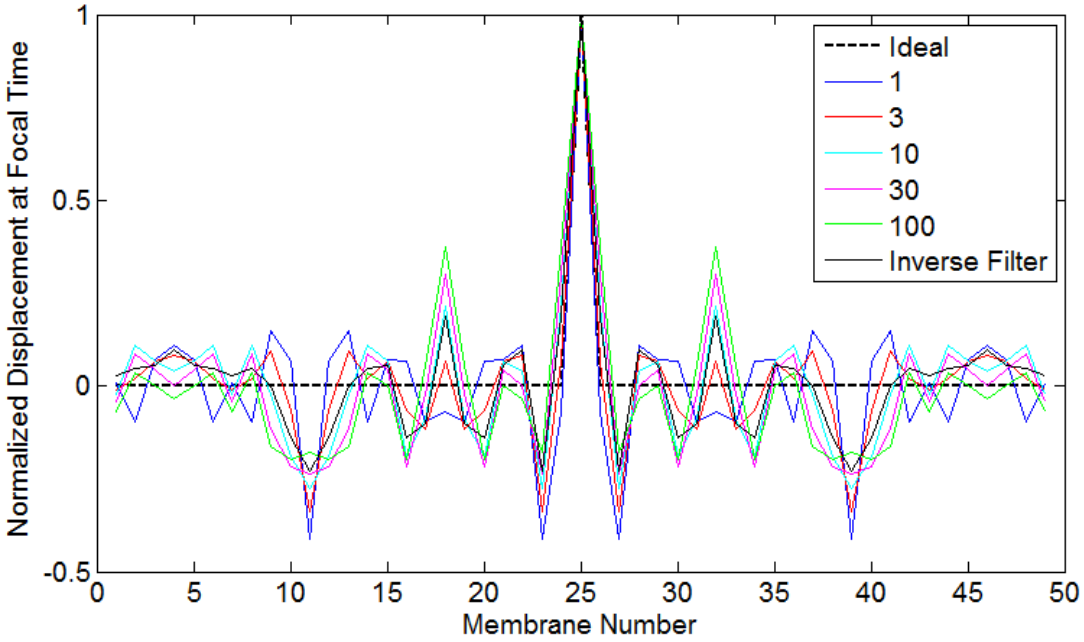

Figure D.5 Normalized displacement of the 49 membranes at the focal time (t_f) for different focusing methods compared to the ideal case which is 1 at the focal membrane (25, center) and 0 on all other membranes.

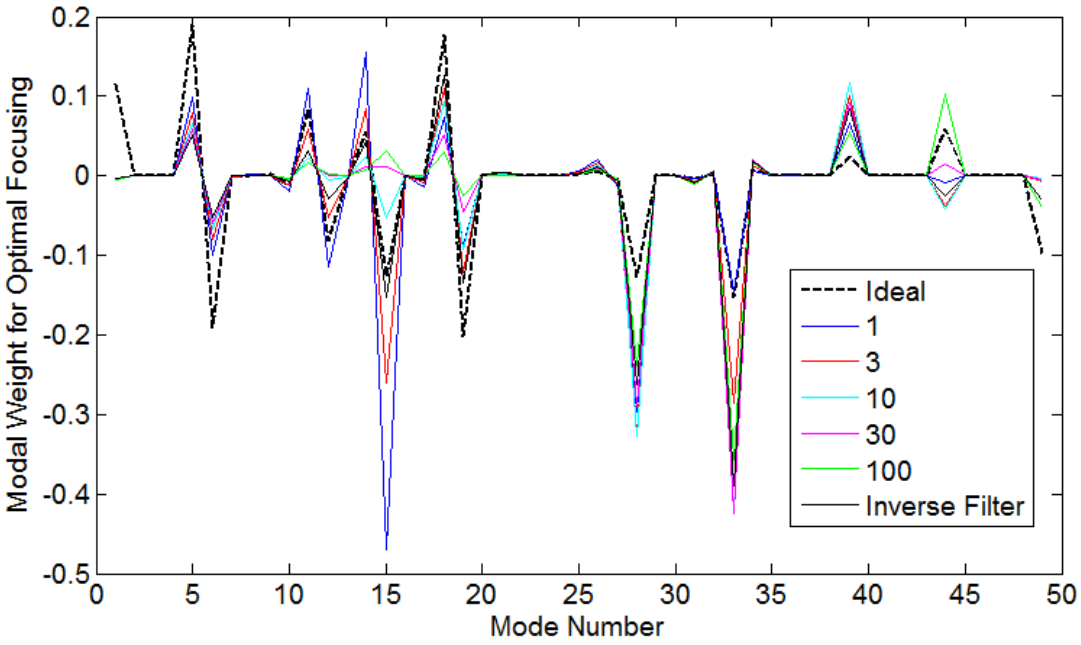

Figure D.6 Modal amplitudes (MW_n) of the 49 modes as obtained by Eq. D.2.

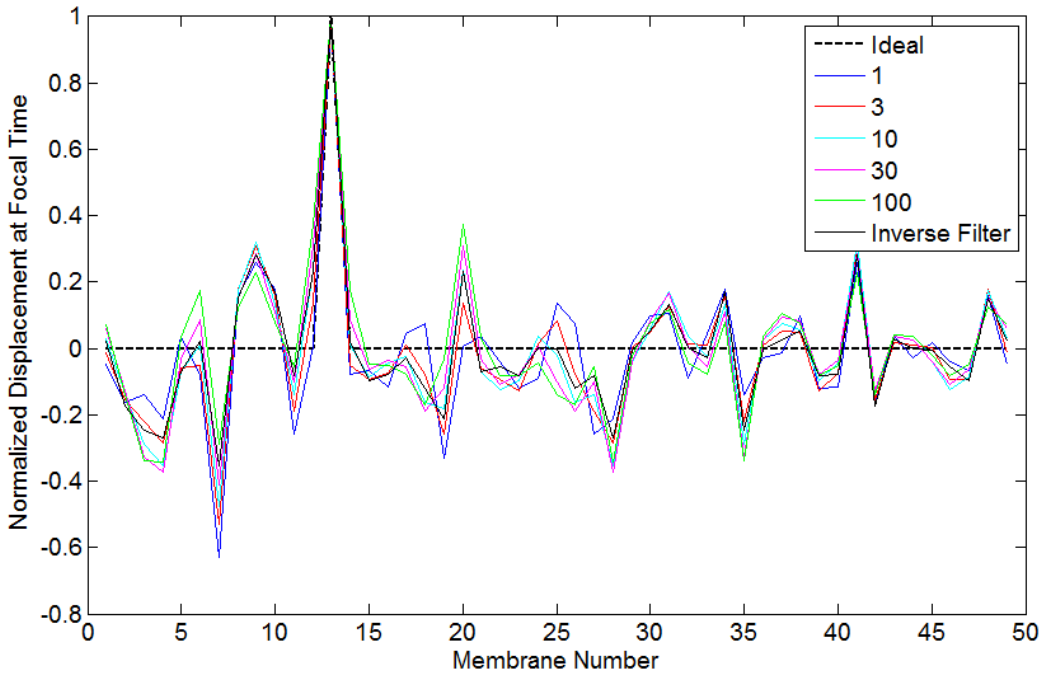

Figure D.7 Normalized displacement of the 49 membranes at the focal time (t_f) for different focusing methods compared to the ideal case which is 1 at the focal membrane (13^{th} membrane) and 0 on all other membranes.

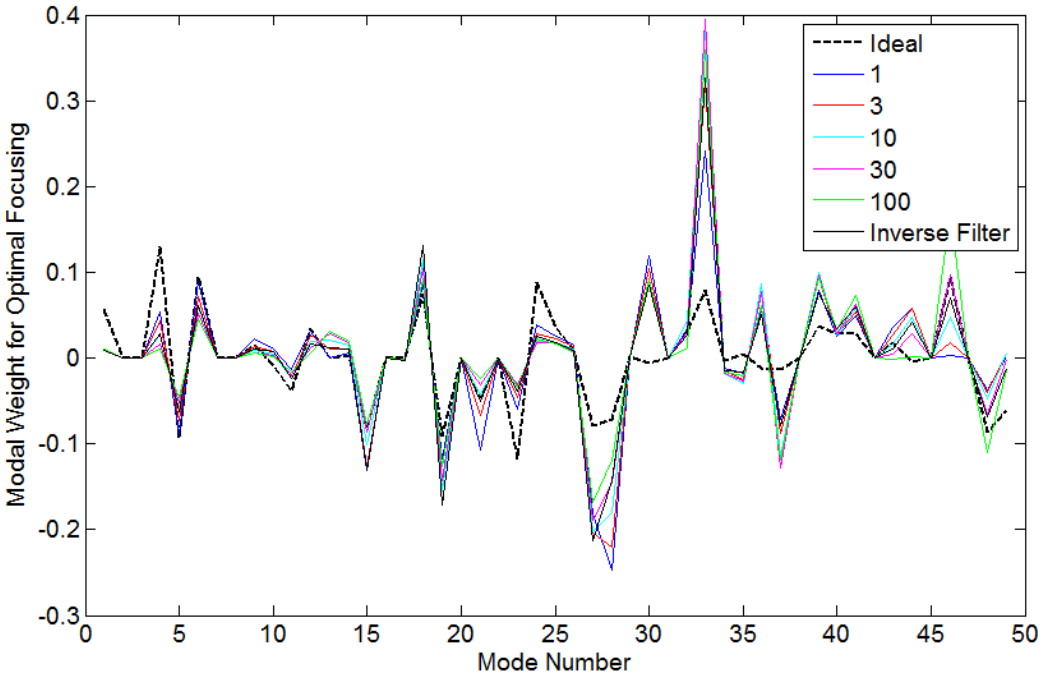

Figure D.8 Modal amplitudes (MW_n) of the 49 modes as obtained by Eq. D.2.

This section shows modes of the 7x7 structure and uses them to decompose the focal fields. The insight that this decomposition gives is that for optimal focusing many modes are needed to be controlled from the exterior emitting array. With only 8 elements in the emitting array it can be difficult to independently excite the 49 modes of the structure and achieve the best focusing. The ideal situation would be that the 49 membranes were all electrically controlled and hence each of the modes could be independently controlled leading to the best focus possible.

APPENDIX E

LASER DOPPLER VIBROMETER WALK THROUGH

This walkthrough goes through the steps required to capture data from the laser Doppler vibrometer recording the displacement of the membranes in the metasurface. The walkthrough consist of three parts. (1) setting up the physical experimental setup (2) Aligning the axes of the stage to that of the membrane metasurface and (3) running the tests. Several instruments were connected and controlled by a computer through MATLAB and GPIB interface. The codes required to communicate through MATLAB are also included.

Experimental Setup

- Install laser head to coupling plate with 2 M6 bolts as shown in the following Figure. The laser should be mounted so that it is pointed directly towards the floor. The use of a carpenter's square can facilitate that the laser is indeed normal to the surface.

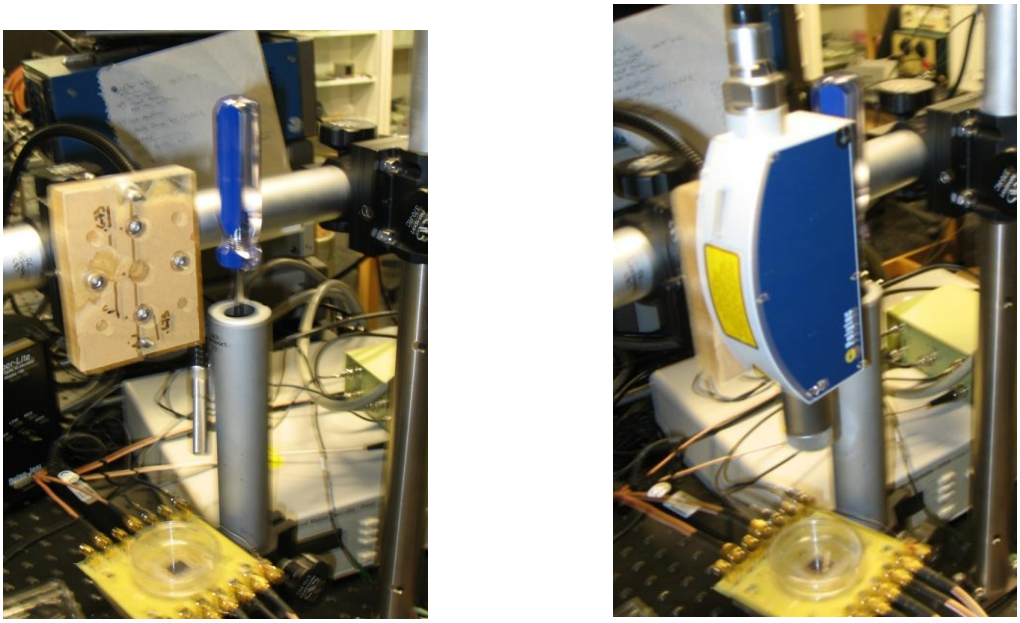

Figure E.9Attach the laser head to the coupling plate with 2 M6 bolts

- Turn on the laser by first turning the key in the controller box and then pressing the yellow button on the laser power unit, both shown in the following figure.

Figure E.10 Laser controller on left with the power key in the lower left. The right box is the laser power supply which is toggled by the yellow button.

- Attach the 10x microscope objective. To do this, loosen the set screw as shown in the following figure. Then focus the laser to infinity by twisting the lens at the tip of the laser until the beam is fully collimated. This means that the beam width should be constant for any standoff distance. Then tighten the set screw and install the 10x microscope objective by screwing it onto the laser head. The addition of the 10x objective allows the focal spot to be as small as 3μm in diameter.

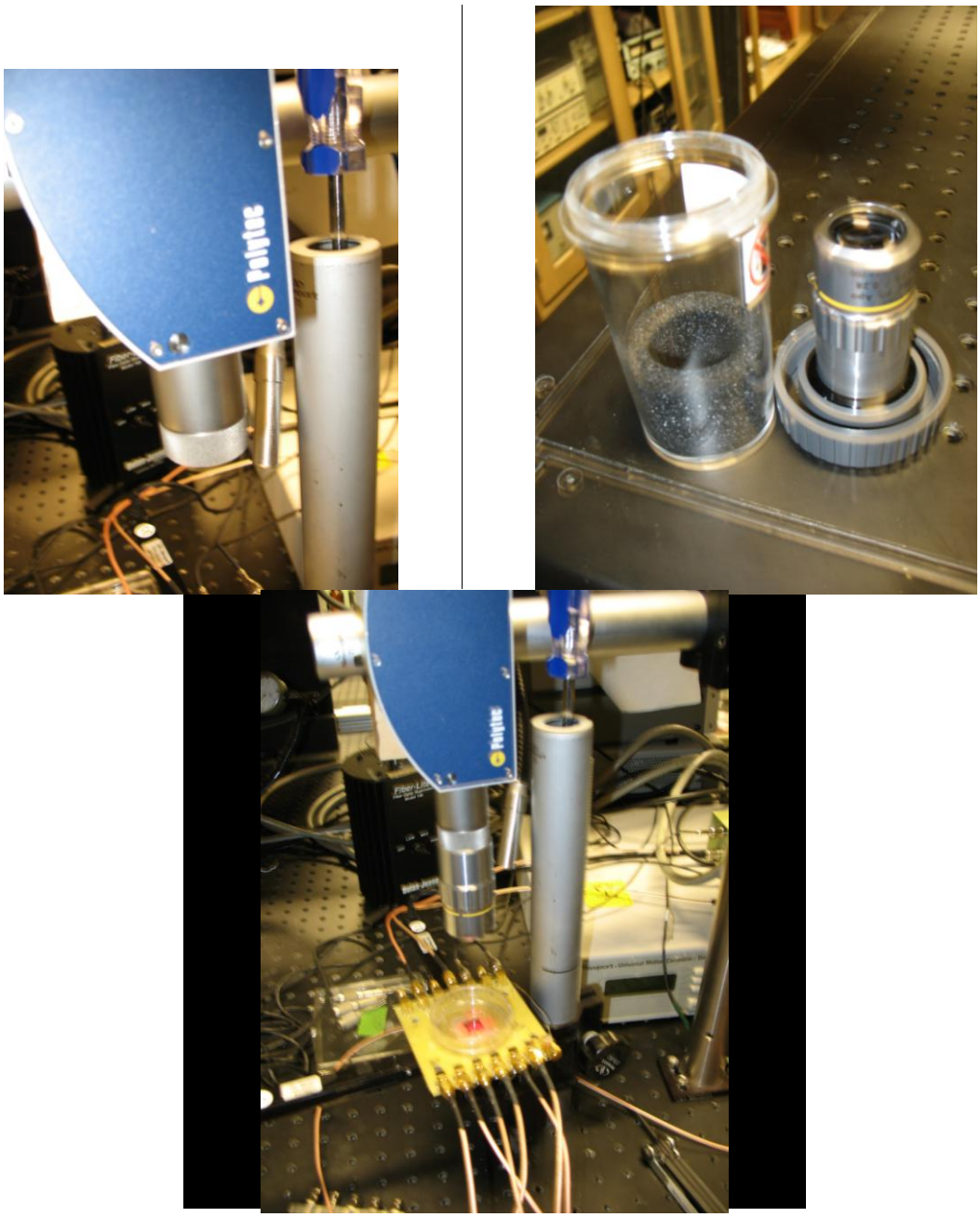

Figure E.11 (upper left) laser without the microscope objective and the set screw positioned above the Polytech logo on the blue face of the laser head. (upper right) microscope objective and its holder (lower) laser with the microscope objective attached.

- With the laser on, adjust the height of the XY stage so that it is roughly in focus. The standoff distance with the 10x microscope objective is 3.7cm.
- Install the CMUT onto the XY stage by use of the coupling plate.

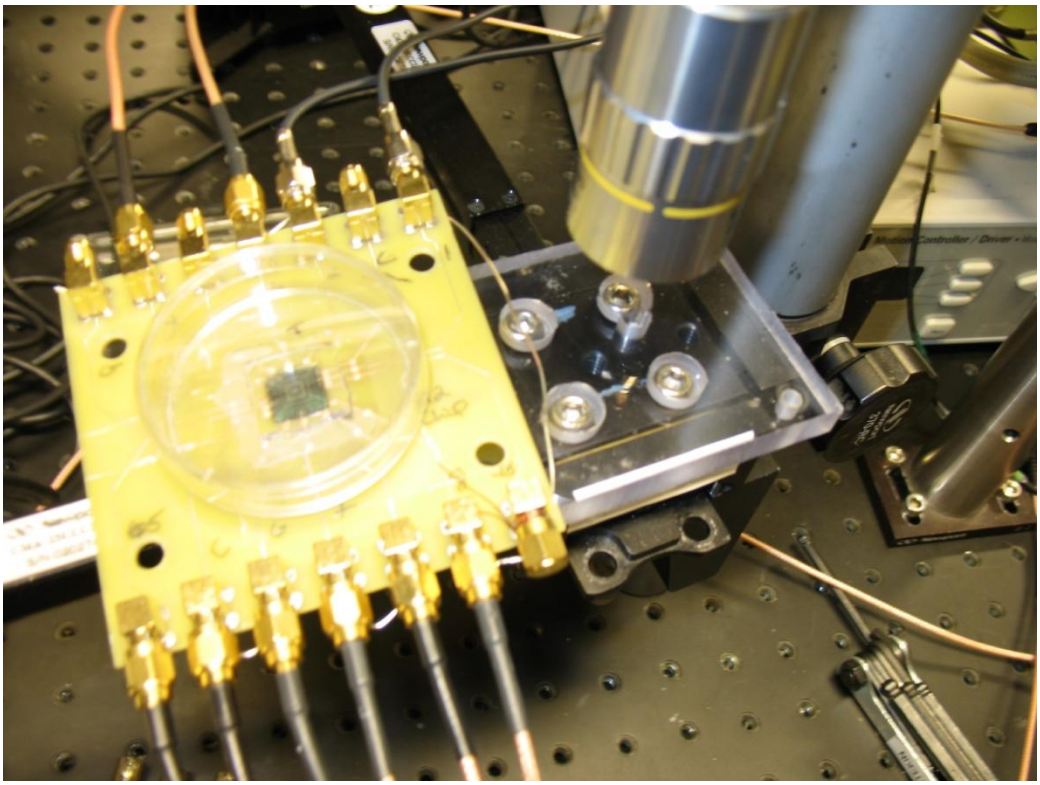

Figure E.12 CMUT attached to the printed control board resting on the left side of the acrylic coupling plate which is anchored to the XY stage.

- Connect all electrical connections that will be used. Any altering of the setup will require additional alignment or calibration.

Align the Membrane Metasurface to the XY Axes

- Using the Z axis of the stage focus the laser so that it is focused to its optimal spot size with visual verification by using a stereomicroscope.
- Use the linear motorized actuators to control the X and Y axis movement and position the primary membrane (center membrane of grid) at the laser focus.
- Readjust the Z axis focus if necessary
- Now since it is hard to visually see the location of the laser focus on the membrane, the maximum of the membrane will be found by pulsing the membrane scanning in the X

and Y directions to find the maximum displacement which corresponds to the center of the membrane.

- Clear the position of the motorized actuators so that the current position is 0mm in the X direction and 0mm in the Y direction.
- Electrically pulse the primary membrane
- Run the code MaxSearchCourse.mat using the initial positions of x=0 and y=0. This code scans the membrane in the X and Y directions by using the MATLAB code mcset.mat to communicate with the motorized actuators. The signals are captured through the oscilloscope by the MATLAB code scopesaveAVG1024.mat. These codes are listed later in this section for future use.
- The results of running the MaxSearchCourse.mat will give an image with each pixel denoting the maximum displacement at that position. If higher resolution is need the code can be altered for smaller step sizes, but at the cost of time to run the scan.
- The location with the highest displacement is set as the new origin. To do this move the position of the array to the position of the highest displacement. Then once again clear the position by using the controls on the controller of the motorized actuators. This now sets the origin.
- If water is to be used, add it now
- Since water has a difference refractive index the standoff distance will have changed. so the array needs to be refocused in the z direction. The optical method that was used in the prior steps cannot be replicated because of the poor viewing quality of the stereomicroscope through the water at an offset angle. To refocus the Z position, use the

noise floor of the oscilloscope to determine the proper standoff. The noise floor will be a minimum when the laser is in focus.

- Repeat the previous steps to align the origin membrane.
- The next step is to find the center of another membrane. By knowing the positions of two membranes in the membrane array it is possible to use a rotational transformation from the XY stage to the membrane array so that the correct coordinates input to the motorized linear actuators will position the array so that the laser is focusing on the proper membrane.

Perform Experiments

Now that the membrane array is aligned with regard to the XY stage it is possible to use the linear motorized actuators to move the laser focus to any particular membrane. This allows to the actual experiments to be performed. However, while the experiments are in process there are several points that should be considered.

- When using water, evaporation will eventually influence the measurements by effecting the focal standoff distance. Hence the Z axis should be recalibrated every two hours to ensure optimal focus.
- The linear stages are accurate for smaller than micron resolution. However, the XY stage can stick at time or backlash may be present in the system. Hence it is good practice to realign the membrane array to the XY stage every 2 hours.

MATLAB Codes

Alignment Script

```
xorig=0;
yorig=0;
```

```
%Find the Maximum of the First Active Membrane
[newxorig, newyorig, indxmax, indxnoise]= MaxSearchCourse(xorig,yorig);
[newxorig, newyorig, indxmax, indxnoise]= MaxSearchCourse(newxorig,newyorig);
%Move to where the maximum displacement was measured
mcset(newxorig, newyorig,0)
%Rezero the motorized actuators controller to x=0 y=0
%Repeat the above block if water is being added on top of the array (after
%refocusing the z-axis by using the noise)

%Set the position of the second active membrane to be tested
xorig=0;
yorig=0+.385;
mcset(xorig,yorig);
%Find the Maximum of the Second Active Membrane
[newxorig, newyorig, indxmax, indxnoise]= MaxSearchCourse(xorig,yorig);
%Set the coordinates of the Second Active Membrane
mem1x=newxorig;
mem1y=newyorig;

%Calculate the rotational paramters between the axes of the actuators and
%the CMUT array
r1=sqrt(mem1x^2+mem1y^2);
%r2=sqrt(x2^2+y2^2);
tan1=atan(mem1x/mem1y);
%tan2=asin(x2/y2);
actualang=0;
angleoffset=tan1*180/pi-actualang;
angleoffsetrad=deg2rad(angleoffset);
```

MaxSearchCourse.mat

```
function [newxorig, newyorig, indxmax, indxnoise]=
MaxSearchCourse(xorig,yorig)

mcset(xorig,yorig,0)        %move to origin
xstep=-15e-3:5e-3:15e-3;    %setup the step sizes and areas to scan
ystep=-15e-3:5e-3:15e-3;
for xx=1:length(xstep)
    xmove=xstep(xx);
    for yy=1:length(xstep)
        ymove=ystep(yy);
        %On first iteration find the window of the signal and the noise
        if xx==1 && yy==1
            [t,data]=scopesaveAVG1024(2,10);    %capture the pulse data from
Function Generator
            [t2,data2]=scopesaveAVG1024(3,10);  %capture the displacement
from the LDV with 10 averages
            figure;subplot(2,1,1)
            plot(t,data)
            subplot(2,1,2)
            plot(t2,data2)
            [gx, gy]=ginput(4);
            indxmax=find(t>=gx(1) & t<=gx(2));
            indxnoise=find(t>=gx(3) & t<=gx(4));
            mcset(xorig+xmove,yorig+ymove,0)
```

```
        end
        mcset(xorig+xmove,yorig+ymove,0)

        pause(3) %give the actuators enough time to move to the new membrane
location
        try
            [t,data]=scopesaveAVG1024(3,100); %capture the displacement from
the LDV with 100 averages
        catch
            [t,data]=scopesaveAVG1024(3,100);
        end
        signalPeak=max(abs(data(indxmax)));
        noisestd=std(data(indxnoise));
        SNRMat(xx,yy)=signalPeak/noisestd;  %calculate the peak to noise
ratio
    end
end
%Plot the SNR over the scan area to ensure the max displacement was properly
found
figure
imagesc(xstep,ystep,SNRMat)
[ii jj]=find(max(max(SNRMat))==SNRMat);
newxorig=xorig+xstep(ii);
newyorig=yorig+ystep(jj);
```

scopesaveAVG1024.mat

```
function [myt,data]=scopesaveAVG1024(ch,numav)
% this codes samples the var(ch) first with 100 averages, determines the
% maximum signal amplitude then resamples the signal for var(numav) times
% with the best possible scale to ensure best A to D conversion

scope = gpib('ni', 0, 1);
set(scope,'InputBufferSize',160000);
set(scope,'Timeout',5);

try

    fopen(scope);

    fprintf(scope, 'Data:Encdg SRPbinary');
    fprintf(scope, 'Data:Width 2');
    %fprintf(scope, 'WFMInpre:BIT_Nr 16');
    fprintf(scope, 'WFMOutpre:BIT_Nr 16');
    % THIS LINE MAY NEED TO BE CHANGED IF THE SIGNAL IS NOT CAPTURED
    % PROPERLY. change LSB to MSB or vice versa
    fprintf(scope, 'WFMOutpre:BYT_OR LSB');
    %fprintf(scope, 'WFMOutpre:BYT_OR MSB');
    % Get a large view of signal to find the max and min
    fprintf(scope, ['Data:Source CH' num2str(ch)]);  %
    % Input the max scale you would expect for all signals
    fprintf(scope, ['CH' num2str(ch) ':SCAle 500e-3'])
    fprintf(scope, 'ACQuire:MODe AVErage')
    fprintf(scope, 'ACQuire:NUMAVg 100')
    fprintf(scope, 'ACQuire:STOPAfter SEQuence')
```

```
    fprintf(scope, 'ACQuire:STATE RUN')
    fprintf(scope, 'HORizontal:ACQLENGTH?')
    num_of_pts=str2num(fscanf(scope));
    %num_of_pts=10000;


    pause(1)
    fprintf(scope, 'ACQuire:NUMACq?');
    num_of_acq=str2num(fscanf(scope));
    while num_of_acq<100
        pause(1)
        fprintf(scope, 'ACQuire:NUMACq?');
        num_of_acq=str2num(fscanf(scope));
    end


    cur_stop=0;
    fprintf(scope, ['Data:Start ' num2str(cur_stop+1)]);
    fprintf(scope, ['Data:Stop ' num2str(cur_stop+num_of_pts+3)]);
    fprintf(scope, 'CURVE?');
    trash = fread(scope, 3, 'uint16');
    datatest= [fread(scope, num_of_pts, 'uint16')];
    %cur_stop=cur_stop+2000;


    fprintf(scope, 'WFMPre:YMult?');
    ymult = fscanf(scope);
    fprintf(scope, 'WFMPre:YOff?');
    yoff = fscanf(scope);
    fprintf(scope, 'WFMPre:YZEro?');
    yzero = fscanf(scope);
    yoff=str2num(yoff);
    yzero=str2num(yzero);
    ymult=str2num(ymult);
    %calculate data and limiting value and the new division
    datatest = (datatest - mean(datatest(2:end))) * ymult + yzero;
%     figure
%     plot(datatest)
    maxdata=max(datatest);
    mindata=max(datatest*-1);
    limval=max(maxdata,mindata);
    possiblediv=[1e-3 2e-3 5e-3 10e-3 20e-3 50e-3 100e-3];
    newdiv=find(limval/5<possiblediv,1);

    fprintf(scope, ['CH' num2str(ch) ':SCAle ' num2str(possiblediv(newdiv))])
    fprintf(scope, 'ACQuire:MODe AVErage')
    fprintf(scope, ['ACQuire:NUMAVg ' num2str(numav)])
    fprintf(scope, 'ACQuire:STOPAfter SEQuence')
    fprintf(scope, 'ACQuire:STATE RUN')
    fprintf(scope, 'HORizontal:ACQLENGTH?')
    num_of_pts=str2num(fscanf(scope));
    %num_of_pts=10000;
    fprintf(scope, 'HORizontal:MAIn:SAMPLERate?')
    samplingrate=str2num(fscanf(scope));
```

```
    pause(1)
    fprintf(scope, 'ACQuire:NUMACq?');
    num_of_acq=str2num(fscanf(scope));
    while num_of_acq<numav
        pause(1)
        fprintf(scope, 'ACQuire:NUMACq?');
        num_of_acq=str2num(fscanf(scope));
    end

    cur_stop=0;
    fprintf(scope, ['Data:Start ' num2str(cur_stop+1)]);
    fprintf(scope, ['Data:Stop ' num2str(cur_stop+num_of_pts+3)]);
    fprintf(scope, 'CURVE?');
    trash = fread(scope, 3, 'uint16');
    data= [fread(scope, num_of_pts, 'uint16')];
    fprintf(scope, 'WFMPre:YMult?');
    ymult = fscanf(scope);
    fprintf(scope, 'WFMPre:YOff?');
    yoff = fscanf(scope);
    fprintf(scope, 'WFMPre:YZEro?');
    yzero = fscanf(scope);
    yoff=str2num(yoff);
    yzero=str2num(yzero);
    ymult=str2num(ymult);

    N=length(data);
    myt=(0:(N-1))/samplingrate;
    %     data(1)

    data = (data - mean(data(2:end))) * ymult + yzero;



    fclose(scope);
    %     plot(myt,data)
catch ME
    'asdkjasdfa'
    fclose(scope);
end
```

mcset.mat

```
function mcset(c1,c2,c3)
%Moves the linear actuator c1=X direction c2=stage Y direction.  The values
%of ch1 and ch2 are in mm
mc = gpib('ni', 0, 6);
fopen(mc);
fprintf(mc,['1PA' num2str(c1)]);
fprintf(mc,['2PA' num2str(c2)]);
fclose(mc)
```

REFERENCES

[1] M. Ambati, N. Fang, C. Sun, and X. Zhang, "Surface resonant states and superlensing in acoustic metamaterials," Phys. Rev. B, **75**, 195447, (2007).

[2] A. Atalar, H. Koymen, H. K. Oguz, "Rayleigh-Bloch waves in CMUT arrays," Ultrasonics, Ferroelectrics and Frequency Control, IEEE Transactions on, **61**, 2139-2148, (2014).

[3] B. Bayram, M. Kupnik, G. G. Yaralioglu, O. Oralkan, A. S. Ergun, D. Lin, S. H. Wong, and B. T. Khuri-Yakub, "Finite Element Modeling and Experimental Characterization of Crosstalk in 1-D CMUT Arrays" Ultrasonics, Ferroelectrics and Frequency Control, IEEE Transactions on, **54**, 418-430, (2007).

[4] K. Bertoldi and M. C. Boyce, "Mechanically triggered transformations of phononic band gaps in periodic elastomeric structures," Phys. Rev. B, **77**, 052105, (2008)

[5] O. Brand, and H. Baltes, "Micromachined resonant sensors-an overview," Sensors Update, **4**, 3–51 (1998).

[6] B. Bonello, L Belliard, J. Pierre, J. O. Vasseur, B. Perrin, and O. Boyko, "Negative refraction of surface acoustic waves in the subgigahertz range," Phys. Rev. B, **82**, 104109, (2010).

[7] A. Boulme, D. Certon, N. Senegond, C. Meynier, F. Teston, "A strategy to predict and reduce baffle effects in linear array of CMUTs," in *Proceedings of the IEEE International Ultrasonics Symposium, San Diego, United States 2010*, (IEEE, 2010) p. 1873-1876.

[8] T. Brunet, J. Vasseur, B. Bonello, B. Djafari-Rouhani, and A. Hladky-Hennion, "Lamb waves in phononic crystal slabs with square or rectangular symmetries," J. Appl. Phys., **104**, 043506 (2008).

[9] B. Buttkus**,** *Spectral Analysis and Filter Theory in Applied Geophysics*, (Springer-Verlag, Berlin, 1991). Chapter 7.

[10] A. Caronti, A. Savoia, G. Caliano, M. Pappalardo, "Acoustic coupling in capacitive microfabricated ultrasonic transducers: modeling and experiments," Ultrasonics, Ferroelectrics and Frequency Control, IEEE Transactions on, **52**, 2220-2234, (2005).

[11] J. Christensen and F. J. Garcia de Abajo, "Acoustic field enhancement and subwavelength imaging by coupling to slap waveguide modes," Appl. Phys. Lett., **97**, 164103, (2010).

[12] J. Christensen, A. I. Fernandez-Domingues, F. De Leon-Perez, L Martin-Moreno, and F. J. Garcia-Vidal, "Collimation of sound assisted by acoustic surface waves," Nature Phys., **3**, 851-852, (2007).

[13] J. Christensen, and M. Willatzen, "Acoustic wave propagation and stochastic effects in metamaterial absorbers," Appl. Phys. Lett., **105**, 043508, (2014)

[14] J.-W. Choi and Y.-H. Kim, "Generation of an acoustically bright zone with an illuminated region using multiple sources," J. Acoust. Soc. Am., **111**, 1695-1700, (2002).

[15] L. Cohen, *Time Frequency Analysis: Theory and Applications*. (Prentice Hall PTR, 1995).
[16] F. Degertekin, R. Guldiken, and M. Karaman, "Annular-ring CMUT arrays for forward-looking IVUS: transducer characterization and imaging," Ultrasonics, Ferroelectrics and Frequency Control, IEEE Transactions on, **53**, 474 –482, (2006).
[17] K. Deng, Y. Ding, Z. He, H. Zhao, J. Shi, and Z. Liu, "Theoretical study of subwavelength imaging by acoustic metamaterial slabs," J. Appl. Phys., **105**, 124909, (2009).
[18] G. Derveaux, G. Papanicolaou, and C. Tsogka, "Time reversal imaging for sensor networks with optimal compensation in time," J. Acoust. Soc. Am., **121**, 2071-2085, (2007).
[19] P. A. Deymier, *Acoustic Metamaterials and Phononic Crystals*, (Springer, 2013).
[20] J. F. Dias, "An experimental investigation of the cross-coupling between elements of an acousitc imaging array transducer," Ultason. Imag., **4**, 44-55, (1982).
[21] Y. Ding, Z. Liu, C. Qiu, and J. Shi, "Metamaterial with simultaneously negative bulk modulus and mass density," Phys. Rev. Lett., **99**, 093904, (2007).
[22] P. -C. Eccardt, A. Lohfink, and H.-G. Garssen, "Analysis of crosstalk between fluid coupled CMUT membranes," *in Proceedings of the IEEE International Ultrasonics Symposium, Rotterdam, Netherlands 2005*, (IEEE, 2005) p. 593-596.
[23] P. -C. Eccardt, P. Wagner, and S. Hansen, "Analytical models for micromachined transducers -an overview," *in Proceedings of the IEEE International Ultrasonics Symposium, Vancouver, Canada 2006*, (IEEE, 2006) pp. 572 – 581.
[24] M. Fink and C. Prada, "Acoustic time-reversal mirrors," Inverse Probl. **17**, R1-R38, (2001).
[25] M. Fink, "Time-Reversed Acoustics," Scientific Amer. 91-97, (1999)
[26] K. Gatzwiller, K.B. Ginn, A. Betts, and S. Morel, "Practical aspect of successful laser Doppler vibrometry based measurements," *in Proceedings of IMAC-XXI: Conference & Exposition on Structural Dynamics Conference: 2003* pp.1-6
[27] J. H. Ginsberg, *Mechanical and Structural Vibrations*, (John Wiley & Sons, Inc., 2001).
[28] S. Guenneau, A. Movchan, G. Pétursson, and S. A. Ramakrishna, "Acoustic metamaterials for sound focusing and confinement," New J. Phys., **9**, 399, (200.
[29] G. Gurun, M. Hochman, P. Hasler, F. Degertekin, "Thermal-mechanical-noise-based CMUT characterization and sensing," Ultrasonics, Ferroelectrics and Frequency Control, IEEE Transactions on, **59**, 1267-1275, (2012).
[30] G. Gurun, P. Hasler and F.L. Degertekin, " Frontend Receiver Electronics for High Frequency Monolithic CMUT-on-CMOS Imaging Arrays," IEEE Trans. Ultrason. Ferroelectr. Freq. Control, IEEE Transactions on, **58**, 1658-1668, (2011).
[31] F. Gustafsson, *Adaptive filtering and change detection,* (Wiley, New York, 2000).
[32] P. Hauptmann, "Resonant sensors and application," Sens. Actuator A-Phys., **26,** 371-377, (1991).

[33] Z. He, H. Jia, C. Qiu, Y. Ye, R. Hao, M. Ke, and Z. Liu, "Nonleaky surface acoustic waves on a textured rigid surface," Phys. Rev. B, **83**, 132101, (2011).
[34] M. Hochman, "Investigation of acoustic crosstalk effects in CMUT arrays," M.S. thesis, Dept. Mech. Eng., Georgia Inst. of Tech., Atlanta, Georgia, (2010).
[35] K. Imamura, S. Tamura, "Negative refraction of phonons and acoustic lensing effect of a crystalline slab." Phys. Rev. B, **70**, 174308, (2004).
[36] H. Jia, M. Lu, X. Ni, M. Bao, and X. Li, "Subwavelength imaging through spoof surface acoustic waves on a two-dimensional structured rigid surface," Appl. Phys. Lett., **103**, 103505, (2013).
[37] X. Jin, O. Oralkan, F. L. Degertekin, B. T. Khuri-Yakub, "Characterization of one-dimensional capacitive micromachined ultrasonic transducer arrays," Ultrasonics, Ferroelectrics and Frequency Control, IEEE Transactions on, **48**, 750-760, (2001).
[38] L. Kelders, J. F. Allard, and W. Lauriks, "Ultrasonic surface waves above rectangular-groove gratings," J. Acoust. Soc. Am., **103**, 2730-2733, (1998).
[39] L. E. Kinsler, A. R. Frey, A. B. Coppens, and J. V. Sanders, *Fundamentals of Acoustics* (John Wiley & Sons, Inc. 2000).
[40] J. G. Knight and F. L. Degertekin, "Fabrication and characterization of cMUTs for forward looking intravascular ultrasound imaging," in *Proceedings of the IEEE International Ultrasonics Symposium, Munich, Germany 2002*, (IEEE, 2002) pp. 577-580.
[41] J. A. Kulpe, K. G. Sabra, M. J. Leamy, "Bloch-wave expansion technique for prediction wave reflection and transmission in two-dimensional phononic crystals," J. Acoust. Soc. Am., **135**, 1808-1819, (2014).
[42] W.A. Kuperman, W.S. Hodgkiss, H.C. Song, T. Akal, C. Ferla, and D.R. Jackson, "Phase conjugation in the ocean: Experimental demonstration of a time reversal mirror," J. Acoust. Soc. Am. **103**, 25-40 (1998).
[43] S. Lani, M. W. Rashid, J. Hasler, K. G. Sabra, and F. L. Degertekin, "Capacitive micromachined ultrasonic transducer arrays as tunable acoustic metamaterials," Appl. Phys. Lett., **104**, 051914, (2014).
[44] S. Lani, M. W. Rashid, K. G. Sabra, and F. L. Degertekin, "Investigation of slow evanescent waves at the surface of immersed micromachined membrane arrays," in *Proceedings of the IEEE International Ultrasonics Symposium, Prague, Czech Republic 2013*, (IEEE, 2013) p. 717–720.
[45] S. Lani, K. G. Sabra, and F. L. Degertekin, "Modal and transient analysis of membrane acoustic metasurfaces," J. Appl. Phys., **117**, 045308, (2015).
[46] F. Lemoult, G. Lerosey, J. de Rosny, and M. Fink, "Resonant Metalenses for Breaking the Diffraction Barrier," Phys. Rev. Lett. **104**, 203901, (2010).
[47] F. Lemoult, M. Fink, and G Lerosey, "Acoustic resonators for far-field control of sound on a subwavelength scale," Phys. Rev. Lett. **107**, 064301, (2011).

[48] J. Li, C. T. Chan, "Double-negative acoustic metamaterial," Phys. Rev. E, **70**, 055602, (2004).
[49] Z. Liang, M. Willatzen, J. Li, and J. Christensen, "Tunable acoustic double negativity metamaterial," Sci. Rep. **2**, 859, (2012).
[50] Z. Lin, X. Guo, J. Tu, J. Cheng, J. Wu, and D. Zhang, "Acoustic focusing of sub-wavelength scale achieved by multiple Fabry-Perot resonance effect," J. Appl. Phys., **115**, 104504, (2014).
[51] F. Liu, F. Cai, S. Peng, R. Hao, M. Ke, and Z. Liu, "Parallel acoustic near-field microscope: a steel slab with a periodic array of slits," Phys. Rev. E, **80**, 026603, (2009).
[52] M.-H. Lu, X. -K. Liu, L. Feng, J. Li, C. -P. Huang, Y. -F. Chen, Y. -Y. Zhu, S. -N. Zhu, and N. -B. Ming, "Extraordinary acoustic transmission through a 1D grating with very narrow apertures," Phys. Rev. Lett., **99**, 174301, (2007).
[53] G. Ma, M. Yang, S. Xiao, Z. Yang, and P. Sheng, "Acoustic metasurface with hybrid resonances," Nature Mater., (2014).
[54] C. Meynier, F. Teston, and D. Certon, "A multiscale model for array of capacitive micromachined ultrasonic transducers," J. Acoust. Soc. Am., **128**, 2549-2561, (2010).
[55] S Mohannadi, A. A. Eftekhar, A. Khelif, W. D. Hunt, and A. Adibi, "Evidence of large high frequency complete phononic band gaps in silicon phononic crystal plates," Appl. Phys. Lett., **92**, 221905, (2008).
[56] G. Montaldo, M. Tanter, and M. Fink, "Real time inverse filter focusing through iterative time reversal," J. Acoust. Soc. Am., **115**, 768-775, (2004).
[57] B. A. Munk, *Frequency Selective Surfaces*, (John Wiley & Sons, Inc., 2000).
[58] C. J. Naify, C.-M. Chang, G. McKnight, S. R. Nutt, "Scaling of membrane-type locally resonant acoustic metamaterial arrays," J. Acoust. Soc. Am., **132**, 2784-2792 (2012).
[59] A. Neice, "Methods and limitations of subwavelength imaging," Advances in Imaging and Electron Physics, **163**, 117-140 (2010).
[60] K. Park, H. J. Lee, P. Crisman, M. Kupnik, O. Oralkan, B. T. Khuri-Yakub, in *Proceedings of the IEEE International Ultrasonics Symposium, Beijing, China 2008*, (IEEE, 2008) p. 504-507.
[61] J. B. Pendry, "Negative refraction make a perfect lens," Phys. Rev. Lett., **85**, 3966-3969, (2000).
[62] C. Pierre, E.H. Dowell, "Localization of vibrations by structural irregularity," J. of Sound and Vib., **114,** 549–564, (1987).
[63] Polytech, "DD-300 24MHz displacement decoder," (www.polytec.com).
[64] Polytech, "OFV-534 compact sensor head," (www.polytec.com).
[65] R. Porter and D. V. Evans, "Rayleigh–Bloch surface waves along periodic gratings and their connection with trapped modes in waveguides" J. Fluid Mech. **386**, 233–258 (1999).
[66] A. Ronnekleiv, "CMUT array modeling through free acoustic CMUT modes and analysis of the fluid CMUT interface through Fourier transform methods," Ultrasonics, Ferroelectrics and Frequency Control, IEEE Transactions on, **52**, 2173-2184, (2005).

[67] A. Ruhe, "Algorithms for the nonlinear eigenvalue problem," SIAM J. Number. Anal., **10**, 674-688, (1973).
[68] S. Satir, J. Zahorian, and F. L. Degertekin, "Large-Signal Model for CMUT Arrays with Arbitrary Membrane Geometry Operating in Non-Collapsed Mode." Ultrasonics, Ferroelectrics and Frequency Control, IEEE Transactions on, **60**, 2426-2439, (2013).
[69] S. D. Senturia, *Microsystem Design*, (Springer, 2000).
[70] J. Q. Shen, "Strong and weak confinement of parity-time-symmetric acoustic surface wave," EPL, **105**, 17006, (2014).
[71] D. R. Smith, "How to build a superlens," Science, **308**, 502-503, (2005).
[72] H. Su, A. Zhou, X. Xu, and G. Hu, "Experimental study on acoustic subwavelength imaging of holey-structured metamaterials by resonant tunneling," J. Acoust. Soc. Am., **135**, 1686-1691, (2014).
[73] A. Sukhovich, B. Merheb, K. Muralidharan, J. O. Vasseur, Y. Pennec, P. A. Deymier, and J. H. Page " Experimental and Theoretical Evidence for Subwavelength Imaging in Phononic Crystals" Phys. Rev. Lett. **102**, 154301 (2009)
[74] A. Sukhovich, L. Jing. and J. H. Page, "Negative refraction and focusing of ultrasound in two-dimensional phononic crystals," Phys. Rev. B, **77**, 014301, (2008).
[75] M. Tanter, J.-F. Aubry, J. Gerber, J.-L. Thomas, and M. Fink, "Optical focusing by spatio-temporal inverse filter. I. Basic pricinples," J. Acoust. Soc. Am., **110**, 37-47, (2001).
[76] M. Tanter, J.-L. Thomas, and M. Fink, "Time reversal and the inverse filter," J. Acoust. Soc. Am. **108**, 223-234, (2000).
[77] M. Thranhardt, P.-C. Eccardt, H. Mooshofer, P. Hauptmann, F. L. Degertekin, "A resonant CMUT sensor for fluid applications," *Proceedings of IEEE Sensors Conf.* (IEEE, 2009), pp.878 -883.
[78] M. Thranhardt, P. -C. Eccardt, H. Mooshofer, and P. Hauptmann, "A resoanant CMUT-based fluid sensor: modeling and simulation," Sens. Actuator A-Phys., **156,** 191-195, (2009).
[79] H. Torun, K. K. Sarangapani, and F. L. Degertekin, "Spring constant tuning of active atomic force microscope probes using electrostatic spring softening effect," Appl. Phys. Lett., **91**, 253113, (2007).
[80] I. A. Veres, T. Berer, O. Matsuda, and P. Burgholzer, "Focusing and subwavelength imaging of surface acoustic waves in a solid-air phononic crystal," J. Appl. Phys., **112**, 053504, (2012).
[81] C. H. Wang, J. T. Rose, and F.-K. Chang, "A synthetic time-reversal imaging method for structural health monitoring," Smart Mater. Struct. **13,** 415-423, (2004).
[82] M. Wilm A. Reinhardt, V. Laude, R. Armati, W. Daniau, S. Ballandras,, Three-dimensional modelling of micromachined-ultrasonic-transducer arrays operating in water," Ultrasonics, **43**, 457-465, (2005).

[83] T. Wu, L. Wu, and Z. Huang, "Frequency band-gap measurement of two-dimensional air/silicon phononic crystals using layered slanted finger interdigital transducers," J. Appl. Phys., **97**, 094916, (2005).
[84] O. Wygant, M. Kupnik, J. C. Windsor, W. M. Wright, M. S. Wochner, G. G. Yaralioglu, M. F. Hamilton, B. T. Khuri-Yakub, Ultrasonics, Ferroelectrics, and Frequency Control, IEEE Transactions on, **56**, 193-203, (2009).
[85] T. Xu, C. Tekes, S. Satir, E. Arkan, M. Ghovanloo, and F. L. Degertekin, "Modeling and Characterization of a 35 MHz Linear CMUT Array" *in Proceedings of the IEEE International Ultrasonics Symposium, Prague, Czech Republic 2013,* (IEEE, 2013) p. 1987-1990.
[86] M. Yang, G. Ma, Z. Yang, and P. Sheng, "Coupled membranes with doubly negative mass density and bulk modulus," Phys. Rev. Lett., **110**, 134301, (2013).
[87] S. Yang, J. H. Page, A. Liu, M. L. Cowan, C. T. Chan, and P. Sheng, "Focusing of sound in a 3D phononic crystal," Phys. Rev. Lett., **93**, 024301, (2004).
[88] W. -X. Yang and P. W. Tse, "Development of an advanced noise reduction method for vibration analysis based on singular value decomposition," NDT & E International, **36**, 419-432 (2003).
[89] Y. Ye, M. Ke, Y. Li, T. Wang, and Z. Liu, "Focusing of spoof surface-acoustic-waves by a gradient-index structure," J. Appl. Phys., **114**, 154504, (2013).
[90] X. Zhang, Z. Liu, "Negative refraction of acoustic waves in two-dimensional phononic crystals." Appl. Phys. Lett., **85**, 341, (2004).
[91] Y. Zhang, J. Wen, Y. Xiao, X. Wen, and J. Wang, "Theoretical investigation of the sound attenuation of membrane-type acoustic metamaterials," Phys. Lett. A, **376**, 1489-1494, (2012).
[92] S. Zhou, and J. A. Hossack, "Reducing inter-element acoustic crosstalk in capacitive micromachined ultrasound transducers," Ultrasonics, Ferroelectrics and Frequency Control, IEEE Transactions on, **54**, 1217-1228, (2007).
[93] Y. Zhou, M. -H. Lu, L. Feng, X. Ni, Y. -F. Chen, Y.- Y. Zhu, S. -N. Zhu, and N. -B. Ming, "Acoustic surface evanescent wave and its dominant contribution to extraordinary acoustic transmission and collimation of sound," Phys. Rev. Lett., **104**, 164301, (2010).
[94] J. Zhu, J. Christensen, J. Jung, L. Martin-Moreno, X. Yin, L. Fok, X. Zhang and F. J. Garcia-Vidal "A holey-structured metamaterial for acoustic deep-subwavelength imaging," Nature Physics, **7**, 52–55, (2011).